SOLAR ASSISTED COMBINED POWER AND COOLING SYSTEM

BY

MD. TAREQ CHOWDHURY

A Thesis Presented to the
DEANSHIP OF GRADUATE STUDIES

KING FAHD UNIVERSITY OF PETROLEUM & MINERALS

DHAHRAN, SAUDI ARABIA

In Partial Fulfillment of the
Requirements for the Degree of

MASTER OF SCIENCE

In

MECHANICAL ENGINEERING

DECEMBER 2018

KING FAHD UNIVERSITY OF PETROLEUM & MINERALS

DHAHRAN- 31261, SAUDI ARABIA

DEANSHIP OF GRADUATE STUDIES

This thesis, written by **Md. Tareq Chowdhury** under the direction of his thesis advisor and approved by his thesis committee, has been presented and accepted by the Dean of Graduate Studies, in partial fulfillment of the requirements for the degree of **MASTER OF SCIENCE IN MECHANICAL ENGINEERING.**

Dr. Zuhair M. Gasem.
Department Chairman

Dr. Salam A. Zummo.
Dean of Graduate Studies

23/5/19
Date

Esmail
Dr. Esmail M.A. Mokheimer.
(Advisor)

Med Hasib
Dr. Mohamed A. Habib.
(Member)

Bilal Ahmed
Dr. Bilal Qureshi.
(Member)

© Md. Tareq Chowdhury
2018

Dedicated to my mother, my father, rest of my family and specially to my beloved twin nieces.

ACKNOWLEDGEMENTS

Alhamdulillah, all praise be to Allah for all the accomplishments I have until now and what is yet to come. It is only because of Allah's mercy, I was able to make it this far. He is the true protector and what an excellent helper he is to support his helpless creations! May peace and blessing prevail in this blessed land of two sanctuaries which was the sole reason to choose KFUPM as my destination. May Allah make my achievements in KFUPM fruitful for the awaiting career and accept my times in here as one of the means of salvation in the hereafter.

After that I would like to remember my dear family for their constant support, because of whom I feel a constant urge to finish my responsibilities in here and to have a happy reuniting with them. Apart from my mother and my father, special thanks to my twin nieces whose lovely faces make their homesick uncle feel like home while he is thousands of miles away.

I would like to thank my supervisor Professor Dr. Esmail Mokheimer for his continuous efforts and kind help. Professor Dr. Mohamed Habib's appreciation of good works and kind advices were a real inspiration indeed. Special thanks to Dr. Bilal Qureshi for his prompt responses and instantaneous supports all through the way. Thanks to honorable department chairman Dr. Zuhair Gasem for his kind support. Last and not the least, gratitude to the Bangladeshi and international community here in KFUPM for their company, being together as a band of brothers in my times at KFUPM.

TABLE OF CONTENTS

LIST OF FIGURES

APPENDIX FIGURES

LIST OF TABLES

APPENDIX TABLES

LIST OF ABBREVIATIONS

Abbreviations

A : area, m^2.

C : concentration ratio.

C_p : specific heat capacity under constant pressure, kJ/kg-K.

D : diameter, m.

Ex : exergy flow, kW.

ex : specific exergy, kJ/kg.

f : focal distance, m.

G_b : solar beam radiation, kW/m^2.

h : specific enthalpy, kJ/kg.

h_x : heat transfer coefficient of substance, W/m^2-K.

k : thermal conductivity, W/m-K.

K : incident angle modifier.

L : tube length, m.

m : mass flow rate, kg/s.

N : number of collectors.

Nu : mean Nusselt number.

P : pressure, kPa.

Pr : Prandtl number.

Q : heat rate, kW.

Ref : reference.

Re : Reynolds number.

s : specific entropy, kJ/kg-K.

T : temperature, K.

u : air velocity, m/s.

v : velocity of refrigerant, m/s.

V : volumetric flow rate of heat transfer fluid, L/min.

w : collector width, m.

W : rate of work, kW.

x : refrigerant mass concentration in solution.

Acronyms

ARC : Absorption Refrigeration Cycle.

BEP : Break-Even Point.

BWR : Back Work Ratio.

CAES : Compressed Air Energy Storage.

CCPP : Combined Cycle Power Plant.

CHP : Combined Heat and Power.

CPV : Concentrated Photovoltaics.

CPV/T : Concentrated Photovoltaics Thermal.

CFC : Chlorofluorocarbon.

COP : Coefficient of Performance.

CSP : Concentrating Solar Power.

CUF : Capacity Utilization factor.

DARC : Diffusion Absorption Refrigeration Cycle.

DNI : Direct Normal Irradiation.

DPL : Double Pressure Level.

EARC : Ejector-Absorption Refrigeration Cycle.

ERC : Ejector Refrigeration Cycle.

EES : Engineering Equation Solver.

ETC : Evacuated Tube Collector.

FPC : Flat Plate Collector.

GAX : Generator Absorber Heat Exchanger.

GT : Gas Turbine.

GTPP : Gas Turbine Power Plant.

HCFC : Hydrochlorofluorocarbon.

HFC : Hydrofluorocarbon.

HFE : Hydrofluoroether.

HFO : Hydrofluoro-olefins.

HRVG : Heat Recovery Vapor Generator.

HTF : Heat Transfer Fluid.

HVAC : Heating Ventilation and Air Conditioning.

LFR : Linear Fresnel Reflector.

LMTD : Log Mean Temperature Difference.

LCOE : Levelized Cost of Electricity.

NBP : Normal Boiling Point.

NFCPV/T : Nanofluid Concentrated Photovoltaics Thermal.

ORC : Organic Rankine Cycle.

PFC : Perchloro-fluoride.

PPT : Pinch Point Temperature.

PTC : Parabolic Trough Collector.

PV : Photovoltaics.

PVPP : Photovoltaic Power Plants.

RC : Rankine Cycle.

SCAES : Solar Compressed Air Energy Storage.

SHX : Solution Heat Exchanger.

SNL : Sandia National Laboratories.

SPAC : Solar Powered Absorption Chiller.

ST : Steam Turbine.

STPP : Steam Turbine Power Plant.

TPL : Triple Pressure Level.

TV : Throttle Valve.

VCRC : Vapor Compression Refrigeration Cycle.

VCARC : Vapor Compression Absorption Refrigeration Cycle.

WF : Working Fluid.

WHR : Waste Heat Recovery.

Subscripts.

0 : atmospheric conditions.

a : aperture.

abs : absorbed, absorber.

air : ambient air.

am : temperature of ambient.

c : cover.

ca : between solar collector cover and ambient.

ci : inner cover.

co : outer cover.

con : condenser of ARC/EARC.

cond : condenser of ORC.

cr : between solar collector cover and receiver.

D : diffuser.

d : destruction.

e : exit.

el : electric.

ev : evaporator.

Ex : exergetic.

Exp : expander.

expv : expansion valve.

fluid : heat transfer fluid.

g : generation.

gen : generator.

i, in : inlet.

is : isentropic.

loss : losses.

mean : mean temperature.

M : mixing chamber.

N : nozzle.

NH_3 : ammonia.

NH_3-$LiNO_3$: ammonium lithium nitrate.

NH_3-NaSCN : ammonium sodium thiocyanate.

o : outlet.

oc : ORC condenser.

op : ORC pump.

ot : ORC turbine.

out : outlet.

opt : optical.

p : pump.

parallel : parallel arrangement of collector.

pp : pump power.

r : receiver.

ri : inside of receiver.

ro : outside of receiver.

r-f : receiver to fluid.

rev : reversible process.

s-r : sun to receiver.

series : series arrangement of collector.

sp : solution pump.

strong : higher concentrated refrigerant solution.

sun : sun outer layer.

th : thermal.

u : useful (PTC).

vap : vaporizer.

weak : lower concentrated refrigerant solution.

Greek symbols

α : absorbance.

γ : intercept factor.

ΔP : pressure drop, kPa.

η : efficiency.

ε : heat exchanger effectiveness.

ϵ : emittance.

μ : viscosity, kg/m-s.

ω : entrainment ratio.

π : pi.

ρ : density, kg/ m^3.

ρ_c : concentrator reflectance.

σ : Stefan-Boltzmann constant, 5.67 x 10-8 W/m^2-K^4

θ : incident angle, degree.

τ : transmittance.

ABSTRACT

Full Name : Md. Tareq Chowdhury.
Thesis Title : Solar assisted combined power and cooling system.
Major Field : Mechanical Engineering.
Date of Degree : December, 2018

With the advent of fast depletion of fossil fuel reserves along with its hazardous impact on the environment, energy industries are coming up with sustainable alternatives like solar assisted integrated system for the combined production of power and cooling. In this regard, a new solar assisted combined power and cooling system is presented and analyzed in this thesis for the climatic conditions of Dhahran, Saudi Arabia. The proposed system consists of parabolic trough collectors (PTC), Organic Rankine Cycle (ORC) and Ejector Absorption Refrigeration Cycle (EARC). The steady state analysis aimed at assessing the performance of solar assisted ORC coupled with EARC using the first and second law analysis. The use of NH_3-$LiNO_3$ as the working pair in EARC is investigated.

PTC is used as the heat source for the combined system and performance of PTC was investigated for different inlet temperatures and various volumetric fluid flow rates. PTC accounted for 60-80% of the total exergy destruction depending on the solar irradiation followed by ORC and EARC. In EARC, generator and evaporator temperature were maintained at 363 K and 273 K respectively, while for both absorber and condenser, the temperature was 308 K. It was found that due to the pressure recovery attained by the ejector, pump power consumption was significantly reduced in EARC thus higher COP was achieved in comparison to basic single effect ARC. Generator temperature and

Solution Heat Exchanger (SHX) effectiveness were also found to be highly influencing the performance of the refrigeration system. Among different types of fluids used in ORC, R134a was found to be a suitable choice for lower turbine inlet temperature around 363 K whereas for higher turbine inlet temperature of 550 K, Toluene showed superior performance. System performance factor of the combined system, which is defined as the ratio of total power and cooling output to the solar energy input, varied from 13.96% to 16.57% of the hourly variation of solar irradiation for the climatic conditions in Dhahran when R134a was used as ORC fluid at the turbine inlet temperature of 362.8 K. The Exergy efficiency of the combined system varied from 5.69% to 7.25%. Toluene exhibited superior performance in the combined system showing highest system performance factor of 25.31% and exergy efficiency of 17% at turbine inlet temperature of 550 K and solar irradiation of 1 kW/m^2.

ملخص الرسالة

الاسم الكامل: محمد طارق شودري

عنوان الرسالة: نظام توليد طاقة وتبريد مدمج مدعوم بنظام شمسي

التخصص: الهندسة الميكانيكية

تاريخ الدرجة العلمية: ديسمبر 2018

مع ظهور النضوب السريع لاحتياطيات الوقود الأحفوري إضافة إلى أخذ جانب تأثيرها الخطير على البيئة، فإن صناعات الطاقة تأتي ببدائل مستدامة مثل النظام المتكامل بمساعدة الطاقة الشمسية للإنتاج المشترك للطاقة والتبريد . في هذا الصدد، تم تقديم وعرض نظام جديد مختلط للطاقة والتبريد مدعوم بالطاقة الشمسية وتحليله في هذه الأطروحة بناء على الظروف المناخية في منطقة الظهران، المملكة العربية السعودية. يهدف تحليل الحالة المستقرة إلى تقييم أداء دورة رانكن العضوية المدعومة بالطاقة الشمسية إلى جانب دورة التبريد الامتصاصي باستخدام القاذف باستخدام تحليل القانون الأول والثاني .تم التحقيق في استخدام (NH_3-$LiNO_3$) كزوج عامل في دورة التبريد الامتصاصي باستخدام القاذف.

تم فحص أداء مجمعات القطع المكافئ كمصدر للحرارة عند درجات حرارة مختلفة عند المدخل ومعدلات تدفق السوائل الحجمي لسائل نقل الحرارة. شكّل نظام مجمعات القطع المكافئ نسبة تتراوح بين 80-60 ٪ من إجمالي تدمير الإكسيرجي اعتمادا على الإشعاع الشمسي تليه دورة رانكن العضوية ودورة التبريد الامتصاصي باستخدام القاذف. وتم الحفاظ على درجة حرارة المولد والمبخر عند 363 K و273 K على التوالي في دورة التبريد بامتصاص القاذف، بينما كانت درجة الحرارة في كل من الامتصاص والمكثف 308 درجة مئوية. انخفض استهلاك طاقة المضخة بشكل كبير في دورة التبريد بالامتصاص والذي يعزى بسبب استرداد الضغط الذي تحقق في القاذف، والذي بدوره ادى الى انجاز أعلى في معامل اداء النظام مقارنةً بالتأثير الفردي الأساسي لدورة التبريد بالامتصاص. مولد الحرارة وفعالية المبادل الحراري المعالج أيضًا وُجد أنَ لهما تأثير بشكل كبير على أداء نظام التبريد .من بين الأنواع المختلفة من السوائل المستخدمة في ودورة رانكن العضوية، تم العثور على (R134a) ليكون خيارًا مناسبًا لدرجات الحرارة المنخفضة عند مدخل التوربينات التي تتراوح في حدود 363 كلفن، في حين أظهر تولين أداءً متفوقاً لدرجة الحرارة العليا عند مدخل التوربين والتي تبلغ 550 كلفن. عامل أداء النظام في النظام المشترك والذي يُعرف بأنه

نسبة إجمالي الطاقة وخرج التبريد إلى مدخلات الطاقة الشمسية، والذي تراوح من 13.96٪ إلى 16.57٪ نسبة للتغير في الساعة للإشعاع الشمسي للظروف المناخية في الظهران عند استخدام R134a كسائل في دورة رانكن العضوية عند درجة حرارة في مدخل التوربين تبلغ 362.8 كلفن. تراوحت كفاءة الإكسيرجي للنظام المشترك من 5.69 ٪ إلى 7.25 ٪ .أظهر التولوين أداءً فائقًا في النظام المشترك، حيث أظهر أعلى عامل أداء للنظام بنسبة 25.31٪ وكفاءة الإكسيرجي بنسبة 17٪ وكانت درجة الحرارة عند مدخل التوربين تبلغ 550 كلفن وإشعاعات شمسية تبلغ 1 كيلو واط / متر مربع.

CHAPTER 1

INTRODUCTION

Harnessing energy has always been a prime concern for the civilization of post-industrial revolution. In recent decades, preservation of the environment has become one of the top priorities while utilizing energy for power and cooling applications due to increasing concern for Ozone depletion, global warming and non-sustainable nature of traditional energy sources. As reported, more than half of the total energy produced is lost without any kind of useful utilization in the form of waste heat [1]. Utilizing the huge amount of waste heat to produce useful energy will be a great mean to relieve the pressure significantly for growing energy needs. That is why the world today is looking for technologies that will be sustainable, environment friendly and at the same time, energy efficient. Energy consumption of heating and cooling systems could be as much as 30% in comparison with the total consumption in developed countries [1]. To compete with the relatively cheap conventional fossil fuel powered energy, renewable energy powered multigeneration systems become an attractive choice to provide power, heating and cooling simultaneously. In the Arabian Gulf region, industrialization and urbanization are thriving at a great momentum resulting in huge energy needs. Particularly in Saudi Arabia 15% of the oil production [2] and more than 50% of the gas production are utilized for the generation of electricity [3]. Apart from the regular needs, desalination accounts for 20% of the total energy consumption and 70% of the electricity is consumed for air conditioning and cooling are consuming lots of energy [4], [5], [6] . So, the country has a challenging task to develop a sustainable solution for its energy needs.

Among the renewable energy technologies, the prospect of solar energy is very promising for Arabian Gulf due to its geographical location. It is clean and endless with more than enough spaces for the installation and distribution of the solar appliances [7]. Solar energy can be utilized to develop power, heating and cooling systems for both residential and industrial applications.

Apart from the popular traditional power producing Rankine and Brayton cycles, emerging technologies like Kalina, Goswami and Organic Rankine Cycles are also securing grounds in the market for their combined power and cooling production capabilities. Goswami cycle is not that compatible for the hot climate region as its difficult to get cooling due to high sink temperature. On the other hand, the Kalina cycle requires way higher optimum pressure in its evaporator, lower net produced power in comparison with ORC [8]. ORC has simple configuration, offers superheated turbine outlet flow with more reliability. Although gas and steam cycles have been playing a dominant role for decades, it is proven that they are not that efficient to produce power using low temperature energy sources [9], [10]. ORC is a deserving candidate to fill that void as it showed a huge promise in generating power and utilizing low temperature heat sources [11]. It is similar to Rankine cycle with the exception of organic substances as working fluid in substitute of water. Along with power generation, the waste heat can be utilized in cogeneration plants or cooling system by means of cascaded refrigeration system or absorption refrigeration system as bottoming cycle [12]. Ejectors can be employed for cooling as well [13]. In case of solar powered trigeneration or multigeneration systems, the Refrigeration cycle can take thermal energy from both the solar collector and the waste heat from the ORC expander exhaust.

The prime objective of the current research is to predict the thermal performance of a proposed solar powered combined power and cooling cycle using first and second law analysis. It is further aimed at tracing the locations of exergy destructions and the amount of energy lost during the processes for further development of the performance of the system.

The following objectives are outlined for the analysis.

1. Conducting a comprehensive literature review on suitable CSP technology for power generation in ORC along with the literature review of the performance of different working fluids in ORC and the absorption cooling system.
2. Develop mathematical models for each component of the proposed system.
3. Develop mathematical model for the whole system.
4. Develop a computer code, using EES software, to simulate the performance of different components and the performance of the whole system.
5. Validate the developed simulation code against previous related work in public literature.
6. Conduct a parametric study to obtain the optimal performance of the system for different operating conditions under first and second laws of thermodynamics.

CHAPTER 2

LITERATURE REVIEW

2.1 Introduction

According to International Energy Agency it is found that the energy matrix is dominated by fossil fuel with 81% contribution in energy production, whereas in case of electricity generation it was 68.5% [14]. But the matter of concern is that more than half of the total energy generated is converted into a form of waste heat without any kind of useful utilization because it is discarded in the absence of efficient energy recovery methods [10]. Among many technologies, Organic Rankine Cycle (ORC) has shown a promising development to recover this energy from being wasted. Low temperature energy sources such as geothermal, industrial waste heat, biomass and solar energy resources can act as suitable heat sources for ORC. ORC can utilize these heat sources effectively up to 400°C and power output lower than 2 MW [15]. ORC is like a classical Rankine cycle where water is substituted with organic substances to work as the working fluid. Organic Rankine cycle (ORC) is an efficient heat to power conversion technology that can be integrated with low temperature heat sources. Since it is taking thermal energy input from external heat sources, there is no need to have a combustion chamber hence no burning of fossil fuels. Combination with cogeneration and cooling system using ORC expander's exhaust heat, enable the combined system to meet up heating and cooling loads on demand.

On the other hand, there are growing cooling needs for industrial and residential appliances. In developed countries, 30% of the power produced are consumed by HVAC systems. For example, in Saudi Arabia, 55% of the electric power produced is consumed for air conditioning and in large cities like Jeddah it can be over 60% [16]. The low temperature heat sources can be utilized to provide cooling needs. Since the conventional Vapor compression Refrigeration Cycle (VCRC) consumes a large amount of electricity, the absorption refrigeration system is a competent alternative because of its capacity to utilize low temperature heat sources to produce cooling. Absorption Refrigeration Cycle (ARC) is capable of working on different pressure levels along with a wide range of temperature ranges.

2.2 Renewable Energy Sources

The total capacity of ORC installed worldwide is around 2,701 MW distributed over 1,754 units as of December 31st, 2016 [16]. A global map of ORC database is created by ORC world map to track the locations of ORC installations worldwide and according to their estimation, planned new capacity of 523.6 MW_{el} in 75 new plants were to be materialized in 2016 [17]. Figure 2.1 is illustrating the heat sources and their contribution in global power production of ORC.

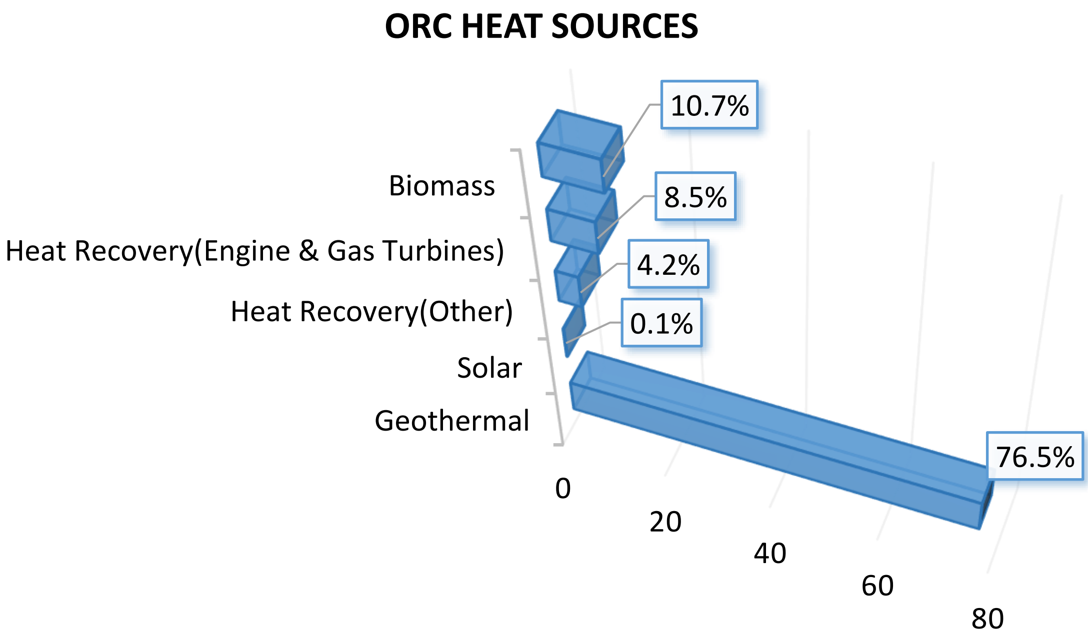

Figure 2.1 Heat Sources of ORC [7], [8].

The largest capacity of ORC installations belongs to USA followed by Turkey, New Zealand and Philippines. Geothermal energy is taking the lead as the heat source for ORC in terms of capacity followed by biomass and other thermal sources. From the ORC map commercially operated 23 solar powered ORCs (s-ORC) can be seen to be commissioned up to 4000 kW range. Low capacity off-grid ORCs and experimentally operated ones in different research facilities were excluded.

Even though solar powered ORC seemed very little in terms of capacity from Figure 2.1, Landelle et al. [18] concluded that 23% of the researches on ORC are on solar applications. An exclusive database of on ORC with 175 scientific references, including over 100 experiments was documented where Combined heat and power (CHP) production accounts for 13% of the ORC projects with mostly closed source applications. All the biomass or gas-powered applications and 30% of the solar targeted applications aim to produce CHP.

Landelle et al. [18] also documented that heat source temperature range of ORC is around 80°- 300°C and capacity to be 10 kW_{el}-10 MW_{el}.

2.3 Solar Energy Assisted Technologies

Two competing technologies in the industry are the solar photovoltaic (PV) and solar thermal technologies. Solar PV technology is emerging as a competent renewable energy source in comparison to conventional fossil fuel-based technologies [19], [20]. The solar cell market is still dominated by silicon based technologies [21] and they are way more expensive to implement in comparison with conventional energy sources [22] . But after the innovation of cheap and highly efficient solar cells like Perovskite and many other parallelly developed new generation of solar cells, PV is coming as a true competitor to conventional technologies [23]. In fact, perovskite's power conversion efficiency (PCE) has increased from 3.8 to 22.7% within a short period of time [24]. On the other hand, solar thermal technologies are gaining strong ground in the industry in parallel to PV technologies as well. Leaving behind the primitive solar still technologies and the last generation flat or non-concentrated solar collectors, concentrated solar collectors are coming with lots of potential over a wide range of operating temperatures [25]. Effective cooling system for PV technologies are still in developing phase to secure high performance of the PV cells since the efficiency of PV cells reduce drastically at higher temperature [26]. Concentrated Solar Power (CSP) technologies like central receiver solar tower technology can generate very high temperature for generating power. There are parabolic trough collectors (PTC) that can operate over a wide range of temperatures according to the needs and it is very widely used in renewable industries for generating power and refrigeration. There are technologies like linear Fresnel reflector (LFR), which also works on low to medium level temperature ranges [27].

2.3.1 An Illustration on PV and CSP Research

As mentioned earlier, many researches are ongoing on solar PV and CSP technologies of different types on diverse concentrations. A life cycle analysis was conducted for PV power plants to investigate their contribution on reducing Green House Gas (GHG) and evaluating the feasibility of PVPP in the long run [14]. Janda et al. [28] did the study on the merit order effect of PV generation, first in Slovakia and concluded that PV generation is contributing to lower the electricity prices analyzing the data of 2011-16. According to their research, 1% increase in solar energy generation reduced the wholesale electricity price by 0.055%. But it was also added that the edge of PV electricity was largely dependent on government subsidies and the savings could not outweigh the solar support costs.

Many hybrid systems are built for higher energy efficient performance by incorporating PV with other renewable technologies like CSP, wind turbines etc. An outstanding technoeconomic study was done by J.A. Aguilar-Jiménez et al. [29] on a hybrid PV-CSP with thermal storage to support the energy needs of an isolated micro-grid. The system incorporated a PV power generation capacity of 73 kW along with an ORC of 30 kW to provide backup power when needed. Levelized cost of electricity (LCOE) for this PV-CSP combination was found to be only 2% higher than the PV-Battery arrangement and it decreased further with increasing demand. If the demands were to exceed 500 kW, the LCOE of PV-CSP would be 26% lower than the PV-Battery combination according to the estimation.

A cogeneration of transmitting PV and solar thermochemical process was devised to produce electricity and solar syngas [30]. After transmitting through the PV modules, the infrared solar spectrum got converted into high grade chemical exergy resulting from thermochemical reactions in syngas. The total efficiency of the system was found to be 55%.

Icaza et al. [31] investigated an off-grid hybrid system of PV and wind turbine in Ecuador and a feasibility analysis was conducted using a model they developed in MATLAB. The investigation concluded that the considered system was favorable and feasible to add to the renewables in the region.

CPVT technologies are widely used for simultaneous generation of electricity and thermal energy [32], [33]. PV and CSP technologies are coupled for this cogeneration purposes. Ben Youssef et al. [34] developed a 2-D numerical model of concentrating PV/T (CPVT) for simultaneous generation of electricity and thermal energy followed by a detailed economic analysis for Tunisia and Chambery. A PTC utilized the solar beam radiation and concentrate it to the rectangular receiver which was in contact with the PV cell. The receiver arrangement worked as coolant for the PV cells and in the meantime produced thermal energy. The research investigated the effect of wind velocity, beam radiation, coolant type, fluid velocity on the thermal and electrical output of the system. A similar Concentrating Photovoltaic Thermal (CPVT) system was developed which was suitable to integrate into building facades. In this case, PV cells were directly immersed into dielectric liquids [35]. Two different dielectric liquids were considered namely, deionized water (DIW) and iso propyl alcohol (IPA). IPA was found to be the better option achieving optical efficiency of 81%.

As for the effect of nanofluids in this regard, a novel nanofluid based CPVT was proposed choosing PTC as the heat source for the ORC [36]. The performance of the Nano-Fluid Concentrating Photovoltaic Thermal (NFCPV/T) was found to be better than conventional CPV/T for the concentration ratios greater than 7. The performance of the system improved further when integrated with ORC.

An experimental trigeneration set up [37] was built in Zaragoza (Spain) to provide electricity, fresh water and sanitary hot water on domestic level. Four PV/T collectors and a wind turbine provided the electricity. On the other hand, sanitary hot water was produced by the joint contribution PV/T collectors and an evacuated tube collector . Membrane desalination and reverse osmosis technique was employed to get fresh water. The setup was tested all over the year and proved to be a sustainable solution for off grid areas. The model was also validated in TRNSYS.

A technoeconomic and environmental feasibility analysis was modelled using the software LINGO to find the most suitable renewable energy technology with the grid. PV, CSP, Biomass, absorption chillers were considered for the comparative analysis [38]. Biomass was found to be a good alternative of natural gas for the production of heat. As for cooling needs, electricity driven technologies were recommended over heat driven absorption chillers. Another technoeconomic assessment was presented for a hybrid system comprising of PV, fuel cell, GT, Compressed Air Energy Storage (CAES). It was reported that the usage of CAES increased the system efficiency by 25% when the compressor was switched off. Optimum pressure for the fuel cell and relevant optimum capacities of components were also determined [39]. It should be noted that the integration of CEAS is well suited for large capacity plants for higher efficiency with the added advantages of lower carbon emission. The research proposed by Chen et al. [40] outlined a novel CSP assisted CAES system to supply the turbine with higher air temperature and reported exergy efficiency of 50%.

Researches on stand-alone CSP systems and hybrid systems involving CSP are also going on [41], [42], [43]. A PTC assisted combined cycle power plant was modelled where the externally fired gas turbine (EFGT) was supported by biomass. An ORC was employed as a bottoming cycle [44]. Presence of Thermal Energy Storage (TES) in between the cycles secured uninterrupted operation of the system. Levelized cost of energy (LCOE) of the proposed system was 140 €/MWh and it was concluded that the system would be profitable only with the support of government subsidies and special tariffs for renewables. With the supply of 9 MW_{th} input, EFGT and ORC system were able to return 1.3 MW_{el} and 0.7 - 0.8 MW_{el} output respectively.

Concentrating Solar Power technologies are extensively used in thermal desalination to produce water. A technoeconomic analysis of a solar tower CSP technology of 100 MW integrated with a Multi Effect Desalination (MED) plant with a capacity of 45000 m^3/day was carried out. It was concluded that the DNI was the main reason affecting the production cost [45]. Low DNI causes higher cost for the molten salt output in the solar tower. As for average unit electricity cost, CSP allocated 83% where RC allocated the rest. A similar model with Rankine cycle analyzed the exergy costs of the plant and concluded that the integration of MED plant increased the exergy destruction in comparison to stand alone CSP-Rankine cycle [46].

A solar dish collector of 10.29 m^2 area and concentration ratio of 28.46 was investigated incorporating four different nanoparticles in the fluid, namely Cu, CuO, TiO_2 and Al_2O_3

[47]. Al_2O_3 was found to be working better in terms of thermal efficiency while on the perspective of exergy, CuO had the edge over the rest of the nanofluids. Exergy efficiency was found to be 10% in general and due to high optical losses, thermal efficiency was limited to 35%.

2.3.2 Solar Photovoltaic (PV) System versus Concentrated Solar Power (CSP)

In case of large-scale power production, cost of concentrated solar power (CSP) with Thermal Energy Storage (TES) is found to be significantly less than the PV installations with electro-chemical batteries. With the same value of capacity utilization factor (CUF), levelized cost of electricity (LCOE) for the PV system was at least 0.26 $/kWh, where for PTC-ORC system it was only 0.19 $/kWh. This result indicates more reliability of PTC-ORC than the PV system if ORC system is coupled with a cost-effective TES. It should be noted that CUF is the ratio of actual energy generated by the plant annually to the expected annual generation of energy if it were to operate at rated capacity for all 8760 hours (24/7) of the whole year. On the other hand, LCOE is defined as the ratio in between the present value (in USD) of lifetime investment in the plant and total expected energy generation (in kWh) over plant life. Figure 2.2 depicts a PTC assisted ORC power model.

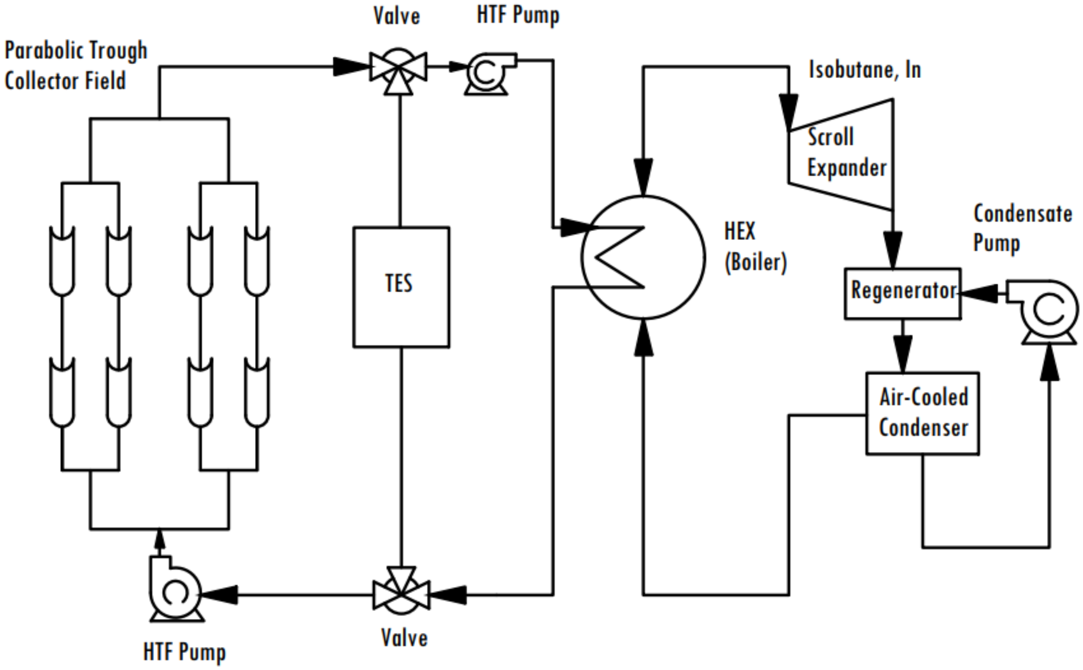

Figure 2.2 PTC-ORC model redrawn from Patil et al. [48].

PV is an intermittent source of electricity in absence of batteries and it is a known fact that storing electricity with batteries are not an economic option till now. When a solar assisted ORC system favors the incorporation of thermal storage, PV becomes expensive with the addition of batteries [48].

Bellos et al. [49] made a comparative analysis of low temperature linear CSP technologies for Greek climate through a technoeconomic assessment in between PTC and LFR. In terms of both yearly thermal and yearly electrical efficiency, PTC was found to be better performing than LFR. At fluid temperature level of 350°C, yearly thermal efficiency of PTC and LFR was found to be 52.25% and 35.39%, respectively whereas for electrical efficiency, it was 16.11% and 10.92% for PTC and LFR respectively. In terms of exergy efficiency LFR performed better than PTC with 29.28% while the latter showed 19.83%.

LFR was also found to be an economic choice if the specific cost could be curtailed to 185 €/m^2.

2.3.3 Parabolic Trough Solar Collector (PTC)

Concentrated Solar Power (CSP) system can be divided into two types: line-focusing type and point focusing type. PTC and LFR collectors are line focusing type where solar energy is designed to focus on a long tube [50]. In point-focusing technologies like solar towers and parabolic dishes, solar energy is directed to a specific point in a receiver which is accommodated in a tower in general. Point focusing technologies can have relatively very high concentration ratio and thermal efficiency. It can operate temperature exceeding even 1500°C [51]. But these technologies are not economical to utilize low temperature waste heat.

According to updated NREL concentrating Solar Power Projects Database including the projects initiated in 2018, it is found that more than 80% of the CSP installations operational globally are based on the parabolic trough technology demonstrating its mature technology [52]. In linear concentrating system, parabolic shaped mirror and a receiver tube are placed along the focal axis of the parabola. To increase collector efficiency by limiting the convection losses, a glass envelope is placed around the heat collection elements (HCE). Operating temperature range is 50-400° C with a concentration ratio range of 15-50 [53]. It should be noted that, concentration ratio is defined as the ratio of aperture area to the area of the receiver. Collector axis should be oriented either in a north-south or east-west direction to minimize losses. This kind of CSP technologies is supported by single axis tracking. PTC concentrates solar Direct Normal Irradiation (DNI) to a heat transfer fluid like Glycerol, Duratherm or the likes of thermal oil. Figure 2.3 is demonstrating an ORC plant utilizing PTC as heat source and it has the capability of district heating and power generation.

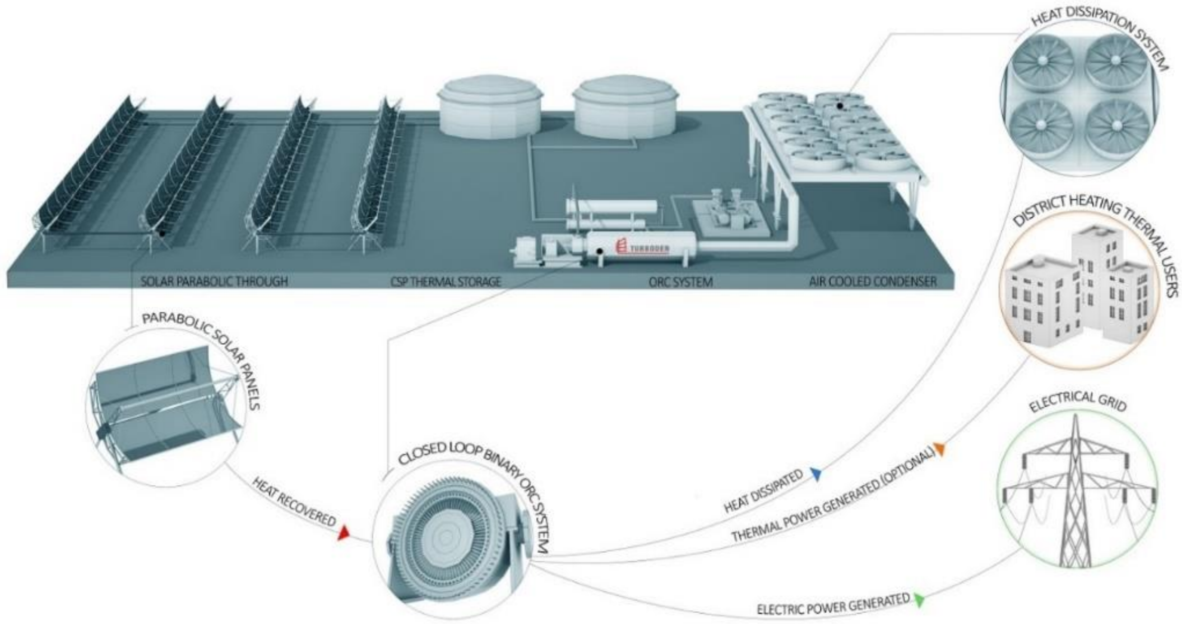

Figure 2.3 A Multigeneration schematic in combination of PTC-ORC of Turboden, Mitsubishi Heavy Industries [54].

Research is being conducted on different directives to improve the optical and thermal efficiency of PTC through the better material, coatings, higher tracking accuracy, curbing heat loss etc. [43]. Bellos et al. [55] investigated on the optimum number and location of internal fins in the absorber of PTC and concluded that higher fins resulted better efficiency but with more pressure drop. Many experimental set ups were built using locally available materials to achieve a competitive market price [56], [57]. PTC is integrated with GTPP, CCPP and similar cycles for better use of energy with higher efficiency [58], [59]. GE, ORMAT, Turboden, GMK, EXERGY are some of the leading companies to invest in Organic Rankine Cycle power projects on various scales in terms of capacity [60].

2.3.4 Linear Fresnel Reflector (LFR)

A Linear Fresnel Reflector (LFR) collector is a line focusing CSP system where direct normal irradiation (DNI) is reflected to a stationary receiver tube. Independently movable long strips of mirrors construct the foundation of this kind of CSP collectors. It also uses single axis tracking like PTC. The main difference of LFR with PTC is that LFR has discrete mirrors close to the ground while PTC has continuous reflector that gradually erects upward from the ground. LFR sometimes includes a secondary reflector to utilize more solar irradiation to its absorber. The use of discrete mirror strips accounts for reduced wind loads and simplicity of construction [61]. A typical LFR plant schematic is shown below in Figure 2.4.

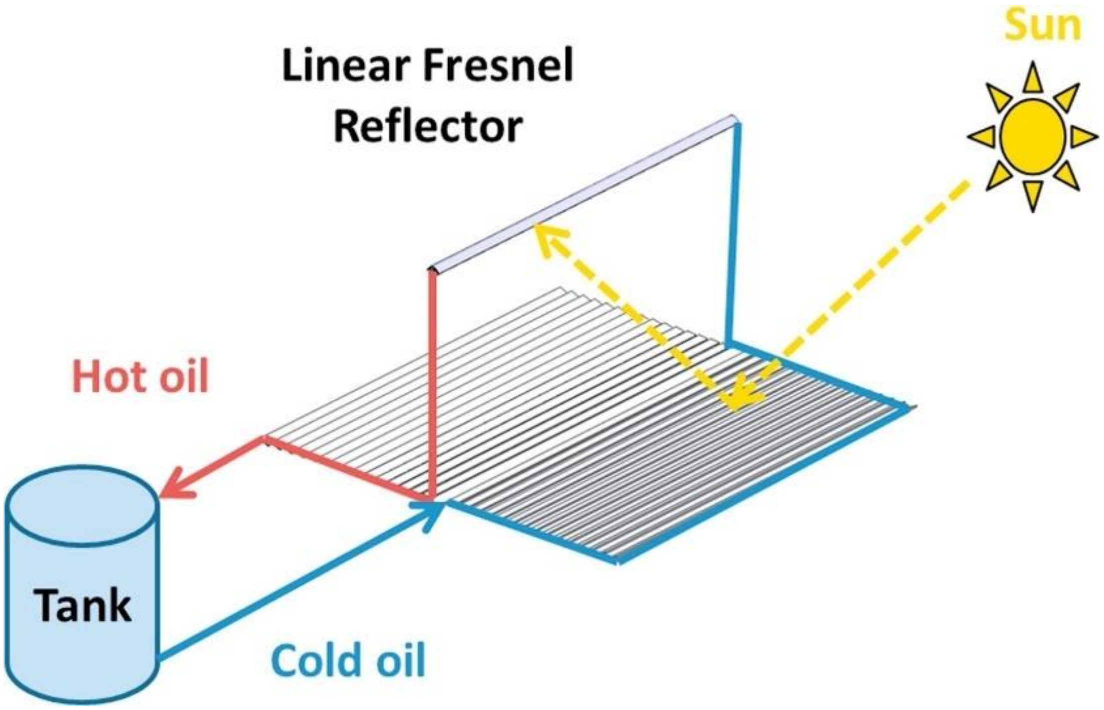

Figure 2.4 Schematic of a LFR plant, used with permission (Appendix D) [61].

Relative cost is very low for this technology. HTF temperature is about 50-300°C range and concentration ratio of 10-40. Thermodynamic efficiency is not that high, but LFR is more economic for its low reflector costs [27].

2.4 Organic Rankine Cycle (ORC)

For utilizing low grade heat sources cycles like ORC, supercritical Rankine cycle [62], [63], [64], Goswami [65], Kalina [66], [67] have been introduced into operation. Numerous researches have been reported integrating these cycles for combined power and cooling production. ORC has gained high reliability due to its simple structure and ease of maintenance. The organic nature of working fluids also acts as lubricators for the rotating equipment.

2.4.1 Components and Working Principle of ORC

ORC has four main components: An evaporator for receiving waste heat or low temperature heat from solar or geothermal sources, an expander or turbine producing work by the expansion of HTF, a condenser for releasing heat to the environment and a pump for increasing the pressure of the working fluid while recirculating HTF back to the evaporator.

When ORC is coupled with cogeneration or cooling systems, the heat is released via heat exchangers or gets stored in a thermal heat storage tank for further utilization. So, from Figure 2.5, the thermodynamics of ORC cycle can be summarized in 4 steps :

- Process 1-2 : liquid compression ($P_{low} \rightarrow P_{high}$)
- Process 2-3 : evaporation (Liquid → Vapor)
- Process 3-4 : vapor expansion ($P_{high} \rightarrow P_{low}$)
- Process 4-1 : condensation (Vapor→Liquid)

Net power output, W_{net} : $W_{exp} - W_{pp} > 0$

Working medium : organic fluid.

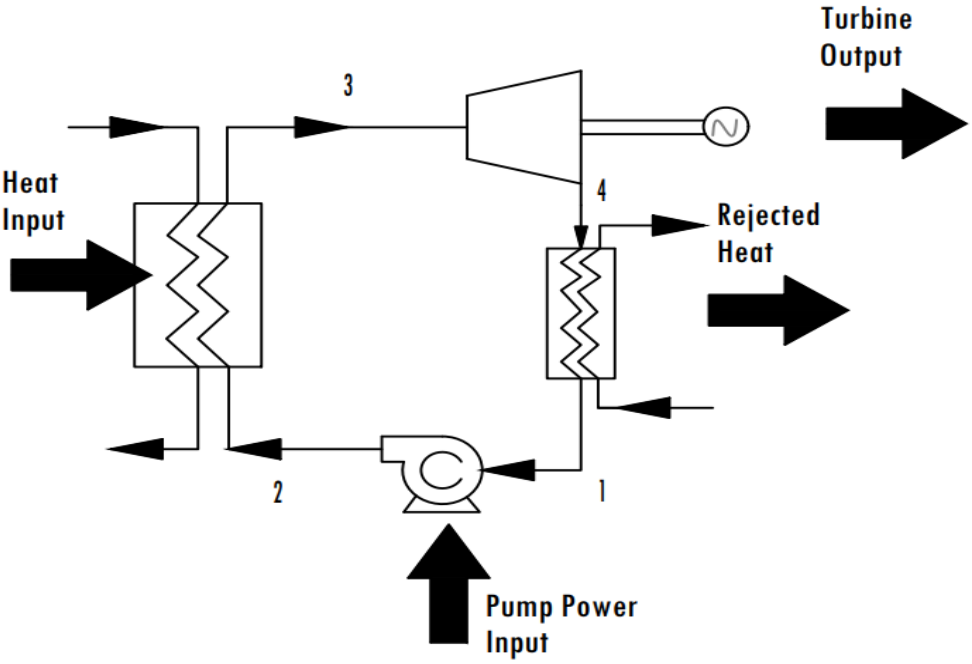

Figure 2.5 Thermodynamic processes of ORC.

Even though higher evaporator pressure gives better efficiencies, there needs to have a minimum temperature difference between the hot and cold fluid to enable heat transfer in between them. This parameter is called pinch point which should always be positive. If pinch point (PP) drops down to a smaller value it will make the temperature gradient very small thus occurring very low heat transfer rate that also corresponds to a large heat transfer area and increasing costs [10]. The significance of pinch point can be seen from the following Figure 2.6.

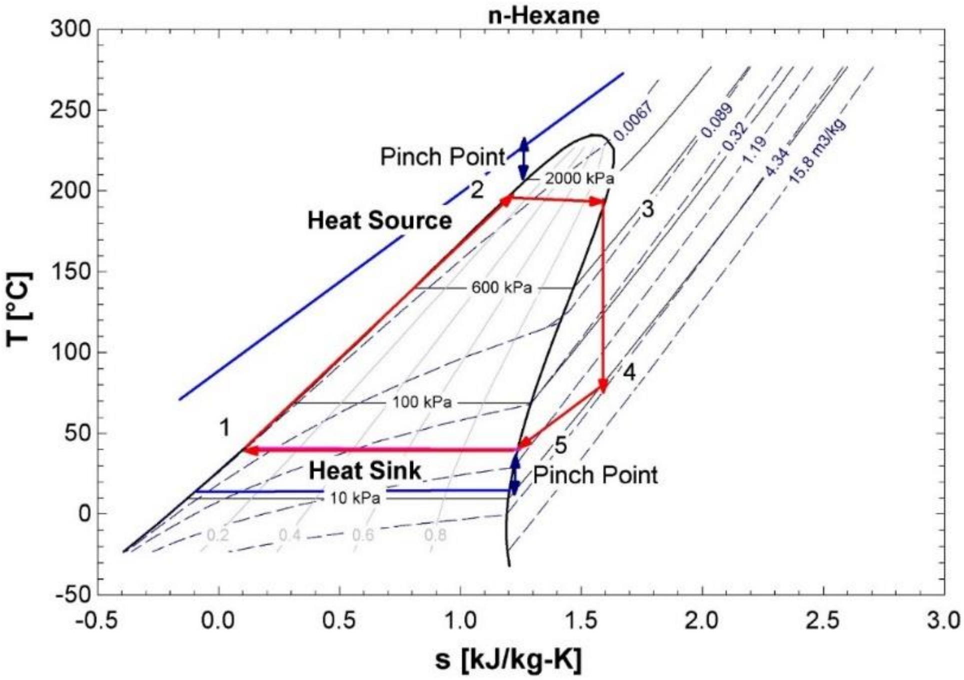

Figure 2.6 Importance of pinch point (PP), redrawn from [10].

2.4.2 ORC Working Fluid Classification and Thermodynamic Properties

Pure heat transfer fluids are classified into three categories according to the nature of their saturation curves: wet, isentropic and dry. Some of the properties are tabulated below in Table 2.1 followed by Figure 2.7 - Figure 2.9 to illustrate the thermodynamic properties of different types of fluids.

Table 2.1 Pure fluid classification.

Type	***Wet***	***Isentropic***	***Dry***
Saturation Curve Slope	Negative	Zero	Positive
Superheating	Needed	Not Needed	Not Needed
Enthalpy drop during Expansion	Higher	Lower	Lower
Expander Type	Multistage	Single Stage	Single stage
Regenerator	Needed	No Need	Needed
Turbine Blade Erosion	High	Low	Low

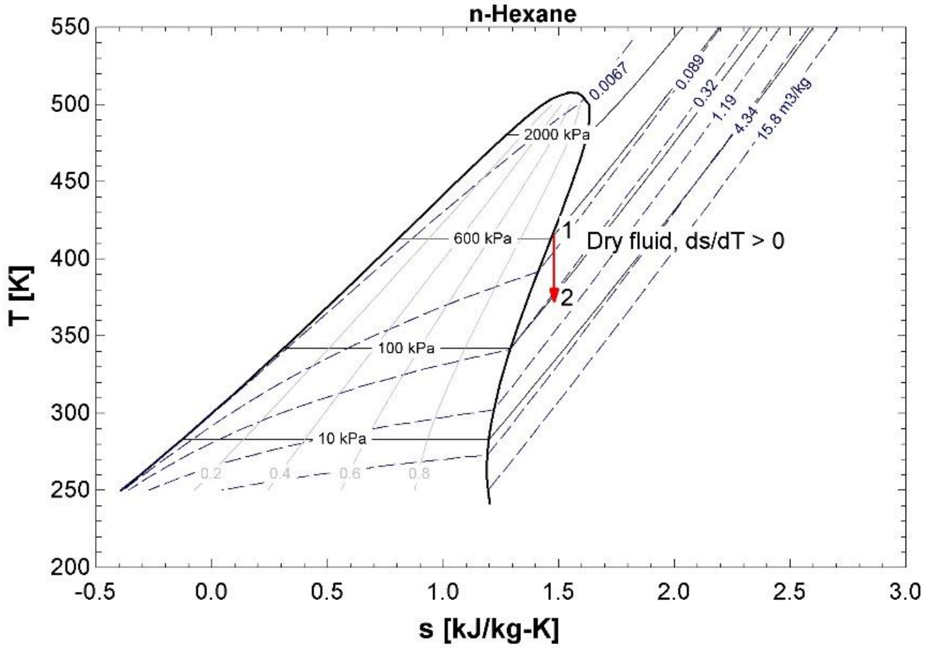

Figure 2.7 T-s diagram of wet fluid (n-Hexane).

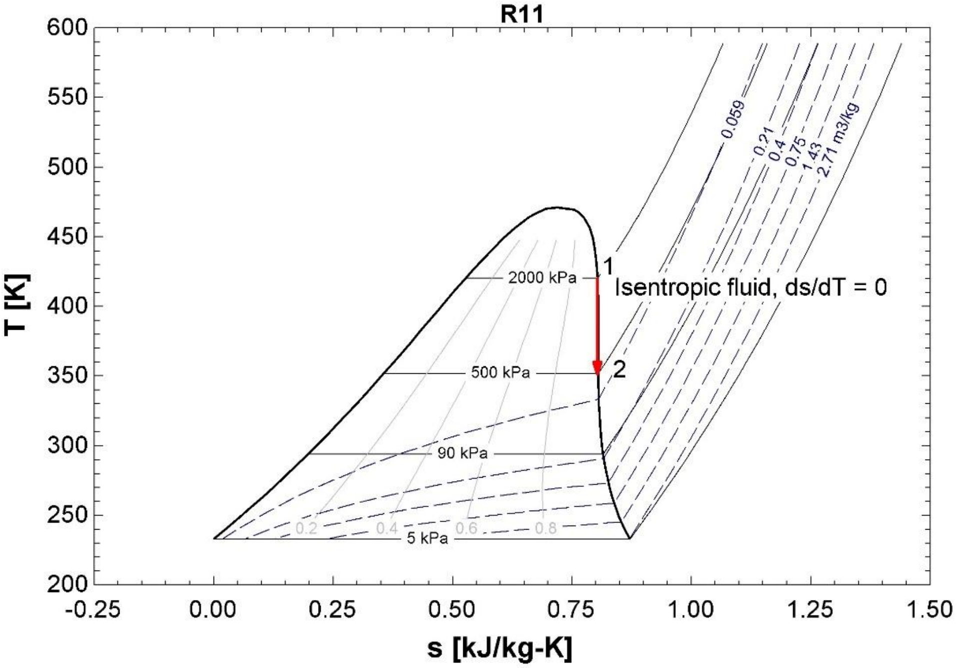

Figure 2.8 T-s diagram of isentropic fluid (R-11).

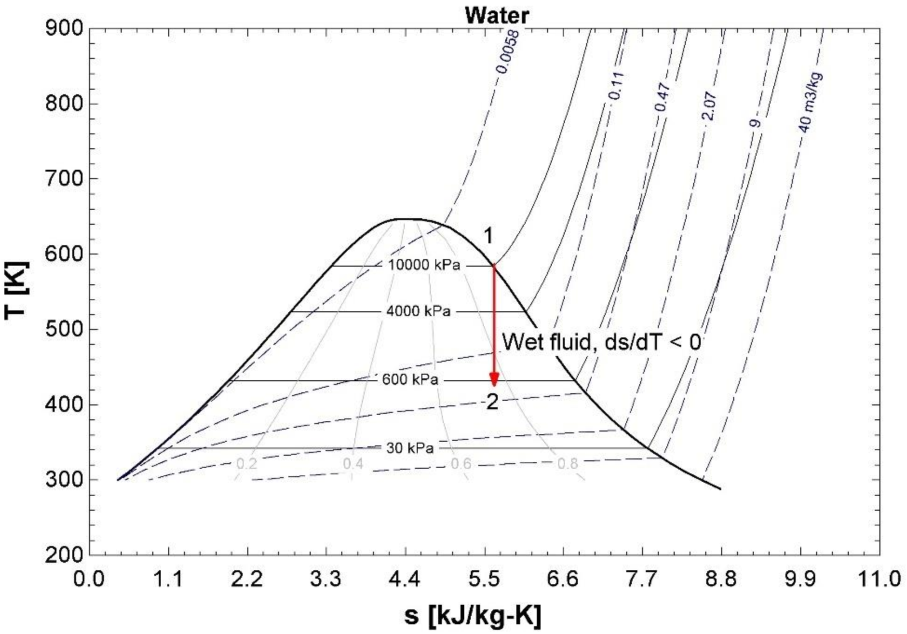

Figure 2.9 T-s diagram of wet fluid (Water).

From the Figure 2.7 - Figure 2.9 it is evident that dry and isentropic fluids are in a better position than the wet fluids when the wetness fraction of vapor is considered during the expansion process in the turbine. As for wet fluid usage in ORC, Rao et al. [68] found an outcome of nearly 82.2% reduction in solar collector area was achieved when ORC was used in combination with a LNG vapor system. The area of heat exchanger was also reduced by 31.7%. R143a was found to be the optimum fluid in the process. Propane and propene took the next positions as suitable fluids. Proposed Cycle power output was 1 MW and turbine inlet temperature was 75 °C. Even though wet fluid is showing some promises, at low temperature region ORC works better than SRC, which will be discussed further in section 2.4.3.

2.4.3 Selecting ORC over SRC for Low Temperature Applications

As water is a wet fluid, during expansion in the turbine, wetness fraction of vapor will not remain zero. A significant percentage of wetness will be present, resulting turbine blade erosion. To prevent this phenomenon with the added problem of high pressure in the evaporator, introducing superheater is essential in a steam Rankine cycle.

ORC turbines incorporate dry and isentropic fluids that can operate with higher efficiency below temperature of 400°C in comparison to SRC. Dry and isentropic fluids are free of condensation during expansion by nature, which also terminates the problem of erosion in turbine blades. Otherwise, much costly ceramic coated expensive turbines need to be used like in steam Rankine cycle (SRC). Mechanical stresses will be reduced to a much lesser degree in absence of wet molecules, so is the running costs associated with it. Lubrication property of Hydrocarbons is an added advantage for rotating equipment of ORC. Boiling points of organic fluids are very low which enables them to evaporate with less heat input from low temperature heat sources [10].

2.4.4 Evolution of Working Fluid Categories in ORC

Landelle et al. [18] showed that 52% of the working fluid used in ORC are HFC (Hydrofluorocarbon), 20% HCFC (Hydrochlorofluorocarbon), 7% Hydrocarbons, 6% HFE (Hydrofluoroether), 4% Mixtures, 2.5% PFC (Perfluorocarbon), 2.5% CFC (Chlorofluorocarbon), 2.5% HFO (Hydrofluoro-olefin) and 5% of others. There are over 30 different fluids, but only these three fluids are used two times out of three: R245fa (38%), R123 (18%) and R134a (7%). They Recommended R245fa for closed heat source (Biomass, Solar) and R404a (WHR, Geothermal) for open heat source as optimum fluids to be used.

2.4.5 Selection of Working Fluid for ORC

The choice of the working fluid in the thermodynamic cycle depends on the temperature of the solar heat captured. It is not possible to single out an optimum Heat Transfer Fluid (HTF) to work on all different conditions and input variables. Temperature of HTF in the heat source, mass and volumetric flow rate of HTF inside ORC, turbine inlet temperature and so many other variables dictate the issue of choosing an optimal working fluid for a configuration. First and second law efficiency, vapor expansion ratio and many other economic aspects are there as well.

Till now almost all the literatures concentrate on pure and homogeneous fluids. There are a few literatures on mixtures and working fluids involving nanofluids and azeotropic mixtures. Commercially popular ORC plants are using R245fa, R134a, SES36, Pentane, Octamethyl Trisiloxane (OMTS), Toluene, etc. The Thermodynamics Laboratory at University of Liège in Belgium investigated this matter and they observed that R134a is used below 110°C, R245fa and Solkatherm (SES36) in 110°-200°C range, n-Pentane in 200°-300°C range and beyond 300°C Toluene is incorporated [69], [70].

Different ORC fluids are suitable for different temperature and pressure ranges with their unique properties like critical temperature, critical pressure etc. [71], [72], [73]. Researches are done on selecting appropriate working fluid in low to medium temperature Rankine cycle [74], [75] which also includes utilizing solar thermal as heat sources [76], [77]. The following Table 2.2 is documenting some properties of fluids for the convenience of choosing appropriate working fluid in ORC. Water is added for the sake of comparison. It should be noted that the normal boiling is the boiling point of fluid at 1 atmospheric pressure.

Table 2.2 Properties of working Fluids in ORC.

Fluids	**Critical Temperature, T_{cr} (°C)**	**Critical Pressure, P_{cr} (MPa)**	**Normal Boiling Point (°C)**	**Temperature range at Turbine Inlet (°C)**
R744 (CO_2)	30.95	7.377	-87.85	125-200
R410A	71.35	4.901	-51.45	-
R134a	101.1	4.06	-26.05	70-200
R245fa	154.05	3.65	15.15	70-250
n-pentane	196.55	3.364	35.85	80-200
Benzene	288.85	4.894	20.05	100-294
Toluene	318.65	4.126	110.35	280-380
Water	373.95	22.064	100	250-390

2.4.6 Thermal Stability Consideration for ORC Working Fluids

The thermal stability is a major limitation of organic working fluid selection that needs careful consideration with heat sources of high temperature. Organic working fluids may decompose at high temperature that is used in supercritical ORCs. Dai et al. [78] reported decomposition temperature of n-pentane as 280 – 300 °C; for n-hexane, Isopentane and cyclopentane the temperature range is 260–280 °C and for n-butane and isobutane it is 300–320 °C. Invernizzi et al. [79] reported maximum functional temperatures for Pentane, Cyclopentane, Toluene are 300°C, 300 °C, and 300–350 °C respectively. For R134a, R245fa, R23, R32 maximum temperatures are reported as 350 –370°C, 300°C, 400°C, 570–590 °C (in a straight heated Inconel 600 pipe), respectively.

2.4.7 Industrial Applications and Researches of ORC

ORC is extensively used in power generation industries concentrated on utilizing low temperature heat sources. ORMAT, Turboden, GE and many other companies are using ORC to harness power [80]. Geothermal, solar, biomass and waste heat are used as heat sources in such plants. Optimum operating conditions of ORC were reported by Seshie et al. [81]. They identified isentropic efficiency of the turbine and evaporator pressure as the most influencing factors in the ORC system efficiency. Increasing these parameters resulted in an increase in the performance of the whole system. Recuperator was mostly responsible for exergy destruction followed by the condenser according to the analysis.

Petrollese et al. [82] reported the optimal configurations of ORC when it is integrated with CHP systems. Four configurations were compared to find the most commercially superior Hear Recovery System (HRS) for two glass furnaces operating through Waste Heat Recovery (WHR) of capacity of 1.2-4 MW at 450°C [83]. These four configurations included ORC, two different configurations of supercritical CO_2 Brayton-Joule cycle and an innovative regenerative air-Brayton-Joule cycle. The thermoeconomic analysis revealed that ORC was the most suitable for small size furnaces and for large capacity furnaces air Brayton-Joule cycle was recommended. Even though supercritical CO_2 (S-CO_2) cycle systems returned highest output, their commercial aspects were found to be less attractive due to high capital cost. Thermodynamic and exergoeconomic analyses [84] were conducted for a combined supercritical CO_2 (S-CO_2) recompression cycle and regenerative ORC using zeotropic mixtures to investigate the significant parameters like pinch point temperature difference, pressure ratio, split temperature, evaporation temperature, product unit cost etc. R236fa/R227ea (0.46/. 54) was found to be the optimum fluid with an exergy efficiency of 73.65% and the novel cycle was performing better than the conventional cycles of similar configurations.

Zhang et al. [85] conducted an emergy analysis to evaluate the sustainability of ORC utilizing waste heat. Sustainability of ORC was found to be less than wind, hydro and geothermal plants in the analysis. emergy yield ratio (EYR) and emergy index of sustainability (ESI) of an ORC were 197.52 and 3.97 respectively. ORC applications are presented in Table 2.3 prioritizing solar assisted plants. Collector area, power capacity and working fluids used are summarized in brief.

Table 2.3 Summary of literature review for ORC with different heat sources.

Authors (Year)	*Experiment/ Simulation*	*Heat Source*	*Collector Area(m^2)*	*Heat Source Working Fluid*	*ORC Working Fluid*	*Output*	*Max Temperature (°C)*
Freeman 2017 [86]	Simulation	Non-concentrating Collector	15	Molten Salt	R245fa	15KW	130
Navarro-Esbrí 2017 [87]	Experiment	Biomass Boiler	-	Thermal Oil	HFC 245fa	27.5kWe, 180kWth	240
Zhang 2016 [88]	Experiment.	PTC	1096	Therminol 55	R123	200 KW	-
Canada 2015 [89]	Experiment.	PTC	10340	Xceltherm 600	n-pentane	1 MW	204
Raush 2013 [90]	Experiment.	PTC	1051	Water	R245fa	50 KW	121
Heberley 2017 [91]	Experiment and Simulation.	Geothermal and Solar Collector	32340, 24964, 17304	-	n-butane	21.6 MW, 16.7 MW, 11.6 MW	290
Patil 2017 [48]	Simulation.	PTC	1029	Glycerol	Iso-butane	50 KW	300

A Combined Heat and Power (CHP) system was devised with PTC and biomass fueled ORC for the generation of combined heat and power on residential level [92]. Integration of CSP to the power cycle reduced the biomass consumption and increased maximum operating hours and global system efficiency. ORC was integrated with the Heat Recovery Steam Generator (HRSG) of the Combined Cycle Power Plant (CCPP). Exergy and energy efficiency improved by 3.32% and 4.09% respectively as reported [93]. A CHP set up in combination with LFR, biomass furnace, TES and ORC was investigated to find out the optimum configuration of the ORC [82]. Siloxanes and linear alkanes like Pentane, Iso-Hexane came out as the highly efficient working fluid to be used in ORC and it was also concluded that condenser temperature is an important parameter to determine the optimum fluid for the cycle. Exergy efficiency was found to be 56-58%. This discussion is followed by Table 2.4 and Table 2.5 where CSP assisted ORC researches are discussed. Table 2.5 mainly concentrated on Zeotropic and Nanofluid mixtures as ORC fluids. The findings of the researches are summarized in both of them.

Table 2.4 Summary of literature review for ORC based CSP plants.

Authors (Year)	*Col. Type*	*HTF*	*Working Fluid (ORC)*	*T_{max} (°C)*	*Simulation Software*	*Remarks*
Rayegan 2011 [73]	PTC	Thermal oil	11 fluids selected	130	Refprop 8.0	Benzene topped up in terms of thermal and exergy efficiency and R245 has average performance
Quoilin 2011 [94]	PTC	Thermal oil	Solkatherm (SES36), R134a, R245fa, n-pentane	190	EES	SE36 and R245fa took the lead with almost same efficiency for single and double stage expansion [Capacity 3kW]
He 2012 [95]	PTC	Thermal oil	R113, R123, pentane	205	TRNSYS	Pentane found to be most efficient.
Calise 2013 [96]	PTC	Thermal oil	Butane	170	EES	Mass flow rate found to be the key variable in power generation.
Ferrara 2014 [97]	PTC	Thermal oil	R134a, R245fa, acetone	390	Custom Math. Model	Synthetic Oil recommended for PTC and Acetone for ORC.
Xu 2015 [98]	LFR	Organic fluid	Isopentane, pentane, hexane, heptane, cyclohexane, toluene	420	EES	Turbine inlet temperature proportional to efficiency. Cyclohexane Recommended.
Coco 2015 [99]	PTC, LFR	Thermal oil	Silicone oil	300	Custom Math. Model	LFR is still not competitive enough with PTC powered ORC for their extra 40 Euro/MWh production cost.

Table 2.5 Zeotropic and Nanofluid mixtures as ORC fluids.

Authors	***Experiment/ Simulation***	***Heat Source***	***Fluid Type***	***ORC Working Fluid***	***Remarks***
Su 2018 [100]	Simulation	Geothermal Water	Zeotropic mixture	R600a/R601a, R600a/R227ea.	Pure fluid has better efficiency than the mixtures.
Wang 2017 [101]	Simulation	Solar Collector.	Zeotropic mixture	R152a/R245fa	Pure R245fa of the mixture could present the highest thermal efficiency but required larger expander size and consequent higher system cost.
Mondejar 2017 [102]	Simulation and experiment.	CO_2 trans-critical power cycle (T-CO_2) exhaust.	R245fa	R245fa	R245fa generated more power with better efficiency.
Li 2018 [103]	Simulation	Waste heat recovery (WHR)	Nanofluid	R32 + (Al_2O_3/ CuO/ ZnO /Ag/ SiO_2/ TiO_2/ SWCNT	Heat Exchange area reduction was achieved.
Andreasen 2016 [104]	Simulation	Boiler	Zeotropic Mixture	R32/R134a	R32/R134a is the best of the three fluids, since it enables the highest net power output at the lowest component cost. R32 is the second-best fluid while R134a is performing least.

Authors	***Experiment/ Simulation***	***Heat Source***	***Fluid Type***	***ORC Working Fluid***	***Remarks***
Dong 2017 [105]	Simulation	Heating fluid: Water	Zeotropic Mixture	R245fa/R123/113/R365mfc combinations.	Zeotropic ORC always presents lower cost-effective performance than pure ORC, and the changes in the cost-effective performance are contrary to the first law efficiency. This illustrates that higher cycle efficiency brought by zeotropic mixtures comes at the cost of much larger heat transfer area.
Hou 2018 [106]	Simulation	Supercritical CO_2 (S-CO_2) recompression cycle exhaust.	Zeotropic mixture	R236fa/R227ea	Proposed cycle works better than the stand- alone cycles.
Singh 2018 [107]	Simulation	Solid oxide fuel cell-gas turbine exhaust.	Organic Fluids	R141b, R245fa and R236fa	R236fa in ORC offers highest output and efficiency of SOFC-GT-ORC system.
Saadatfar 2014 [108]	Simulation	Solar collector	Nano-fluids	Silver Nano pentane	Better efficiency and reduced HX area in comparison to pentane.
Saadatfar 2014 [109]	Simulation	Hybrid Gas Turbine Exhaust.	Nano-fluids.	n-ORC fluid	Higher exergy efficiency, less exergy destruction, and less CO_2 emissions.

2.5 Absorption Cooling System

According to estimation of the International Institute of Refrigeration (IIR), refrigeration and air conditioning processes consume around 15% of the electricity produced in the whole world. It is important to distinguish between air-conditioning and refrigeration processes. Where in the first case of air conditioning, the system is designed to provide cooling above 0°C, the latter i.e. the refrigeration system is meant to provide cooling for both below and above 0°C [110], [111].

Conventional refrigeration processes like vapor compression system that are adopted worldwide on large scales, consume lots of energy and such systems involve the release of toxic gases to the environment [112]. Energy hungry compressors affects both the environment and the running costs of the plant quite badly. So ecofriendly, energy saving technologies like absorption refrigeration technologies are coming to the forefront of consumer demand now a day. It is used extensively in both residential and industrial applications [113].

To substitute the high electricity consuming compressor run refrigeration system, the absorption refrigeration system is a competent substitute that can utilize waste heat or solar thermal energy to produce cooling. In this process two fluids entering a different state, as either a gas or a liquid are coupled to leave in a single state.

2.5.1 Construction of Absorption Refrigeration Cycle (ARC)

Basic single effect absorption refrigeration cycle is driven by heat and works on two different pressure levels. Generator, condenser, absorber and evaporator are the four basic components of the cycle. In generator, heat source like solar energy boils the rich solution coming from the absorber by the means of thermal storage tank or heat exchangers. Concentration of refrigerant becomes very less in the solution and that is how refrigerant gets separated from the solution in the generator. The resulting weak solution is circulated to the absorber with a pressure relief valve. The refrigerant vapor from the generator then flows into the condenser to be condensed by the ambient. From the condenser, the liquid refrigerant makes their way to the evaporator expanding through a throttle valve. Reaching low pressure level after throttling, the refrigerant liquid evaporates in the evaporator achieving its cooling effect at the same time. Evaporator feeds the absorber with refrigerant vapor. Then the refrigerant vapor is absorbed by the solution on absorber releasing heat to the sink. This binary solution becomes highly concentrated with refrigerant and the rich solution is pumped to the generator and the cycle is repeated. Solution heat exchanger (SHE) recovers internal heat, which enhances the COP significantly.

An excellent literature review of experimental studies was reported by Aliane et al. [114] enumerating the classifications of ARC. Single, double, triple and half effect solar assisted systems were enlisted in the study with their working pairs and COPs. Excerpt from the literature is tabulated below in Table 2.6.

Table 2.6 Classifications of ARC systems.

No. of Effects	***Solar Heat Source***	***Configuration***	***Driving Temperature (°C)***	***COP***
Single Effect	ETC, FPC	Basic cycle.	80-100 (water-cooled). 30K more for air cooled.	0.6-0.8
Double Effect	PTC, LFR	2 generators with high and low pressure, 2 condenser and rest similar to basic cycle.	140-180	1.1-1.2
Triple Effect	ETC, CPC	3 generators with 3 condenser and rest similar to basic cycle.	200-220	≈ 1.7
Half Effect	Low temperature collectors.	2 generators, 2 absorber and rest similar to basic cycle.	55-75 (generator temperature.)	0.36 – 0.40

A single effect absorption system [115] was analyzed using the method of energy and exergy analysis and the results revealed that highest COP and exergy efficiency for a particular temperature were observed at maximum cooling capacity, also an increase in evaporator temperature was improving the COP. Similar configurations are also discussed in a critical review [116] adding more classifications to it.

In Figure 2.10, a solar driven single-effect absorption refrigeration system is shown where the pressure level can be seen on different operational phases. Double effect and half effect absorption refrigeration system are also shown on Figure 2.11 and Figure 2.12 respectively.

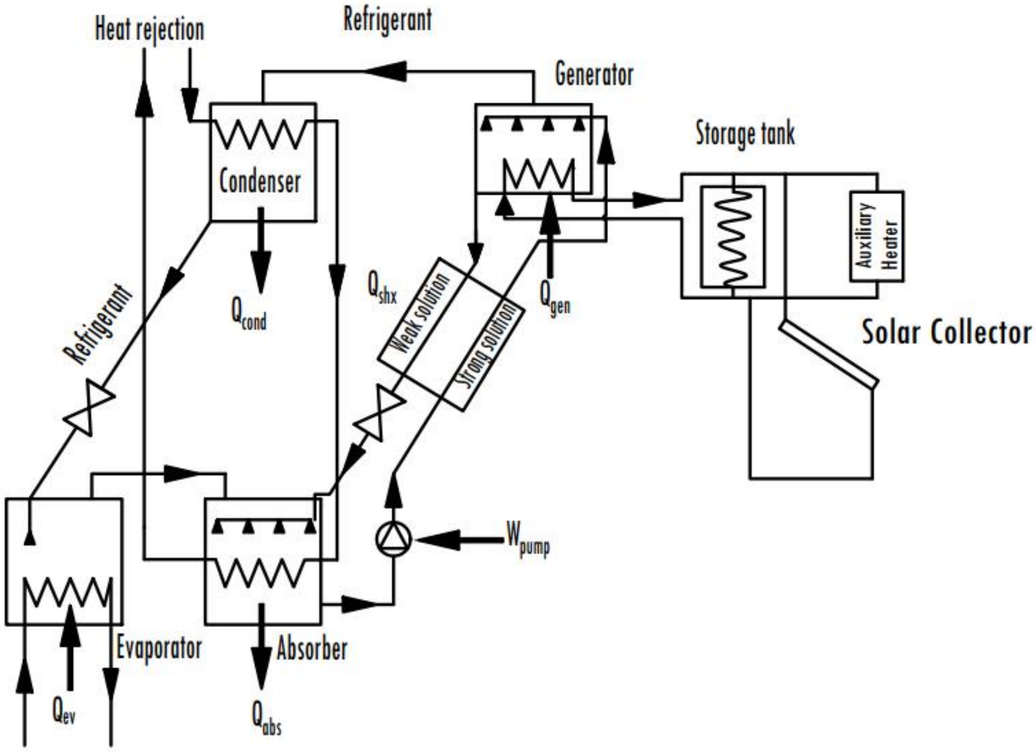

Figure 2.10 Schematic of a solar driven single-effect absorption refrigeration system redrawn from [103].

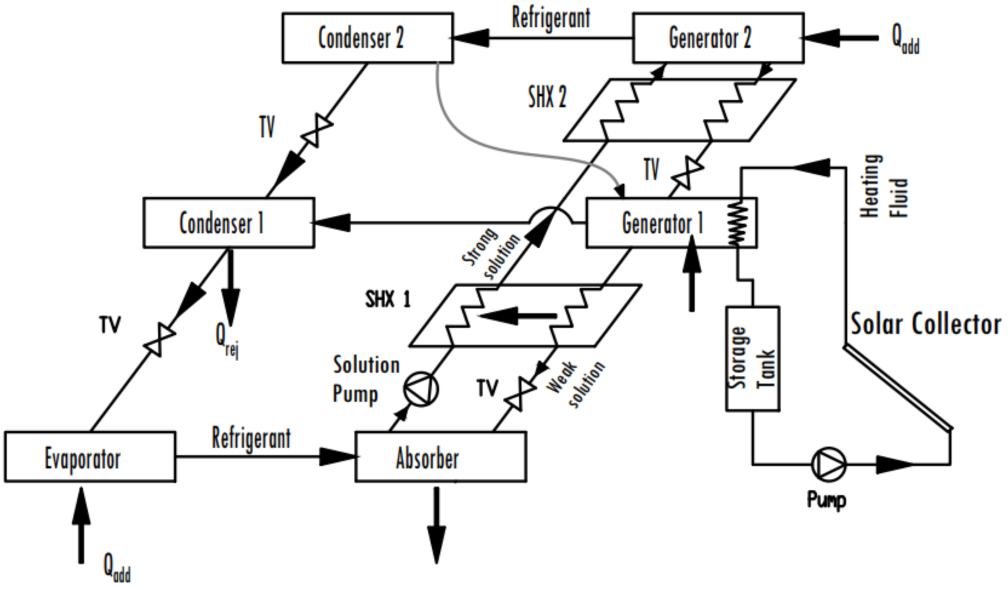

Figure 2.11 Schematic of a solar driven double-effect absorption refrigeration system redrawn from [114].

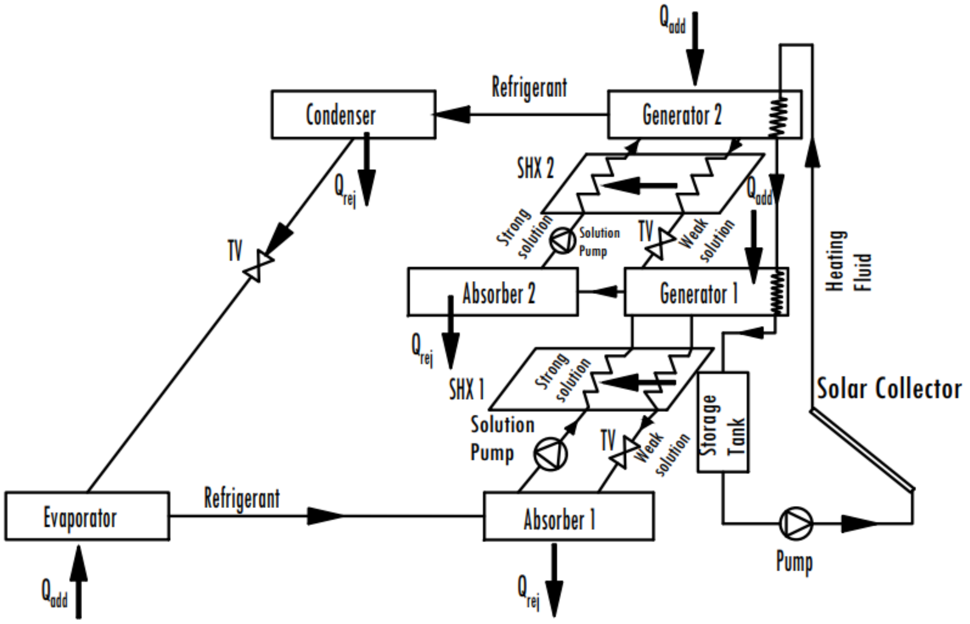

Figure 2.12 Schematic of a half-effect solar driven absorption refrigeration system redrawn from [114].

Xu et al. [117] made some excellent contribution well explaining the configurations and classifications of ARCs. Apart from the basic cycle, different combination of thermal processes is discussed with resulting effects. Multi-effect cycles were classified into external and internal cycle coupling, where the coupling is divided into heat coupling and mass coupling. Triple pressure cycles involving ejector and cycles including compressor were found to return higher COP. Table 2.7 outlines the work in brief which is used with permission (Appendix D) to be used in the thesis.

Table 2.7 Couplings for ARC cycle construction.

Cycle Type	***Integration***	***Cycle Description***	***Effect***
Single effect	None	Basic cycle	Basic results upon fundamental concepts.
External-circuit integration	Heat pair.	Condensation–Desorption	Higher COP, driving temperature and system pressure.
		Absorption–Desorption	Higher COP and driving temperature, larger concentration field.
		Absorption–evaporation	Larger temperature lift, lower driving temperature, more pressure levels.
	Mass pair.	Absorption–Desorption	Larger temperature lift, lower driving temperature, more circuits and pressure levels.
Internal-circuit integration	Heat pair.	Absorption–Desorption	Higher COP and driving temperature, more flexibility.
	Mass pair.	Absorption–Desorption	Larger temperatures overlap for GAX, more pumping processes.
Combination	Ejector		Higher COP and driving temperature with fewer components.
	Compressor		Higher COP with low driving temperature, extra work input.

Another addition to the single effect cycle is Diffusion-Absorption Refrigeration Cycle (DARC). DARC runs without mechanical or electrical input and pressure compensation gas is mixed with the working pair in the process. Apart from conventional thermal driven ARC and DARC there are non-thermal driven absorption systems that are assisted by mechanical input, membrane separation or even capillary force.

Single stage has a limitation on the temperature of the heat source, and the condensation temperature is high under harsh conditions [118]. So, to better utilize the heat, Condensation-Generation heat coupling is introduced to form new cycles like double and triple effect ARCs. Double and triple effect cycles can form from the Absorption-Generation heat couplings [117]. Higher generator temperature is needed to generate more refrigerant vapor. This is not achievable by single stage absorption cycle. The multi pressure absorption cycles like double effect or double stage cycles can operate at high temperature heat source. COP also is significantly higher in multi stage cycles (0.8 - 1.4).

In many cases the temperature of the source is not high enough for the activation of the single effect cycle. That is when double and triple lift cycles are introduced in the scenario. Here, absorption-generation mass coupling is applied to lift the temperature up creating new pressure levels. Double and triple lift cycles can be also formed from absorption-evaporation heat couplings that are similar to absorption-generation mass couplings.

2.5.2 Working Pair: Refrigerant and Absorbent

As the name implies in the absorption refrigeration systems, the working fluid is a mixture of two fluids, one is called the absorbent and the other one is the refrigerant. This working pair is used in such a way that saturation temperature of one of the fluids is less than the other to boost separation between them for the process to work out. The fluid with lower saturation temperature is called the Refrigerant. It evaporates faster than the absorbent and expected to get separated easily. The other fluid acting as an absorbent, absorbs the refrigerant in the absorber [112]. Most commonly used working pairs are Ammonia-Water and Lithium Bromide ($LiBr-H_2O$). Aqua Ammonia (NH_3-H_2O) is popular in the industrial applications as it can operate at high temperature without having any crystallization problems, whereas the rest of the fluids have the tendency to fall into it often. Less corrosion and very economical running costs are also at its advantage. The Lithium Bromide solution is preferred in the residential air conditional requirements for its high COP. But over 473.15 K temperature, it faces the corrosion problem. With a very costly corrosion curing process and crystallization problems it might not be a very popular choice under certain conditions [112].

Majority of refrigeration applications preferred to use Aqua Ammonia and Lithium Bromide solutions for the refrigeration purpose. Aqua Ammonia has a higher heat of vaporization and more stable over different pressure and temperature ranges. For refrigeration below 0°C it is still a favorite choice. It has no damaging effect on ozone layers and global warming potential is insignificant. The only significant setback is the addition of a rectifier or analyzer that complicates operations and adds to capital cost [119].

On the other hand, the NH_3-$LiNO_3$ solution does not need a rectification tower unlike other aqueous solutions, which reduces the investment cost. It offers notably higher COP as well [120]. But the NH_3-$LiNO_3$ mixture is highly viscous that can limit the heat and mass transfer in the absorber of the system. This is the main disadvantage of this working pair. But recent researches are working on its mitigation as well. Ventas et al, [121] atomized the solution to obtain small droplets inside the absorber plenum which resulted in mitigating the viscosity related problems and tube wetting difficulties.

2.5.3 Ejector Cooling System

The ejector is a device that works on the principle of Venturi effects of a converging-diverging nozzle driven by low temperature waste heat or renewable energy sources. It is directly activated by a thermal source to produce heating, cooling or refrigeration. It can be utilized also in cascaded refrigeration cycles or sub-cooling purposes. In case of Ejector-Absorption Cycle (EARC), ejector is a replacement of the compressor used in the absorption cycle to increase the pressure without consuming mechanical energy directly. That is why it is also known as thermally activated static compressor.

Ejector has a converging-diverging nozzle embedded in a cylindrical body as shown in Figure 2.13. Primary flow is also known as motive stream and the secondary flow is known as suction stream. There are three zones in an ejector, namely suction, mixing and diffusing zones. The compression effect results from the interaction of motive and suction stream. Motive stream is produced in a generator using a heat source. Heat source can be utilized from low temperature waste heat or renewable sources like solar energy. In the converging section pressure energy of a motive fluid (Primary flow) at high pressure is converted to kinetic energy resulting a vacuum that entrains the suction fluid (Secondary flow) at low pressure. Both of fluids gets mixed and passed to the diverging section where it recompresses the mixed fluids by converting kinetic energy back into pressure energy [122].

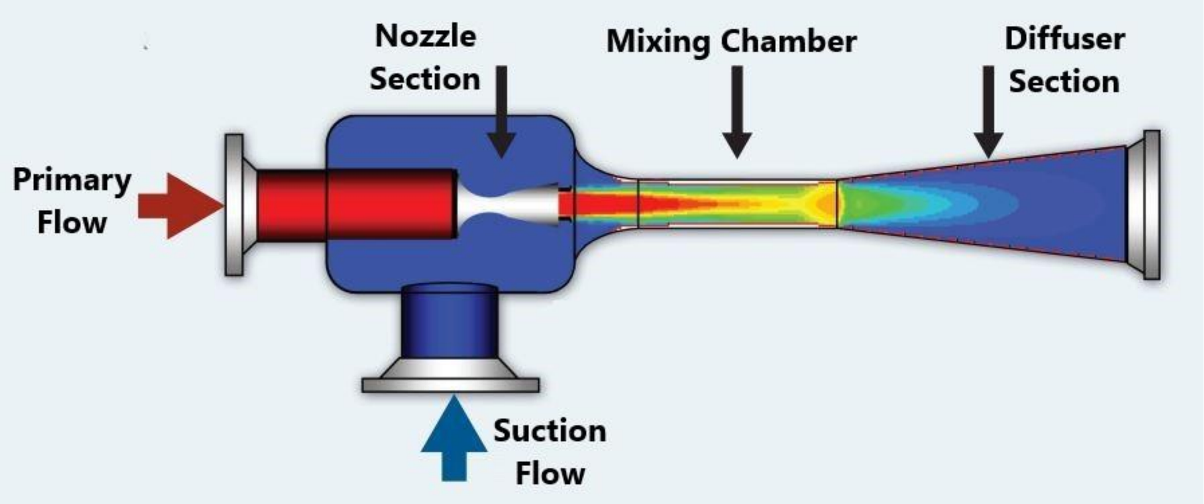

Figure 2.13 Operation of an Ejector redrawn from [123].

Here is a typical heat pump model illustrating the principle of ejector in Figure 2.14. In this ejector-based heat pump model, the compressor is replaced by an ejector, a pump and a generator. The generator takes heat from a heat source and then supply high pressure vapor to the primary inlet of ejector at pressure P_2. This motive flow is accelerated at the primary nozzle where it reaches supersonic velocity. This results in a steep pressure fall in the primary nozzle and it creates a depression at the nozzle outlet. Due to this pressure vacuum it starts drawing the low-pressure suction stream coming from the evaporator at pressure P_3. Both flows get mixed in the mixing chamber. A shock wave takes place when the two velocities equalize at a constant pressure in the mixing chamber. This shockwave raises the pressure and lower the velocity consequently to subsonic level. The diffuser allows the conversion of the remainder velocity into static pressure and mixed flow reaches the intermediate pressure P_5 which is also the pressure of the condenser.

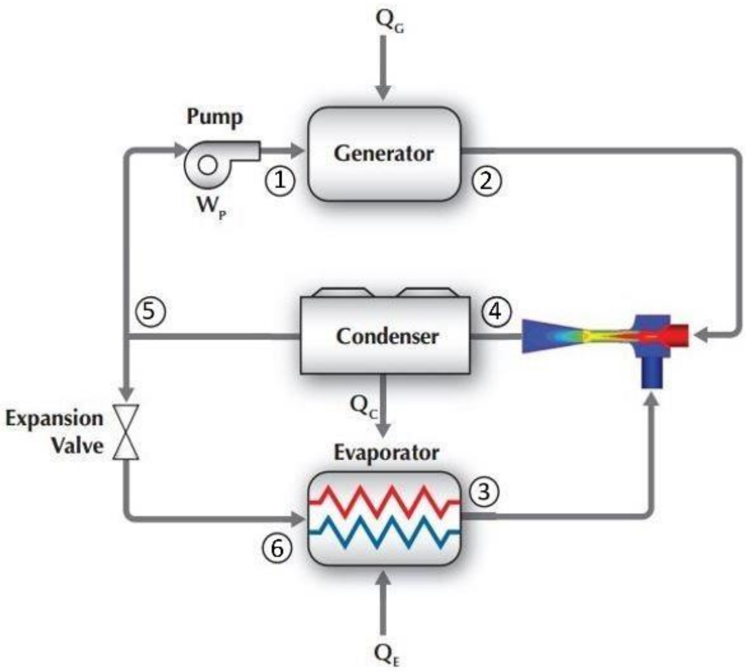

Figure 2.14 An Ejector based heat pump model redrawn from [123].

After condensation part of the flow is expanded to evaporator pressure P_6 to supply the suction stream again and the remainder is pumped back to the generator. Even though the ejector system has lower efficiency in comparison to the compressor due to simplicity, lower maintenance cost and less power consumption make it a competitive choice in the industry.

2.5.4 Advantage of Ejector Usage in Absorption Refrigeration System

Ejector has two main functions. First one is to aid pressure recovery from the evaporator and the second one is to facilitate the mixing process and pre-absorption by the weak solution coming from the evaporator. Normally its employed either on Absorber or condenser inlet [124]. Higher absorber pressure facilitates when it exceeds the evaporator pressure, the solution circulation ratio gets reduced which results in a better COP. But, in this case the refrigerant vapor density must be very high as similar to the LiBr-Water system [125].

For boosting the pressure, ejector is a better choice than using a compressor. Even though EARC has less COP in comparison to conventional compression-absorption system, but efficiency can be improved if the more refrigerant flow is coming from the evaporator [126]. EARC is simple and it requires much less investment than the compressor. It enables the operation on the triple pressure level that can operate a lower circulation ratio, lower generation temperature. In the meantime, it facilitates higher condenser and absorber temperatures as well [127], [118].

2.5.5 Positioning of Ejector

Placement of an ejector can boost the absorption and condensation process when positioned before absorber and condenser respectively. When applied to absorber inlet, absorption cycle operated on a triple pressure level (TPL) reduces the required generator temperature significantly, which increases the potentials for the usage of low temperature heat source. Increased COP, lower circulation ratio and relatively smaller SHE is some of the benefits of this arrangement [127], [128], [129], [130].

Vereda et al. [131] used ejector for multipurpose objectives namely as booster for more refrigerant vapor, regulated solution expansion valve and adiabatic absorber. It is observed that higher circulation ratio results reduced activation temperature (minimum temperature for refrigerant production) and lower activation temperature means higher COP. When the ejector is placed before the condenser inlet it expands the high pressure from a generator by creating a vacuum on the other side of the ejector. This vacuum drives more vapor from the evaporator [132]. The ejector enhances utilization of energy and improves condensation process. COP of EARC is found better than the basic absorption cycles. Significant works are done on understanding the mechanism of an ejector, its geometry and the aftereffects of it [133], [134], [135]. Some excellent literature reviews are also reported by Besagni et al. [136] and Abed et al. [137]. Some of the literatures on Ejector-Absorption system are tabulated below.

Table 2.8 Summary of literature review on EARC Systems.

Authors (Year)	***Model***	***Working Pair***	***Ejector Location***	***T_e (°C)***	***T_g (°C)***	***T_a (°C)***	***T_c (°C)***	***Remarks***
Sözen 2003 [119]	Custom Math. Model.	NH_3-H_2O	Condenser Inlet	5	90	30	40	High performance Collector surface area of 3m^2 is sufficient for 8-9 months in a year all over Turkey for Refrigeration. Max COP is found to be 0.739.
Hong 2010 [138]	Custom Math. Model.	H_2O/LiBr	Condenser Inlet	5	[130]	40	40	122.5 <T_{source}<150, within this range COP of the proposed cycle is higher than conventional single and double effect cycle with COP above 1.0.
Abdulateef 2011 [139]	Exp.	NH_3-H_2O	Condenser Inlet	3-16	60-98	30	23-39	COP increased by 50% after introducing the ejector to the basic EARC cycle.
Vereda 2012 [120]	EES	NH_3-$LiNO_3$	Absorber Inlet	0-8	61-70 (Activation) 91-101 (COP_{max})	30-39	30	Diameter of the adaptable ejector has a great influence on the EARC performance. Activation temperature decrease by 9°C due to Ejector geometry.
Garousi 2013 [140]	EES	LiBr-H_2O	Condenser Inlet	4	[127]	37	37	Double effect EARC has proven to be more economical than the basic double effect cycle in the Exergonomic analysis.
Garousi 2014 [141]	Custom Math. Model.	NH_3-$LiNO_3$, NH_3-NaSCN	Absorber Inlet	0	90	35	35	For low temperature heat source and lower generator temperature combined EARC model is better than the basic ARC. Effectiveness of SHE found out to be very significant for COP and Exergy Efficiency.
Abed et al. 2017 [142]	Exp.	NH_3-H_2O	Condenser Inlet	13-19	80-90	30-33	32-37	Dual ejector-Flash tank in combination with ARC showed significant improved in performance than the Basic cycle and the single ejector ARC Cycle.

2.6 Energy, Exergy and Economic Assessments of Solar Assisted Multipurpose Cycles

To achieve higher overall efficiency utilizing all the power input, technologies like trigeneration, multigeneration and combined cogeneration and power, power and cooling are introduced. Solar energy can be coupled with power and cooling cycles. Power cycle can be Rankine, Stirling or any other conventional cycles. Vapor compression, vapor absorption, ejector cooling or their combinations are used for the purpose of cooling. Power and cooling cycle can be accommodated with cogeneration, desalination etc. accordingly. Following figure is demonstrating the use of solar technologies in power and cooling systems. There are power cycles like Kalina and Goswami, which produce power and cooling simultaneously. Combinations of different power and cooling cycles are also put into effect using solar PV and CSP technologies. Classifications of these power and cooling cycles are summarized in the following Figure 2.15 in brief.

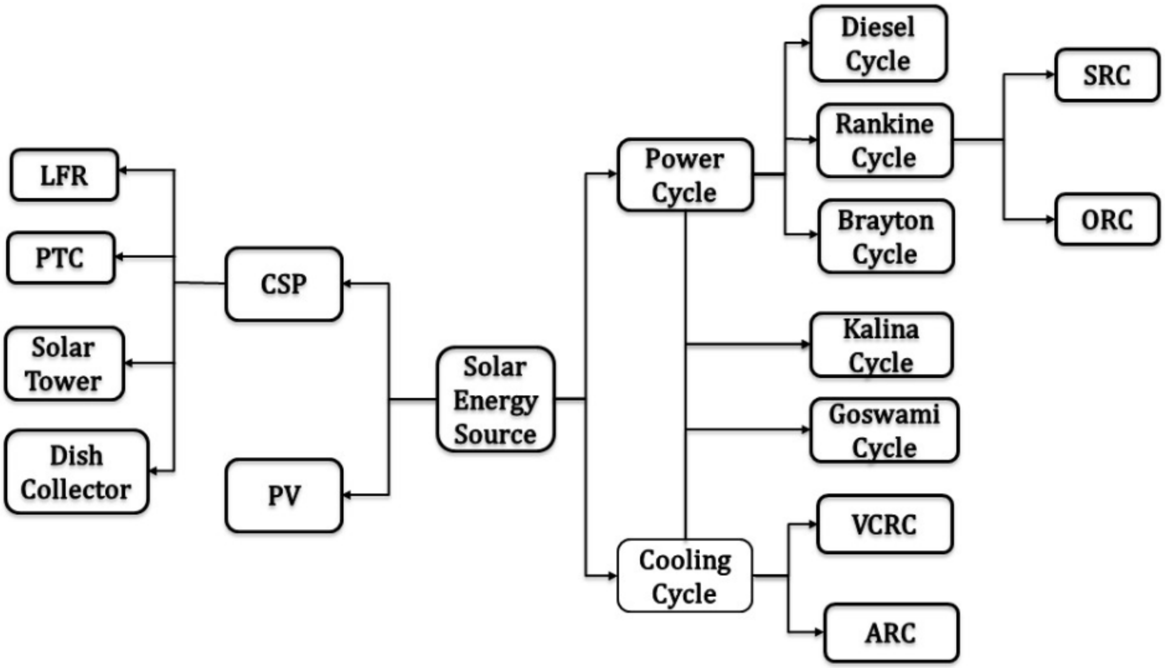

Figure 2.15 Solar assisted combined power and cooling technologies.

Thermo-economic, exergonomic and many other works are done on experimental and theoretical level for the increasing demand of efficient and cost-effective sustainable technologies. The researches on energy and exergy analysis concentrated on thermal efficiency and utilized the useful energy available for the configured system. These researches are conducted to find out the locations or components mostly liable for exergy destructions. Thermo-economic or Exergo-economic researches added the cost analysis in their research and calculated BEP, LCOE, CUF etc.

In a solar multigeneration scheme [143], an exergy cost analysis was done for 21 configurations producing thermal energy, water, power and cooling. It was recommended to couple the refrigeration and process heat module with the turbine extractions for better outcomes. Condenser of the power cycle was recommended to be replaced with the desalination plants. Unit exergy cost reduction for process heat, water, power and cooling was found to be 32.2%, 59.2%, 6.8% and 45.6%, respectively.

A free-piston Stirling engine (FPSE) was conceptualized [144] with a CHP system that could provide thermal and electrical outputs of 1.1 kW_{th} and $1kW_{el}$ respectively at 38% fuel to electricity efficiency. The hybrid system was found to be efficient and cost effective than regular CHP systems.

Hybrid systems for multigeneration are getting popular in Europe. In Denmark, a hybrid system of subcooled CAES and SPAC [145] was proposed and analyzed to reduce the dependence of district heating. The analysis showed a reduction in LCOE in the hybrid system in comparison to conventional systems. Dependence on district heating in summer was totally resolved as well. Similar research concluded that SCAES is capable of producing heat, cooling and electricity with higher COP. Here the combined system of SCAES and SPAC reduced the LCOE and cooling loads of the absorption chiller [146].

A solar tower operated by molten salt [147] was integrated with a GT based CHP system to produce methanol and Hydrogen along with other regular outcomes. The parametric study found the reforming temperature and mass flow rate of methanol playing an important role on the efficiency of the system.

Flat plate Evacuated Tube Collector (ETC) assisted Combined Cycle Power Plant (CCPP) [148] including a double stage LiBr-H_2O trigeneration model was presented for power, cooling and heating needs. The electrical efficiency was found to be 56% with a payback period of 10.7 years and recommended for hot and dry areas.

A CCPP was integrated with PTC [59] arrangement and high temperature energy storage system using ASPEN-HYSYS and MATLAB to trace the locations of exergy destruction in the system. CSP and TES in combine contributed to 43% of the overall exergy destruction of the plant followed by combustion chamber with 15.7%. Exergy and electrical efficiency of the power cycle was found to be 38.2% and 47% respectively.

Aluminum Oxide (Al_2O_3) nanoparticles were mixed with heat transfer fluid of PTC integrated with 60 MW_{el} production capability [149]. After the exergy analysis, it was concluded that the turbine was mostly responsible for exergy destruction followed by feedwater heaters and boilers. Exergy and energy efficiency of the system was found to be 23.83% and 22.44%, respectively along with the outcome of CO_2 reduction by almost 33%. A novel hybrid geothermal-biogas multigeneration [150] system was proposed and optimized, where thermal and exergy efficiency increased by 12.07% and 5.16%, respectively which contributed to the reduction of overall cost by 3.7%.

Mosaffa et al. [147] made a thermoeconomic analysis where a solar tower operated by molten salt was integrated with a GT based CHP system to produce methanol and Hydrogen along with other regular outcomes. The parametric study found the reforming temperature and mass flow rate of methanol playing an important role on the efficiency of the system.

A trigeneration system consisting of LFR arrangement and GTPP was modelled in Thermoflex and PEACE platform to produce power, heat and cooling [151]. It was found that gas turbine sizes of 130-190 MW_{el} had more economic feasibility to be integrated with LFR. If LFR is substituted by solar tower technology, then the GT size should be less than 50 MW_{el} [152]. Annual CO_2 emissions were also reduced significantly [153].

Incorporating PTC, TES, ORC and VCRS, a solar biomass polygeneration system [154] was designed. PTC and TES arrangement produced useful heat at 350°C. Also, from the rest of the cycle, useful heat was produced on two different temperature levels of 50°C and 150°C. The energy and exergy efficiency were found to be 51.26% and 21.26%, respectively.

For the purpose of generating of power, cooling, heating, drying and hydrogen simultaneously, a solar dish collector assisted multigeneration system [155] including ORC, RC, PEM-electrolyzer, double effect absorption chiller, dryer and heat pump was utilized Energy and exergy efficiency of the overall system were found to be 48.19% and 43.57% respectively. Solar dish collectors were identified to be the highest contributor for exergy destruction whereas, the dryer contributed the least. A concentrated solar assisted power (ORC) and cooling system (ARC) were modelled on EES [156]. The system incorporates TES and optimum conditions occurred when 73.33% of the stored energy utilized for ORC and remaining energy utilized by ARC. At optimum condition 24kW of power and 24kW cooling were produced by the system. Table 2.9 documented some notable combined cycles using ORC to produce power, cooling etc.

Table 2.9 ORC based trigeneration system modelling.

Author	***Analysis Type***	***Heat Source***	***Bottoming Cycle***	***Remarks on Modelling***
Patel 2017 [157]	Thermo-Economic	Solar and Biomass	VCARC	Modelled a general equation of Solar Collector Model and then derived the first law efficiency. Breakeven point (BEP) calculated for LFR in combination with ORC and VCARC.
Patel 2017 [158]	Thermo-Economic	Waste Heat	VCARC	The fundamental equations proposed by Jain et al. [159], [160], Desai and Bandyopadhyay (2009) [161]are used to formulate mathematical model of the cascaded refrigeration system and basic organic Rankine cycle. Rational efficiency is calculated as proposed by Nikolaidis and Probert (1998) [162] in terms of efficiency defect.
Tchanche 2010 [163]	Exergy	Solar	Desalination	Made an excellent analysis of exergy and mathematical graph theory known as exergy topological method developed by Nikulshin et al.[164] [165][166]
Jradi 2014 [167]	Experimental	Biomass	Desiccant cooling unit	Effectiveness of cooling system components is calculated, and overall efficiency found to be 85%.
Desai 2014 [168]	Experimental	Solar	Power Cycle	Optimal design calculation of DNI is presented for CSP plants esp. PTC and LFR. DNI data for the simulation are taken from Ramaswamy et al. (2013).

Baghernejad 2016 [169]	Exergo-economic	Solar	ARC	PTC designed as proposed by Kalogirou (20009) [1] and Duffie and Beckman (2006) [170]. Exergy, energy and Exergoeconomics is based on the works of Bejan et al. (1996) [171].
Buonomano 2015 [172]	Energy - Economic	Geothermal Solar	ARC	The system is simulated in TRNSYS, all the components of ORC are modeled in EES. ETC is used as solar heat source.
Boyaghchi 2016 [173]	Exergo-economic	Solar	VCACRC	Detailed Heat exchanger model along with ejector and storage tank.
Al-Sulaiman 2011 [174]	Exergy	Solar	ARC	Detailed PTC and Storage tank is modelled and overall analysis of Trigeneration system is calculated by EES.
Al-Sulaiman 2012 [175]	Energy	Solar	ARC	Three different mode namely Solar mood, solar and storage mood, storage mode is compared after validating PTC model. Effect of pinch point temperature is discussed as well.
Al-Sulaiman 2012 [176]	Energy & Exergy	Biomass	ARC	Energy and exergy analysis of the biomass burner and the rest of the components of ORC and chilling cycle is done.
Suleman 2014 [177]	Energy	Solar & Geothermal	ARC	Energy analysis of the multigeneration system is done with modeling ORC components, drying and absorption chilling systems.

2.7 Conclusion

From the foregoing literature review, it is seen that no notable research is reported that deals with the analysis of a solar based combined power and cooling cycle which integrates the Organic Rankine Cycle with absorption cooling cycle using NH_3-$LiNO_3$ or NH_3-NaSCN as working pairs. Moreover, integrating the ejector at absorption inlet for the combined power and cooling cycle is found to be a unique feature. Significant knowledge gaps are found regarding the thermophysical properties of NH_3-$LiNO_3$ and NH_3-NaSCN at temperature beyond 80°C. These researches are necessary to investigate multi-effect the performance of ARC with higher generator temperature. Added to the discussion, the inclusion of heat sources other than PTC can be considered as well in these multigeneration systems. Combinations of CSP, PV, WHR, Biomass as a heat source can be investigated to remove interruption coming from low irradiation or fluctuations in the load so that alternative supports are available to cope with different scenarios.

CHAPTER 3

THERMODYNAMIC MODELLING OF THE PROPOSED SYSTEM

3.1 System Description

The proposed system shown in Figure 3.1 can be divided into three subsystems, which are namely the heat source (PTC), power system (ORC) and the cooling (EARC) system. The Parabolic Trough Collector (PTC) is a competent CSP technology to act as a heat source for the power and cooling system. The incident solar radiation is utilized by the parabolic trough collector (PTC) to increase the temperature of the recirculating heat transfer fluid. Vaporizer or the Heat Recovery Vapor Generator (HRVG) of the power system is coupled with the PTC outlet hot fluid to generate fluid vapor to be fed into ORC turbine.

In the HRVG, as shown in Figure 3.1, this heat is transferred from the heat transfer fluid to the ORC working fluid and evaporates ORC fluid. This vapor is fed to the turbine for the generation of power. After a significant portion of the heat being utilized by HRVG, the fluid temperature of hot fluid is reduced to a certain degree and heat transfer fluid from HRVG is directed to exchange heat with the generator of the Ejector-Absorption cycle (EARC). Generator receives heat from this external source and refrigerant NH_3 gets separated from the strong NH_3-$LiNO_3$ solution and directed to the condenser then to the evaporator through a throttling valve to provide necessary cooling.

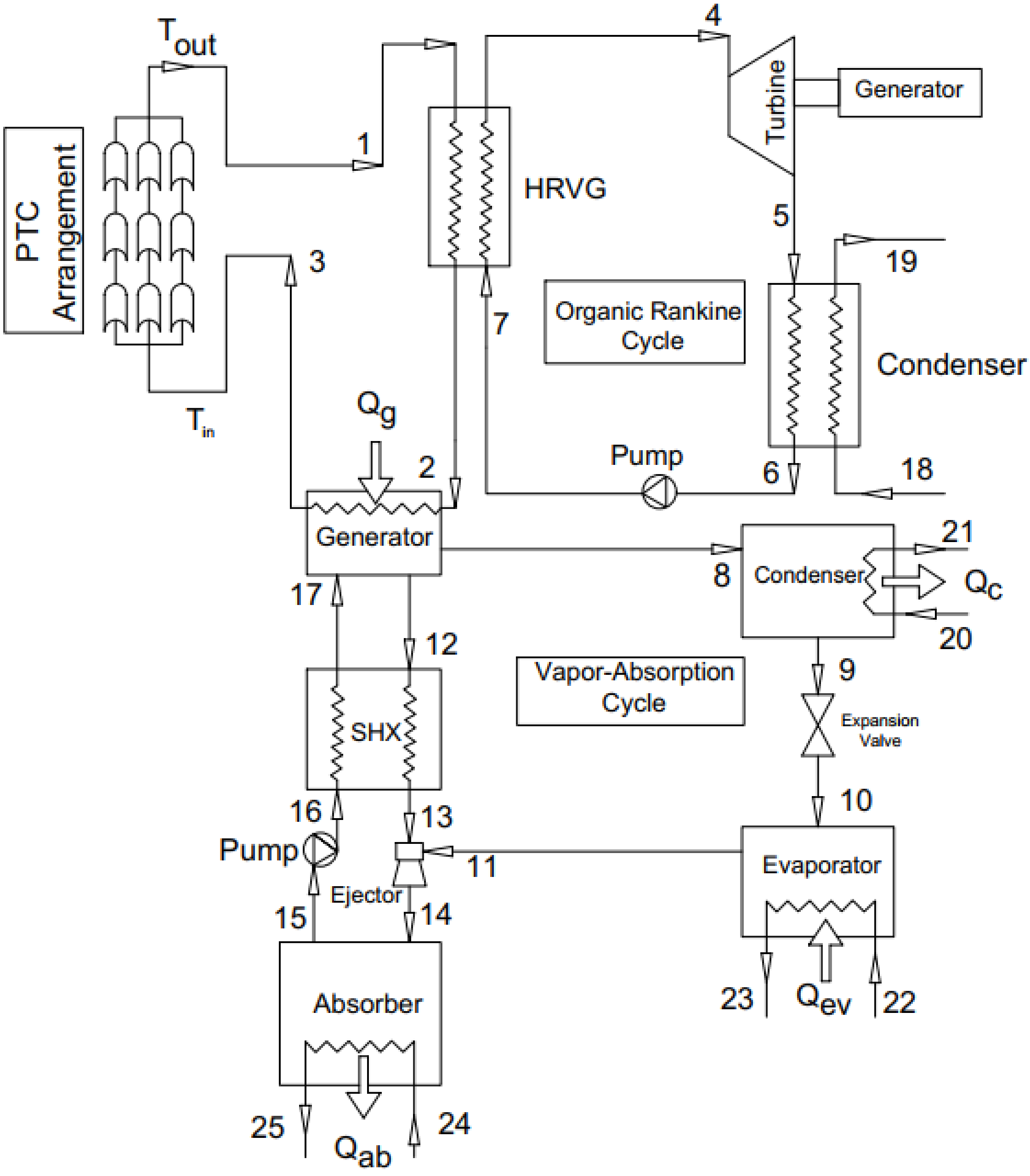

Figure 3.1 Schematic of the solar assisted combined power and cooling system.

3.2 Thermodynamic Modelling of Parabolic Trough Solar Collector

In this section, the energy and exergy analysis of the parabolic trough solar collectors are presented. Figure 3.2 depicts the PTC arrangement where HTF is passing through the receiver. Solar rays reflected to the receiver from the reflector and the receiver absorbs heat during the process resulting in heating the fluid coming out at higher temperatures.

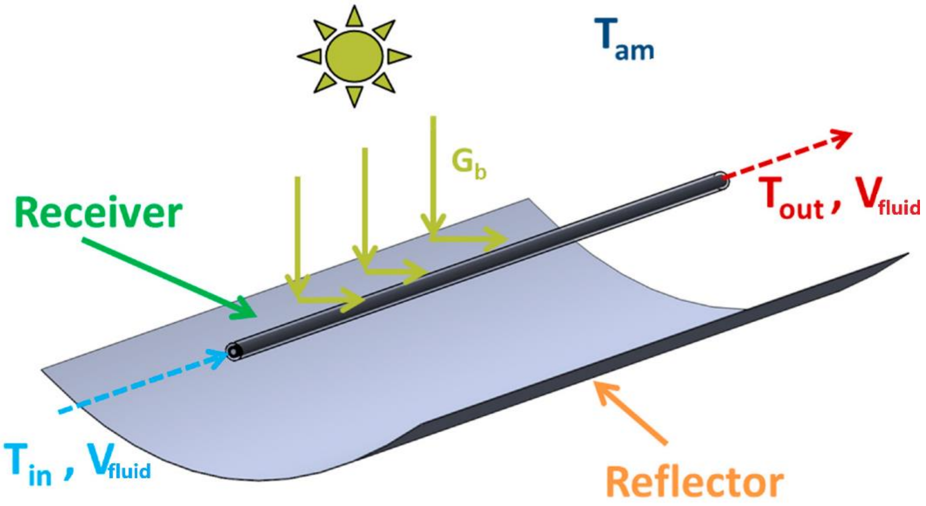

Figure 3.2 PTC arrangement redrawn from [178].

There are different models proposed by Duffie [170], Kalogirou [179] and other authors to assess the performance of PTC. In this research, the equations for mathematical modelling and input parameters for the LS-2 PTC model are adopted from Bellos [180], [181], [182]. The model includes optical, thermal and exergetic modelling widely used for thermal modelling of LS-2 PTC [183]. After illustrating the modelling of a single PTC, this section is followed by a section where design of multiple PTC module is discussed. Now, the equations related to energy balances and important parameters associated with the analysis for a single PTC are elaborated here.

3.2.1 Optical Modelling of PTC

The solar energy received by the collector is not fully utilized fully because a significant portion of it is lost being reflected by the solar collector. Some energy is transmitted through the cover and it is also lost. On the other hand, because of considering only direct beam radiation as the receivable solar energy for the PTC, another portion of solar energy is lost. The absorber material itself consumes some of the energies before it reaches the HTF flowing inside of it. These losses should be taken into account while calculating the utilizable solar energy received by the collector.

The solar energy received by the solar collector $\dot{Q}_s$ is the product of direct beam solar irradiation (G_b) and the aperture area (A_a) of the collector as shown in the following equation.

$$\dot{Q}_s = A_a \times G_b \tag{3.1}$$

A fraction of the energy received is lost and not utilizable due to the optical losses of the solar collector as mentioned earlier. The utilizable solar energy absorbed ($\dot{Q}_{abs}$) can be calculated by multiplying Q_s with the optical efficiency of the collector.

$$\dot{Q}_{abs} = \dot{Q}_s \times \eta_{opt} \tag{3.2}$$

All forms of optical losses are represented by a single parameter called optical efficiency. The factors contributing to optical losses are multiplied together to get the value of optical efficiency (η_{opt}). By definition, η_{opt} is the product of concentrator reflectance (ρ), incident angle modifier (K), transmittance of the cover (τ) and absorbance of the receiver (α). The incident angle modifier K(θ) is a function of the incident angle (θ) in degrees. For zero incident angle considered, $K_{(\theta=0)} = 1$.

$$\eta_{opt} = \rho \times \gamma \times \tau \times \alpha \times K(\theta) \tag{3.3}$$

All the energy absorbed by the collector cannot be utilized fully by the fluid inside the receiver of the PTC. There are heat losses due to convection and radiation heat transfer. As evacuated tube collectors are considered here, due to the vacuum in between the glass and the receiver the convection heat losses are negligible. Only radiation heat losses are considered while calculating heat losses [182]. After subtracting this heat loss ($\dot{Q}_{loss}$) from the absorbed heat in the receiver ($\dot{Q}_{abs}$), the remaining heat is utilized ($\dot{Q}_u$) in the receiver which detailed in the following section.

3.2.2 Thermal Modelling of PTC

The overall energy efficiency (η_{en}) of the PTC is defined as the ratio of useful heat production ($\dot{Q}_u$) to the solar energy received by the concentrator ($\dot{Q}_s$) as shown in the formulation below [181].

$$\eta_{en} = \frac{\dot{Q}_u}{\dot{Q}_s} \tag{3.4}$$

The useful heat production from the collector can be calculated with a typical heat equation with the mass flow rate of the heat transfer fluid in the receiver, specific heat of the fluid considered and the temperature difference in between the outlet ($T_{r,o}$) and inlet ($T_{r,i}$) of the fluid.

$$\dot{Q}_u = \dot{m} \times c_{p,fluid} \times (T_{r,o} - T_{r,i}) \tag{3.5}$$

This useful heat is actually coming from the hot receiver tube (at temperature T_r) to the relatively cold HTF (at temperature T_{fluid}) inside the receiver by the means of convection heat transfer. So, the useful heat can be also calculated by examining the heat transfer between the working fluid and the absorber tube. Heat transfer coefficient (h_{fluid}) and receiver inner area (A_{ri}) are the values associated with the heat transfer calculation.

$$\dot{Q}_u = h_{fluid} \times A_{ri} \times (T_r - T_{fluid}) \tag{3.6}$$

As the fluid temperature varies over the length of the tube, a mean temperature is considered for the simplicity of the calculation. Mean fluid temperature (T_{fluid}) is the average of the inlet ($T_{r,i}$) and outlet ($T_{r,o}$) fluid temperatures. This temperature level is also used for the working fluid properties calculation [181].

$$T_{fluid} = \frac{(T_{r,i} + T_{r,o})}{2} \tag{3.7}$$

Nusselt number is used to estimate the heat transfer coefficient in between the receiver and the fluid inside of it. Nusselt number of the fluid is defined as:

$$Nu_{fluid} = \frac{h_{fluid} \times D_{ri}}{k_{fluid}} \tag{3.8}$$

All the examined cases here are considered to be turbulent flow ($Re > 2300$). For turbulent flow cases, Nusselt number can be estimated by using the Dittus-Boelter equation [184].

$$Nu_{fluid} = 0.023 \times Re_{fluid}^{0.8} \times Pr_{fluid}^{0.4} \tag{3.9}$$

The Reynolds number (*Re*) and the Prandtl number (*Pr*) are defined as,

$$Re_{fluid} = \frac{4 \times \dot{m}}{\pi \times D_{ri} \times \mu_{fluid}} \tag{3.10}$$

$$Pr_{fluid} = \frac{\mu_{fluid} \times C_{p,fluid}}{k_{fluid}} \tag{3.11}$$

The thermal model is developed based on the energy balance on the absorber tube. The absorbed solar energy ($\dot{Q}_{abs}$) has two constituents, namely the useful heat ($\dot{Q}_{u}$) and the thermal losses ($\dot{Q}_{loss}$).

$$\dot{Q}_{abs} = \dot{Q}_{u} + \dot{Q}_{loss} \tag{3.12}$$

The thermal losses of the solar collector are associated with the undesirable loss of heat from the absorber to the cover. As the space in between the cover and the receiver is considered to be evacuated (pressure level of some Pascal) only radiation thermal losses are considered neglecting any form of convection heat transfer [181].

$$\dot{Q}_{loss} = \frac{A_r \times \sigma \times ({T_r}^4 - {T_c}^4)}{\frac{1}{\epsilon_r} + \frac{A_{ro}}{A_{ci}} \times \left(\frac{1}{\epsilon_c} - 1\right)} \tag{3.13}$$

The examined model is focused to develop a thermal model at steady state conditions only. For steady state conditions, thermal losses from the absorber to the cover are equal to the thermal losses from the cover to the ambient. These thermal losses include radiation and convection losses, as shown below [185].

$$\dot{Q}_{loss} = A_{co} \times h_{air} \times (T_c - T_{am)} + A_{co} \times \sigma \times \mathcal{E}_c \times ({T_c}^4 - {T_{sky}}^4) \tag{3.14}$$

It is should be noted that the sky temperature (T_{sky}) used in the radiation losses term above, can be calculated using following Eq. for clear skies [180].

$$T_{sky} = 0.0553 \times {T_{am}}^{1.5} \tag{3.15}$$

The heat convection coefficient between the cover and the ambient air is calculated by using following literature equation for the Nusselt number [186].

$$Nu_{fluid} = 0.193 \times Re_{air}^{0.618} \times Pr_{air}^{0.33} \tag{3.16}$$

The Nusselt number and Reynolds number of fluids are calculated according to the definition outlined below. While calculating these numbers, outer diameter of the cover tube (D_{co}) is used as the characteristic length:

$$Nu_{air} = \frac{h_{air} \times D_{co}}{k_{air}} \tag{3.17}$$

$$Re_{air} = \frac{\rho_{air} \times D_{co} \times u_{air}}{\mu_{air}} \tag{3.18}$$

Added to that, the air properties are calculated to the mean temperature (T_{mean}) between the cover and the ambient.

$$T_{mean} = \frac{(T_c + T_{am})}{2} \tag{3.19}$$

The pressure losses along the receiver tube (ΔP) can be calculated using following equation [186].

$$\Delta P = f_r \times \frac{L}{D_{ri}} \times (\frac{1}{2} \times \rho_{fluid} \times u_{fluid}{}^2) \tag{3.20}$$

The friction factor (f_r) in the equation above is estimated in accordance with this Eq. for turbulent flow [184].

$$f_r = \frac{1}{[0.79 \times \ln(Re_{fluid}) - 1.64]^2} \tag{3.21}$$

The mean working fluid velocity is estimated as:

$$u_{fluid} = \frac{\dot{m}}{\rho_{fluid} \times \left(\pi \times \frac{D_{ri}{}^4}{4}\right)} \tag{3.22}$$

Finally, volumetric flow of the working fluid is calculated as:

$$V_{fluid}(l/min) = 60000 \times u_{fluid} \times \left(\pi \times \frac{D_{ri}^{\,2}}{4}\right)(m^3/s) \tag{3.23}$$

3.2.3 Exergetic Modelling of PTC

In this section, a detailed analysis is done elaborating the estimation of available exergy from the solar irradiation, useful exergy production followed by the estimation of the exergetic losses and finally, the exergy destruction. Parabolic trough collectors utilize only direct beam irradiation from the sun that can be assumed as undiluted. For the estimation of exergy flow resulting from incoming solar irradiation, the model developed by Petela [187] is used. Petela model [187] considers the sun to be the radiation reservoir of temperature (T_{sun}). The temperature is estimated to be 5770K in the outer layers. Exergy flow of the undiluted solar radiation (Ex_s) is described as follows [187]:

$$\dot{Ex}_s = \dot{Q}_s \times [1 + \frac{1}{3} \times \left(\frac{T_{am}}{T_{sun}}\right)^4 - \frac{4}{3} \times \left(\frac{T_{am}}{T_{sun}}\right)] \tag{3.24}$$

The useful exergy output can be calculated using the following equation [180]:

$$\dot{Ex}_u = \dot{Q}_u - \dot{m} \times c_{p,fluid} \times T_{am} \times ln\left(\frac{T_{r,o}}{T_{r,i}}\right) - \dot{m} \times T_{am} \times \frac{\Delta P}{\rho_{fluid} \cdot T_{fluid}} \tag{3.25}$$

The equation above applies for both gases and liquids. But it is important to note that pressure drop term (ΔP) in the equation has different implications for gases and liquids. For liquids, ΔP is very small thus it is neglected. But when used for gases, ΔP has to be considered due to the low density of gases.

It should be noted that exergy for a specific state with reference to the environment is defined as follows:

$$\dot{Ex} = \dot{m} \times [(h - h_0) - T_0 \times (s - s_0)] \tag{3.26}$$

The exergetic efficiency of the solar collector (η_{ex}) is defined as the ratio of the useful production to the exergy input, as indicated by the following equation [180]:

$$\eta_{ex} = \frac{\dot{Ex}_u}{\dot{Ex}_s} \tag{3.27}$$

Using equation 3.4 and equations 3.24 - 3.26, following relation can be established in between thermal and exergy efficiency.

$$\eta_{ex} = \frac{\eta_{th} - [\dot{m} \times c_{p,fluid} \times T_{am} \times ln\left(\frac{T_{r,o}}{T_{r,i}}\right) - \dot{m} \times T_{am} \times \frac{\Delta P}{\rho_{fluid} \cdot T_{fluid}}]/\dot{Q}_s}{1 + \frac{1}{3} \times \left(\frac{T_{am}}{T_{sun}}\right)^4 - \frac{4}{3} \times \left(\frac{T_{am}}{T_{sun}}\right)} \tag{3.28}$$

To get the complete scenario on exergetic analysis of the solar collector, the exergy losses and the exergy destruction have to be calculated. It should be noted that these two important parameters, namely “Exergy Destruction” and “Exergy Losses” are two different concepts. Exergy destruction refers to an internal phenomenon resulting from irreversibilities which can be decreased through the enhancement of the investigated system while exergy losses is considered as an external phenomenon representing the exergy content associated with a stream which is completely rejected into the surroundings. For example, in a refrigeration system with an air-cooled condenser, the exergy content associated with the cooling medium (air) is an exergy loss while the exergy content associated heat transfer irreversibilities or pressure drop in a heat exchanger is an exergy destruction.

As told earlier, the exergy losses (Ex_{loss}) are associated with the heat losses of the system which cannot be utilized further since it is already lost to the surroundings. Exergy losses consist of optical and thermal losses. The optical component of exergetic losses ($Ex_{loss,opt}$) is estimated as:

$$\dot{E}x_{loss,opt} = \dot{E}x_s \times (1 - \eta_{opt}) \tag{3.29}$$

Other component, exergetic thermal losses ($Ex_{loss,th}$) are calculated as:

$$\dot{E}x_{loss,th} = \dot{Q}_{loss} \times (1 - \frac{T_{am}}{T_r}) \tag{3.30}$$

So, the total exergetic losses are calculated as:

$$\dot{E}x_{loss} = \dot{E}x_{loss,opt} + \ \dot{E}x_{loss,th} \tag{3.31}$$

Now we are discussing exergy destruction that expresses the irreversibilities during the occurrence of heat transfer, exergy destruction actually indicates the possible work which is lost and can’t be utilized anymore when thermal energy is transferred to a colder heat reservoir from a warmer one. In this discussion, two cases of irreversibilities are observed to occur during the transfer of heat. The first case of exergy destruction ($Ex_{d,s-r}$) occurs in the heat transfer process in between the sun and the receiver while the rest ($Ex_{d,r-f}$) is the exergy destruction taking place between the warmer receiver and the relatively cold fluid flowing inside of it.

The exergy destruction during the solar energy absorption in the absorber (from the sun to receiver) is calculated as [180]:

$$\dot{E}x_{d,s-r} = \eta_{opt} \times \dot{E}x_s - \dot{Q}_{abs} \times (1 - \frac{T_{am}}{T_r}) \tag{3.32}$$

The exergy destruction during the useful heat production (from receiver to fluid) is formulated as [180]:

$$\dot{E}x_{d,r-f} = \dot{Q}_u \times \left(1 - \frac{T_{am}}{T_r}\right) - \dot{E}x_u \tag{3.33}$$

The total exergy destruction (E_d) is given as:

$$\dot{E}x_d = \dot{E}x_{d,s-r} + \dot{E}x_{d,r-f} \tag{3.34}$$

So, the total exergy balance of the system can be written as:

$$\dot{E}x_s = \dot{E}x_u + \dot{E}x_{loss} + \dot{E}x_d \tag{3.35}$$

3.2.4 PTC Arrangement for Multiple PTC Module

The previous section elaborated the thermodynamic model of a single PTC. Now the design methodology is discussed when multiple PTCs are connected together in a module. In general, many PTCs are connected together in a module to produce high temperature outlet. A series of interconnected PTC modules are connected in parallel through a header for matching the required mass flow rate. The arrangement can be adjusted by regulating the number of PTC modules in series and parallel. The following figure is demonstrating the multiple PTC arrangement considered in this discussion.

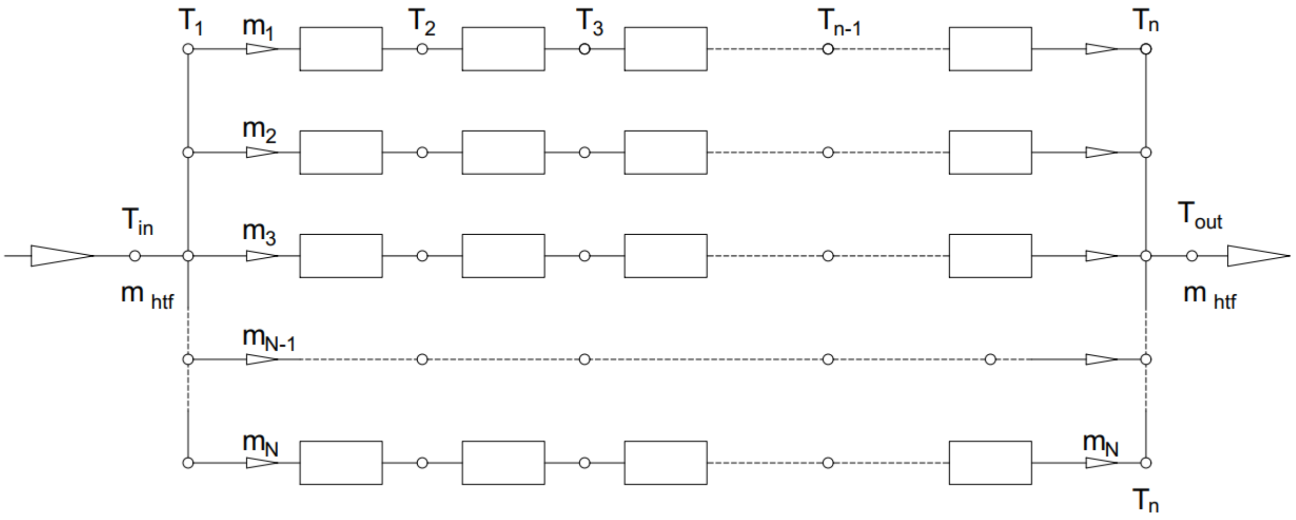

Figure 3.3 Solar PTC arrangement.

HTF fluid at temperature T_{in} is fed into the PTC inlet. The arrangement has N number of rows connected in parallel, whereas each row has (n-1) number of PTC modules connected in series. It is assumed that all the rows have the same fluid flow rate where m_{htf} is the total mass flow rate of HTF.

$$m_1 = m_2 = \cdots\cdot = m_N \tag{3.36}$$

$$m_1 + m_2 + \cdots \ldots \ldots \ldots .. + m_N = m_{htf}$$

It is also assumed for simplicity that the temperature difference in between the inlets and outlets of the successive PTC modules will be the same for a particular solar irradiation and other variables like ambient temperature, fluid flow rate etc.

$$T_1 - T_2 = T_2 - T_3 = \cdots\cdot = T_{n-1} - T_n \tag{3.37}$$

Now for the whole system with multiple PTCs, expressions of total incoming solar energy, exergy and exergy destruction are given below where N_{PTC} is the total number of PTCs :

$$\dot{Q}_{solar} = \dot{Q}_s \times N_{PTC} \tag{3.38}$$

$$\dot{E}x_{solar} = \dot{E}x_s \times N_{PTC} \tag{3.39}$$

$$\dot{E}x_{d,total} = \dot{E}x_d \times N_{PTC} \tag{3.40}$$

3.3 Thermodynamic Modeling of ORC

The thermodynamic modeling of the ORC is presented in this section for the system shown in Figure 3.4. Governing equations are applied to the control volumes enclosing individual components of the system.

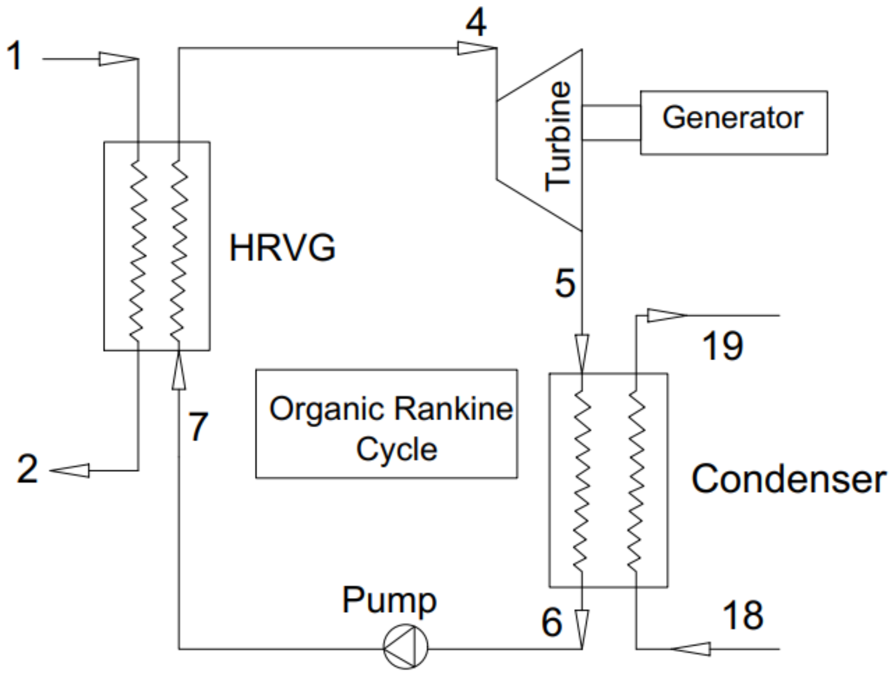

Figure 3.4 Organic Rankine Cycle.

Mass, energy, entropy, exergy and relevant efficiency and effectiveness equations are outlined. The mass flow rate is constant throughout the Organic Rankine Cycle. (ORC). The mass balance equations are as follows:

$$\dot{m}_4 = \dot{m}_5 = \dot{m}_6 = \dot{m}_7 = \dot{m}_o \tag{3.41}$$

where the subscripts 4−7 refer to the states shown in Figure 3.4 and the subscript o indicates the flow inside the organic Rankine cycle.

3.3.1 HRVG

Mass Balance:

As shown in Figure 3.4, the HTF flow from the PTC outlet to the HRVG which is also known as vaporizer, its balance is given in the equation below. As the mass flow rate is same for inlet and exit, it is convenient to denote them by a single entity $\dot{m}_{htf}$.

$$\dot{m}_1 = \dot{m}_2 = \dot{m}_{htf} \tag{3.42}$$

where $\dot{m}_{htf}$ is mass flow rate of heat transfer fluid in solar collector.

On the side of the ORC, the fluid flow rate is uniform all over the cycle and it is denoted by $\dot{m}_o$.

$$\dot{m}_7 = \dot{m}_4 = \dot{m}_o \tag{3.43}$$

where $\dot{m}_o$ is the mass flow rate of fluid in ORC.

Energy Balance:

Energy balance in the HRVG is as follows:

$$\dot{Q}_{HRVG} = \dot{m}_{htf} \times (h_1 - h_2) = \dot{m}_o \times (h_4 - h_7) \tag{3.44}$$

Entropy Balance:

Entropy balance is given as follows:

$$\dot{m}_{htf} \times (s_1 - s_2) + \dot{S}_g = \dot{m}_o \times (s_4 - s_7) \tag{3.45}$$

Exergy Balance:

Exergy balance equations for the HRVG and relevant exergy terms to calculate exergy destruction are given as follows:

$$\dot{m}_{htf} \times ex_1 + \dot{m}_o \times \ ex_7 = \dot{m}_{htf} \times ex_2 + \dot{m}_o \times ex_4 + \dot{E}x_{d,vap} \tag{3.46}$$

Exergy destruction can be calculated using specific entropy from the expression below:

$$\dot{E}x_{d,vap} = T_0 \times [\dot{m}_{htf} \times (s_2 - s_1) + \dot{m}_o \times (s_4 - s_7)] \tag{3.47}$$

Exergy efficiency can be defined in general as ratio of total exergy output to exergy input. Here, exergy efficiency of HRVG can be defined as exergy increase of cold stream to exergy decrease of hot stream.

$$\eta_{ex,vap} = \frac{\dot{m}_o \times (ex_4 - ex_7)}{\dot{m}_{htf} \times (ex_1 - ex_2)} \tag{3.48}$$

3.3.2 ORC Turbine

Mass Balance:

Mass balance of ORC turbine is given by,

$$\dot{m}_4 = \dot{m}_5 = \dot{m}_o \tag{3.49}$$

Energy Balance:

Rate of work generated by turbine, $\dot{W}_{ot}$ is expressed as follows:

$$\dot{W}_{ot,actual} = \dot{m}_o \times (h_4 - h_5) \tag{3.50}$$

The isentropic efficiency of the turbine can be defined as the ratio of the work output from turbine to the work output. For an isentropic process the efficiency is expressed as:

$$\eta_{is,ot} = \frac{\dot{W}_{ot,actual}}{\dot{W}_{ot,isentropic}} = \frac{(h_4 - h_5)}{(h_4 - h_{s,5})} \tag{3.51}$$

Enthalpy at Turbine outlet (h_5) can be calculated as follows:

$$h_5 = h_4 + \eta_{is,ot} \times (h_{s,5} - h_4) \tag{3.52}$$

Entropy Balance:

Entropy balance of the Turbine is given by,

$$\dot{m}_o \times s_5 = \dot{S}_g + \dot{m}_o \times s_4 \tag{3.53}$$

Exergy Balance:

Following expressions are given for the exergy balance in terms of specific exergy:

$$\dot{m}_o \times ex_4 = \dot{m}_o \times ex_5 + \dot{W}_{ot} + \dot{Ex}_{d,ot} \tag{3.54}$$

Or, $\dot{Ex}_{d,ot} = -\dot{W}_{ot} + \dot{m}_o \times (ex_4 - ex_5)$

Exergy destruction is calculated in terms of specific entropy as given below:

$$\dot{Ex}_{d,ot} = T_0 \times [\dot{m}_o \times (s_5 - s_4)] \tag{3.55}$$

The exergy efficiency of the turbine can be defined as the ratio of the work output to reversible work and given as follows:

$$\eta_{ex,ot} = \frac{\dot{W}_{ot,out}}{\dot{W}_{ot,rev}} = \frac{\dot{W}_{ot}}{\dot{m}_o \times (ex_4 - ex_5)} \tag{3.56}$$

3.3.3 ORC Condenser

In ORC condenser the high temperature exhaust vapor of the Turbine gets condensed and turns into saturated liquid as shown in Figure 3.4. The external flow can be coupled with the PTC HTF feed system as we have assumed here. PTC feed can take this high temperature exhaust heat from the condenser and can go into the receiver at a high temperature hence contributing to higher efficiency.

Mass Balance:

Mass balance of the ORC fluid and the external cooling fluids are given as follows,

$$\dot{m}_5 = \dot{m}_6 = \dot{m}_o \tag{3.57}$$

$$\dot{m}_{18} = \dot{m}_{19} = \dot{m}_{cond} \tag{3.58}$$

Energy Balance:

Energy balance is given by,

$$\dot{Q}_{cond} = \dot{m}_o \times (h_5 - h_6) = \dot{m}_{cond} \times (h_{19} - h_{18}) \tag{3.59}$$

Entropy Balance:

Entropy balance is given by,

$$\dot{m}_o \times s_5 + \dot{S}_g + \dot{m}_{cond} \times s_{18} = \dot{m}_o \times s_6 + \dot{m}_{cond} \times s_{19} \tag{3.60}$$

Exergy Balance:

Exergy balance in terms of specific exergy is given as:

$$\dot{E}x_{d,cond} = \dot{m}_{cond} \times (ex_{18} - ex_{19}) + \dot{m}_o \times (ex_5 - ex_6) \tag{3.61}$$

Exergy destruction in terms of specific entropy is given as:

$$\dot{E}x_{d,cond} = T_0 \times [\dot{m}_o \times (s_6 - s_5) + \dot{m}_{cond} \times (s_{19} - s_{18})] \tag{3.62}$$

Exergy efficiency of the condenser is given as follows:

$$\eta_{ex,oc} = \frac{\dot{m}_{cond} \times (ex_{18} - ex_{19})}{\dot{m}_o \times (ex_5 - ex_6)} \tag{3.63}$$

3.3.4 ORC pump

Mass Balance:

Mass flow rate of fluid flowing in and out from the pump is same in ORC pump and given by,

$$\dot{\mathrm{m}}_6 = \dot{\mathrm{m}}_7 \tag{3.64}$$

Pump Work:

Isentropic and actual pump work is outlined below:

$$\dot{W}_{op} = \dot{m}_o \times (h_7 - h_6) \tag{3.65}$$

$$\dot{W}_{op,is} = \dot{m}_o \times (h_{s,7} - h_6) \tag{3.66}$$

Where,

$\dot{W}_{op}$ is ORC Pump power, kW.

$\dot{W}_{op,is}$ is isentropic power of the pump, kW.

Isentropic efficiency of the pump is defined as follows.

$$\eta_{op,is} = \frac{\dot{W}_{op,is}}{\dot{W}_{op}} = \frac{(h_{s,7} - h_6)}{(h_7 - h_6)} \tag{3.67}$$

Entropy Balance:

Entropy balance for the pump is given as,

$$\dot{S}_g = \dot{m}_o \times (s_7 - s_6) \tag{3.68}$$

Exergy Balance:

Exergy balance is given as,

$$\dot{m}_o \times ex_7 + \dot{E}x_{d,op} = \dot{m}_o \times ex_6 + \dot{W}_{op} \tag{3.69}$$

Exergy destruction can be calculated from the expressions below:

$$\dot{E}x_{d,op} = \dot{W}_{op} + \dot{m}_o \times (ex_6 - ex_7) \tag{3.70}$$

$$\dot{E}x_{d,op} = T_0 \times \dot{S}_g = T_0 \times \dot{m}_o \cdot (s_7 - s_6) \tag{3.71}$$

Exergy efficiency of the pump is given by,

$$\eta_{ex,op} = \frac{\dot{m}_o \times (ex_7 - ex_6)}{\dot{W}_{op}} \tag{3.72}$$

Where $\eta_{ex,op}$ is the exergy efficiency of ORC pump and $\dot{W}_{op}$ is the actual pump work.

3.3.5 Cycle Efficiency of ORC

Thermal efficiency of the ORC is given by,

$$\eta_{ORC} = \frac{\dot{W}_{net}}{\dot{Q}_{HRVG}} = \frac{\dot{W}_{ORC\ Turbine} - \dot{W}_{ORC\ Pump}}{\dot{Q}_{HRVG}} \tag{3.73}$$

Where,

$\dot{W}_{net}$ is the net work output of the power cycle i.e.

$\dot{Q}_{HRVG}$ is the heat input in the ORC.

Second law efficiency of ORC is given by [188] ,

$$\eta_{ex,ORC} = \frac{\dot{W}_{net}}{\dot{m}_{htf} \times \{(h_1 - h_0) - T_0 \times (s_1 - s_0)\}} \tag{3.74}$$

3.4 Modelling Ejector-Absorption Refrigeration cycle (EARC)

The thermodynamic modelling of EARC is elaborated here for the system in Figure 3.5. EARC generator is set up before the inlet of the PTC arrangement. The generator outlet of the external heat source is fed directly as the inlet of PTC arrangement. To start with, the HTF leaving the PTC passes through the HRVG of the ORC and after losing a significant amount of heat which is utilized to rise the turbine inlet fluid temperature as high as possible, the HTF of PTC cycle comes to the generator of the absorption cycle. The generator takes heat from the incoming external flow of HTF and the refrigerant is separated from the absorbent solution due the action of this receival of heat.

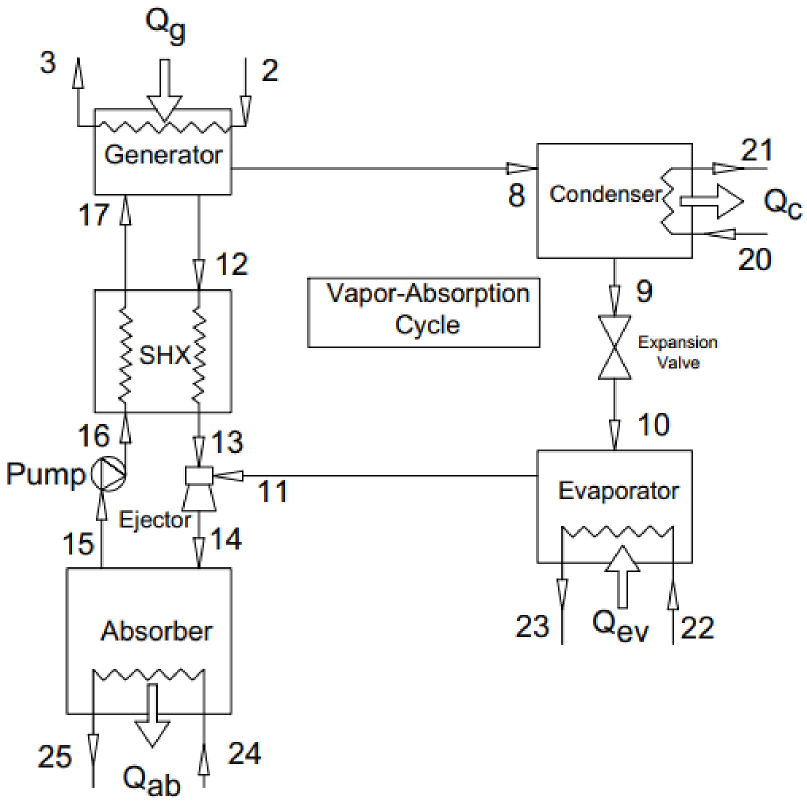

Figure 3.5 Schematic of Ejector-Absorption Refrigeration Cycle (EARC).

After that the refrigerant takes its path to the condenser before diverting to the evaporator and producing the desired cooling effect. The strong solution intake of generator becomes weak in concentration of refrigerant while exiting the generator and taking its way to the Absorber via SHX. This is how the operations take place in EARC and the mathematical modelling [189] of the EARC system and its components is detailed on the following subsections.

3.4.1 Generator

Mass Balance:

Mass balance of the internal flow of EARC and external flow of HTF from PTC cycle is given as follows:

$$\dot{m}_2 = \dot{m}_3 = \dot{m}_{htf} \tag{3.75}$$

$$\dot{m}_{17} = \dot{m}_8 + \dot{m}_{12} \tag{3.76}$$

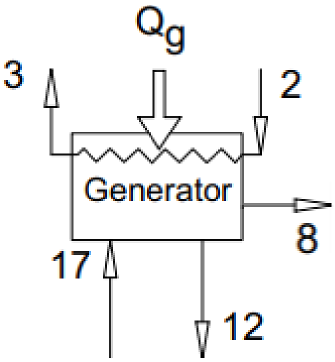

Figure 3.6 Generator fluid flow.

Energy Balance:

From Figure 3.6 one can write down the mass balance in the generator considering the flows limited to EARC, as follows:

$$\dot{m}_{17} \times h_{17} - \dot{m}_8 \times h_8 - \dot{m}_{12} \times h_{12} + \dot{Q}_g = 0 \tag{3.77}$$

Or, $\dot{Q}_g = \dot{m}_{12} \times h_{12} + \dot{m}_8 \times h_8 - \dot{m}_{17} \times h_{17}$

Where, $\dot{Q}_g$ is the heat received by the generator from the PTC heat source.

Now, as heat dissipated by the PTC fluid is received by the generator we can write $\dot{Q}_g$ as follows:

$$\dot{Q}_g = \dot{m}_2 \times (h_2 - h_3) = \dot{m}_{htf} \times (h_2 - h_3) \tag{3.78}$$

Entropy Balance:

Entropy balance of the generator is given as follows:

$$\dot{S}_g = \dot{m}_{12} \times s_{12} + \dot{m}_8 \times s_8 - \dot{m}_{17} \times s_{17} + \dot{m}_{htf} \times (s_3 - s_2) \qquad (3.79)$$

Exergy Balance:

Exergy balance of the generator is given as follows in terms of specific exergy:

$$\dot{E}x_{d,g} = \dot{m}_{17} \times ex_{17} - \dot{m}_8 \times ex_8 - \dot{m}_{12} \times ex_{12} + \dot{m}_{htf} \times (ex_2 - ex_3) \qquad (3.80)$$

Exergy destruction can also be expressed as follows:

$$\dot{E}x_{d,g} = T_0 \times [\dot{m}_{12} \times s_{12} + \dot{m}_8 \times s_8 - \dot{m}_{17} \times s_{17} + \dot{m}_{htf} \times (s_3 - s_2)] \qquad (3.81)$$

Exergy efficiency of the generator is given as follows:

$$\eta_{ex,g} = 1 - \frac{\dot{m}_{17} \times ex_{17} - \dot{m}_8 \times ex_8 - \dot{m}_{12} \times ex_{12} + \dot{m}_{htf} \times (ex_2 - ex_3)}{\dot{m}_{htf} \times (ex_2 - e_3)} \qquad (3.82)$$

3.4.2 Condenser

Mass Balance:

After getting separated from the solution in the generator, the refrigerant is flowing into the EARC condenser and exits towards the evaporator to produce the refrigerating effect. External cooling passes through the condenser taking away the releasing heat. $\dot{m}_{con}$ is the mass flow rate of the cooling fluid. Mass balance of the condenser is given as:

$$\dot{m}_8 = \dot{m}_9 = \dot{m}_r \qquad (3.83)$$

$$\dot{m}_{20} = \dot{m}_{21} = \dot{m}_{con} \qquad (3.84)$$

Energy Balance:

The condenser is releasing heat to the ambient amounted as $\dot{Q}_{con}$ and the refrigerant turns into saturated liquid from the vapor state releasing heat. $\dot{m}_{20}$ and $\dot{m}_{21}$ represent inlet and exit of the external cooling fluid. Energy balance in the condenser is given as follows.

$$\dot{Q}_{cond} = \dot{m}_8 \times (h_8 - h_9) = \dot{m}_r \times (h_8 - h_9) \tag{3.85}$$

$$= \dot{m}_{con} \times (h_{21} - h_{20})$$

Entropy Balance:

$$\dot{m}_{con} \times s_{21} + \dot{m}_r \times s_9 = \dot{m}_{con} \times s_{20} + \dot{m}_r \times s_8 + \dot{S}_g \tag{3.86}$$

Exergy Balance Equation:

Exergy balance in terms of specific exergies are given as follows:

$$\dot{m}_{con} \times (ex_{21} - ex_{20}) = \dot{m}_r \times (ex_8 - ex_9) + \dot{E}x_{d,con} \tag{3.87}$$

Exergy destruction in terms of specific entropy are given as:

$$\dot{E}x_{d,con} = T_0 \times \{\dot{m}_r \times (s_9 - s_8) + \dot{m}_{con} \times (s_{21} - s_{20})\} \tag{3.88}$$

Exergy efficiency of EARC condenser is given as:

$$\eta_{ex,con} = \frac{\dot{m}_{con} \times (ex_{20} - ex_{21})}{\dot{m}_o \times (ex_8 - ex_9)} \tag{3.89}$$

3.4.3 Throttling Valve

Mass Balance:

Mass balance of throttle valve is given as follows:

$$\dot{m}_9 = \dot{m}_{10} = \dot{m}_r \tag{3.90}$$

Energy Balance:

Energy balance is given as follows:

$$h_9 = h_{10} \tag{3.91}$$

Entropy Balance:

Entropy balance is given as follows:

$$\dot{S}_g = \dot{m}_r \times (s_{10} - s_9) \tag{3.92}$$

Exergy Balance:

Exergy balance is given as follows:

$$\dot{m}_r \times ex_9 = \dot{m}_r \times ex_{10} + \dot{Ex}_{d,expv} \tag{3.93}$$

$$\dot{Ex}_{d,expv} = T_0 \times \dot{m}_r \times (s_{10} - s_9) \tag{3.94}$$

Exergy efficiency is termed as,

$$\eta_{ex,expv} = \frac{ex_{10}}{ex_9} \tag{3.95}$$

3.4.4 Evaporator

Mass Balance:

Mass balance of evaporator is given as follows:

$$\dot{m}_{11} = \dot{m}_{10} = \dot{m}_r \tag{3.96}$$

$$\dot{m}_{22} = \dot{m}_{23} = \dot{m}_{ev} \tag{3.97}$$

Energy Balance:

Energy balance of Evaporator is expressed as follows:

$$\dot{Q}_{ev} = \dot{m}_{10} \times (h_{11} - h_{10}) \tag{3.98}$$

$$= \dot{m}_r \times (h_{11} - h_{10}) = \dot{m}_{ev} \times (h_{22} - h_{23})$$

Entropy Balance:

Entropy balance is given by,

$$\dot{S}_g = \dot{m}_r \times (s_{11} - s_{10}) + \dot{m}_{ev} \times (s_{23} - s_{22}) \tag{3.99}$$

Exergy Balance:

$$\dot{m}_{ev} \times (ex_{22} - ex_{23}) = \dot{m}_r \times (ex_{11} - ex_{10}) + \dot{Ex}_{d,ev} \tag{3.100}$$

Exergy destruction in the evaporator is given as follows:

$$\dot{E}x_{d,ev} = T_0 \times [\dot{m}_r \times (s_{11} - s_{10}) + \dot{m}_{ev} \times (s_{23} - s_{22})] \tag{3.101}$$

Exergy efficiency of the evaporator is given by,

$$\eta_{ex,ev} = \frac{\dot{m}_r \times (ex_{10} - ex_{11})}{\dot{m}_{ev} \times (ex_{22} - ex_{23})} \tag{3.102}$$

3.4.5 Ejector

Ejector is a device that upon receiving two streams of high and low pressure creates an intermediate pressure without any electrical power consumption. It receives a primary flow of weak solution with high pressure through the nozzle from the generator and other secondary flow of refrigerant from the evaporator, then mix them together in a mixing tube. After mixing the streams the solution is passed to the absorber.

Governing equations for the modelling and flow analysis of ejector are given below [190]:

Nozzle:

$$V_N = \left(\eta_N \times 2 \times \frac{1000 \times (P_{con} - P_{eva})}{\rho_{13}}\right)^{0.5} \tag{3.103}$$

$$A_N = \pi \times \frac{{D_N}^2}{4} \tag{3.104}$$

$$\rho_{13} = f(T_{13}, X_{13}) \tag{3.105}$$

$$A_N = \frac{\dot{m}_{12}}{\rho_{13} \times V_N} \tag{3.106}$$

Mixing section:

$$V_M = \frac{\dot{m}_9 + \dot{m}_{12}}{A_M + \rho_M} \tag{3.107}$$

$$A_M = \pi \times \frac{{D_M}^2}{4} \tag{3.108}$$

$$\rho_M = \frac{\dot{m}_9 + \dot{m}_{12}}{\frac{\dot{m}_9}{\rho_{11}} + \frac{\dot{m}_{12}}{\rho_{13}}} \tag{3.109}$$

$$P_M = P_{eva} + \eta_M \times \frac{\dot{m}_{12} \times V_N - (\dot{m}_{12} + \dot{m}_9) \times V_M}{A_M \times 1000} \tag{3.110}$$

Diffuser:

$$P_D = P_M + \frac{0.5 \cdot \rho_M \times \left({V_M}^2 - {V_D}^2\right) \times \eta_D}{1000} \tag{3.111}$$

$$P_{abs} = P_D \tag{3.112}$$

$$\dot{m}_{12} \times h_{13} + \dot{m}_{11} \times h_{11} = \dot{m}_{12} \times h_{14s} + \dot{m}_{11} \times h_{14r} \tag{3.113}$$

$$h_{14s} = f(T_{14}, X_{12}) \tag{3.114}$$

$$h_{14r} = f(T_{14}, P_{abs}) \tag{3.115}$$

$$V_D = \frac{\dot{m}_{12} + \dot{m}_9}{A_D \times \rho_M} \tag{3.116}$$

$$A_D = \pi \times \frac{{D_D}^2}{4} \tag{3.117}$$

From, Figure 3.7 we can see that,

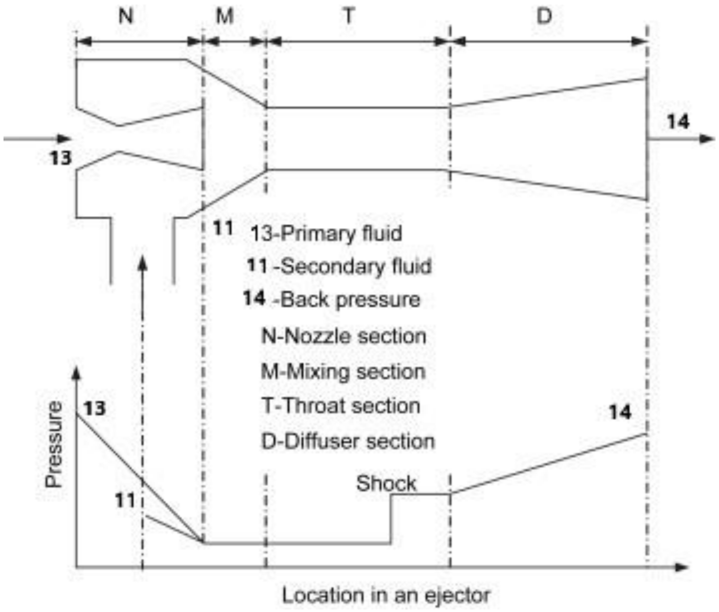

Figure 3.7 Ejector structure and working process redrawn from [191].

Mass Balance:

Mass balance is given as,

$$\dot{m}_{pf} + \dot{m}_{sf} = \dot{m}_{14} \tag{3.118}$$

Energy Balance:

Energy balance is given as,

$$\dot{m}_{pf} \times h_{13} + \dot{m}_{sf} \times h_{11} = \dot{m}_{14} \times h_{14} \tag{3.119}$$

Entropy Balance:

Entropy balance is given as,

$$\dot{m}_{pf} \times s_{13} + \dot{m}_{sf} \times s_{11} + \dot{S}_g = \dot{m}_{14} \times s_{14} \tag{3.120}$$

Exergy Balance:

Exergy destruction in terms of specific exergy is given by,

$$\dot{m}_{pf} \times ex_{13} + \dot{m}_{sf} \times ex_{11} = \dot{m}_{14} \times ex_{14} + \dot{E}x_{d,ej} \tag{3.121}$$

Exergy destruction in terms of specific entropy is given by,

$$\dot{E}x_{d,ej} = T_0 \times (\dot{m}_{14} \times s_{14} - \dot{m}_{pf} \times s_{13} - \dot{m}_{sf} \times s_{11}) \tag{3.122}$$

Ejector exergy efficiency is given by,

$$\eta_{ex,ej} = \frac{\dot{m}_{sf} \times (ex_{14} - ex_{11})}{\dot{m}_{pf} \times (ex_{13} - ex_{14})} \tag{3.123}$$

3.4.6 Absorber

Mass Balance:

Mass balance of the absorber is given by,

$$\dot{m}_{24} = \dot{m}_{25} = \dot{m}_{ab} \tag{3.124}$$

$$\dot{m}_{14} = \dot{m}_{15} \tag{3.125}$$

Energy Balance:

Energy released by the absorber, $\dot{Q}_{ab}$ is given as:

$$\dot{m}_{14} \times h_{14} - \dot{m}_{15} \times h_{15} - \dot{Q}_{ab} = 0 \tag{3.126}$$

Energy balance with the absorber internal flow and coolant flow is given as,

$$\dot{Q}_{ab} = \dot{m}_{ab} \times (h_{25} - h_{24}) \tag{3.127}$$

Entropy Balance:

$$\dot{m}_{ab} \times (s_{25} - s_{24}) + \dot{S}_g = \dot{m}_{14} \times (s_{15} - s_{14}) \tag{3.128}$$

Exergy Balance:

$$\dot{Ex}_{d,ab} = \dot{m}_{ab} \times (ex_{24} - ex_{25}) + \dot{m}_{10} \times (ex_{10} - ex_{11}) \tag{3.129}$$

3.4.7 Liquid Solution Pump

Mass Balance:

Solution pump’s mass balance is given as,

$$\dot{m}_{16} = \dot{m}_{15} = \dot{m}_s \tag{3.130}$$

Energy Balance:

When an ejector is employed in the EARC, the system runs on three pressure level. Generator and evaporator operate on the high-pressure and low-pressure level respectively. Ejector creates an intermediate pressure level and passes the solution to the absorber. The pump upon receiving the solution from the absorber at intermediate pressure, will raise the pressure to generator pressure in the cycle. Solution pump work is defined as following:

$$\dot{W}_{sp} = \dot{m}_{15} \times v_{15} \times \left(P_{high} - P_{absorber}\right) = \dot{m}_{15} \times (h_{16} - h_{15}) \tag{3.131}$$

If the refrigeration cycle is run by simple ARC, the ejector is replaced by an expansion valve and the cycle will operate on two pressure level only.

$$\dot{W}_{sp} = \dot{m}_{15} \times v_{15} \times \left(P_{high} - P_{low}\right) = \dot{m}_{15} \times (h_{16} - h_{15}) \tag{3.132}$$

Entropy Balance:

$$\dot{S}_g = \dot{m}_s \times (s_{16} - s_{15}) \tag{3.133}$$

Exergy Balance:

$$\dot{E}x_{d,sp} = W_{sp} + \dot{m}_{14} \times (ex_{15} - ex_{16}) \tag{3.134}$$

3.4.8 Solution Heat Exchanger

Mass Balance:

$$\dot{m}_{13} = \dot{m}_{12} \tag{3.135}$$

$$\dot{m}_{17} = \dot{m}_{16} \tag{3.136}$$

Energy Balance:

$$\dot{Q}_{shx} = \dot{m}_{15} \times (h_{17} - h_{16}) = \dot{m}_{12} \times (h_{12} - h_{13}) \tag{3.137}$$

Heat Exchanger Effectiveness:

Heat exchanger effectiveness is defined as follows [189],

$$\mathcal{E}_{shx} = \frac{\dot{Q}_{shx}}{\dot{C}_{min} \times (T_{12} - T_{16})} \tag{3.138}$$

Where, $\dot{C}_{min}$ is the minimum capacitance rate between two counter flows in SHX. Capacitance rates of the two flows are given as follows,

$$\dot{C}_{16-17} = \dot{m}_{16} \times \frac{h_{16} - h_{17}}{(T_{16} - T_{17})} \tag{3.139}$$

$$\dot{C}_{12-13} = \dot{m}_{12} \times \frac{h_{12} - h_{13}}{(T_{12} - T_{13})} \tag{3.140}$$

Exergy Balance:

$$\dot{E}x_{d,hx} = \dot{m}_{12} \times (ex_{12} - ex_{13}) + \dot{m}_{16} \times (ex_{16} - ex_{17}) \tag{3.141}$$

3.4.9 Cycle Efficiency of EARC

COP of the EARC is given as,

$$COP_{EARC} = \frac{\dot{Q}_{ev}}{\dot{Q}_{gen} + W_p} \tag{3.142}$$

Second law efficiency of EARC is given by [141], [111],

$$\eta_{II,\ EARC} = \frac{\dot{Q}_{ev} \times (\frac{T_0}{T_{cold}} - 1)}{\dot{Q}_{gen} \times \left(1 - \frac{T_0}{T_{hot}}\right) + W_p} \tag{3.143}$$

$$T_{hot} = \frac{(T_2 + T_3)}{2} \tag{3.144}$$

$$T_{cold} = \frac{(T_{22} + T_{23})}{2} \tag{3.145}$$

Here, T_{hot} is the mean temperature of the heat source and T_{cold} is the mean temperature of the stream to be cooled.

3.5 First and Second Law Efficiency of the PTC Integrated ORC

The first law efficiency of the PTC integrated ORC is given as,

$$\eta_I = \frac{\dot{W}_{net}}{\dot{Q}_{solar}} \tag{3.146}$$

The second law efficiency of the PTC integrated ORC is given as,

$$\eta_{II} = \frac{\dot{W}_{net}}{\dot{E}x_{solar}} \tag{3.147}$$

Where,

$\dot{W}_{net}$ is the net work output of the power cycle.

$\dot{Q}_{solar}$ is the solar energy received by the solar collector.

$\dot{E}x_{solar}$ is the total incoming exergy associate with the solar radiation falling on the concentrating solar collector.

3.6 System Performance Factor and Exergy Efficiency of the Combined Power and Cooling System

The system performance factor of the total system is given by [192],

$$\eta_{\mathrm{I}} = \frac{\dot{W}_{net} + \dot{Q}_{ev}}{\dot{Q}_{solar}} \tag{3.148}$$

Where,

$\dot{W}_{net}$ is the net work output of the power cycle.

$\dot{Q}_{ev}$ is the cooling effect produced by the evaporator in EARC.

$\dot{Q}_{solar}$ is the solar energy received by the solar collector.

The exergy efficiency of the total system is given by [192],

$$\eta_{\mathrm{II}} = \frac{\dot{W}_{net} + \dot{Ex}_{ev}}{\dot{Ex}_{solar}} \tag{3.149}$$

$$\dot{Ex}_{ev} = \dot{Q}_{ev} \times (\frac{T_0}{T_{ev}} - 1) \tag{3.150}$$

Where,

$\dot{Ex}_{solar}$ is the total incoming exergy associate with the solar radiation falling on the PTC [187] . T_0 and T_{ev} stand for the standard atmospheric temperature (298 K) and the evaporator temperature. $\dot{W}_{net}$ is the power output and $\dot{Ex}_{ev}$ is the change in exergy is EARC Evaporator.

3.7 Methodology and Solution Approach

The proposed model is developed to conduct a parametric study to find out the optimal performance of the system. Various hydrocarbon fluids can be used in the concentrated solar power receiver. The prospect of different heat transfer fluids in Organic Rankine Cycle (ORC) and working pairs in the Ejector-Absorption Refrigeration system (EARS) will be analyzed. Weather and solar DNI data will be taken accordingly. The overall efficiency of the power system powered by PTC will be calculated. The COP of the EARC system will be calculated as well for the proposed system. The proposed mathematical model will be formulated in Engineering Equation Solver (EES) for the analysis.

The system is novel model, so it cannot be validated as a whole. Therefore, it would be validated by parts. The Solar collector model can be validated using a reference paper on PTC. The organic Rankine cycle can be validated individually or in combination with the solar collector as there are literatures in combination of ORC and solar collector. The absorption refrigeration system will be validated along with the ejector from suitable reference paper.

The following flow chart is given below for the sequentialization of the tasks.

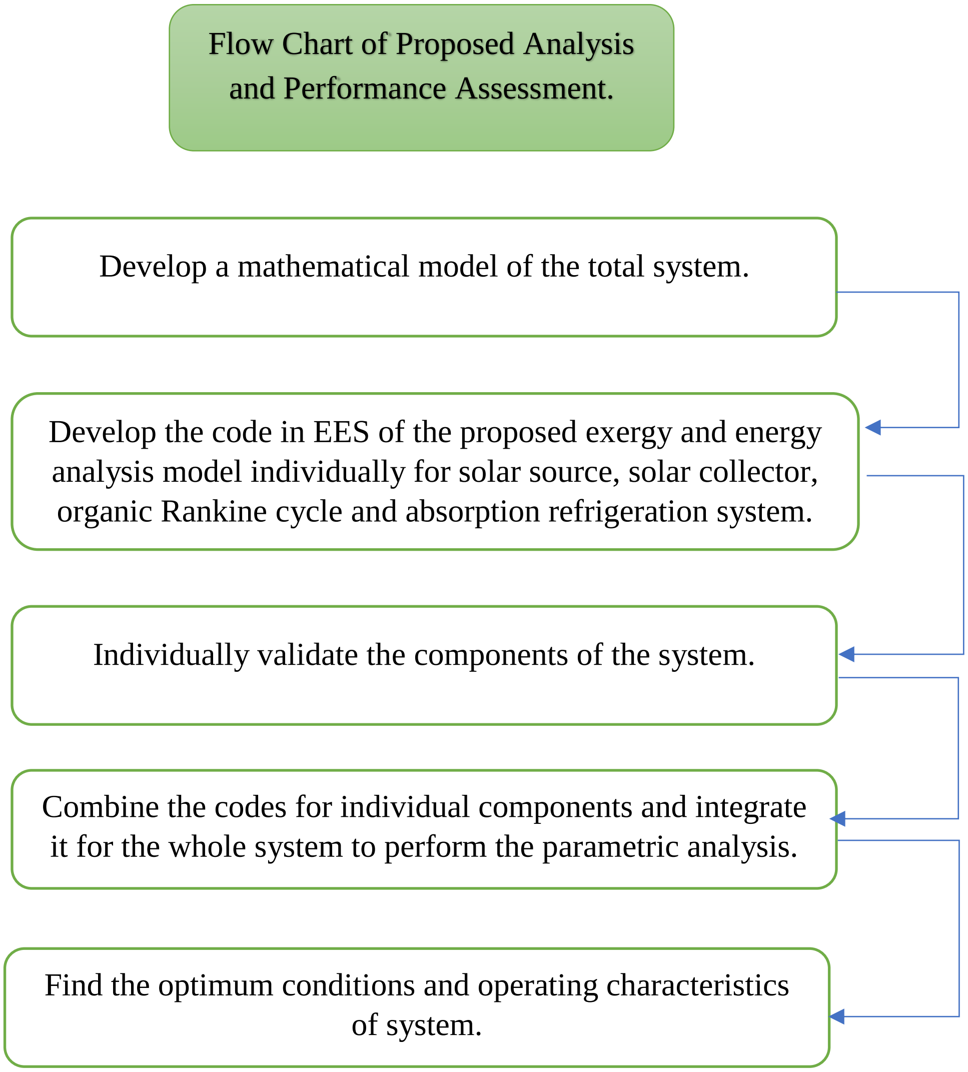

Figure 3.8 Solution flow chart.

CHAPTER 4

PERFORMANCE ANALYSIS OF ORC INTEGRATED WITH PTC

4.1 Introduction

The worldwide concern for a safe environment is redirecting the industries to produce clean energy with lower carbon emissions and reduced global warming potentials. Adding to the equation is the limited reserves of the conventional fossil fuels. Solar energy is proven to be an efficient tool to tackle the crisis of limited energy reserves and at the same time achieving the goal of producing sufficient energy that is clean. Along with solar PV, a growing number of CSP technologies are used to produce power using conventional power cycles. Parabolic Trough Collector (PTC) is a mature CSP technology as heat source that can operate on a wide level of temperatures with high efficiency. Organic Rankine Cycle (ORC) is a proven technology to harness power from low temperature heat sources. In this study, the performance of PTC integrated with ORC will be investigated to find out the optimum operating scenarios and assessing the exergy destruction at different components of the combined system.

4.2 System Description

PTC model is integrated with ORC as a heat source for the latter as outlined in Figure 4.1. Final outlet feed of the solar PTC field is coupled with the vaporizer or HRVG of ORC. The HRVG working principle is like a counter flow heat exchanger and consists of economizer, evaporator and superheater. Subcooled or liquid ORC fluid becomes saturated liquid in economizer, saturated vapor in evaporator and gets superheated in the superheater.

For simplicity, we will only use HRVG or vaporizer in our discussion instead of referring to its components.

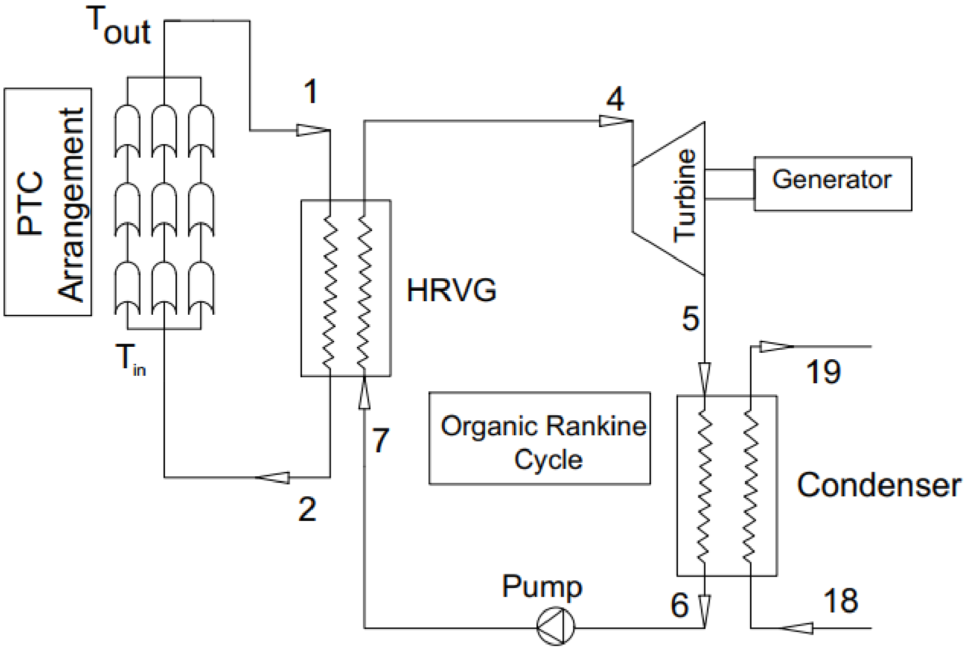

Figure 4.1 PTC integrated with ORC.

Also, there needs to be a minimum temperature difference to facilitate heat transfer in between the hot fluid flow of the PTC receiver feed and the cold ORC fluid feed to HRVG coming from the ORC feed pump. This temperature difference is called pinch point temperature. To make the integrated system work, the temperature difference between PTC receiver feed and HRVG can't go lower than the pinch point temperature [193].

4.3 Stand-Alone PTC Model Validation

PTC LS-2 Model is examined in the analysis reported by [180]. The developed PTC model is validated with literature result to prove its correctness to standardize the analysis. Constant and variable inputs are outline din the following sections. In the validation process, Syltherm 800 is used as the working fluid under various combinations of volumetric flow rates of fluid, inlet temperature, ambient temperatures, air velocity and solar intensities. Thermophysical properties of fluids are taken directly from EES library [194]. For validation, the data are compared as found in [180]. Similar analysis was also done by [186]. The original experiment was done by Sandia national laboratory funded by US department of energy [195], [196], [197].

4.3.1 Constant Inputs in PTC

Width of the PTC, W : 5.0 m.

Length of the PTC, L : 7.8 m.

Focal distance of the PTC, f : 1.71 m.

Aperture of the PTC, A_a : 39.0 m^2.

Concentration ratio of the PTC, C : 22.74.

Receiver inner diameter, D_{ri} : 66 $x10^{-3}$ m.

Receiver outer diameter, D_{ro} : 70 $x10^{-3}$ m.

Cover inner diameter, D_{ci} : 109 $x10^{-3}$ m.

Cover outer diameter, D_{co} : 115 $x10^{-3}$ m.

Receiver inner surface, A_{ri} : 1.617 m^2.

Receiver outer surface, A_{ro} : 1.715 m^2.

Cover inner surface, A_{ci} : $2.671\ m^2$.

Cover outer surface, A_{co} : $2.818\ m^2$.

Receiver emittance, ε_r : 0.2.

Cover emittance, ε_c : 0.9.

Absorber absorbance, α : 0.96.

Cover transmittance, T_r : 0.95.

Concentrator reflectance, ρ : 0.83.

Intercept factor, γ : 0.99.

Incident angle modifier, $K_{(\theta=0)}$: 1.

Incident angle, θ : 0.

4.3.2 Input Variables in PTC

Receiver inlet fluid temperature : T_{in} (°C).

Air velocity : u_{air} (m/s).

Solar Beam radiation : G_b (W/ m^2).

Volumetric flow rate of fluid, : V_{fluid} (L/min).

Ambient Temperature, : T_{am} (°C).

4.3.3 Output Parameters to Validate with Reference for PTC

Receiver outlet fluid temperature : T_{out} (°C).

Energy efficiency of the PTC : η_{en}.

Exergy efficiency of the PTC : η_{ex}.

4.3.4 Validation Results of PTC

PTC outlet temperature and efficiency parameters are validated comparing with the test data of Sandia National Laboratory [180]. In Figure 4.2 and Figure 4.3, energy and exergy efficiencies of the model are compared with the experimental values. The data table enumerating the parameters of the examined cases is available in the Appendices. The standard deviation is found to be 0.135% in case of outlet temperature of HTF. For energy and exergy efficiencies, standard deviations are found to be 1.595% and 1.654% respectively. Maximum deviations for outlet temperature, thermal efficiency and exergy efficiency are found to be 0.231%, 2.093% and 3.181%, respectively. These data trends with extremely low standard deviations are affirming the authenticity of the developed model. Detail data can be found in Appendix Table B - 1.

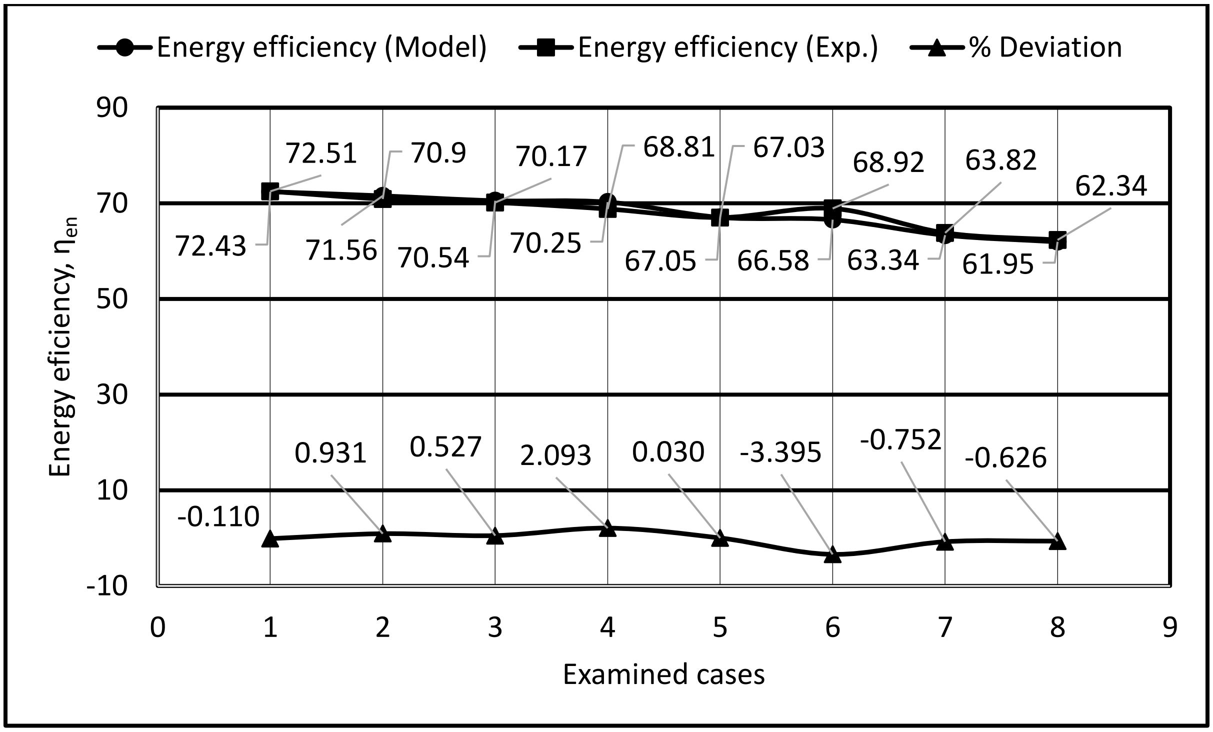

Figure 4.2 Energy efficiency validation results of PTC.

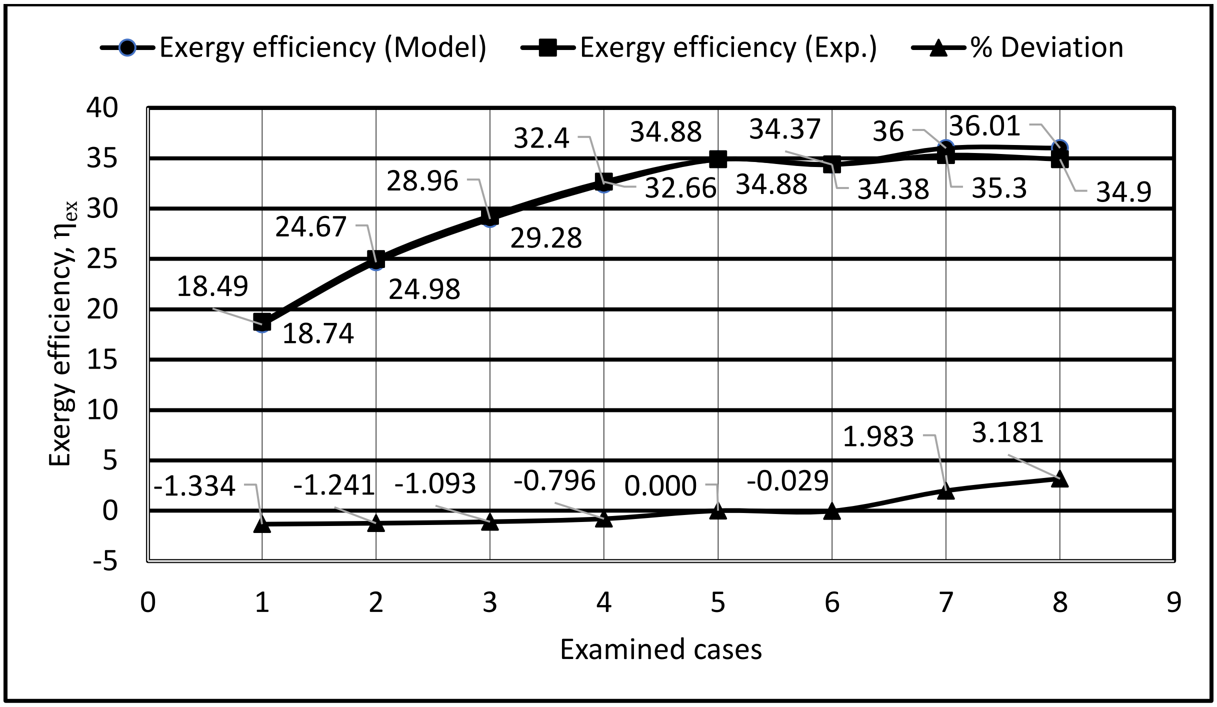

Figure 4.3 Exergy efficiency validation results of PTC.

4.4 Results and Discussions on PTC

The developed thermal model was used to analyze the solar collector performance. Various operating conditions were examined to check its effect on the thermal and exergetic performance of the system. Therminol VP-1, a liquid working fluid that can operate safely from 285 K to 673 K was used as the heat transfer fluid in the CSP cycle. As our primary goal was to introduce the CSP for ORC which is more effective at low temperature in comparison to steam, the inlet temperature of the HTF in between 333 K and 513 K are considered in the analysis. The volumetric flow rate in a single PTC was ranged from 25 L/min. to 200 L/min, an adequate range to assess the performance of a solar collector [180]. It should be noted that, high pressure is not required inside the PTC to keep Therminol VP-1 liquid in this case unlike the case with pressurized water. Normal boiling point of Therminol is 523 K [198] and the analysis was kept well inside the range to work with this fluid in normal atmospheric pressure.

In case of multiple PTC in series, it was assumed for simplicity that the temperature difference between the inlet and outlet of the consecutive PTCs will be uniform throughout the series arrangement and the temperature difference will be equal to the inlet and outlet temperature difference of the first PTC in series. For an example, from the developed EES model it was found that with an inlet temperature of 375.4 K and 0.8 kW/m^2 solar intensity, the temperature difference between the inlet and outlet of three consecutive PTCs in series were 15.38 K, 15.17 K and 15 K. So, it is practical to assume as such since it was found that the temperature difference reduced through the consecutive PTCs in a very lower rate when the other factors remain constant.

4.4.1 Inlet Temperature Effect on PTC

In this section, energy and exergy results of the PTC are presented for the heat transfer fluid Therminol VP-1. The effect of inlet temperature is examined in this section. It should be noted that the temperature is expressed with the parameter $[(T_{in} – T_{am})/G_b]$ which is usually used in the solar collector performance presentations [180]. The efficiency equations of PTCs of various types include this term in general. Following input parameters were maintained while doing the analysis. The optimum fluid flow rate is used to determine the effects. Wind velocities of Dhahran, Saudi Arabia are used for the analysis taken from Naif et al. [199].

Volumetric flow rate, V_{fluid} : 50 L/min.

Number of PTC : 1.

Solar irradiation, G_b : 0.8 kW/m^2.

Ambient temperature, T_{am} : 298.15 K.

Air velocity, u_{air} : 5.3 m/s.

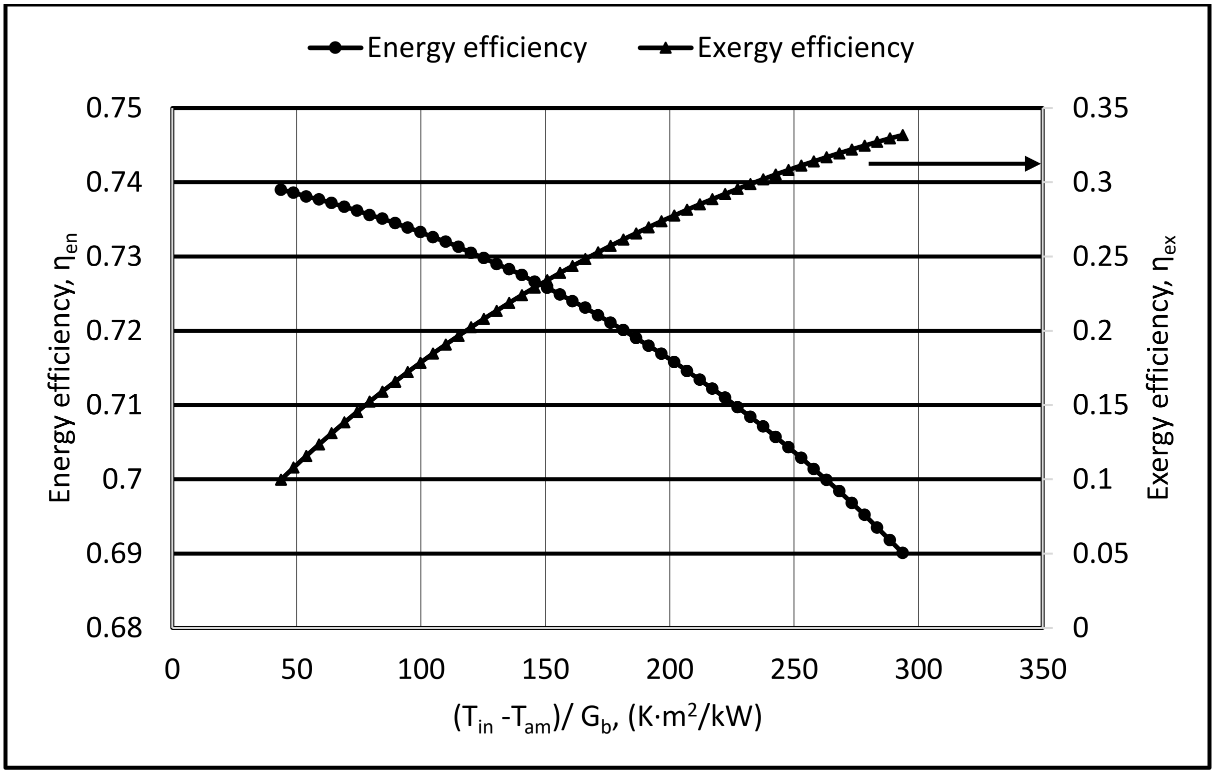

Figure 4.4 Inlet temperature effect on energy and exergy efficiency in PTC for V_{fluid} = 50 L/min and G_b = 0.8 kW/m^2.

From Figure 4.4 it is evident that the energy efficiency is reduced with the increase of temperature. The curvature on efficiency is due to the radiation thermal losses which are the main constituent for thermal losses in PTC. Even from the equation of thermal losses i.e. Q_{loss} in section 3.2.2 it can be seen that the increase in inlet temperature caused the rise in temperature in the receiver tube, resulting in more thermal losses, so is the energy efficiency. It is also attesting to the fact that the higher inlet temperature makes the collector to work better on the exergetical perspective. But it should be noted that, doing so would sacrifice the energy efficiency of the PTC as shown in Figure 4.4.

One of the important parameters here is the exergy destruction which has two components in the discussion. First one is the exergy destruction generated while the heat is transferred from the sun to the receiver. Next one is associated with the heat transfer between the receiver tube and the fluid inside of it. The total exergy destruction was getting lower for higher inlet temperatures as observed from Figure 4.5.

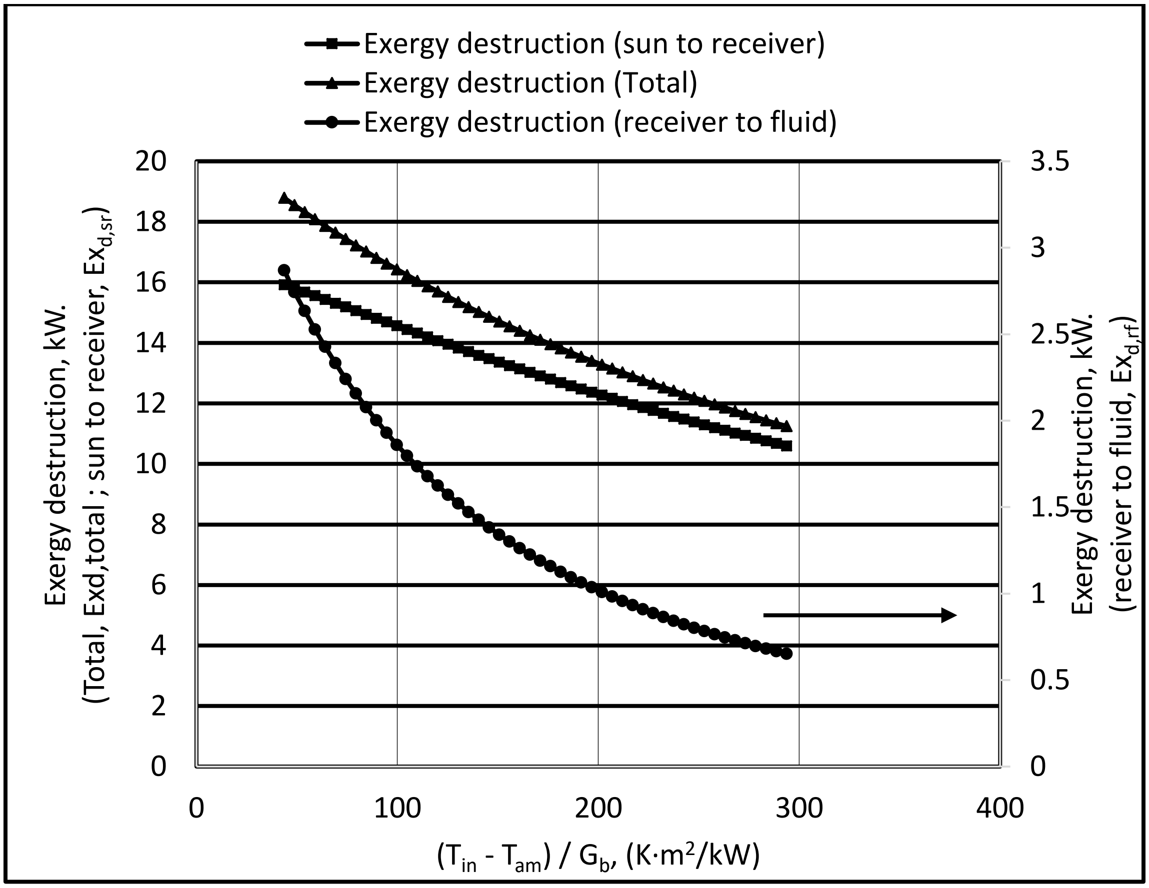

Figure 4.5 Effect of inlet temperature on exergy destruction in PTC for V_{fluid} = 50 L/min and G_b = 0.8 kW/m^2.

Higher fluid temperature and lower fluid flow both resulted in an increase in temperature inside the receiver making it warmer with greater mean temperature. Increase in temperature of the receiver, reduced the exergy destruction in between the sun and the receiver which reduced the overall exergy destruction to a great extent. The total exergy destruction was getting less with increasing temperature of the inlet fluid in PTC as seen in Figure 4.5, consequently exergy efficiency was getting higher as seen from Figure 4.4.

Figure 4.5 depicts a reducing trend on exergy destruction from the receiver to the fluid that is directly linked with the heat transfer from the hot receiver tube to the relatively cold fluid flowing inside it. In this case as well the higher temperature resulted lower exergy destruction because with a higher inlet temperature of fluid heat transfer coefficient increased in between the fluid and the receiver tube which reduced the difference of temperature in between the receiver and the fluid.

Exergy destruction of the sun to the receiver was found to be way higher in comparison to the exergy destruction between receiver to fluid as evident from the figure above. Due to the greater difference in temperature between the sun and the receiver, higher amount of exergy is lost in the process of absorbing energy from the sun to the receiver hence higher exergy destruction as well.

The scenario of higher exergy losses with the increasing temperature can be seen in Figure 4.6. The exergetic losses are connected with the optical and thermal losses. In our analysis, the optical losses were considered to be constant since the solar intensity and incident angle was selected to be constant.

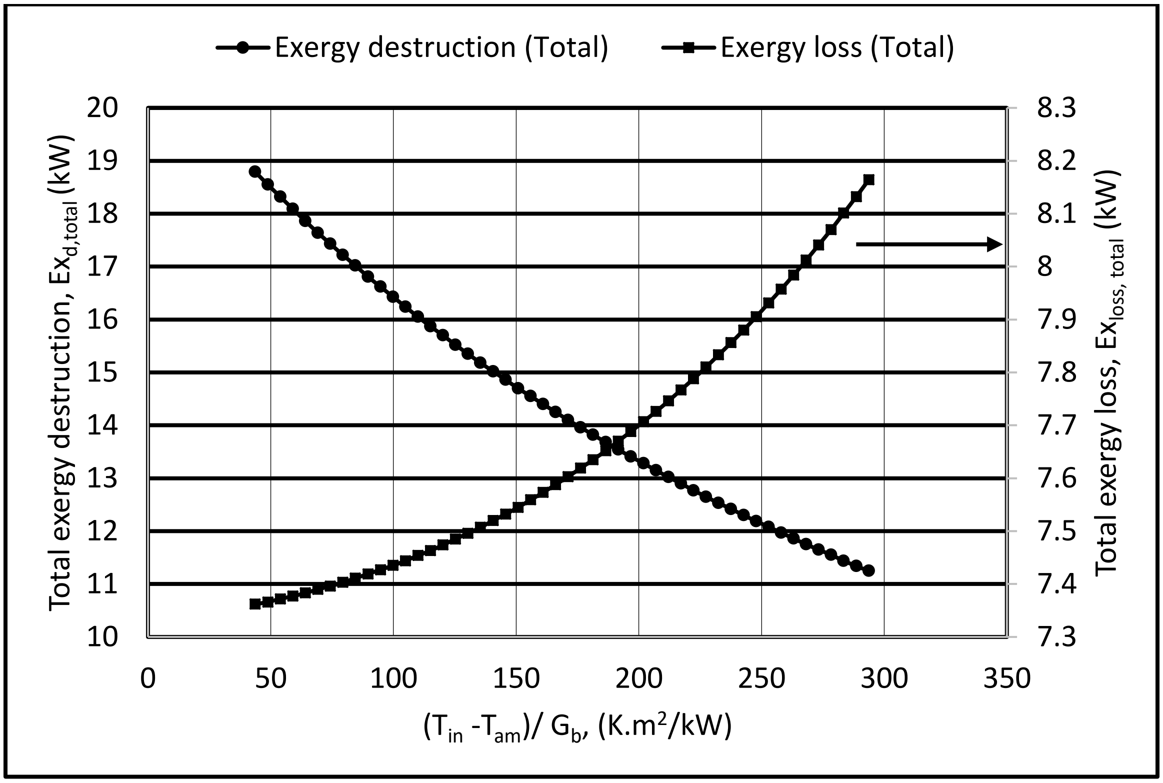

Figure 4.6 Effect of inlet temperature on exergy destruction and exergy loss in PTC for V_{fluid} = 50 L/min and G_b = 0.8 kW/m^2.

Exergy loss proportionally increased with higher temperature, which was quite the opposite scenario in comparison to exergy destruction. It is due to the fact that exergy loss is related to the surrounding temperature and with higher temperature difference in between the HTF and surroundings exergy loss will be higher.

4.4.2 Volumetric Flow Effect on PTC

This section outlines the influence of the volumetric fluid flow rate of the heat transfer fluid inside the receiver pipe in the PTC with the following parameters.

HTF : Therminol VP-1.
Solar irradiation, G_b : 0.8 kW/m^2.
Number of PTC : 1.
Ambient temperature, T_{am} : 298.15 K.
Air velocity : 5.3 m/s.
PTC Inlet temperature, T_{in} : 375.4 K.

Increasing the fluid flow rate in the receiver is reducing the outlet temperature as evident from the following Figure 4.7, which can be explained by the simple fact that the same heat energy absorbed by larger fluid volume would reduce the resulting temperature of the fluid.

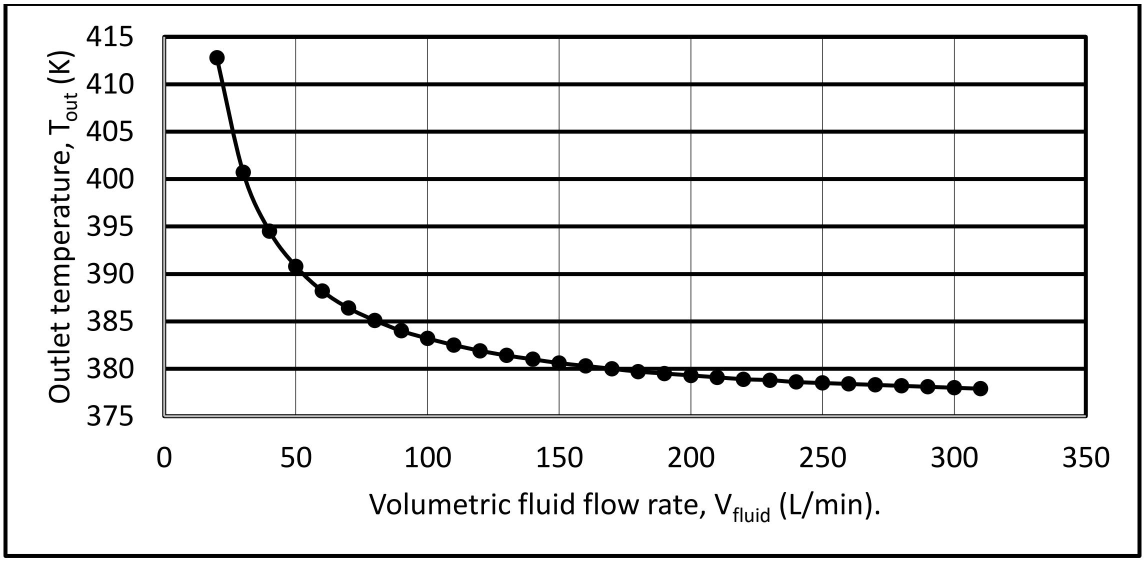

Figure 4.7 Effect of HTF flow rate on the outlet temperature of PTC receiver for T_{in} = 375.4 K and G_b = 0.8 kW/m^2.

It is observed from Figure 4.8 that lowering the fluid flow is reducing the energy efficiency of the PTC. In the range of 100 L/min and above there was a slight level of increase in the energy efficiency, which also determined the limits of optimum fluid flow rate. At the other end fluid flow of 25 L/min. and within its proximity were returning a drastically reduced energy efficiency hence not recommended. Even in Sandia National Laboratory (SNL) tests the performance within 47.7 - 56.8 L/min volumetric fluid range that can be seen from Appendix Table B - 1.

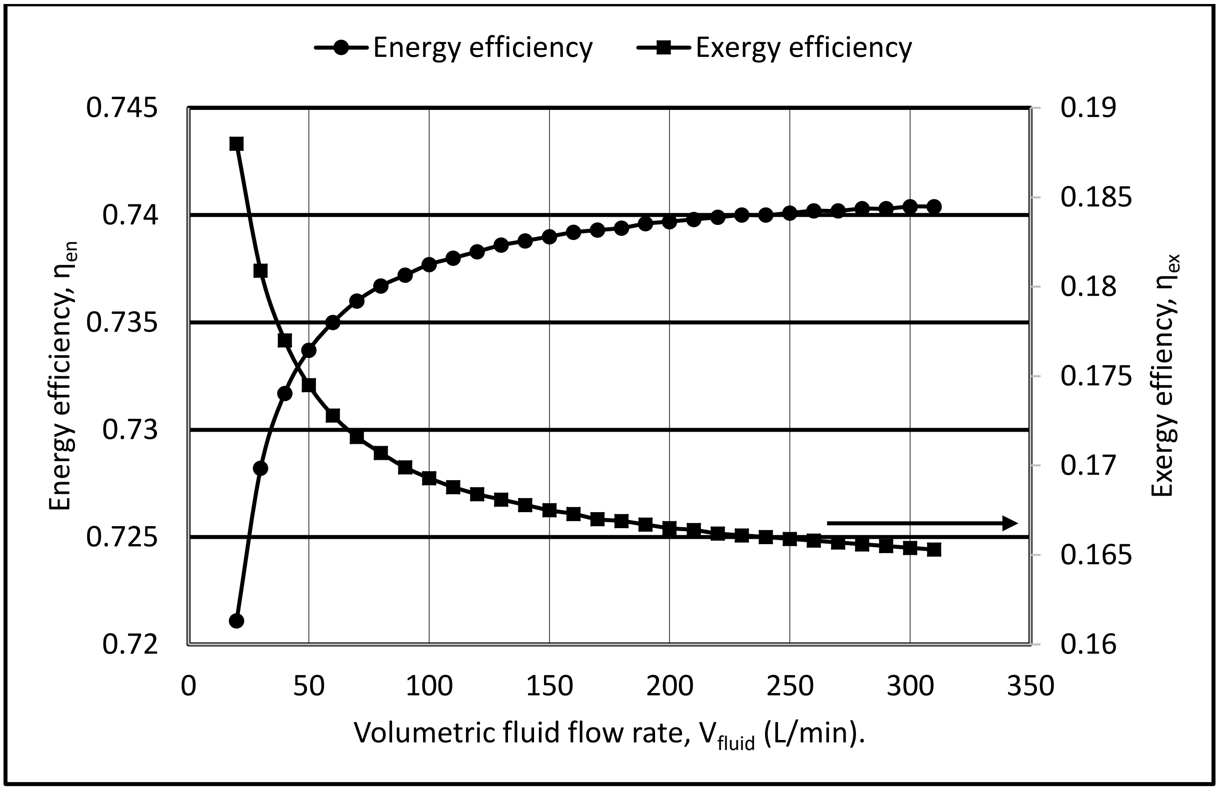

Figure 4.8 Effect of HTF flow rate on energy and exergy efficiency of PTC for T_{in} = 375.4 K and G_b = 0.8 kW/m^2.

Higher flow rate reduced the exergetic performance of the collector according to Figure 4.8. Reducing it to less than 50 L/min. and beyond was resulting sharp increase in the exergy efficiency, but at the same time it has to be noted that reducing to 25 L and beyond will result drastically reduced thermal performance. It is crucial to find an optimum value of volumetric fluid flow rate to utilize a better performance from the PTC.

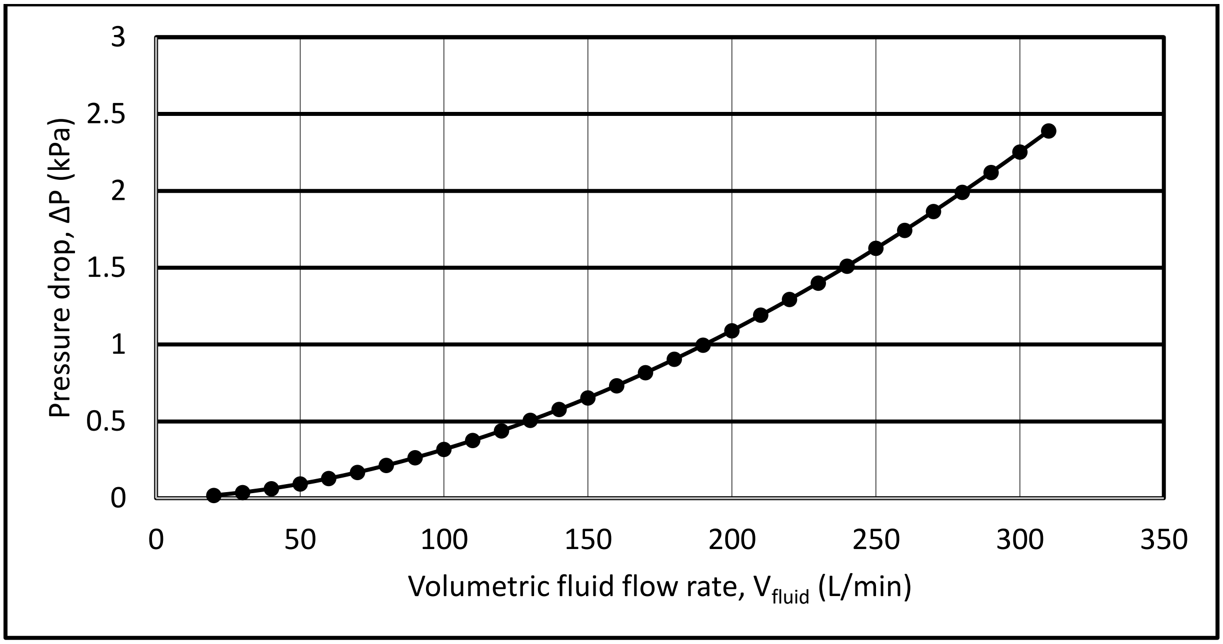

Figure 4.9 Effect of HTF flow rate on pressure drop in PTC for T_{in} = 375.4 K and G_b = 0.8 kW/m^2.

An interesting fact can be observed from Figure 4.10. With the same inlet temperature, when the HTF flow went higher, the exergy destruction of the sun to receive increased, but the exergy destruction from receiver to fluid reduced. It happened because the increase in HTF flow with certain inlet temp reduced the receiver temperature, hence the higher temperature difference in between the sun and the receiver which resulted greater exergy destruction.

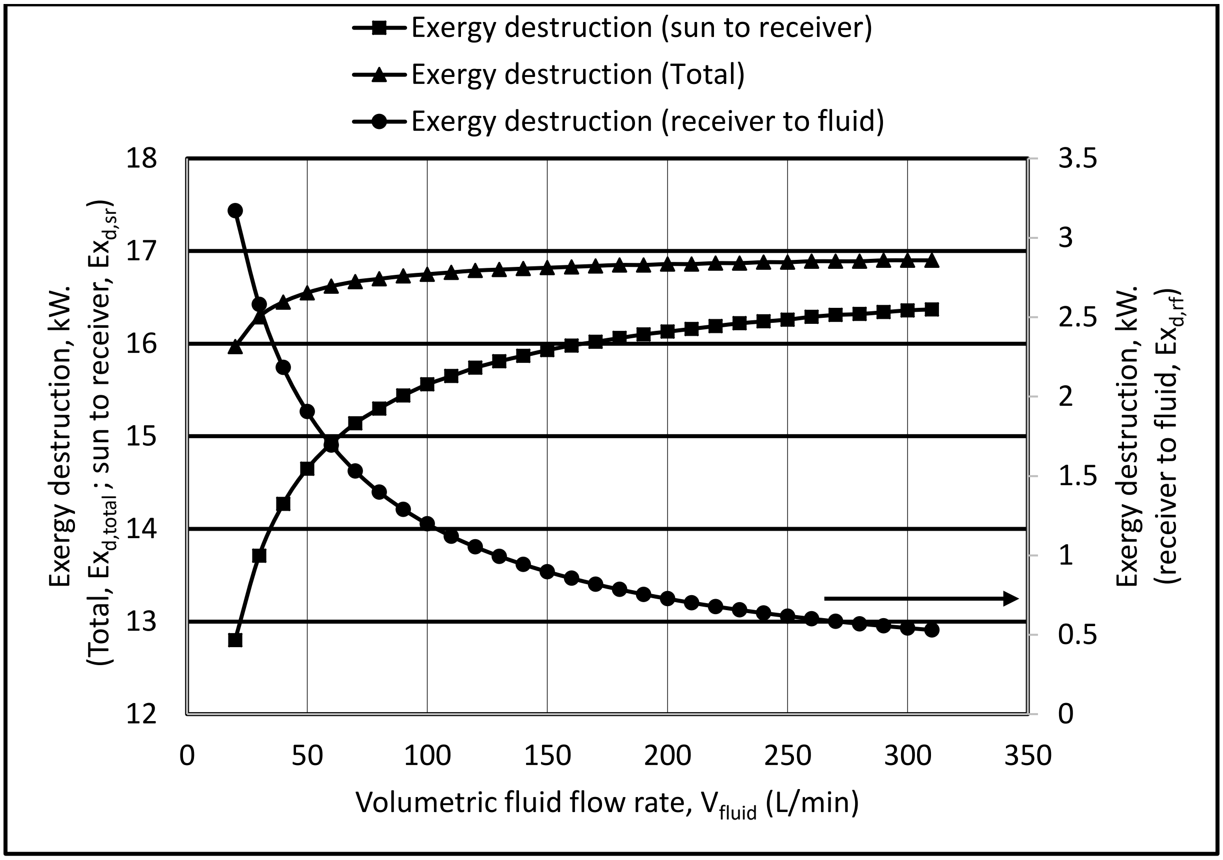

Figure 4.10 Effect of HTF flow rate on exergy destruction in PTC for T_{in} = 375.4 K and G_b = 0.8 kW/m^2.

In the latter case, higher fluid flow reduced the temperature difference in between the receiver and the fluid flowing inside of it hence reduction in exergy destruction. For example, in a PTC unit, with inlet fluid temperature of 376 K and solar intensity 0.8 kW/m^2 with 50 L/min flow rate exhibited temperature difference between the receiver and outlet to be 38 K and for 100 L/min it turned out to be 23 K which explained this exergy reduction in between the receiver and the fluid. Added to that, when the fluid flow rate increased from 50 L/min to 100 L/min receiver temperature decreased to 406.7 K from 429.4 K. This 22.7 K temperature reduction of the receiver actually increased the temperature difference between the sun and the receiver hence higher exergy destruction.

From Figure 4.11 it is observed that higher fluid flow is reducing the exergy loss. Actually, the higher fluid flow is reducing the mean temperature of the fluid flowing inside the receiver, thus reducing the temperature difference with the environment which results lower exergy loss.

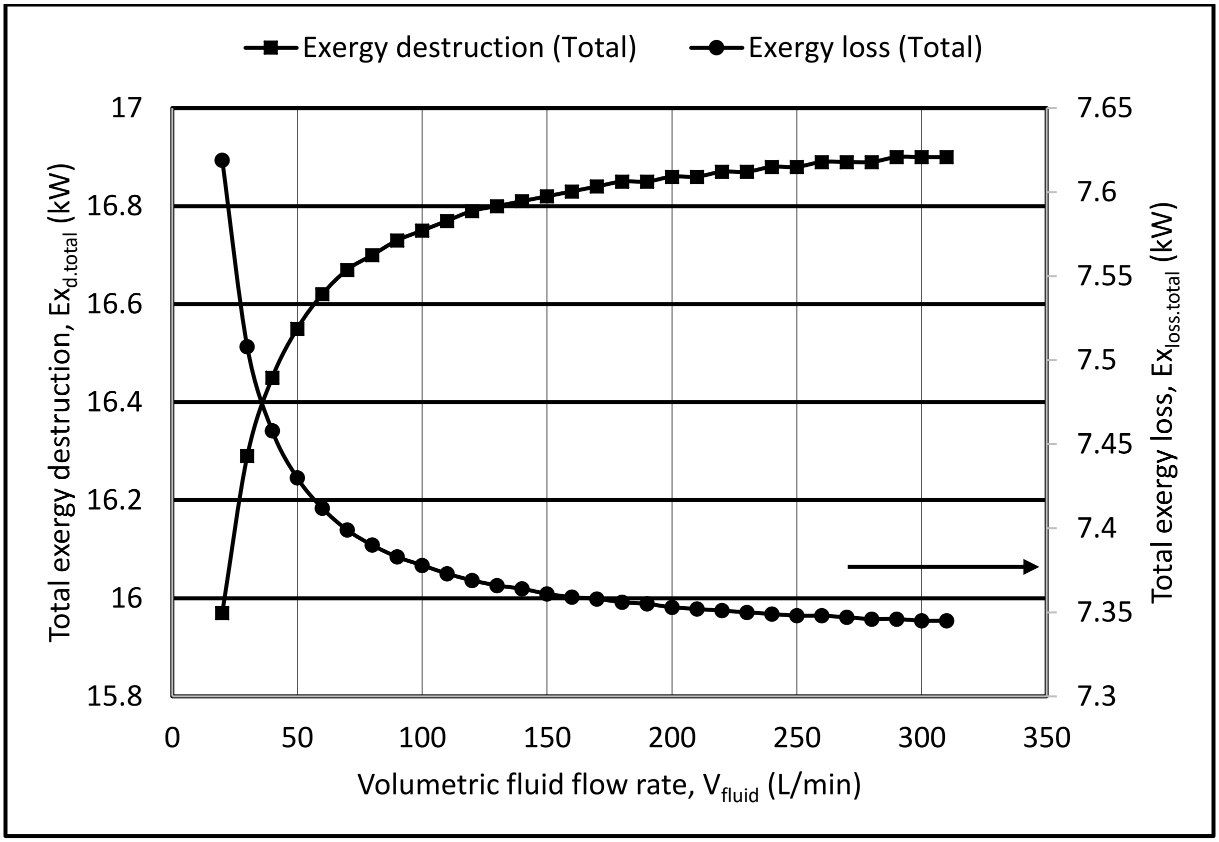

Figure 4.11 Effect of HTF flow rate on exergy loss for $T_{in} = 375.4$ K and $G_b = 0.8$ kW/m^2.

4.5 Organic Rankine Cycle

As said previously, ORC is like a steam cycle except the operating fluid is organic instead of steam. Conventional steam cycle utilizes boiler as its heat source to produce steam with high temperature and pressure for higher efficiency. If the external heat source is waste heat or CSP, then HRVG (Heat Recovery Vapor Generator) will be used substituting the boiler. Heat Recovery Vapor Generator (HRVG), which is denoted as vaporizer in our discussion, is practically a heat exchanger. The economizer is the component where organic fluid becomes saturated liquid of high pressure, while the evaporator is the component where the organic fluid becomes saturated vapor. Addition of superheater accounts for superheated vapor to achieve higher temperatures. High vapor temperature and pressure is desired to feed into the turbine from the vaporizer outlet for higher efficiency of ORC.

4.6 ORC Model Validation

The developed ORC model is validated from [183] comparing enthalpy and exergies at different positions of ORC and its shown in following figures. The detail data table can be found in Appendix Table B - 2.

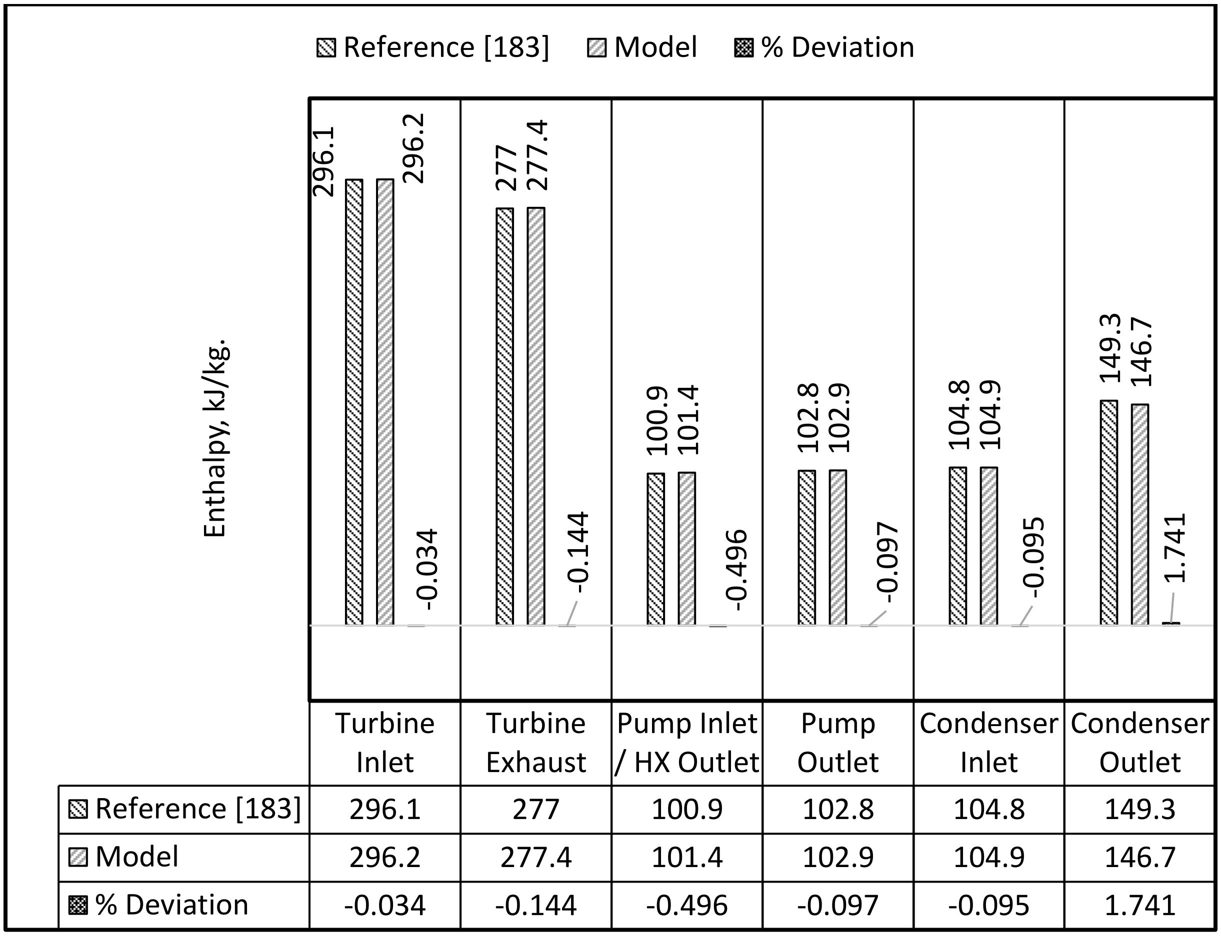

	Turbine Inlet	Turbine Exhaust	Pump Inlet / HX Outlet	Pump Outlet	Condenser Inlet	Condenser Outlet
▧ Reference [183]	296.1	277	100.9	102.8	104.8	149.3
▨ Model	296.2	277.4	101.4	102.9	104.9	146.7
▩ % Deviation	-0.034	-0.144	-0.496	-0.097	-0.095	1.741

Figure 4.12 Enthalpy result validation of ORC at turbine inlet temperature of 362.8 K and pressure of 2678.9 kPa.

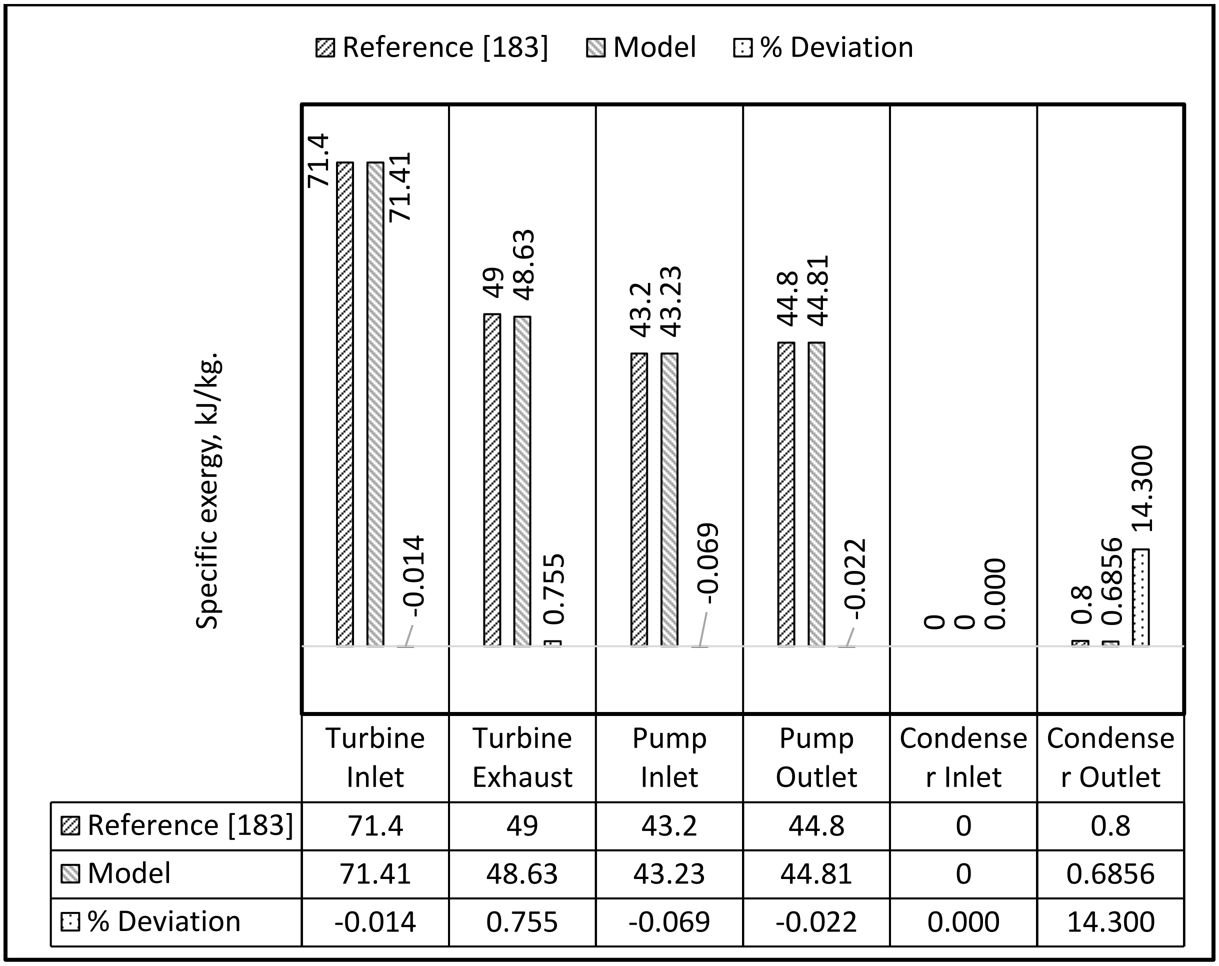

	Turbine Inlet	Turbine Exhaust	Pump Inlet	Pump Outlet	Condenser Inlet	Condenser Outlet
▨ Reference [183]	71.4	49	43.2	44.8	0	0.8
▨ Model	71.41	48.63	43.23	44.81	0	0.6856
☐ % Deviation	-0.014	0.755	-0.069	-0.022	0.000	14.300

Figure 4.13 Specific exergy result validation of ORC at turbine inlet temperature of 362.8 K and pressure of 2678.9 kPa.

4.7 Results and Discussions on PTC integrated ORC

In this section, optimum operating conditions and performance of Organic Rankine Cycle are investigated when its integrated with PTC as its heat source to produce ORC fluid vapor in HRVG (Heat Recovery Vapor Generator). Performances of different organic fluids are examined along with the parameters to secure higher efficiency of ORC.

4.7.1 Input Parameters for the ORC Performance Analysis

To check the performances of different working fluids, following are the parameters for the analysis. 15 PTC in series and 10 in parallel combination are used. Wind velocity was taken as the yearly average for Dhahran, Saudi Arabia [199].

Heat source : PTC.

Solar intensity, G_b : 0.8 kW/m^2.

Wind velocity, u_{air} : 5.3 m/s.

Ambient temperature, T_{am} : 298.15 K.

Volumetric flow of fluid, V_{htf} : 50 L / min.

HRVG HTF from heat source : Therminol VP-1

Temperature drop in HRVG, ($T_{01} – T_{02}$) : 204.2 K.

Turbine Inlet pressure, P_{04} : 100 kPa - 25000 kPa.

Turbine inlet temperature, T_{04} : 340 K - 550 K.

Turbine exhaust temperature, T_{05} : 315.5 K.

Pump inlet temperature, T_{06} : (T_{05} – 7) K.

Coolant in condenser : Water.

Coolant inlet temperature in condenser, T_{18} : 298.15 K

Coolant inlet pressure in condenser, P_{18} : 101.325 kPa.

Coolant outlet temperature in condenser, T_{19} : (T_{18} + 10) K.

Pinch point temperature in HRVG : 20 K.

4.7.2 Optimum Operating Conditions of ORC Fluids

Practical temperature and pressure limit for different organic fluids are derived in Figure 4.14-Figure 4.19 for ORC given a constant heat input from the heat source, here PTC. Suitable pressure ranges are obtained for different temperatures of ORC operating fluids. Resulting energy and exergy efficiencies are also derived to choose the appropriate fluid for ORC. Essential parameters for the analysis are mentioned in 4.7.1 . The detail data tables can be found in Appendix B.

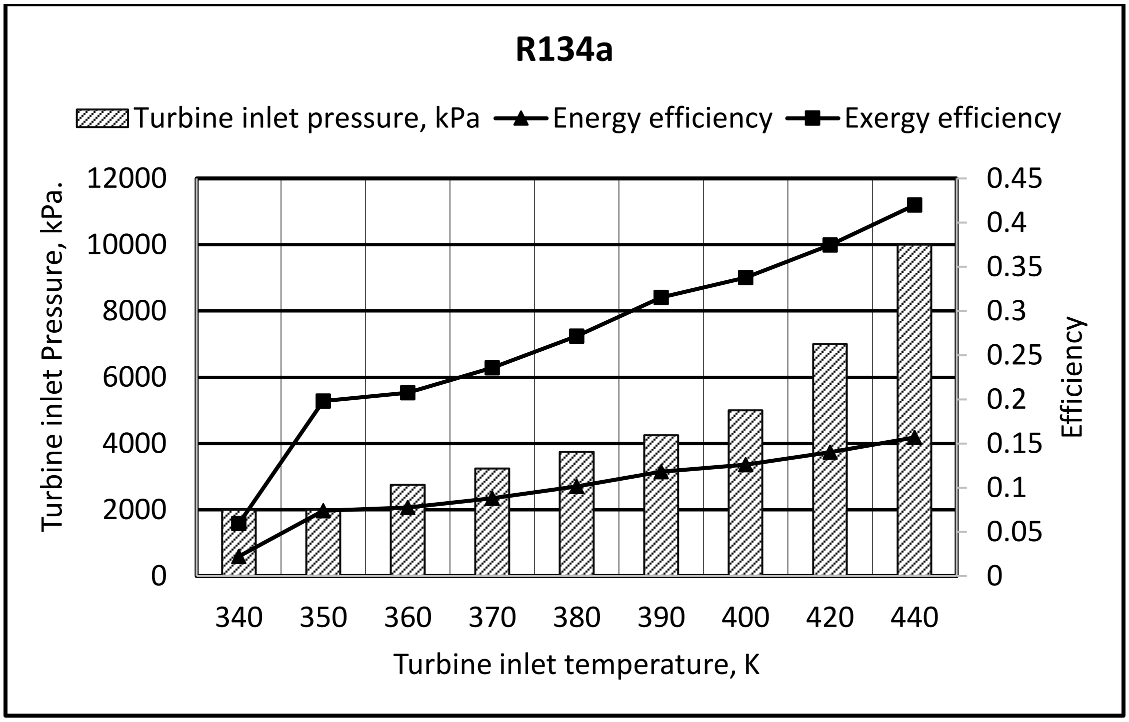

Figure 4.14 Performance characteristics of R134a at various turbine inlet temperatures and pressures.

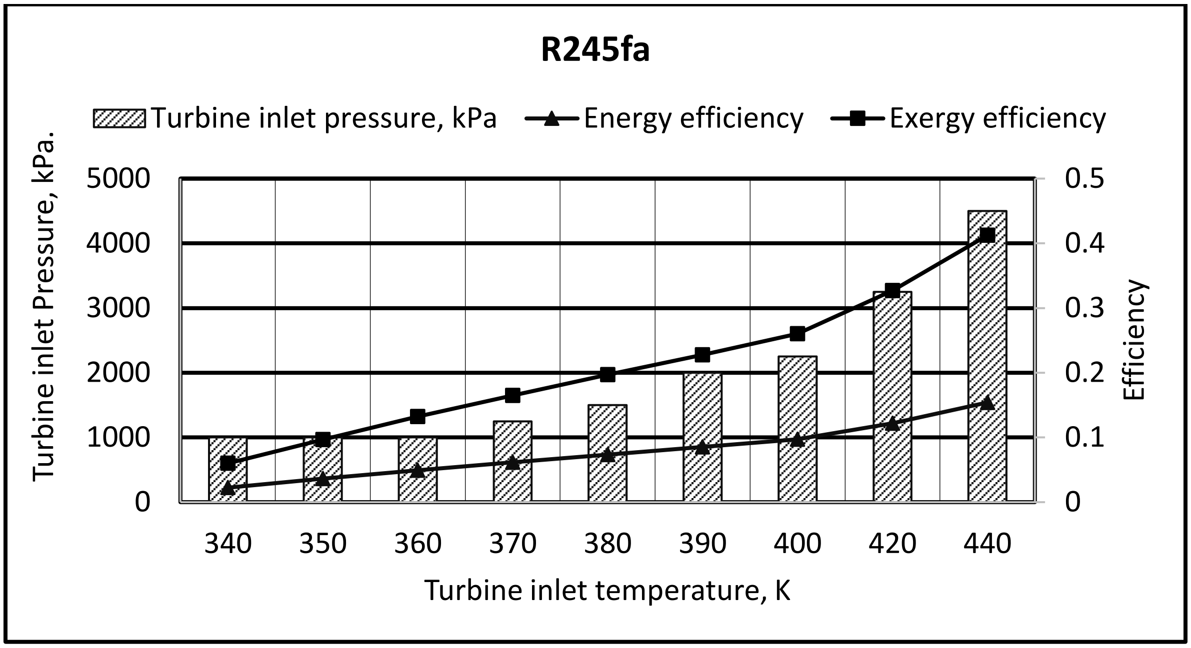

Figure 4.15 Performance characteristics of R245fa at various turbine inlet temperatures and pressures.

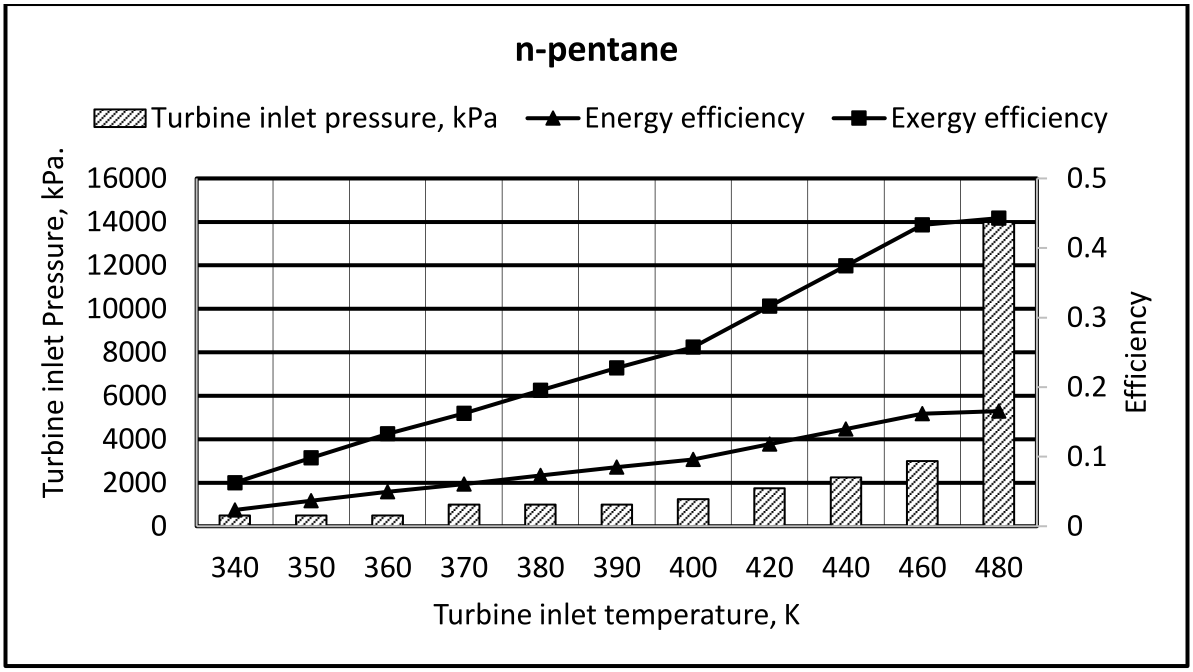

Figure 4.16 Performance characteristics of n-pentane at various turbine inlet temperatures and pressures.

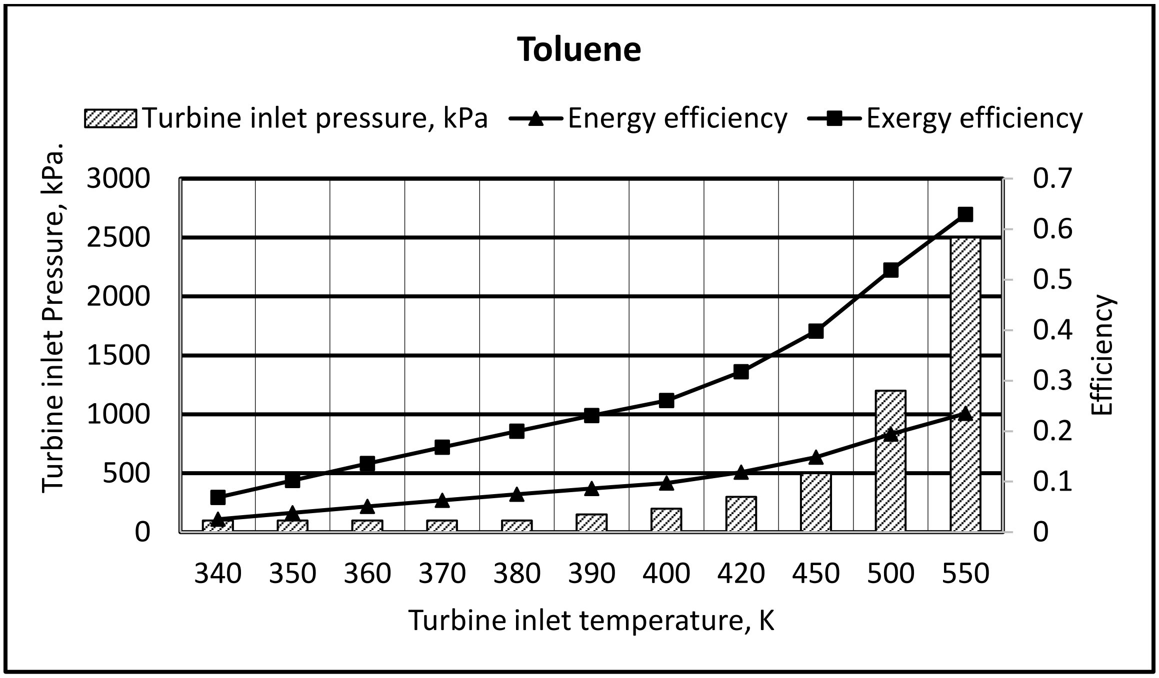

Figure 4.17 Performance characteristics of Toluene at various turbine inlet temperatures and pressures.

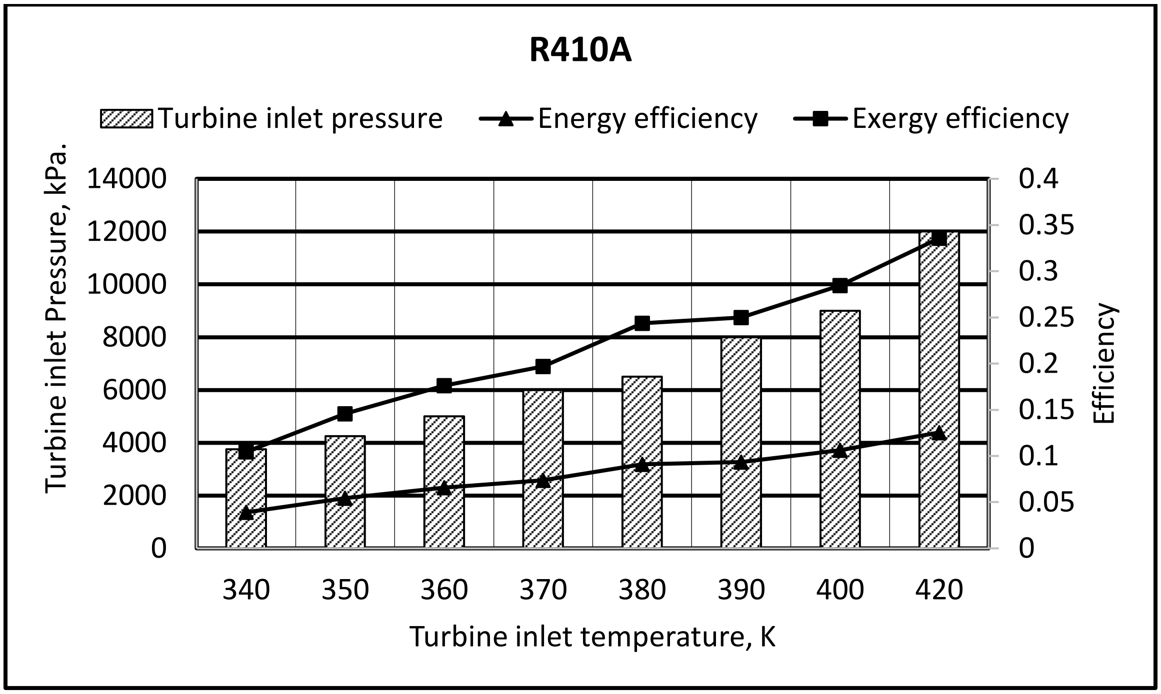

Figure 4.18 Performance characteristics of R410A at various turbine inlet temperatures and pressures.

It was observed that at low temperature and pressure range, which is suitable for ORC, fluids like R134a and R245fa were showing better performance, while fluids like n-pentane and Toluene were found to be highly efficient when both the pressure and temperature were very high. R410A showed lower performance in comparison to other fluids discussed here.

R744 (CO_2) was also investigated for its performance characteristics (Figure 4.19) and due to its exclusively different thermodynamic properties in comparison to rest of the fluid considered in this discussion, the turbine exhaust temperature was selected to be 253 K whereas for the rest of the fluids this input parameter was chosen as 315.5 K.

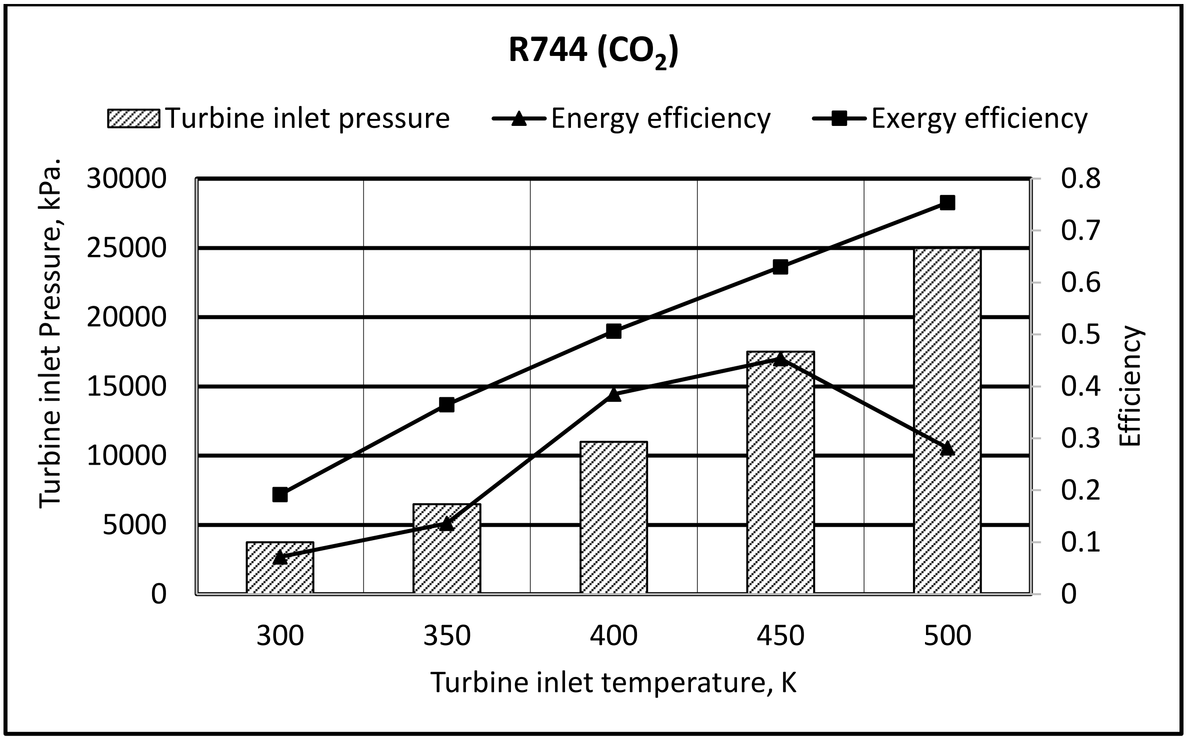

Figure 4.19 Performance characteristics of R744 (CO_2) at various turbine inlet temperatures and pressures.

4.7.3 Organic Fluid Performances in ORC

In this section, the ORC is integrated with the PTC arrangement as the heat source for the HRVG of ORC with inlet parameters mentioned in section 4.7.1 . The effects are observed from Figure 4.20 when same thermal energy was delivered from the PTC to the ORC

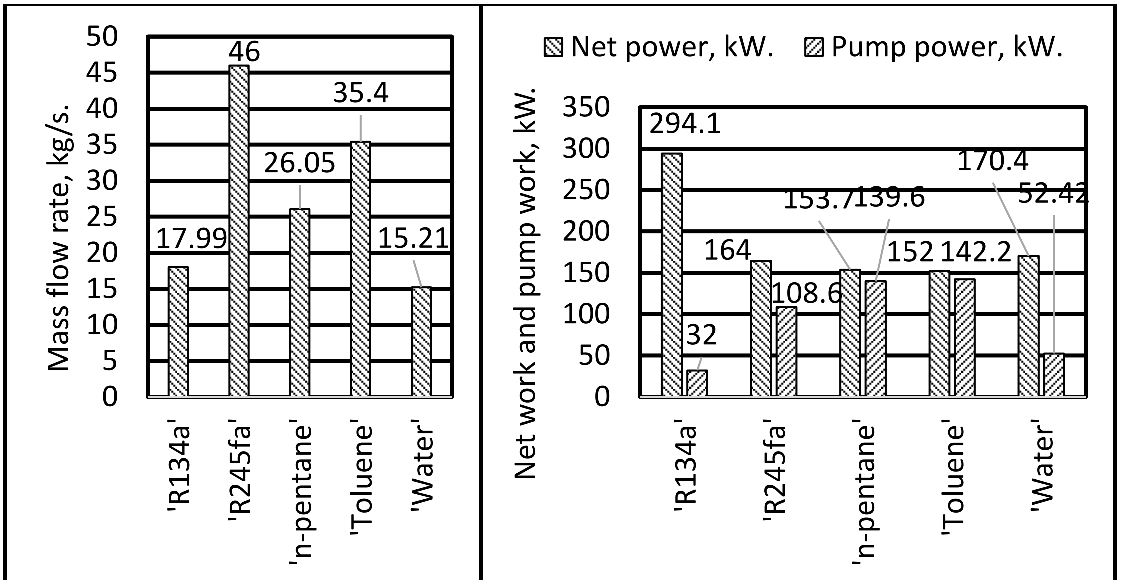

(a) Mass flow rates of ORC fluids.

(b) Net power produced by ORC fluids.

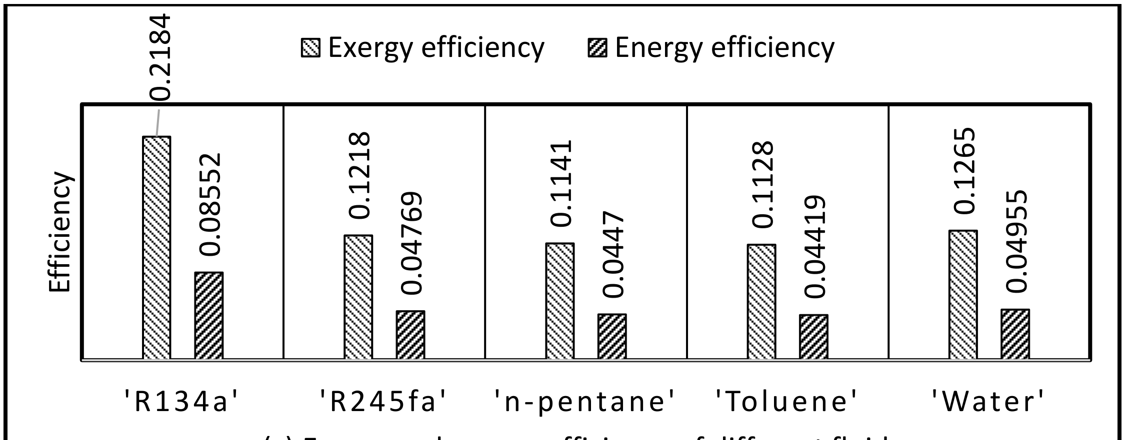

(c) Exergy and energy efficiency of different fluids.

Figure 4.20 Organic fluid performances in ORC at turbine inlet temperature of 362.8 K and pressure of 2750 kPa.

HRVG using different organic fluids in ORC. R134a was found to be the most efficient in terms of thermal efficiency of the system followed by steam at temperature of 362.8 K and a pressure of 2750 kPa. The mass flow rate of R134a was also lowest among the fluids which implied relatively smaller equipment size needed compared to the rest. In R134a, the contribution of the pump and the turbine was found to be very low for causing exergy destruction. As seen from the previous section 4.7.2 and Appendix Table B - 13, R134a showed the best performance for the turbine inlet temperature range from 340 K – 440 K in terms of both energy and exergy efficiency. At higher turbine inlet temperature range of 550 K Toluene was found to be more efficient. Since higher turbine inlet temperature causes higher efficiency of the ORC, it can be said that any fluid working at a higher turbine inlet temperature will have lower exergy destruction. An ORC fluid working on its optimum operating condition will have less exergy destruction than other fluids at that condition.

Exergy destructions occurred in different components of ORC are also investigated. Figure 4.21 is describing the contribution of different components in exergy destruction at turbine inlet temperature of 362.8 K and a pressure of 2750 K.

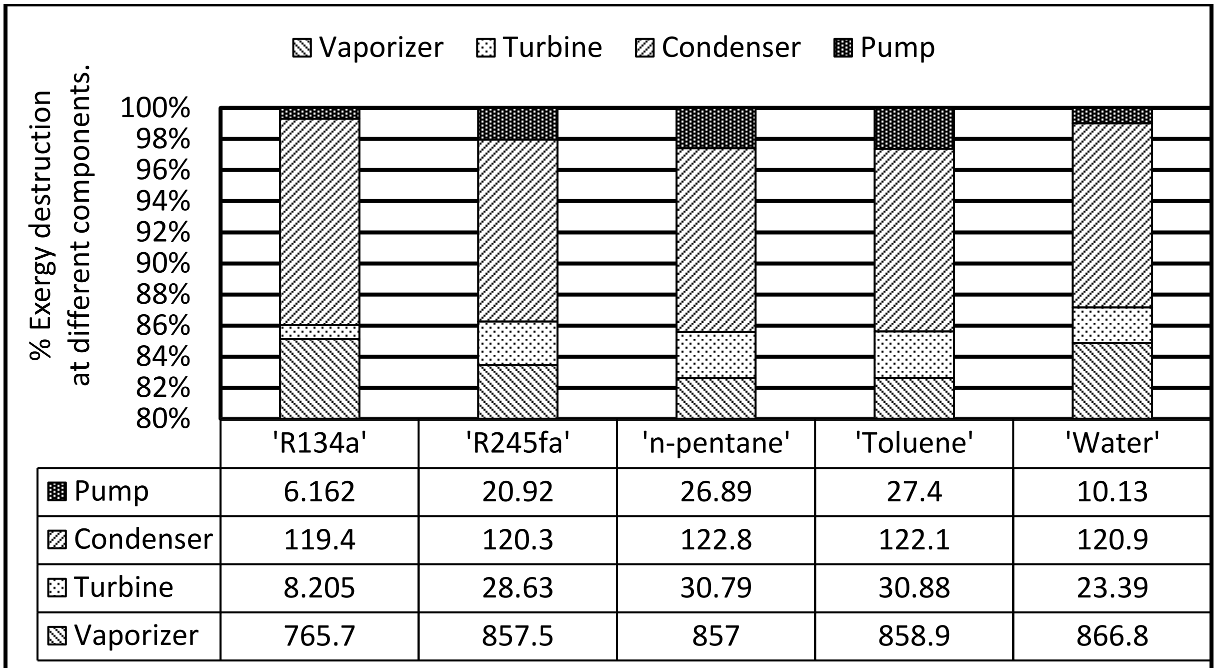

	'R134a'	'R245fa'	'n-pentane'	'Toluene'	'Water'
▦ Pump	6.162	20.92	26.89	27.4	10.13
▨ Condenser	119.4	120.3	122.8	122.1	120.9
⊡ Turbine	8.205	28.63	30.79	30.88	23.39
▧ Vaporizer	765.7	857.5	857	858.9	866.8

(a) Exergy destruction in ORC components, kW.

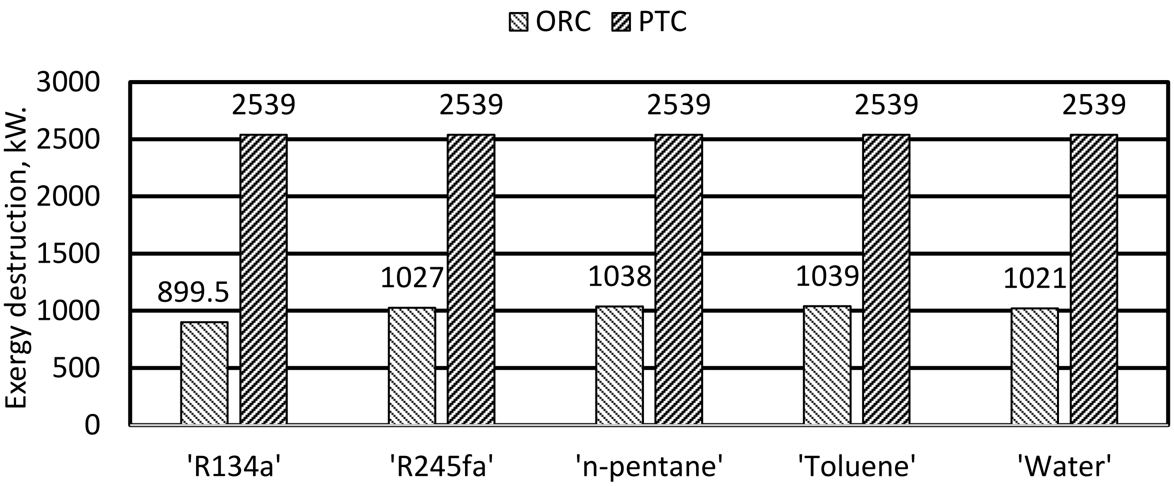

(b) Total exergy destruction in ORC and PTC utlizing same heat input from PTC

Figure 4.21 Exergy destruction of different components in ORC at turbine inlet temperature of 362.8 K and pressure of 2750 kPa.

The comparison is then made for five different fluids, including Steam for its relevance to the discussion. Exergy destruction in HRVG contributed most of the exergy destruction in the whole cycle for all ORC fluids. For all the fluids, exergy destruction of vaporizer was found to be higher than any other components of ORC. Condenser came second in that respect as evident from the figure above. Turbine and pump also contributed to exergy destruction, but very insignificant in comparison to HRVG and condenser. For the same heat input utilized by ORC, R134a had the least exergy destruction in ORC. But the exergy destruction in PTC was way higher than that of ORC (Figure 4.21). R410A and R744 (CO_2) was not added to the list since the pressure and temperature range were not suitable for its thermophysical properties and inclusion of them resulted negative exergy destruction or non-executable program conditions.

4.7.4 Performance of the PTC Integrated ORC

Since the optimum operating characteristics and the ORC fluid are identified, and the performance of the PTC integrated ORC is discussed in this section choosing ORC fluid R134a at its optimum operating condition of temperature 362.8 K and a pressure of 2750 kPa. The parametric analysis is done for variable volumetric fluid flow rate in PTC and on different solar irradiation conditions for R134a. Essential input parameters are mentioned in section 4.7.1 . Performances of other fluids can be found in the Appendix B.

From Figure 4.22 it is observed that the increase in flow rates in the PTC is reducing the power output. First and second law efficiency of the integrated cycle are going down due to increasing flow rates in PTC as observed from Figure 4.23. This is happening due to the fact that increasing fluid flow rates are reducing the temperature of fluid inside the receiver resulting reduced heat input to HRVG of the ORC hence reduced energy and exergy efficiencies. First and second law efficiencies can be termed as energy and exergy efficiencies as mentioned earlier in section 3.5.

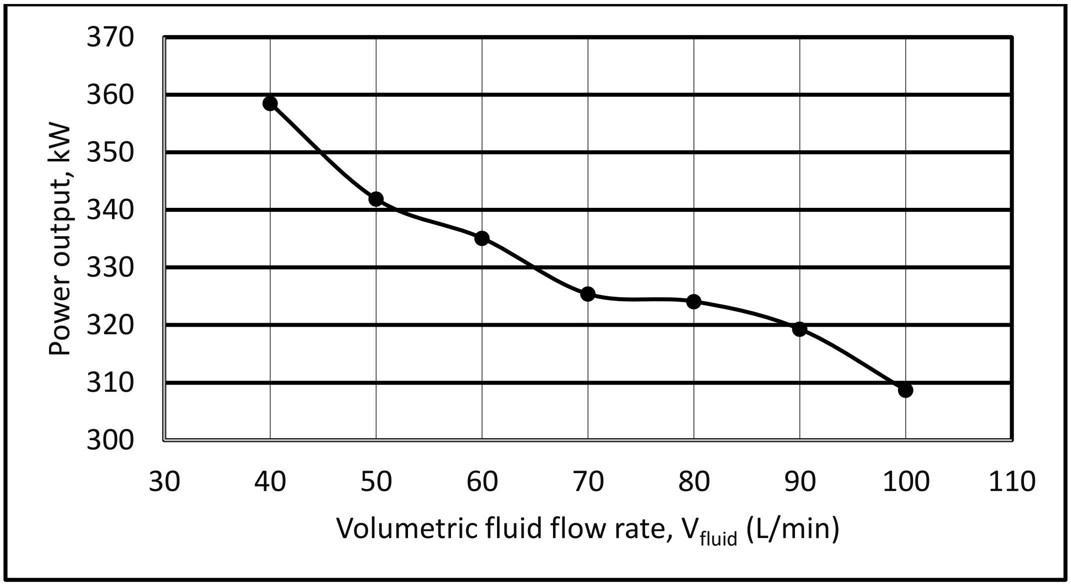

Figure 4.22 Power output of the PTC integrated ORC at different fluid flow rates at G_b = 0.8 kW/m^2 and R134a as ORC fluid.

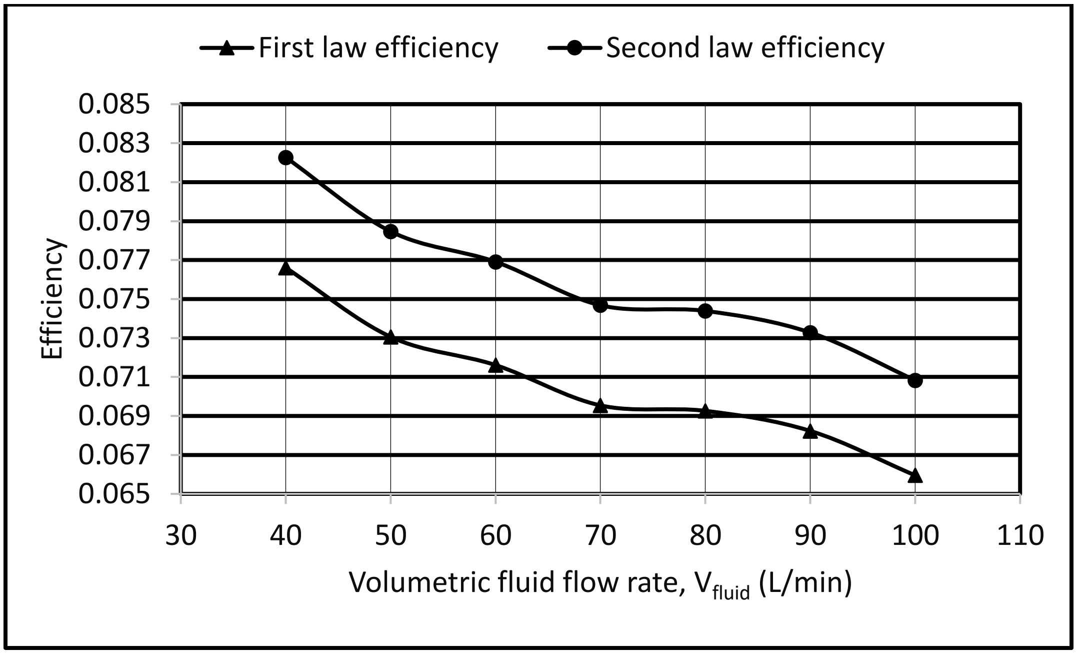

Figure 4.23 First and second law efficiency of the PTC integrated ORC at different fluid flow rates at G_b = 0.8 kW/m^2 and R134a as ORC fluid.

Power output and efficiency trends in terms of energy and exergy are shown in the following figures varying solar irradiation using the parameters mentioned in section 4.7.1.

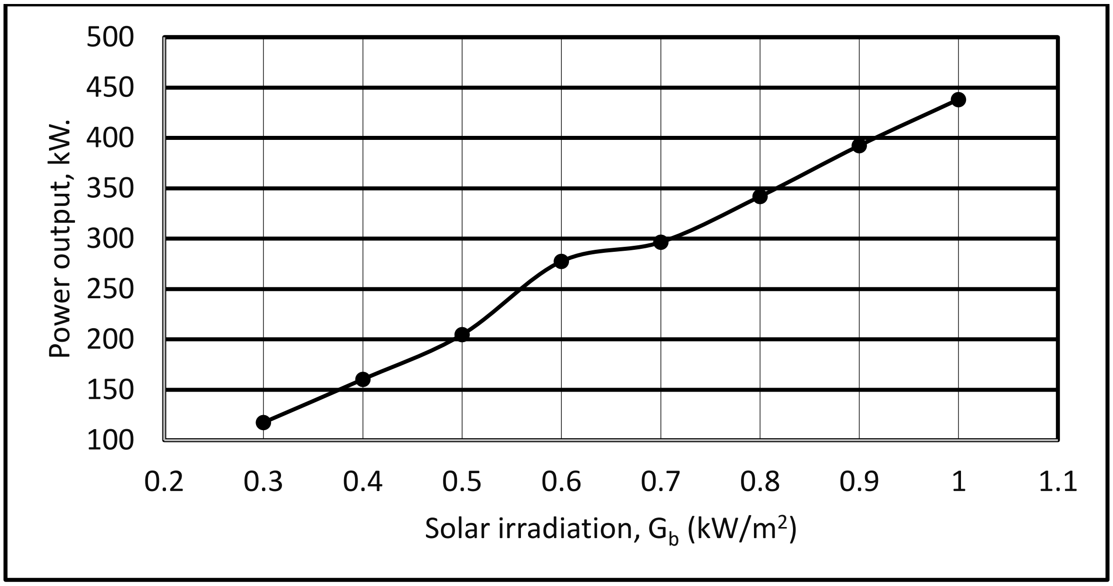

Figure 4.24 Power output of the PTC integrated ORC varying solar irradiation using R134a as ORC fluid.

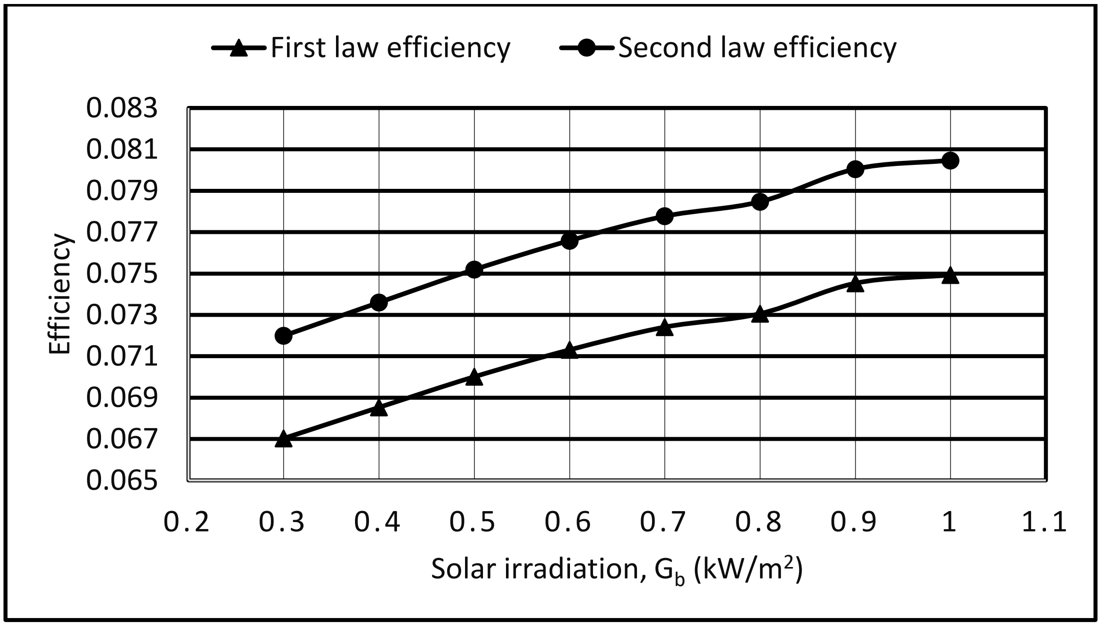

Figure 4.25 First and second law efficiency of the PTC integrated ORC varying solar irradiation R134a as ORC fluid.

Monthly and hourly variation of power outputs, first law efficiency and second law efficiency are illustrated in Figure 4.26 - Figure 4.31 utilizing the weather data of Dhahran [199], [200], [201].

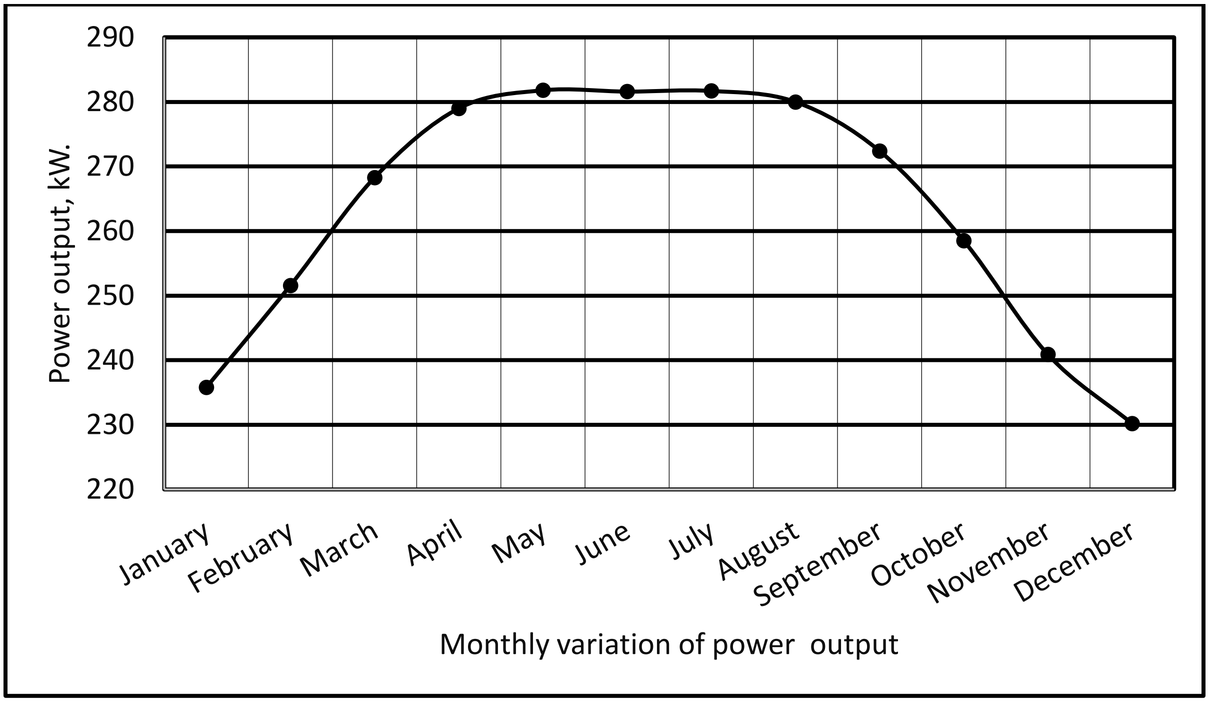

Figure 4.26 Monthly average power output all over the year using R134a as ORC fluid for Dhahran, Saudi Arabia.

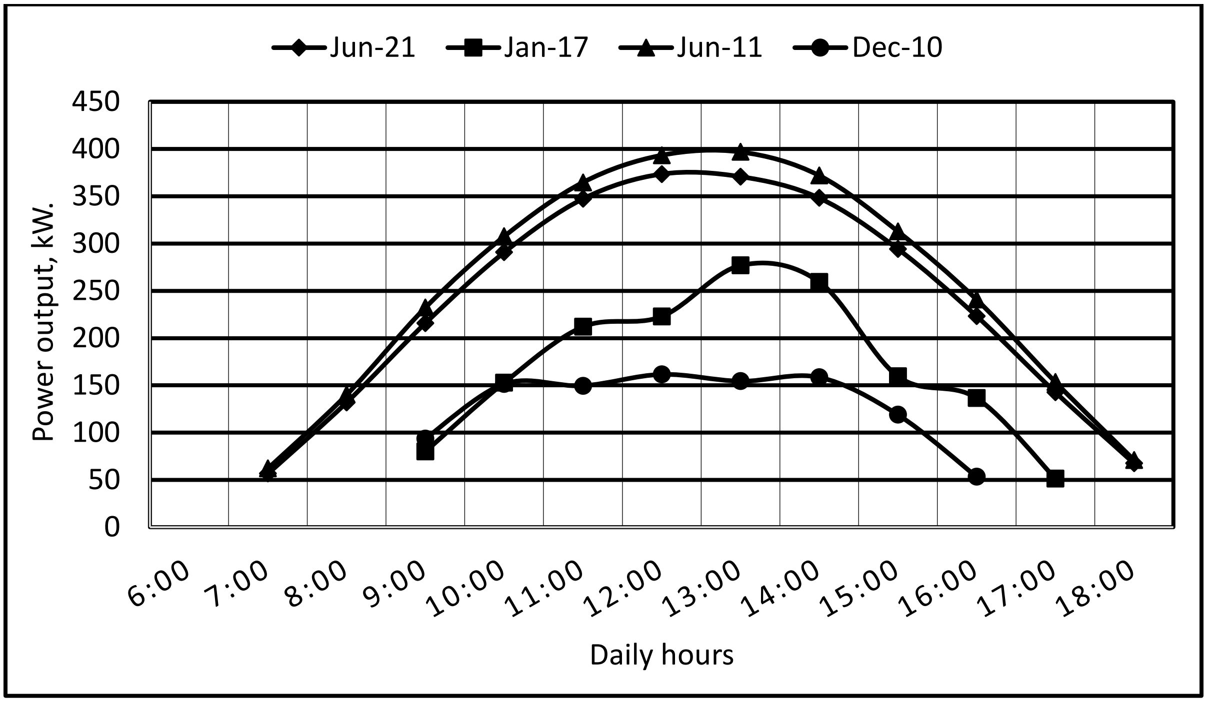

Figure 4.27 Hourly average power output R134a as ORC fluid for Dhahran, Saudi Arabia.

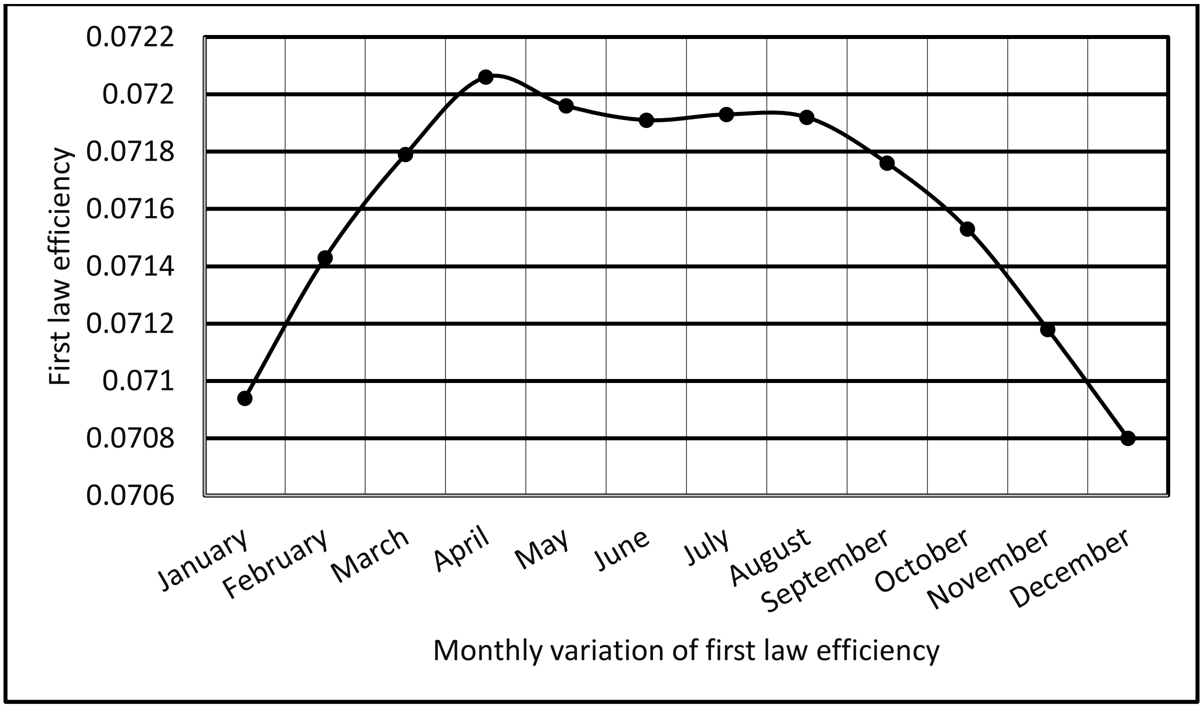

Figure 4.28 Monthly variation of first law efficiency using R134a as ORC fluid for Dhahran, Saudi Arabia.

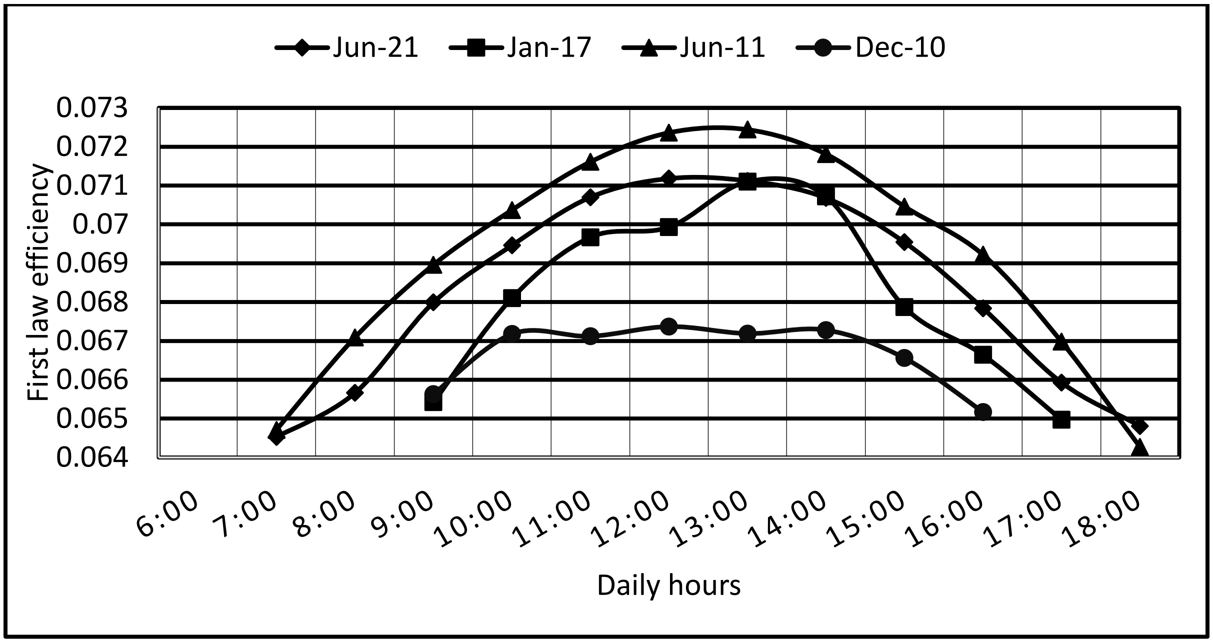

Figure 4.29 Hourly variation of first law efficiency using R134a as ORC fluid for Dhahran, Saudi Arabia.

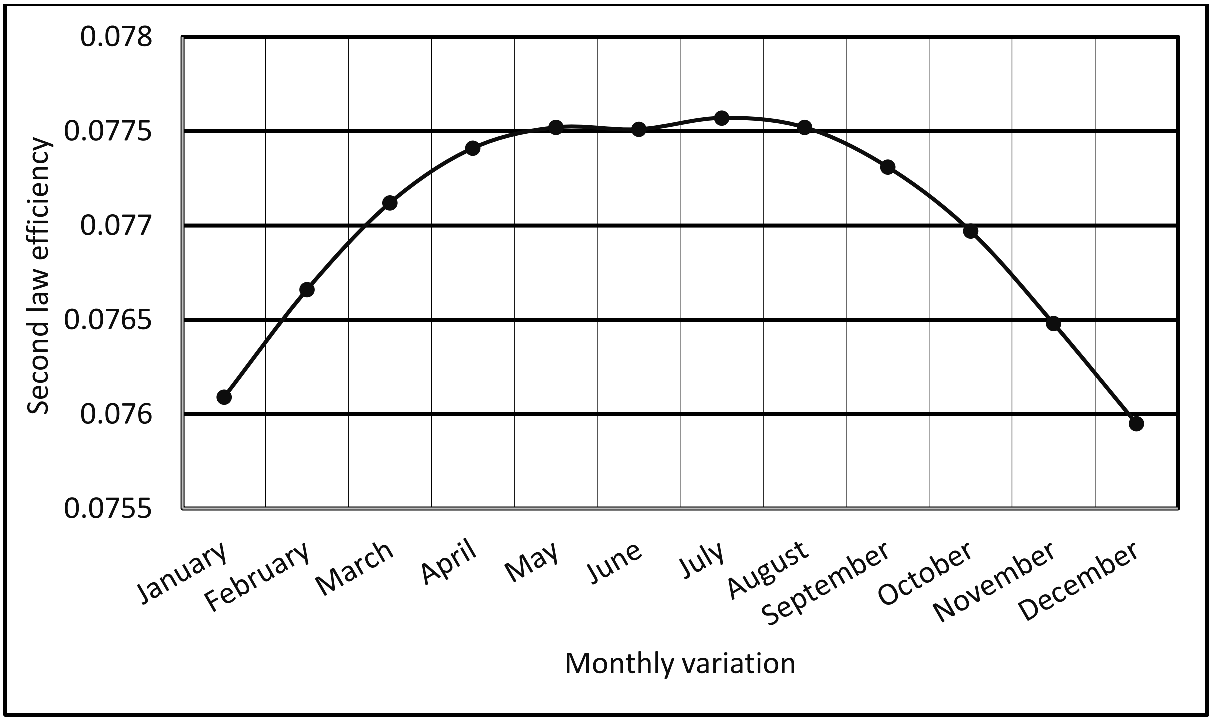

Figure 4.30 Monthly variation of second law efficiency using R134a as ORC fluid for Dhahran, Saudi Arabia.

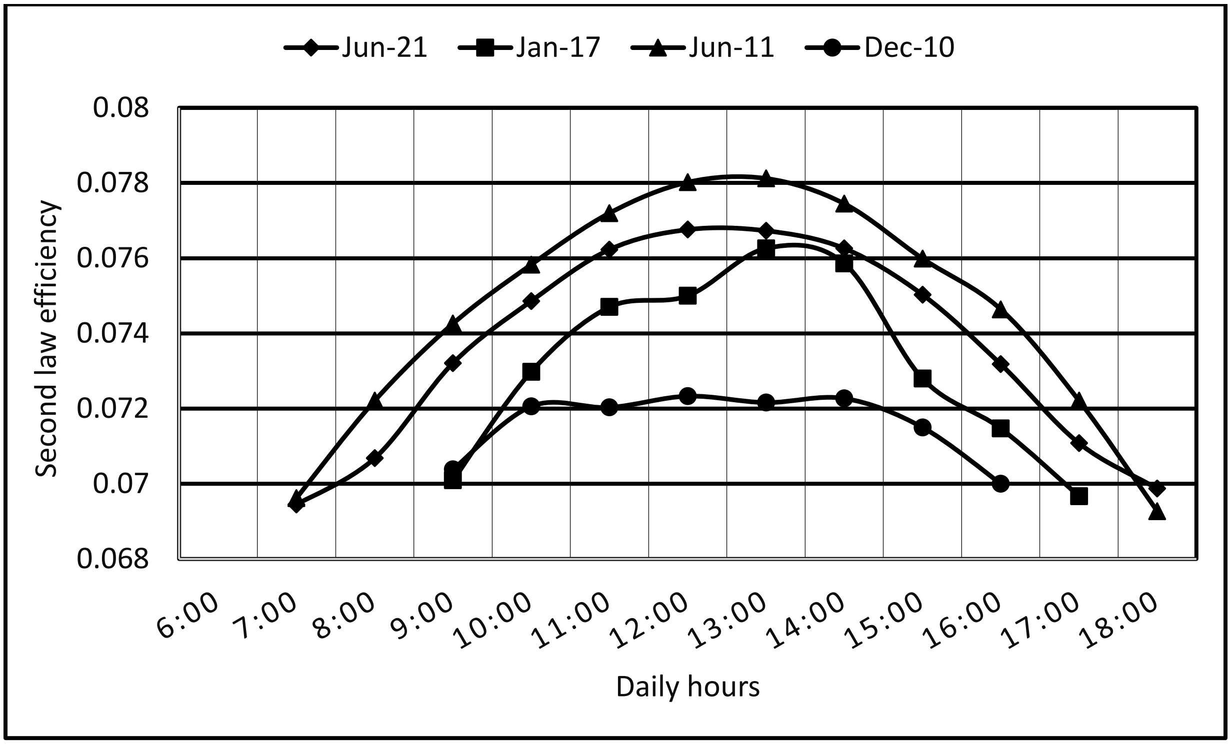

Figure 4.31 Hourly variation of second law efficiency using R134a as ORC fluid for Dhahran, Saudi Arabia.

From the power outputs and the trends in efficiency curves it is evident that the higher solar irradiation resulted higher outputs. In between 12:00 to 13:00, the integrated system worked with highest efficiency returning maximum power outputs. Among the four dates chosen, Jun-11 had the highest outputs in summer time, whereas Dec-10 had the lowest of outputs in winter due to reduced solar irradiation. It should be noted that the outputs resulting from solar irradiation of minimum 100 W/m^2 are considered for the analysis.

4.8 Concluding Remarks

PTC LS-2 model with Therminol VP-1 as heat transfer fluid was examined for its thermal and exergetic performance. Exergy losses and destruction were calculated and analyzed along with the parametric analysis for different inlet temperature and flow rate. Exergy destruction from receiver to fluid was found way higher in comparison to exergy destruction from receiver to fluid. Exergy losses were significantly less than the exergy destruction in PTC. It was found that every fluid has an optimum pressure and temperature level at which it works better than other fluids in ORC. R134a showed the best performance for the turbine inlet temperature range from 340 K – 440 K in terms of both energy and exergy efficiency. For example, at a temperature of 362.8 K and a pressure of 2750 kPa, R134a showed the highest thermal efficiency of 8.55% with the lowest mass flow rate required in ORC. Energy efficiency of rest of the fluids namely, R245fa, n-pentane and Toluene were less than 5%. R134a also showed the highest exergy efficiency of 21.84% in ORC at that operating condition. R134a retained to be the most efficient fluid up to turbine inlet temperature of 440 K. On the other hand, Toluene was found to be the most suitable fluid at higher turbine inlet temperature as seen from Figure 4.17 in section 4.7.2. At turbine inlet temperature of 550 K and a pressure of 2500 kPa, Toluene exhibited thermal efficiency of 23.5 %, while the exergy efficiency was found to be 62.89 %.

ORC energy efficiency was found to be very low due to large exergy destruction in HRVG and lack of efficient heat recovery method like recuperator to utilize turbine exhaust heat. HRVG contributed for the most exergy destruction in ORC. Exergy destruction caused by the PTC was multiple times higher than in ORC for all working fluids in ORC. The parametric analysis of the integrated cycle varying volumetric fluid rate in PTC and solar irradiation revealed that the increasing fluid flow in PTC circuit is sacrificing power output in ORC and operating efficiencies whereas for solar irradiation, increasing solar irradiation resulted higher efficiencies and power output.

CHAPTER 5

PERFORMANCE ANALYSIS OF ABSORPTION REFRIGERATION CYCLE

5.1 Introduction

Energy consumption for heating and cooling account for more than 30% of the total energy generation. In countries like Saudi Arabia, about 55% of the electricity produced is used for Air-Conditioning [16]. The Absorption Refrigeration Cycle (ARC) is an alternative to highly power consuming vapor compression cycle. Normally it operates on a dual pressure level and it can utilize low temperature heat sources. Introduction of ejector makes the EARC to work on triple pressure levels and the ejector works as a booster for pressure recovery. This study aims at assessing the performance of the single effect ARC with the addition of ejector and advantages of it over the basic Absorption refrigeration cycle (ARC).

5.2 System Description

Basic Absorption refrigeration cycle (ARC) is heat driven and has four basic components in general, namely generator, condenser, absorber and an evaporator. Generator and condenser operate on a high-pressure level while evaporator and absorber operate on a lower pressure level. Pressure drop in between the components of same pressure level is not considered in the present analysis. In generator, heat source like solar energy heats the rich solution coming from the absorber by the means of storage tank or heat exchangers. Concentration of refrigerant becomes very less in the solution and that is how refrigerant gets separated from the solution in the generator. The resulting weak solution is circulated to the absorber with an expansion valve. The refrigerant vapor from the generator then flows into the condenser to be condensed by the ambient. From the condenser the liquid refrigerant makes their way to the evaporator expanding through a throttle valve. Reaching low pressure level after throttling, the refrigerant liquid evaporates in the evaporator and releasing its cooling power at the same time.

In case of basic ARC, evaporator feeds the absorber with refrigerant vapor. Then the refrigerant vapor is absorbed by the solution on absorber releasing heat to the sink as shown in Figure 5.1.

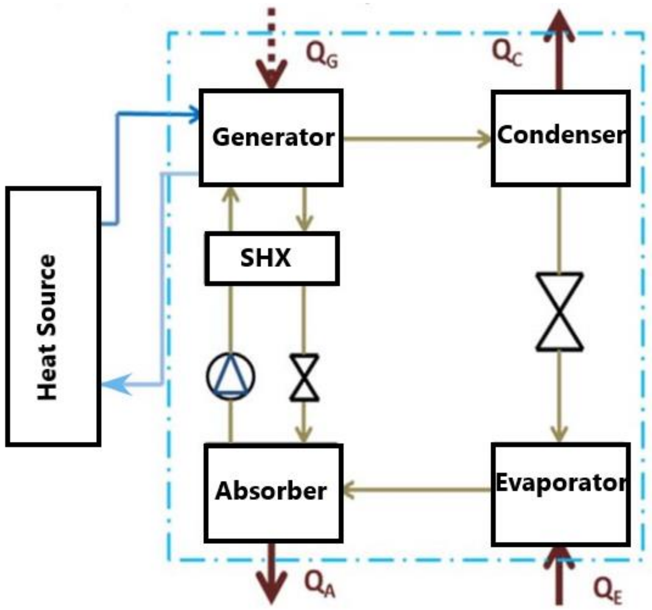

Figure 5.1 Absorption Refrigeration Cycle (ARC).

This binary solution become highly concentrated with refrigerant and this rich solution is pumped to the generator and the cycle is repeated. Solution heat exchanger (SHX) recovers internal heat that enhances the COP significantly.

In case combined ejector absorption refrigeration cycle, expansion valve in between solution heat exchanger (SHX) and the absorber is replaced by an ejector as shown in Figure 5.2.

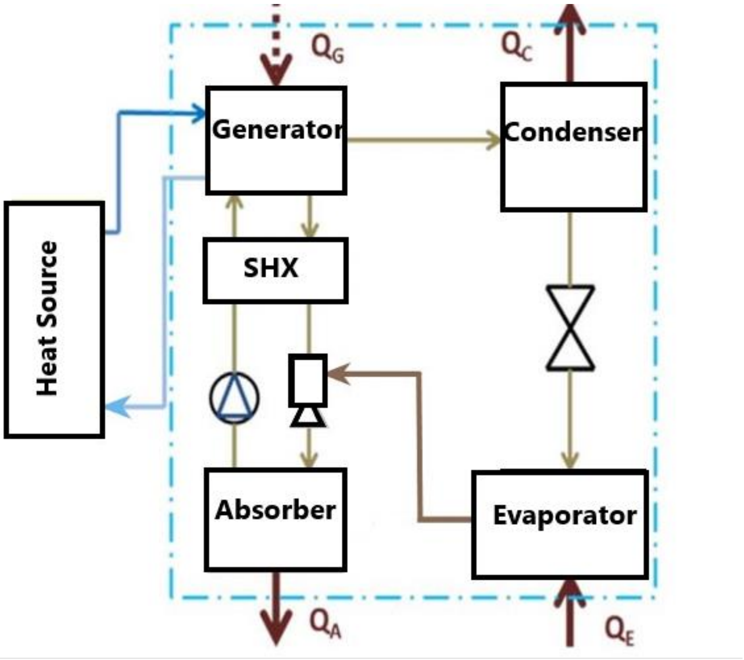

Figure 5.2 Ejector-Absorption Refrigeration Cycle (EARC)

The ejector creates an intermediate pressure level for the absorber to operate. As shown in the EARC system in our present analysis, evaporator refrigerant NH_3 (Flow path 10-11) is diverted to the ejector instead of the absorber which is termed as the secondary flow (Flow path 11-14) while the solution coming from generator via SHX is called the primary flow (Flow path 13-14). Primary flow has less concentrated refrigerant solution named as weak solution (Flow path 12-13-14), while the solution leaving the absorber after NH_3 absorption (Flow path 14-15), is called strong solution (Flow path 15-16-17).

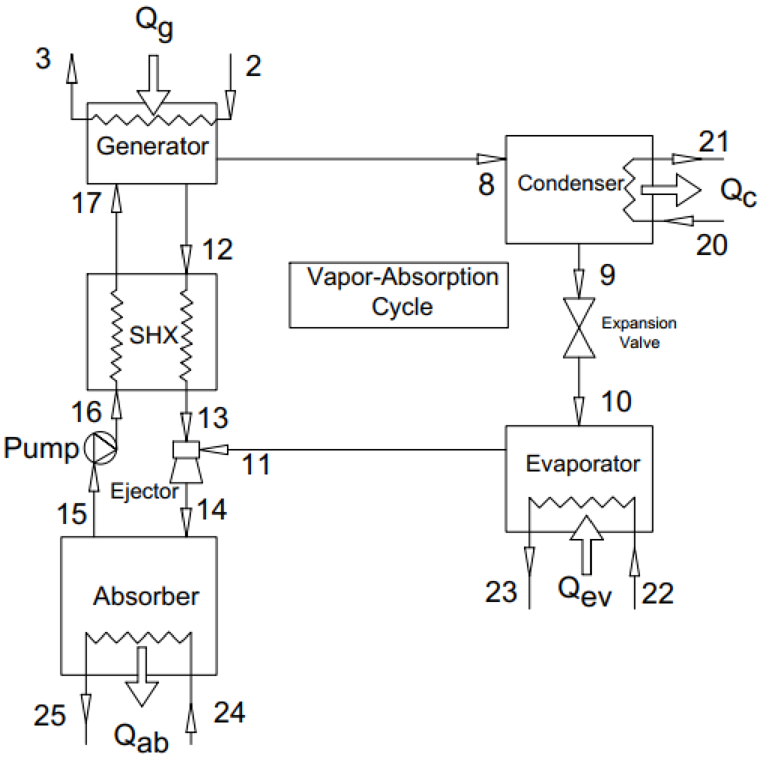

Figure 5.3 EARC System.

This strong solution passes through the generator parting their ways (Flow path 17-12 for weak solution and flow path 17-8 for refrigerant). A high temperature heat source generates NH_3 vapor from the strong solution which is sent to the evaporator via condenser (Flow path 8-9) while the remaining weak solution makes its way for the ejector via SHX (Flow path 12-13). Through an expansion valve (Flow path 9-10), Ammonia condensate passes to the evaporator where it vaporizes again by the heat received from the external system thus producing the desired cooling effect for the designated space.

5.3 Thermodynamic Design Considerations for the Ejector

Incorporating ejector in the cycle is a proven performance booster for absorption cycle [141]. The one dimensional model is based on the model proposed by [125]. The design methodology outlined in [141] is taken as reference for the analysis of Ejector under following assumptions.

- No external heat transfers are considered.
- Stagnation conditions are considered at the entrance of ejector for both primary and secondary fluids.
- Potential energy is neglected.
- The flow is assumed to be incompressible due the fact that the Mach number of Ammonia vapor is very low.
- Absorption process does not occur in the missing tube, neither in the diffuser.
- The weak solution flows through the nozzle from the generator pressure to the evaporator pressure.

5.4 Model Validation

In this section input variables and constant parameters for the first and second law analysis of the refrigeration system is defined followed by the validation thermophysical properties of NH_3-$LiNO_3$. Ammonia properties were directly used from the EES function library. NH_3-$LiNO_3$ properties are developed for the analysis and details are presented in Appendix-A for the analysis. EARC model validations are presented in the following subsections.

5.4.1 Pressure Model Validation of NH_3-$LiNO_3$

Liquid vapor pressures are determined according to the correlations provided by [202]. From a wide range of temperatures and mass concentrations of ammonia some data were taken, and the model is found to be in excellent agreement with the experimental results. Standard deviation is found to be only 1.853%. Relevant data can be found in Appendix Table B - 3**Error! Reference source not found.**.

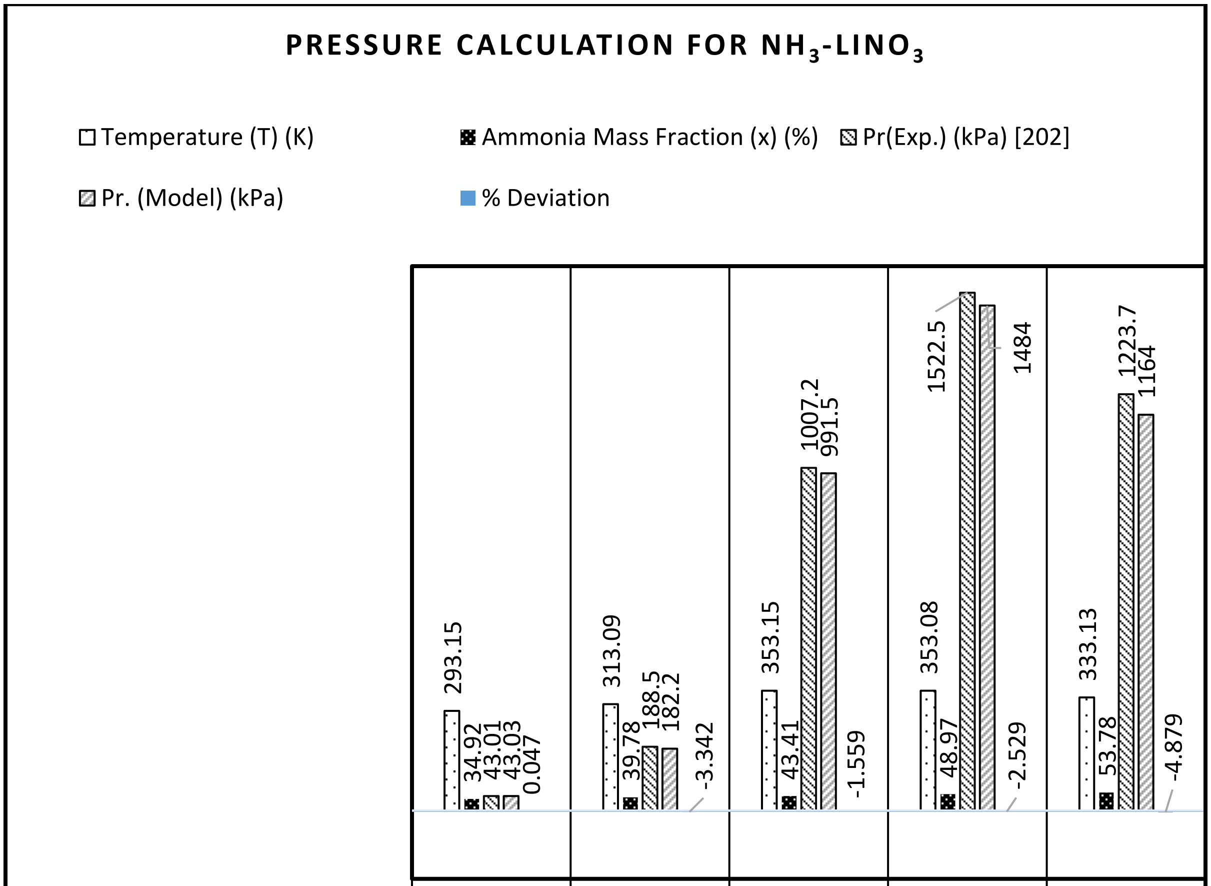

	1	2	3	4	5
☐ Temperature (T) (K)	293.15	313.09	353.15	353.08	333.13
▩ Ammonia Mass Fraction (x) (%)	34.92	39.78	43.41	48.97	53.78
▧ Pr(Exp.) (kPa) [202]	43.01	188.5	1007.2	1522.5	1223.7
▨ Pr. (Model) (kPa)	43.03	182.2	991.5	1484	1164
🟦 % Deviation	0.047	-3.342	-1.559	-2.529	-4.879

Figure 5.4 Pressure result validation of NH_3-$LiNO_3$.

5.4.2 Density Model Validation of NH_3-$LiNO_3$

Density correlations were taken from [203] and validation results are provided in the following table. Standard deviation is found to be 0.32%. Relevant data of operating conditions can be found in Appendix Table B - 4.

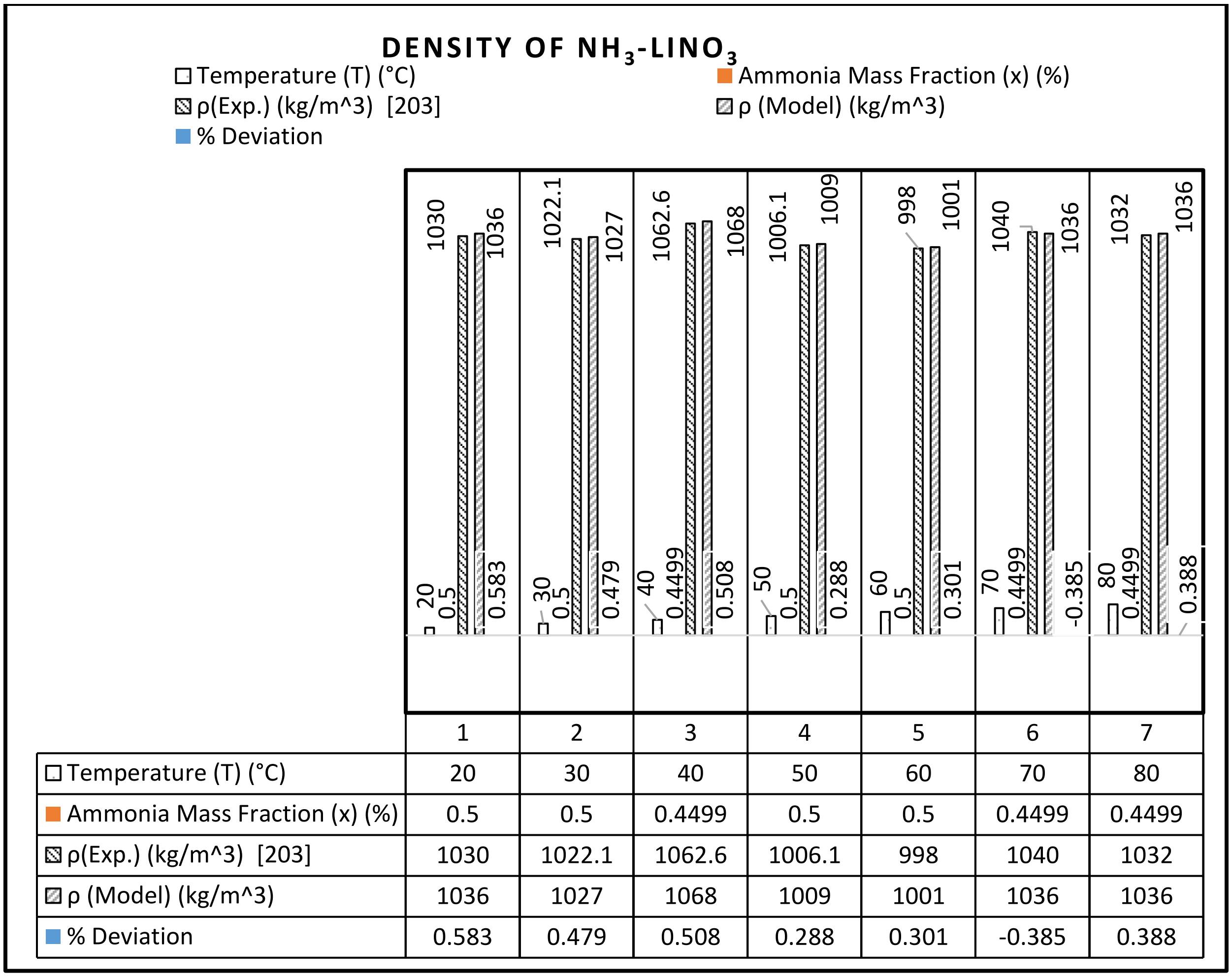

	1	2	3	4	5	6	7
□ Temperature (T) (°C)	20	30	40	50	60	70	80
🟧 Ammonia Mass Fraction (x) (%)	0.5	0.5	0.4499	0.5	0.5	0.4499	0.4499
▧ ρ(Exp.) (kg/m^3) [203]	1030	1022.1	1062.6	1006.1	998	1040	1032
▨ ρ (Model) (kg/m^3)	1036	1027	1068	1009	1001	1036	1036
🟦 % Deviation	0.583	0.479	0.508	0.288	0.301	-0.385	0.388

Figure 5.5 Density result validation of NH_3-$LiNO_3$.

5.4.3 Ejector-Absorption Cycle Validation

Enthalpy and entropy data are validated from Farshi et al. [141] to validate the EARC . The correlations for deriving the enthalpy and entropy properties are outlined by the same author [113]. Standard deviations for enthalpy and entropy are found to be 4.8 and 2.5% respectively. Entropy and exergy values at different positions of EARC are shown in following Figure 5.6 and Figure 5.7. Detail data can be found in Appendix Table B - 6.

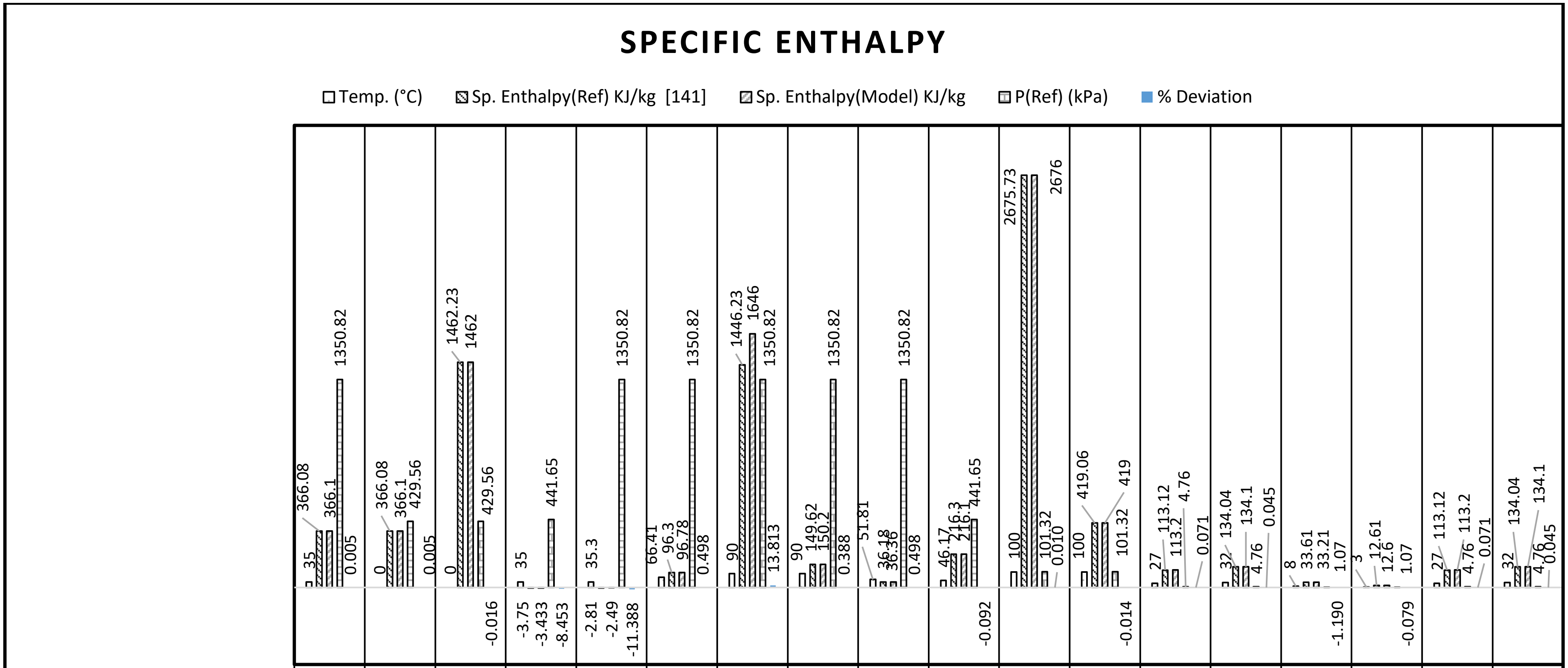

	Cond. Exit	Ev. Inlet	Ev. Exit	Abs. Exit	Pump Exit	Gen. strong sol. Inlet	Gen. ref. Exit	Gen. weak sol. Exit	Pr. flow Ejector inlet	Sec. ref. Ejector inlet	Gen. HTF Inlet	Gen. HTF Exit	Cond. coolant inlet	Cond. colant Exit	Ev. coolant inlet	Ev. Coolant Exit	Abs. coolant inlet	Abs. coolant Exit
□ Temp. (°C)	35	0	0	35	35.3	66.41	90	90	51.81	46.17	100	100	27	32	8	3	27	32
▧ Sp. Enthalpy(Ref) KJ/kg [141]	366.08	366.08	1462.23	-3.75	-2.81	96.3	1446.23	149.62	36.18	216.3	2675.73	419.06	113.12	134.04	33.61	12.61	113.12	134.04
▨ Sp. Enthalpy(Model) KJ/kg	366.1	366.1	1462	-3.433	-2.49	96.78	1646	150.2	36.36	216.1	2676	419	113.2	134.1	33.21	12.6	113.2	134.1
▤ P(Ref) (kPa)	1350.82	429.56	429.56	441.65	1350.82	1350.82	1350.82	1350.82	1350.82	441.65	101.32	101.32	4.76	4.76	1.07	1.07	4.76	4.76
■ % Deviation	0.005	0.005	-0.016	-8.453	-11.388	0.498	13.813	0.388	0.498	-0.092	0.010	-0.014	0.071	0.045	-1.190	-0.079	0.071	0.045

Figure 5.6 Specific enthalpy validation of NH_3-$LiNO_3$.

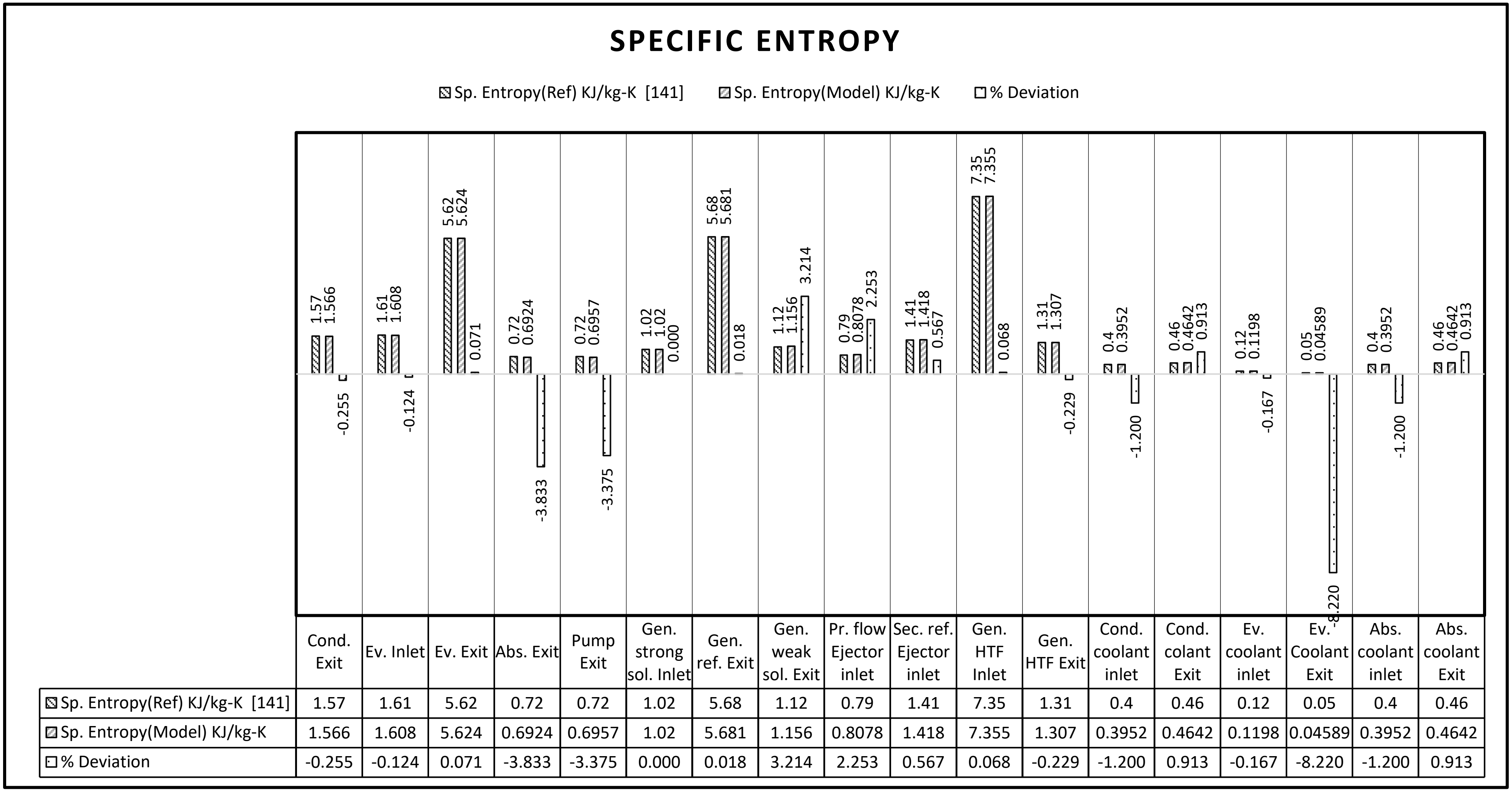

	Cond. Exit	Ev. Inlet	Ev. Exit	Abs. Exit	Pump Exit	Gen. strong sol. Inlet	Gen. ref. Exit	Gen. weak sol. Exit	Pr. flow Ejector inlet	Sec. ref. Ejector inlet	Gen. HTF Inlet	Gen. HTF Exit	Cond. coolant inlet	Cond. colant Exit	Ev. coolant inlet	Ev. Coolant Exit	Abs. coolant inlet	Abs. coolant Exit
▧ Sp. Entropy(Ref) KJ/kg-K [141]	1.57	1.61	5.62	0.72	0.72	1.02	5.68	1.12	0.79	1.41	7.35	1.31	0.4	0.46	0.12	0.05	0.4	0.46
▨ Sp. Entropy(Model) KJ/kg-K	1.566	1.608	5.624	0.6924	0.6957	1.02	5.681	1.156	0.8078	1.418	7.355	1.307	0.3952	0.4642	0.1198	0.04589	0.3952	0.4642
☐ % Deviation	-0.255	-0.124	0.071	-3.833	-3.375	0.000	0.018	3.214	2.253	0.567	0.068	-0.229	-1.200	0.913	-0.167	-8.220	-1.200	0.913

Figure 5.7 Specific entropy result validation of NH_3-$LiNO_3$.

5.5 Modelling and Input Parameters of Analysis

Coefficient of performance and other necessary outputs were derived from different input parameters as shown below for both basic absorption cycle (ARC) and ejector-absorption refrigeration cycle (EARC). It should be noted that the EES model for EARC is developed utilizing the mathematical model of Farshi [141] and the EES formulations of ARC by Herold et al. [189].

Generator refrigerant exit temperature, T_{14} : 90 °C.

Condenser refrigerant exit temperature, T_1 : 35 °C.

Evaporator refrigerant exit temperature, T_3 : 0 °C.

Absorber solution exit temperature, T_4 : 35 °C.

Strong solution NH_3 mass fraction, X_{strong} : 0.51.

Weak solution NH_3 mass fraction, X_{weak} : 0.44.

Ejector nozzle efficiency, η_N : 0.85.

Ejector mixing efficiency, η_M : 0.90.

Ejector diffuser efficiency, η_D : 0.80.

Diffuser diameter : 150 mm.

Mixing tube diameter : 58.4 mm.

Entrainment ratio : 0.1429.

5.6 Results and Discussions

In all the cases of parametric analysis, namely generator temperature, evaporator temperature and solution heat exchanger effectiveness are showing higher COP for EARC in comparison to ARC. With reduced generator temperature COP is getting higher in both cases as seen in the following Figure 5.8. COP for EARC rises from 0.53 to 0.64 when temperature gradually reduces to 67°C – 107 °C (340 K – 380 K).

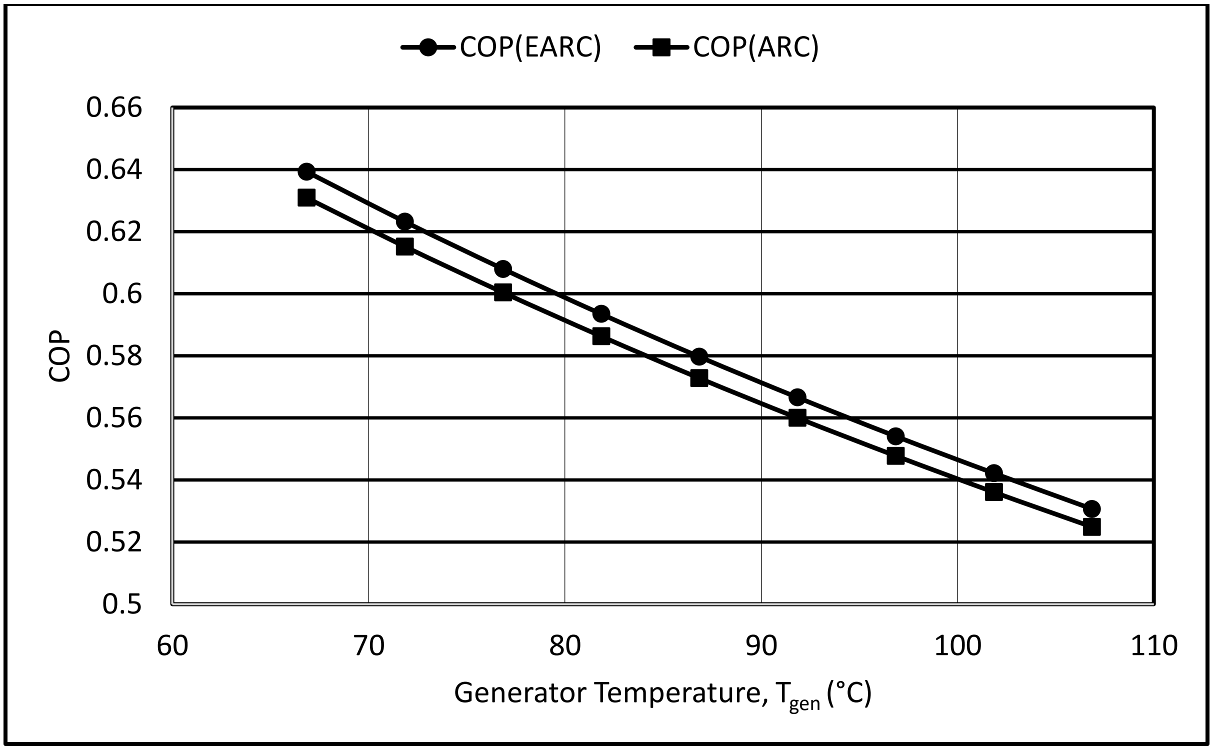

Figure 5.8 Effect of Generator temperature on COP.

Similar case is observed with evaporator temperature in Figure 5.9 but at a slower pace than generator temperature change. The 20°C temperature difference is returning about 1% increase in COP.

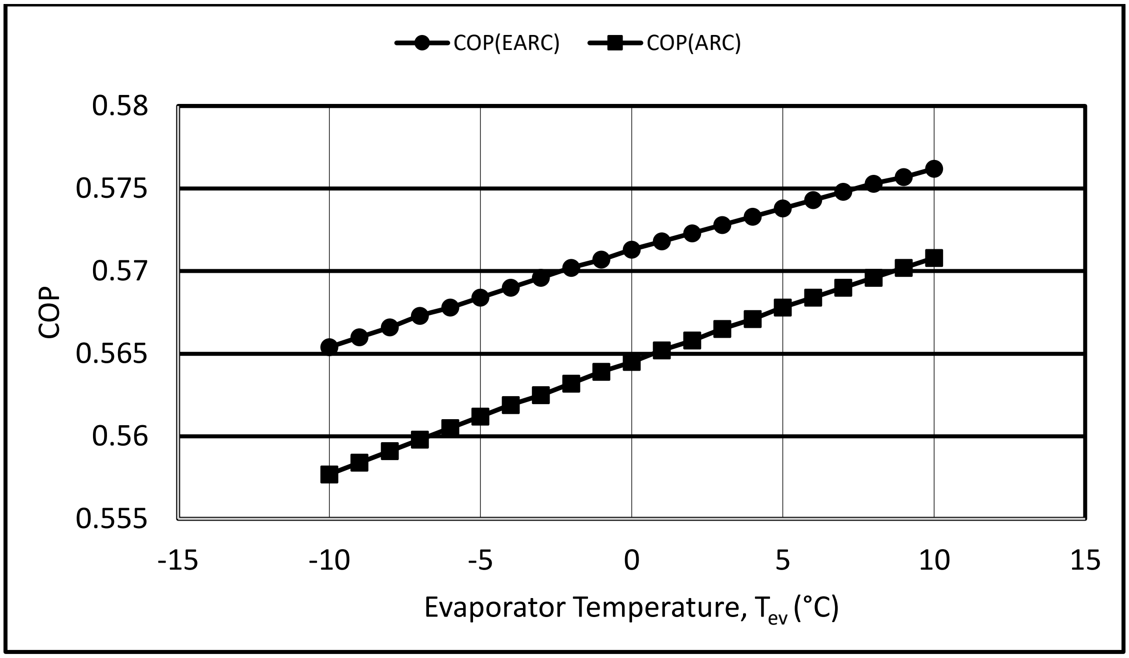

Figure 5.9 Effect of Evaporator temperature on COP.

SHX effectiveness is proven to be another prime contributing factor for higher thermal performance of the refrigeration system. Sharp increase in COP is observed from Figure 5.10 when effectiveness grows higher.

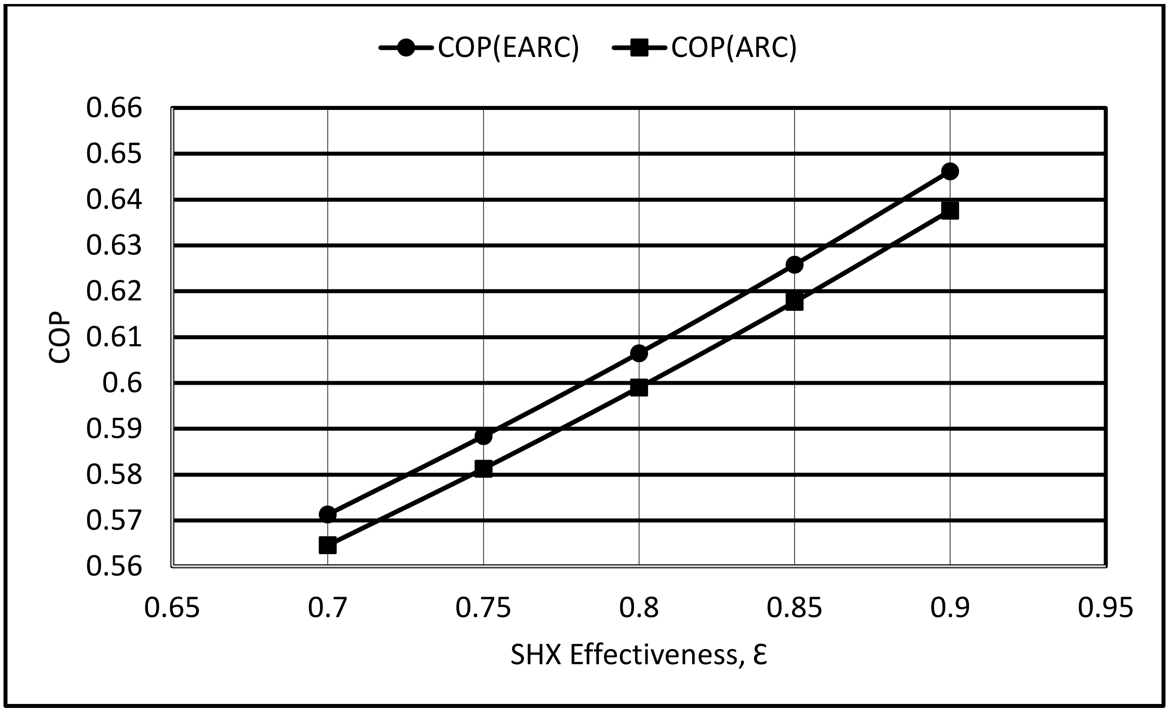

Figure 5.10 Effect of solution heat exchanger effectiveness on COP.

In Figure 5.11 and Figure 5.12, pump work consumptions for both cycles are presented. It is evident from the figure is that EARC consumes way lower power consumption for operating the solution pump in comparison to ARC. Reduction in power consumption in pump is boosting the COP of EARC.

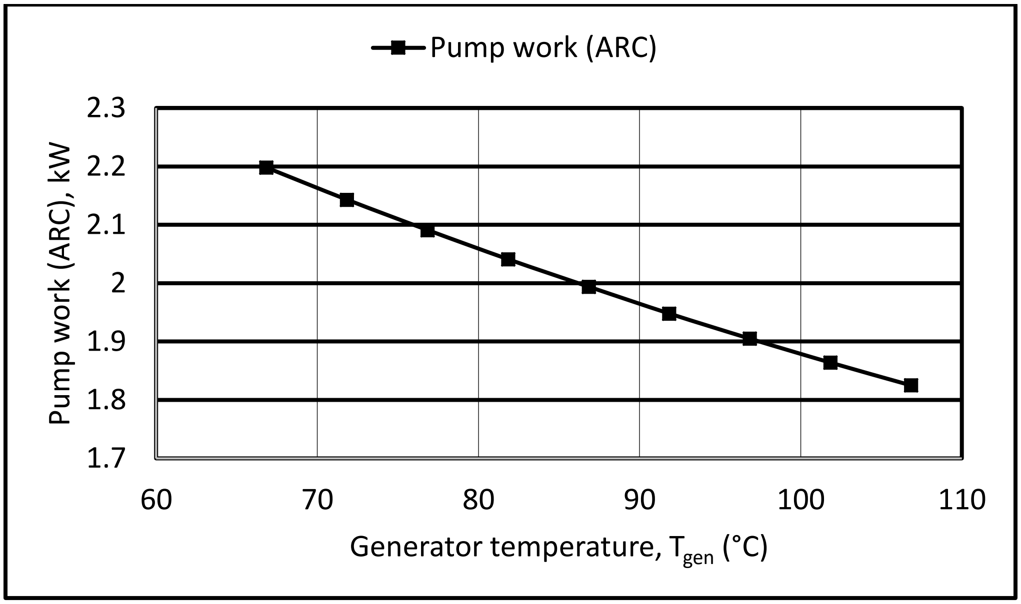

Figure 5.11 Effect of generator temperature on ARC solution pump work.

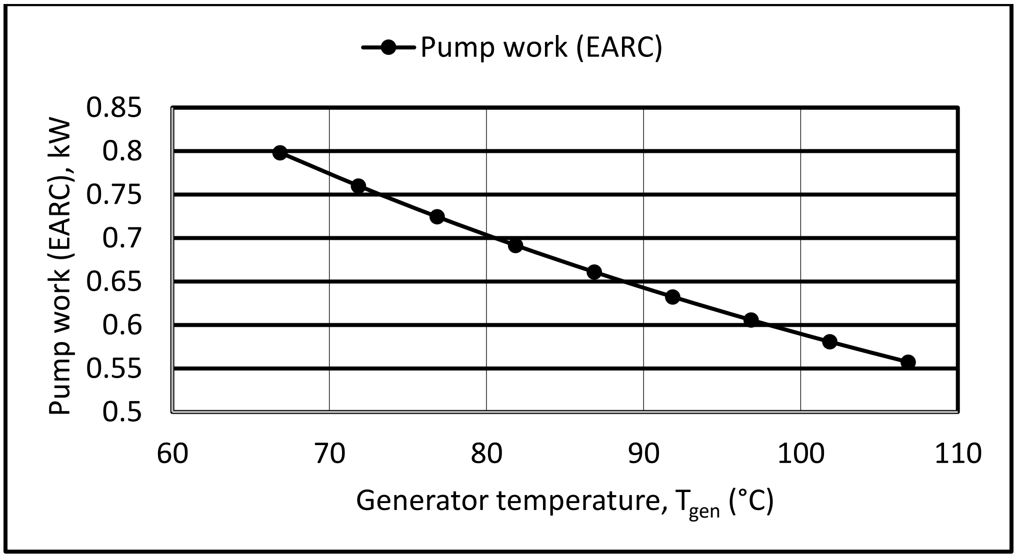

Figure 5.12 Effect of generator temperature on EARC solution pump work.

Figure 5.13 and Figure 5.14 are showing the exergy efficiency trends of both cycles. Higher temperature is reducing exergetic performance of both EARC and ARC. The trend is similar to COP and EARC is found to be more efficient in terms of exergy utilization.

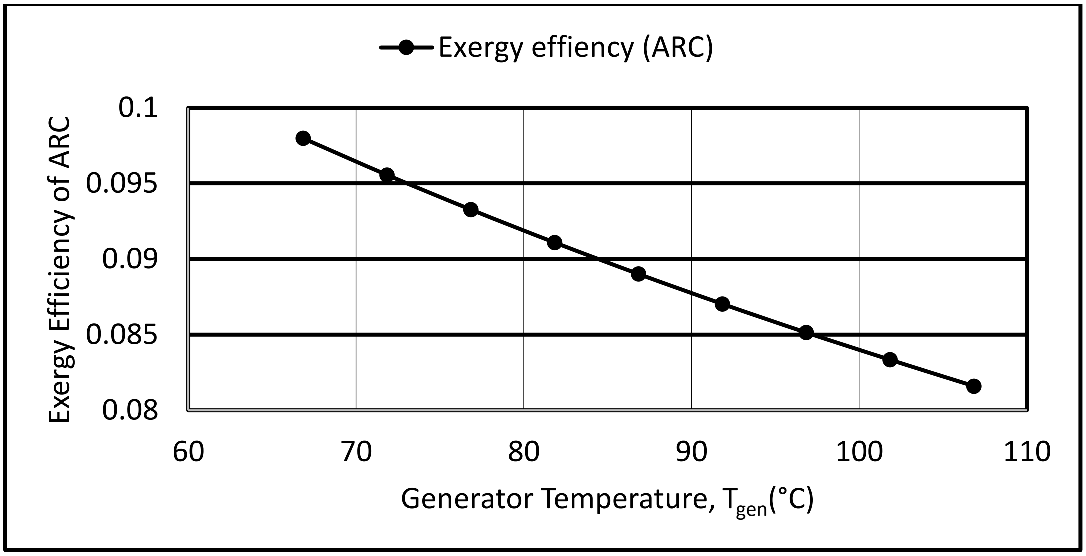

Figure 5.13 Effect of Generator temperature on exergy efficiency of ARC.

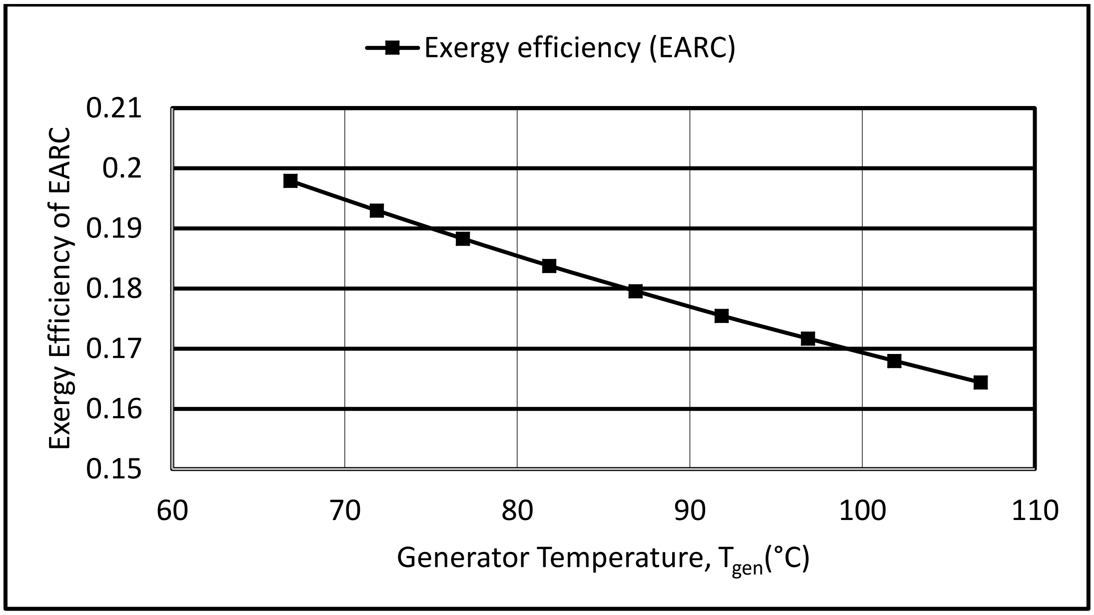

Figure 5.14 Effect of Generator temperature on exergy efficiency of EARC.

5.7 Concluding Remarks

EARC is found superior than ARC for higher COP, exergy efficiency, reduction in solution pump work etc. A great reduction in pump work is observed when ejector is used. This will have more positive effect on large absorption systems where huge energy consumption of the pump can be marginalized with the introduction of the ejector. Generator temperature is found to be highly influencing the COP and exergy efficiency of the refrigeration system as observed in Figure 5.8, Figure 5.13 and Figure 5.14. With the reduced temperature of the generator, the COP and exergy efficiency were found to be going higher. Similar results were reported by Farshi et al. [141] for COP with varying generator temperature for a wider range of generator temperature. But in this analysis, the generator temperature was kept limited within 67°-107°C temperature range since the correlations we have used for NH_3-$LiNO_3$ is produced from the experimental values taken within 20°-80°C temperature range [202], [204]. So, it might not be feasible or convenient to extrapolate the range way beyond the range considered. Solution heat exchanger effectiveness also has a significant level of influence on the performance of the system as seen from Figure 5.10. With the increase of heat exchanger effectiveness, the COP was found to be sharply increasing. Evaporator temperature was examined within -10°C to 10°C temperature range to check the performance of the refrigeration system. With the increase in temperature, the COP was increasing but response was very slow in comparison to the effect of generator temperature and SHX effectiveness.

CHAPTER 6

PERFORMANCE ANALYSIS OF SOLAR ASSISTED POWER (ORC) AND REFRIGERATION (EARC) SYSTEM

6.1 Introduction

Organic Rankine Cycle (ORC) is an environment friendly technology capable of generating power utilizing thermal heat energy from a low temperature source such as waste heat, concentrated solar power (CSP). It is widely adopted for cogeneration, heating, cooling and even desalination along with power harnessing in recent days. As most of the organic working fluids in ORC can no longer be thermally stable at temperatures ranging 300°-400°C (573 K – 673 K) [15], not all form of CSP technology can be integrated with ORC. In case of Parabolic dish collector and solar central tower, receiver temperature can go way beyond the capacity of ORC. Solar technologies like PTC or LFR suit for ORC as low temperature heat sources for the ORC [53], [61]. PTC is well matured and can cope with wide range of temperatures [58], [59]. This solar powered ORC can be further integrated with the absorption refrigeration cycle or with cascaded refrigeration cycle to serve the cooling needs at variable temperatures. The addition of ejector as a replacement of expansion valve in the absorption cycle is also a proven efficiency enhancement tool [141]. In this analysis, a solar assisted combined power and cooling cycle is proposed. The study aims at assessing the performance of PTC assisted ORC and EARC for simultaneous production of power and cooling.

6.2 System Description

The proposed system can be divided into three subsystems, namely the heat source (PTC), power (ORC) and the cooling (EARC) system. In this analysis, PTC is utilized as the heat source for the combined power (ORC) and refrigeration (EARC) system. Figure 6.1 is demonstrating a PTC arrangement where incident solar radiation is utilized by an arrangement of parabolic trough collectors (PTC) to increase the temperature of the recirculating heat transfer fluid. It should be noted that this recirculating HTF exchanges heat with two components from two different circuits. After coming out of PTC outlet, it exchanges heat with the HRVG of the ORC power circuit first and then it exchanges heat with the generator of the EARC cooling circuit.

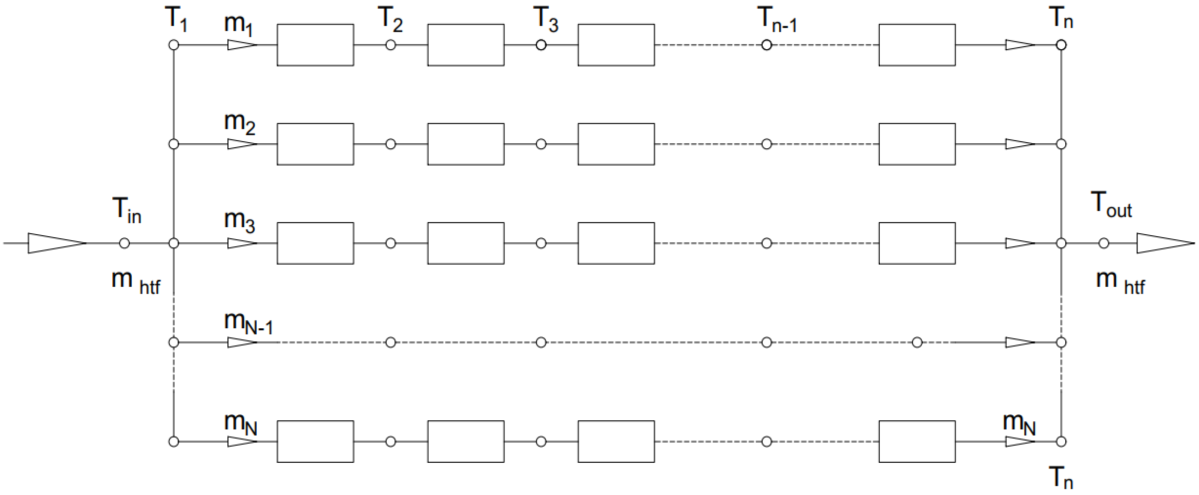

Figure 6.1 PTC Arrangement

To start with, HTF fluid of certain mass (m_{htf}) at temperature T_{in} is fed into the PTC inlet which comes from the outlet of the EARC generator. HTF pass through the receivers of consecutive PTCs. The arrangement has N number of rows connected in parallel, whereas each row has (n-1) number of PTCs connected in series. It is assumed that all the rows have the same volumetric fluid flow rate where m_{htf} is the resulting total mass flow rate of HTF. Solar rays reflected to the receiver from the reflector and the receiver absorbs heat during the process resulting fluid coming out at higher temperatures. In general, many PTC modules are connected together to produce high temperature at the outlet. A series of interconnected PTCs are connected in parallel through a header for matching the required mass flow rate. The arrangement can be adjusted by regulating the number of PTC modules in series and parallel.

As mentioned earlier, the heat collected by the PTC arrangement is exchanged with the HRVG of ORC power circuit first (Process 1-2 and Process 7-4). ORC has four main components: HRVG for receiving waste heat or low temperature heat from solar or geothermal sources, an expander or turbine for producing work by the expansion of HTF, a condenser for releasing heat to the environment and a pump for increasing the pressure of the working fluid while recirculating HTF back to HRVG.

In HRVG, as shown (Figure 6.2) this high heating energy of PTC fluid is transferred to the low temperature heat transfer fluid of ORC (Process 7-4). It provides necessary heat input to evaporate ORC fluid to an acceptable degree which then fed into the ORC turbine (Process 4-5). The power is produced in the process by the generator which is coupled with the turbine.

In the power circuit, the ORC working fluid loses its pressure in the turbine. At turbine outlet, the exhaust heat of the ORC fluid is released in the condenser. The vapor of ORC working fluid turns to saturated liquid (Process 5-6). The saturated liquid with reduced pressure is subjected to a pump for the recovery of the pressure and after the pressure recovery (Process 6-7), the flow is directed to the HRVG and the whole power cycle repeats as mentioned.

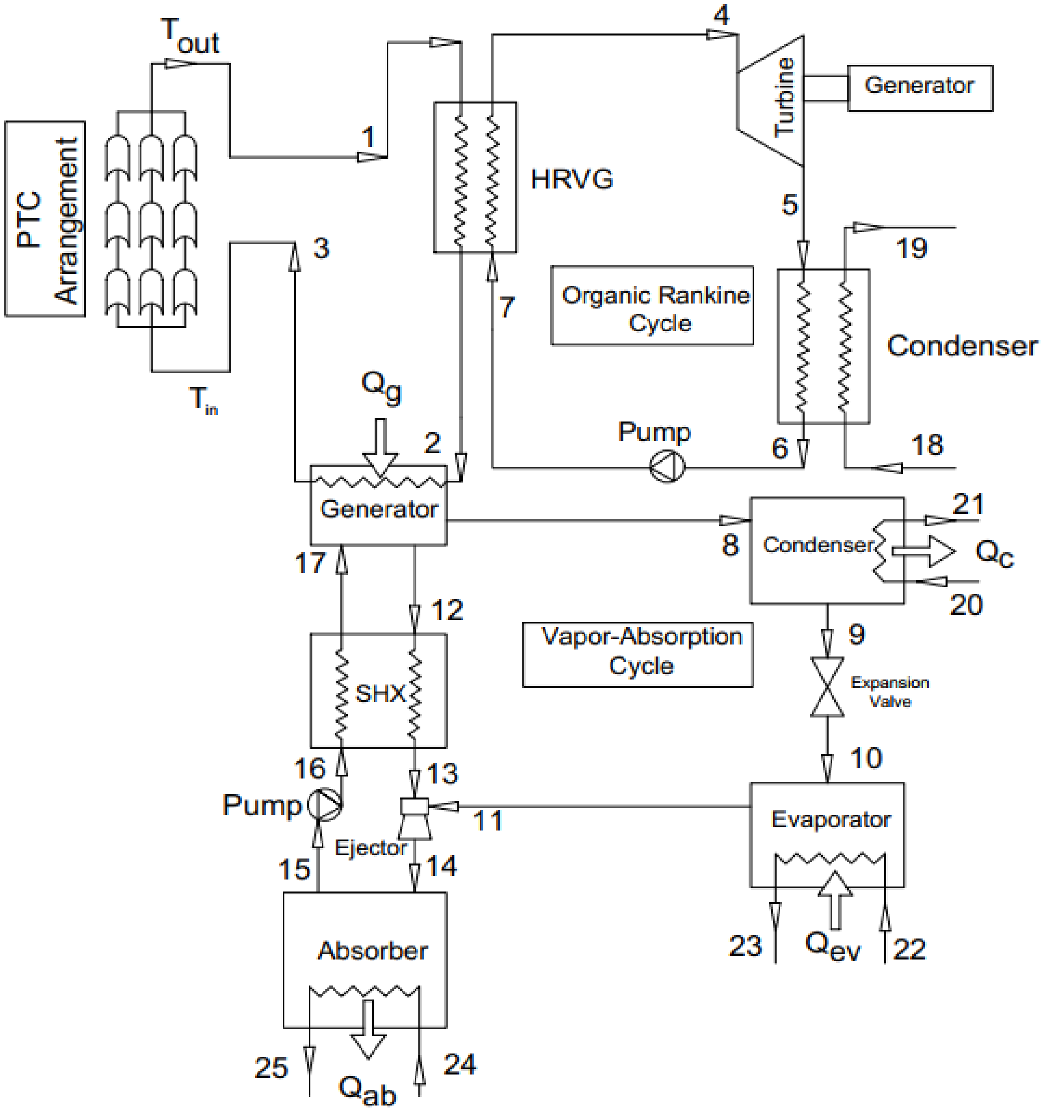

Figure 6.2 Schematic of the solar assisted combined power and cooling system.

After a significant portion of the heat is utilized to HRVG, the temperature of HTF originally coming from PTC outlet is reduced to a certain degree. Then the HTF is directed to exchange heat with the generator of the Absorption cycle (ARC), the second component with which HTF of PTC exchanges heat (Process 2-3).

Basic single effect Absorption Refrigeration cycle is driven by heat and works on two different pressure levels. Here in the case of Ejector-Absorption refrigeration cycle (EARC), the throttle valve in between the SHX and the absorber is substituted with an ejector to create an intermediate pressure level by the ejector and the system works on three pressure levels. The rest of the components are similar to single effect ARC.

Apart from ejector and other regular components - generator, condenser, absorber and evaporator are the four basic components of the cycle. In generator, heat released by the PTC boils the rich solution (NH_3-$LiNO_3$ solution with a higher concentration of NH_3) coming from the absorber. During this process, the concentration of refrigerant (NH_3) becomes very less in the solution and that is how refrigerant gets separated (Process 17-8) from the solution in the generator. The remaining weak solution which is now less concentrated in $NH_{3,}$ (Process 17-12) is circulated to the absorber through the ejector (Process 13-14). In case of double pressure single effect ARC, weak solution (NH_3-$LiNO_3$ solution with a lower concentration of NH_3) passed to the absorber through a pressure relief valve placed in between the SHX and the absorber. Solution heat exchanger (SHX) recovers internal heat that enhances the COP significantly. Here in the case of Ejector-Absorption refrigeration cycle (EARC), this throttle valve is substituted with an ejector as mentioned earlier (Process 13-14). The weak solution coming from the generator and the refrigerant NH_3 coming from the evaporator are mixed together in the ejector.

The separated NH_3 refrigerant vapor from the generator flows into the condenser (Process 8-9) to be condensed by the ambient. From the condenser the liquid refrigerant makes their way to the evaporator expanding through a throttle valve (Process 9-10). Reaching low pressure level after throttling, the refrigerant liquid evaporates in the evaporator and releasing its cooling power at the same time (Process 10-11). The evaporated refrigerant NH_3 then gets directed to ejector where it mixed with the weak solution coming from the EARC generator via SHX. The two streams are discharged together for the absorber. Then the refrigerant vapor (pure NH_3) is absorbed by the solution on absorber releasing heat into the sink (Process 14-15). This binary solution becomes highly concentrated with refrigerant and this rich solution (NH_3-$LiNO_3$ solution with higher concentration of ammonia) is pumped to the generator via SHX and this is how the cooling cycle is repeated.

To sum up, the EARC generator receives heat from the HTF of PTC to separate the refrigerant from the absorbent solution. The refrigerant NH_3 gets separated from the strong NH_3-$LiNO_3$ solution in this case and separated NH_3 is directed to the evaporator to provide necessary cooling (Process 10-11). Weak solution of NH_3-$LiNO_3$ coming from the generator via SHX (Process 12-13) and the pure NH_3 refrigerant coming from the evaporator (Process 10-11) are mixed together in the ejector and gets directed to the absorber (Process 13-14 and 11-14) for the absorption of NH_3 to take place. NH_3 is absorbed by the $LiNO_3$ solution and the concentration of NH_3 gets higher and this highly concentrated solution of NH_3-$LiNO_3$ is directed to the generator of ARC through SHX (Process 14-15-16).

The output of the whole system will vary depending on PTC fluid flow rates, outlet temperature of the PTC, available solar intensity and so on. Coolants will flow through the components accordingly to receive the heat like in absorber and condenser. In case of the evaporator, the evaporator will take away the heat from the enclosed space to maintain the cooling or refrigeration there.

6.3 Design Parameters of the Combined System

The performance of the integrated cycle is analyzed to get power and cooling outputs on varying solar intensities. Parabolic collector receivers are normally 100-120 meters long [205]. So, the number of PTC is chosen accordingly. Optimum conditions observed in previous sections of the power and cooling cycles are used for the combined system. It should be noted that the outlet temperature of HTF after coming out of the EARC is used as the inlet temperature of the PTC collector arrangement. Since there is no TES to store the energy in this system, the useful heat produced by the PTC arrangement will be fully consumed by the HRVG and the EARC generator. As recommended by [156], the 75% of the heat generated is designed to utilize by the HRVG and rest for the EARC generator. Power output, refrigeration output and efficiencies are derived for the considered cases using the parameters outlined in the following section.

6.3.1 Input Parameters of the Combined System

Following parameters are selected to analyze the performance of the solar assisted combined power and cooling system.

Heat Transfer Fluid in PTC : Therminol VP-1.

No. of PTC in series, N_s : 15.

No. of PTC in parallel, N_p : 10.

Volumetric flow rate in a single PTC, V_{fluid} : 50 L/min.

HRVG inlet pressure, P_{01} : 101.325 kPa.

Temperature drop in HRVG, $(T_{01} – T_{02})$: $0.75 * (T_{out} - T_{in})$.

Turbine exhaust temperature, T_{05} : 315.5 K.

Pump inlet temperature, T_{06} : $(T_{05} – 7)$ K.

Pinch point temperature in HRVG : 20 K.

EARC working pair : NH_3-$LiNO_3$.

EARC generator temperature : 363.15 K.

EARC evaporator temperature : 273.15 K.

EARC condenser temperature : 308.15 K.

EARC absorber temperature : 308.15 K.

Entrainment Ratio in EARC : 0.1429.

Strong NH_3 solution concentration, X_{strong} : 0.51.

Weak NH_3 solution concentration, X_{weak} : 0.44.

Pinch point temperature in EARC generator : 7 K.

6.3.2 Weather data inputs for Dhahran, Saudi Arabia

To evaluate the power and cooling outputs of the integrated cycle, respective solar intensities need to be provided along with other necessary inputs. Monthly average solar intensities are taken from Dabwan et al. [200]. Monthly average wind velocities over the year in Dhahran, Saudi Arabia are taken from Naif et al. [199] as tabulated in the following table.

Table 6.1 Weather data and average daily solar radiation in Dhahran.

Month	Average day in the month	Day in the year	Number of solar hours	Wind Velocity (m/s)	Average daily radiation (kW/m^2)	Average ambient temperature (K)	Average relative Humidity(%)
January	17	17	9	5.2	568.1	292.55	46
February	16	47	9	5.7	602.1	295.25	45
March	16	75	11	5.8	638.8	299.05	45
April	15	105	11	5.9	661.8	299.05	45
May	15	135	11	5.2	669.3	310.15	24
June	11	162	11	5.7	669.5	313.05	22
July	17	198	11	5.7	669.5	314.85	25
August	16	228	11	5.1	665.4	312.45	36
September	15	258	11	4.8	649.0	310.95	27
October	15	288	9	4.7	617.7	305.45	42
November	14	318	9	5.0	578.5	300.05	29
December	10	344	9	4.9	555.9	293.55	43

Two days are selected from summer and winter each to investigate the scenario for varying hourly solar radiation. June-11 and June 21 are the dates for summer, December-10 and January-17 are the dates for winter. Relevant weather data collected and calculated utilizing Renewable Resource Atlas for Dhahran [201] and shown below.

Table 6.2 Hourly solar radiation at Dhahran, Saudi Arabia.

	Average hourly solar irradiation (W/m^2)			
Daily Hours	Jan-17	Jun-11	Jun-21	Dec-10
6:00	3.500	15.250	15.500	3.500
7:00	12.125	164.325	150.000	12.700
8:00	39.050	357.325	343.575	79.900
9:00	208.975	575.950	542.725	243.850
10:00	383.775	747.125	715.375	385.650
11:00	519.850	870.475	839.600	381.050
12:00	544.500	929.450	896.875	410.050
13:00	665.375	936.625	891.200	392.675
14:00	627.125	885.550	842.050	402.575
15:00	402.025	759.150	723.500	305.575
16:00	350.225	594.650	562.600	139.900
17:00	135.425	391.925	370.250	48.6000
18:00	14.800	188.850	178.100	12.4500

Table 6.3 Hourly average wind velocity at Dhahran, Saudi Arabia.

Daily Hours	Average wind velocity (m/s)			
	Jan-17	Jun-11	Jun-21	Dec-10
6:00	5.8050	4.5425	4.9350	4.3550
7:00	6.9200	4.5525	4.5700	3.8400
8:00	6.7000	4.4150	4.8350	4.0675
9:00	7.2350	6.0300	5.2875	3.8300
10:00	6.7375	6.2425	5.0975	4.3750
11:00	6.9725	6.6750	5.4200	4.2900
12:00	6.0275	6.6350	5.2525	3.7600
13:00	6.6725	7.5600	5.0375	3.9375
14:00	6.2925	8.8450	4.7275	3.8550
15:00	5.6150	9.4225	4.8100	4.4275
16:00	6.8675	9.6325	6.4650	4.5650
17:00	6.6500	8.6050	6.3750	4.2575
18:00	6.4250	7.9475	5.7100	3.9825

Table 6.4 Hourly average ambient temperature at Dhahran, Saudi Arabia.

Daily Hours	Average ambient temperature (°C)			
	Jan-17	Jun-11	Jun-21	Dec-10
6:00	288.050	303.800	306.375	291.375
7:00	287.975	304.900	306.500	290.925
8:00	288.000	306.950	307.475	290.825
9:00	288.450	309.125	308.850	291.775
10:00	289.700	311.375	311.875	293.075
11:00	291.400	313.350	313.725	294.750
12:00	292.175	314.175	314.825	296.500
13:00	292.775	314.525	316.025	298.150
14:00	293.175	315.125	316.875	298.925
15:00	292.975	315.000	316.625	298.925
16:00	292.675	314.600	315.625	298.275
17:00	291.975	313.550	313.625	297.475
18:00	291.075	312.550	313.125	295.900

6.4 Results and Discussions on the Combined Power and Cooling System

The performance of the combined power and cooling system is analyzed and discussed in this section. Analysis on first subsection 6.4.1 concentrates on the hourly and monthly variation of performance of the combined cycle, selecting the fluid R134a with appropriate input parameters and weather data outlined in section 6.3. The second subsection 6.4.2 analyzed the performance of the combined system using different fluids at their optimum operating conditions.

6.4.1 Hourly and Monthly Performance Analysis of the Combined System

Utilizing the weather data for the parameters mentioned in the previous section, hourly and monthly performance of the combined system is analyzed for Dhahran, Saudi Arabia. Following input parameters were used for the analysis along with the appropriate parameters mentioned in section 6.3.

Working fluid in ORC	:	R134a
Turbine Inlet pressure, P_{04}	:	2750 kPa.
Turbine inlet temperature, T_{04}	:	362.8 K.
Turbine exhaust temperature, T_{05}	:	315.5 K.

An average day in a month is selected to represent the month for the simplicity of calculation as seen from Table 6.1. HTF temperature at three different positions are calculated, namely at the PTC outlet (T_{01}), HRVG outlet (T_{02}) and PTC inlet (T_{03}).

Using the weather data of Dhahran from Table 6.2 - Table 6.4 , hourly variation of temperatures at different positions of the PTC HTF circuit are calculated for June-11, June-

21, December-10 and January-17. Respective solar intensity, wind velocity and ambient temperature are used to calculate each set of data. Following figures (Figure 6.3 - Figure 6.5) are demonstrating the resulting hourly and yearly average temperatures in the PTC HTF circuit. Both hourly and monthly variation of the temperatures are shown in the following figures for the three locations.

As observed from Figure 6.3, June-11 had the highest PTC outlet temperature recorded, 679.8 K at 13:00 followed by 644.6 K in June 21 at 12:00. In winter time, the month January showed a better temperature rise than in December. In winter time the peak was observed in between 12:00 to 13:00. While progressing to summer the peak was seen to shift itself more towards 13:00 and so on, in between 14:00 to be precise. Then the temperature falls due to reduced irradiation. In terms of monthly average, June and July had the highest PTC outlet temperature due to the higher solar irradiation at that time. A similar trend is observed for HRVG outlet and PTC inlet temperatures in the consecutive figures.

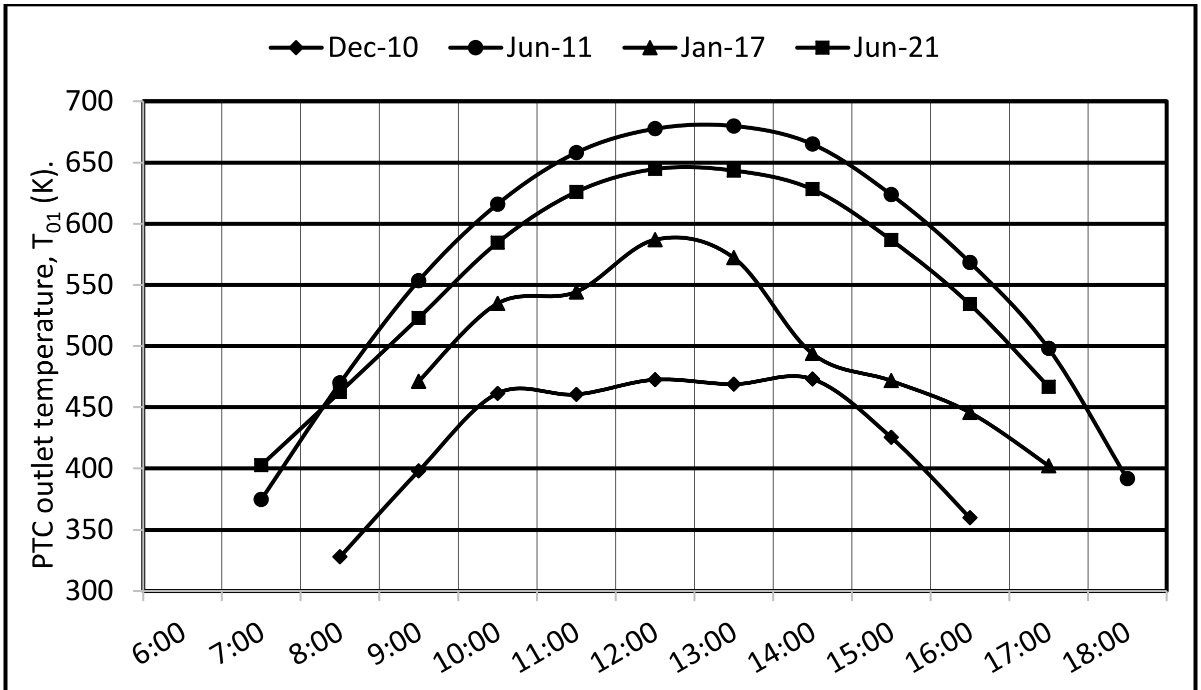

(a) Hourly variation of PTC outlet temperature.

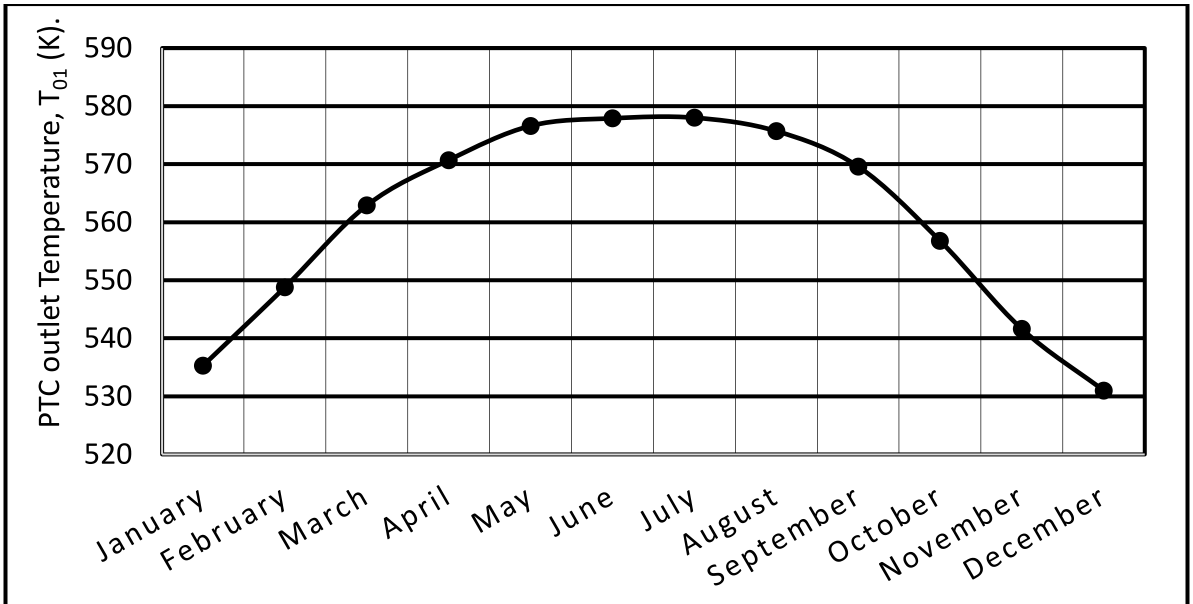

(b) Monthly variation of PTC outlet temperature

Figure 6.3 Hourly and monthly variation of PTC outlet temperature in the combined system for Dhahran, Saudi Arabia.

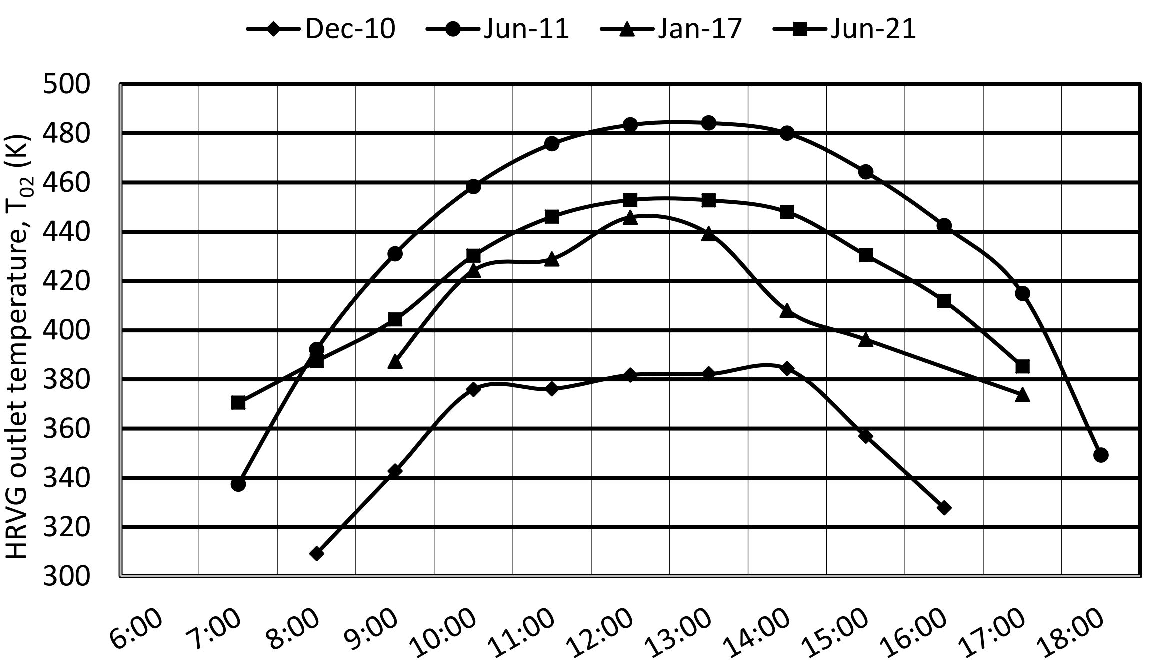

(a) Hourly variation of HRVG outlet temperature

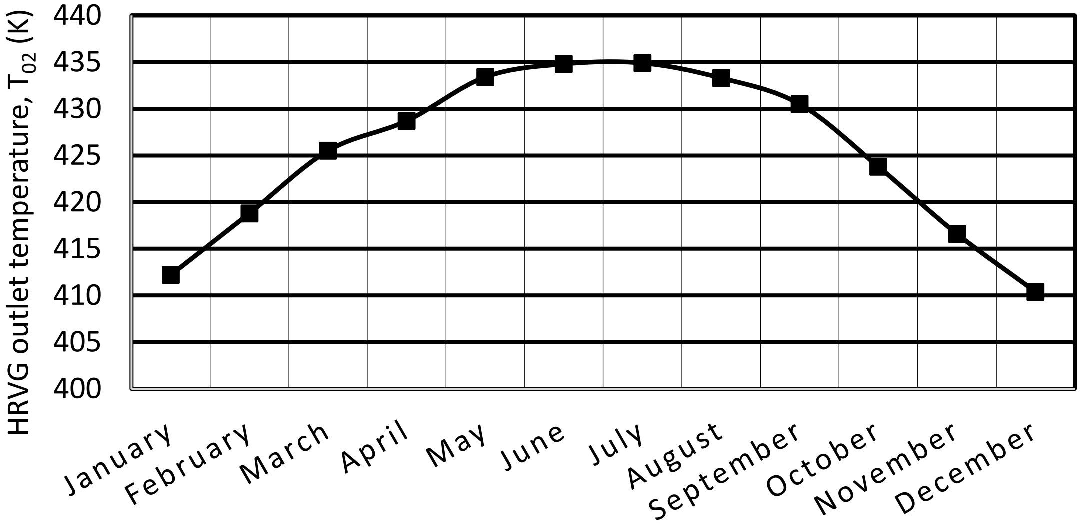

(b) Monthly variation of HRVG outlet temperature.

Figure 6.4 Hourly and Monthly variation of HRVG outlet temperature in the combined system for Dhahran, Saudi Arabia.

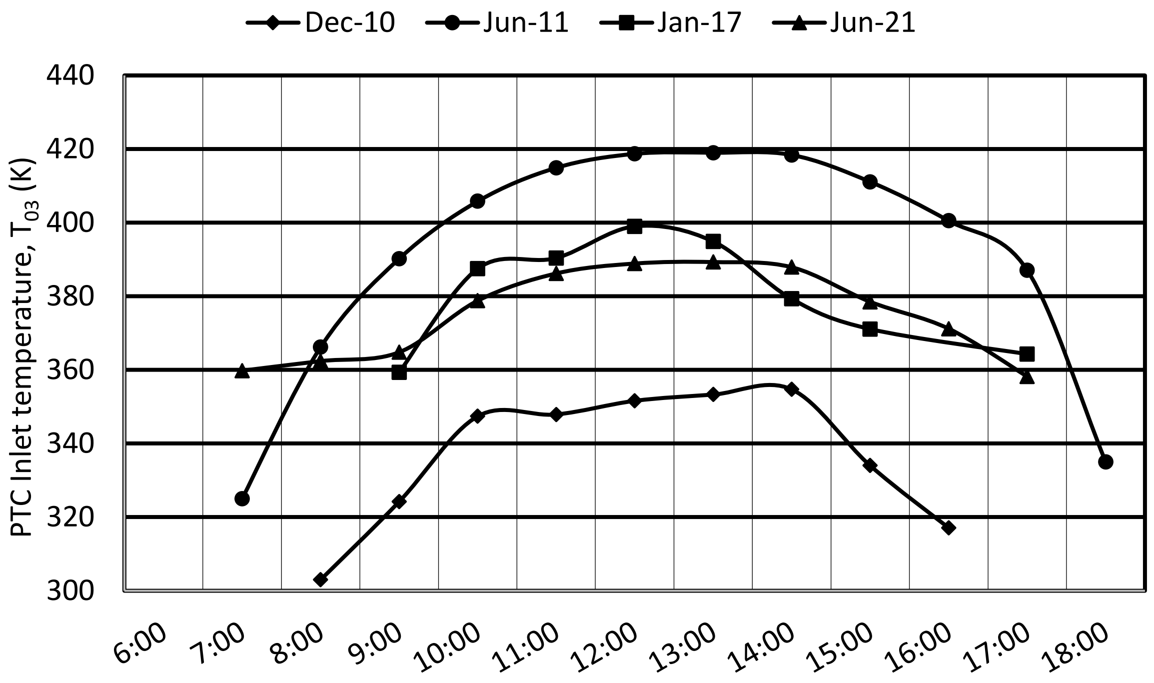

(a) Hourly variation of PTC inlet temperature.

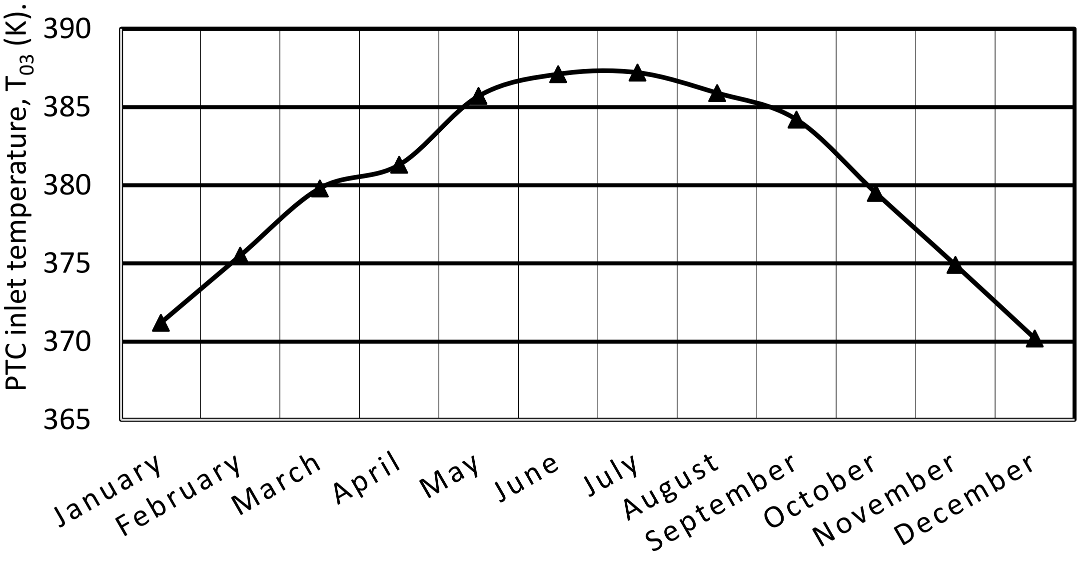

(b) Monthly variation of PTC inlet temperature.

Figure 6.5 Hourly and Monthly average variation of PTC inlet temperature in the combined system for Dhahran, Saudi Arabia.

Daily and monthly variation of Solar energy and incoming solar exergy are calculated as shown in the following figures (Figure 6.6 - Figure 6.8).

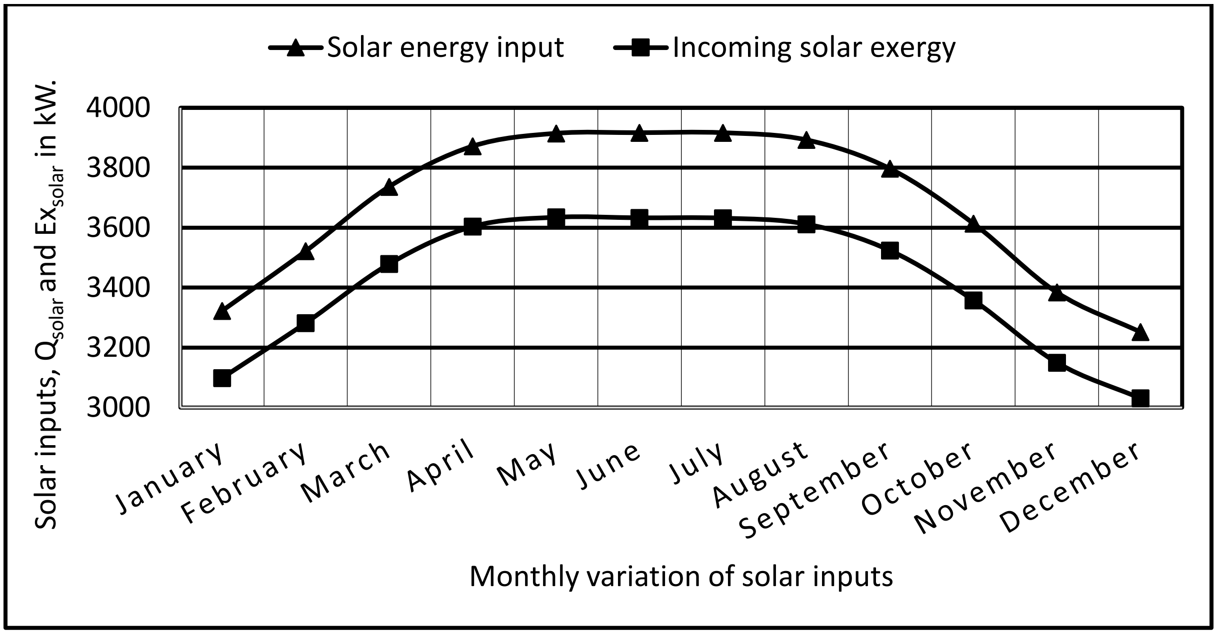

Figure 6.6 Monthly variation of solar inputs in the combined system for Dhahran, Saudi Arabia.

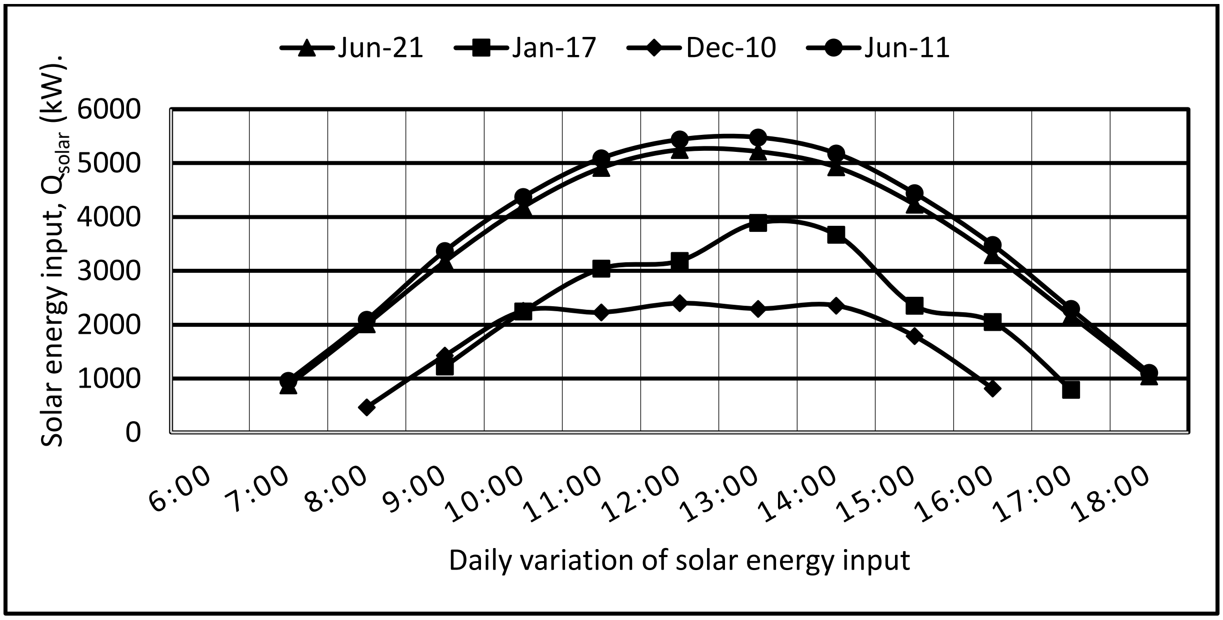

Figure 6.7 Daily variation of solar energy input in the combined system for Dhahran, Saudi Arabia.

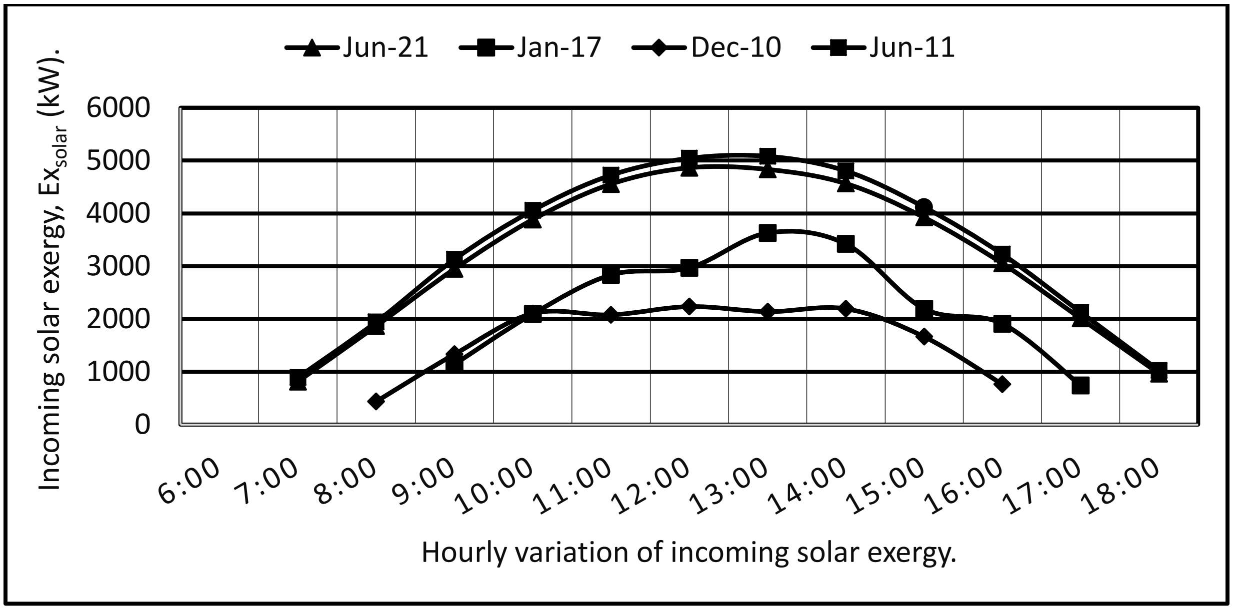

Figure 6.8 Monthly variation of incoming solar exergy in the combined system for Dhahran, Saudi Arabia.

Hourly and monthly averages of net ORC power output and EARC cooling output are calculated for Dhahran as shown in Figure 6.9 and Figure 6.10 respectively. As the solar intensity goes higher in June-July outputs are found to be higher in comparison to rest of the months. During winter time, namely, December-January the output is lower due to reduced solar intensity.

The highest monthly solar intensity 669.5 W/m^2 is observed in June and July, lowest 555.9 W/m^2 in December with respective ambient temperature. The power available ranged from 175 kW-214 kW on monthly average, whereas in the day time it varied over the range of 22.6 kW – 311.5 kW. Cooling output over the year varied from 347.9 kW – 419.5 kW over the year and daily output varied over a wide range of 49.31 kW - 588.9 kW. It is evident from the figures that higher power and cooling outputs resulted from the higher solar irradiation. In both hourly and monthly variations in outputs, power and cooling are higher for summer time in comparison to winter due to increased solar irradiation. The effect of wind velocity and ambient temperature is not that significant in comparison to the solar irradiation.

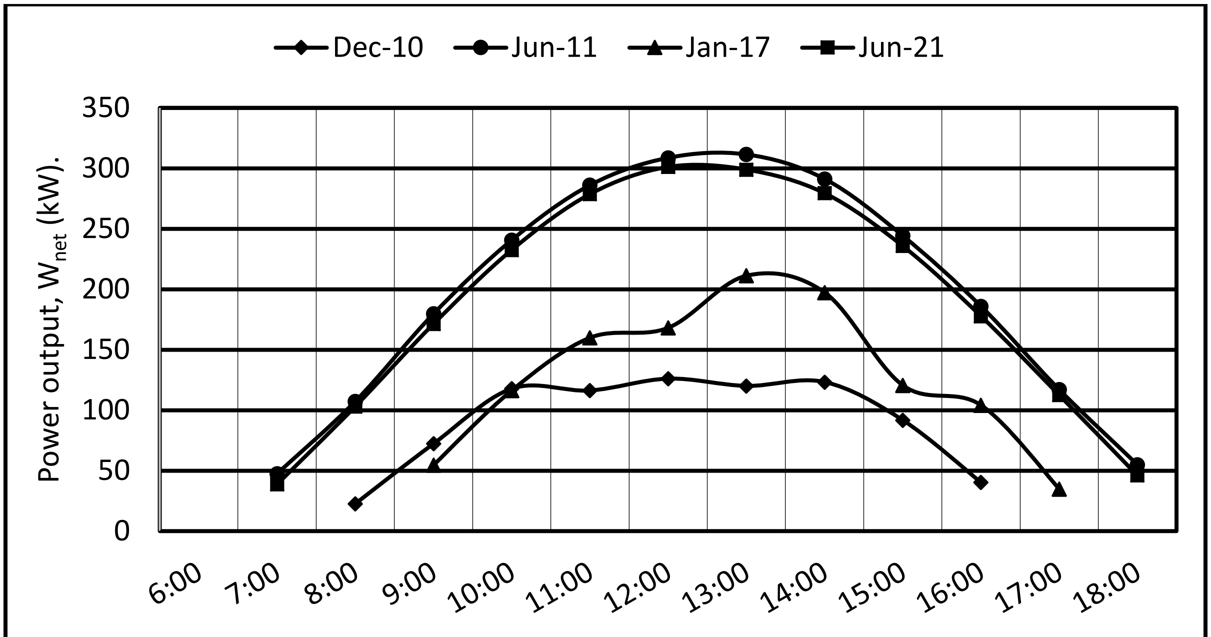

(a) Hourly variation of power output.

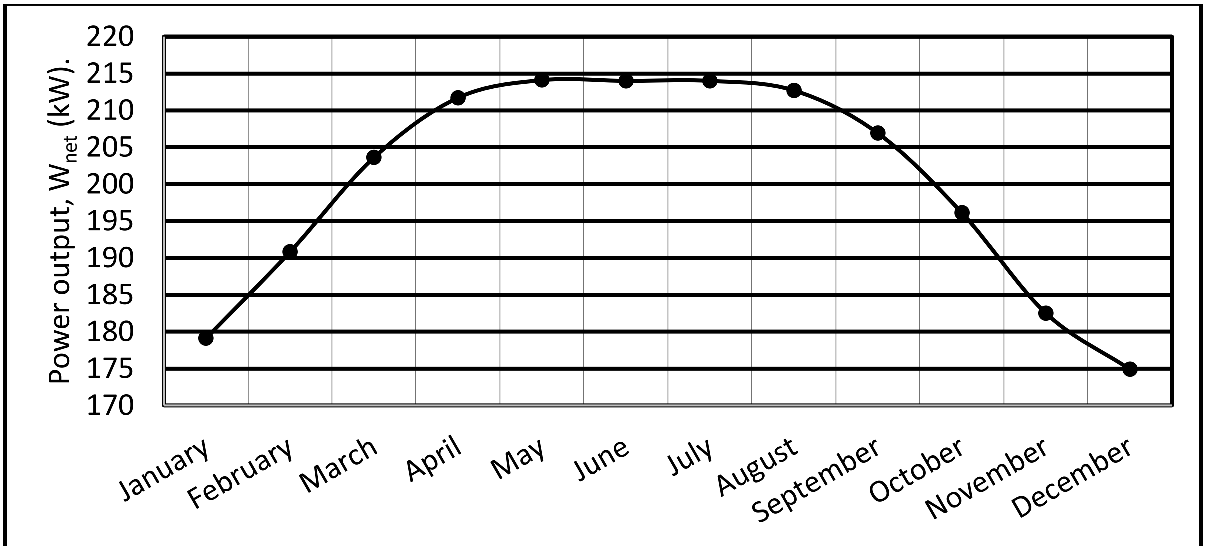

(b) Net power output over the year.

Figure 6.9 Hourly and monthly average power outputs in the combined system for Dhahran, Saudi Arabia.

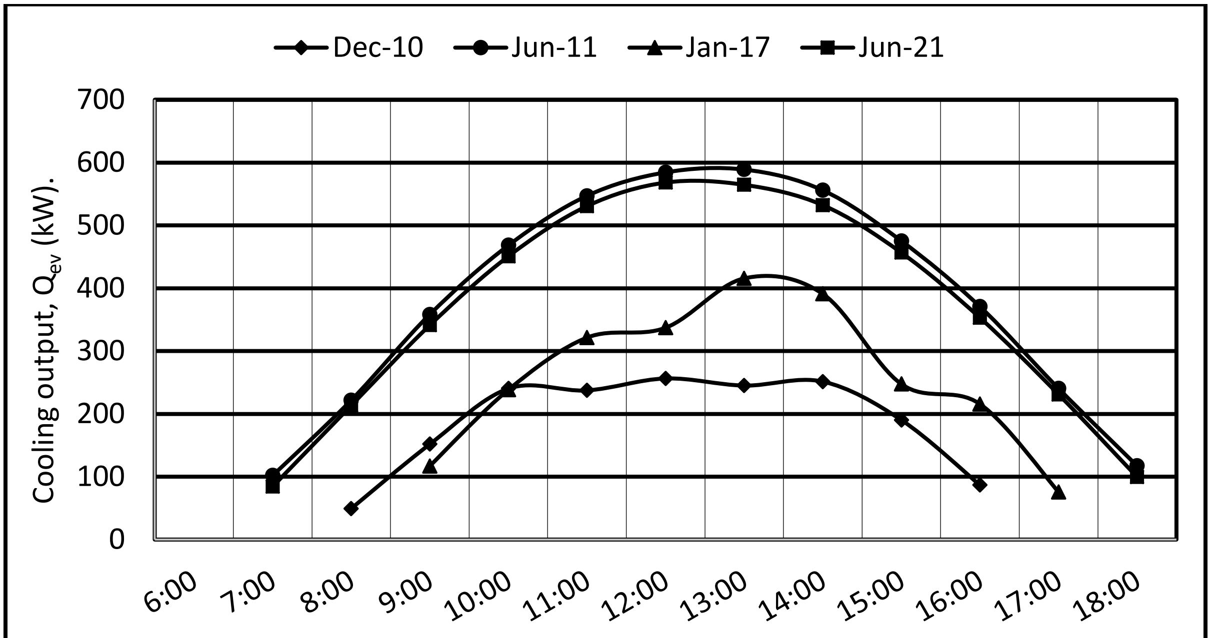

(a) Hourly vaiation of cooling output.

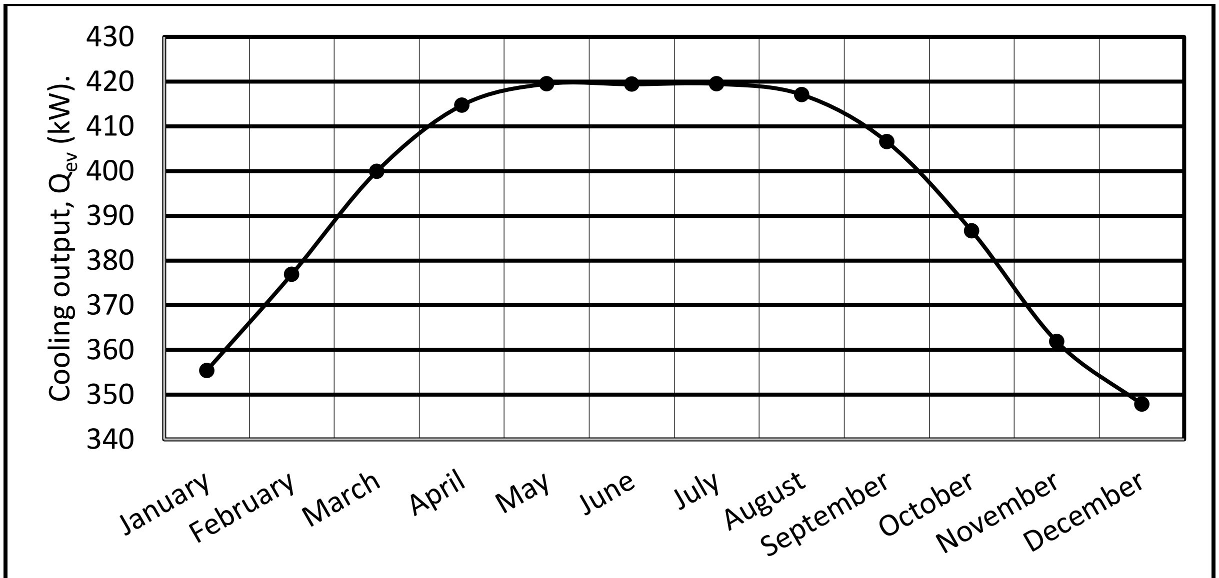

(b) Cooling output over the year.

Figure 6.10 Hourly and monthly cooling outputs in the combined system for Dhahran, Saudi Arabia.

Figure 6.11 and Figure 6.12 are representing the system performance factor and exergy efficiency of the combined power and cooling cycle. Solar intensities, wind velocities and respective ambient temperatures are taken into account for the analysis.

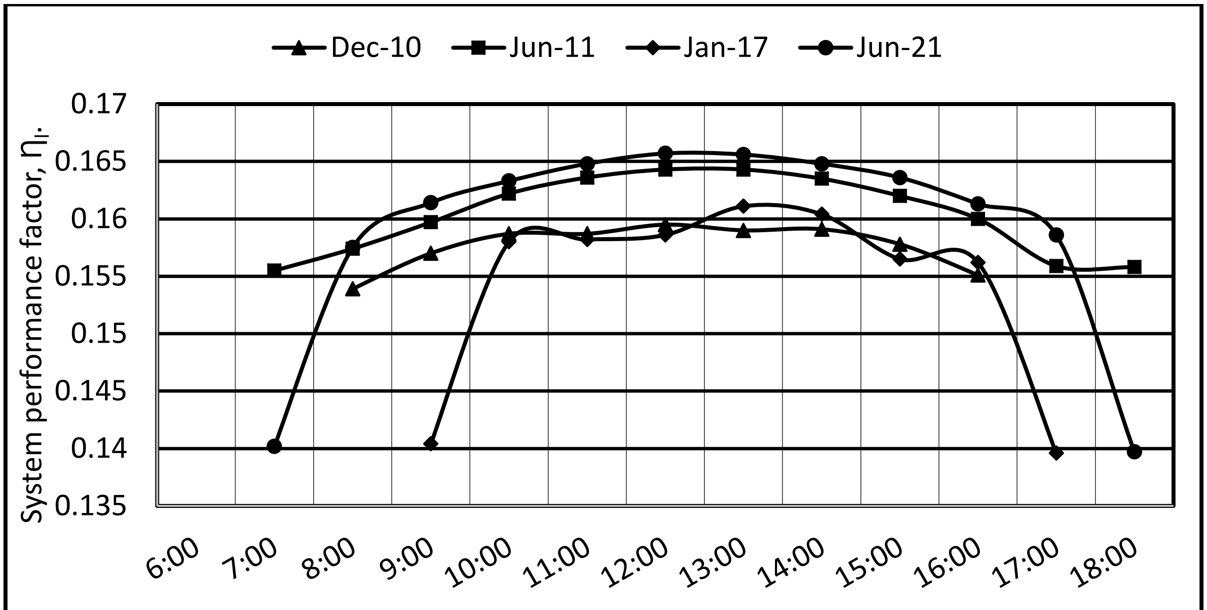

(a) Hourly variation of system performance factor.

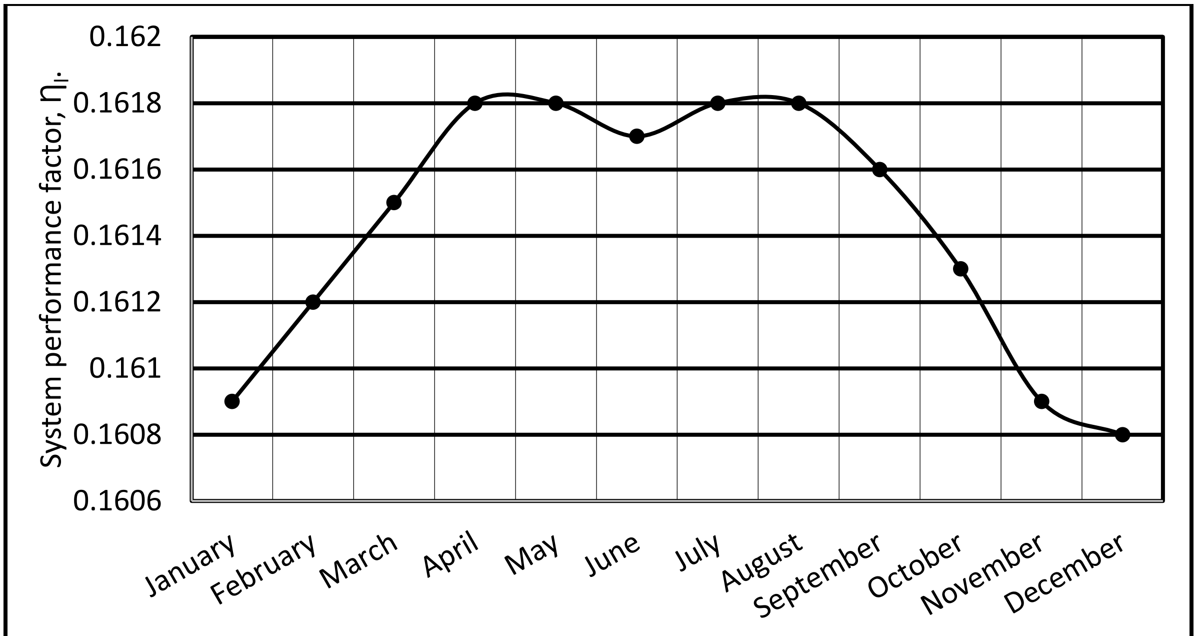

(b) Monthly variation of system performance factor.

Figure 6.11 System performance factor of the combined system for Dhahran, Saudi Arabia.

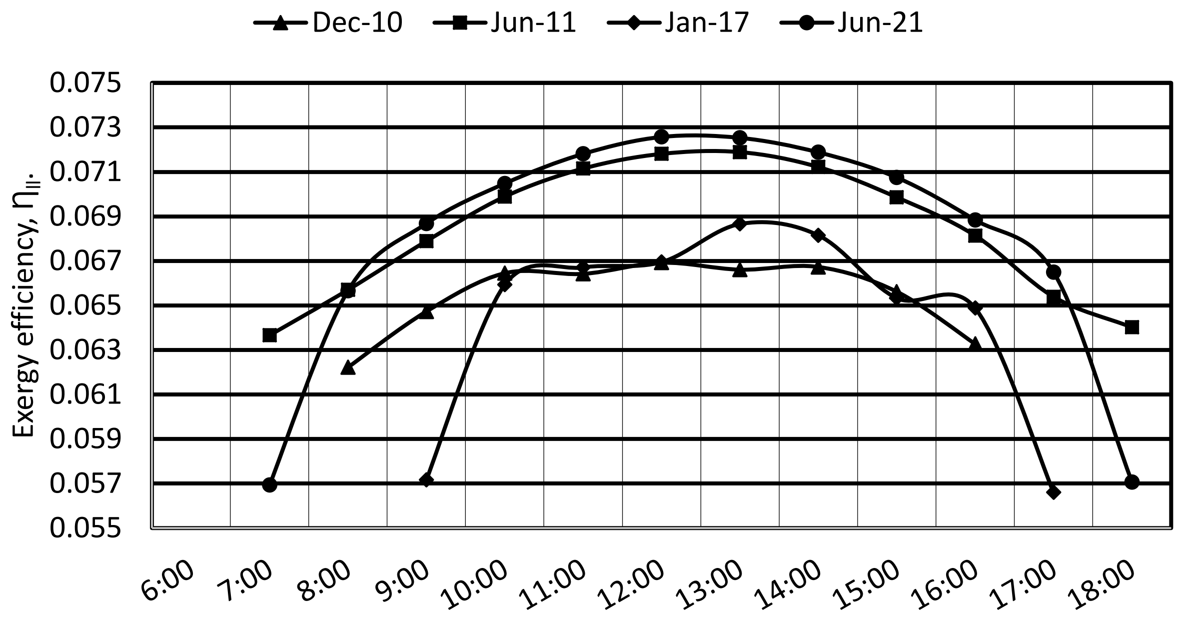

(a) Hourly variation of exergy efficiency.

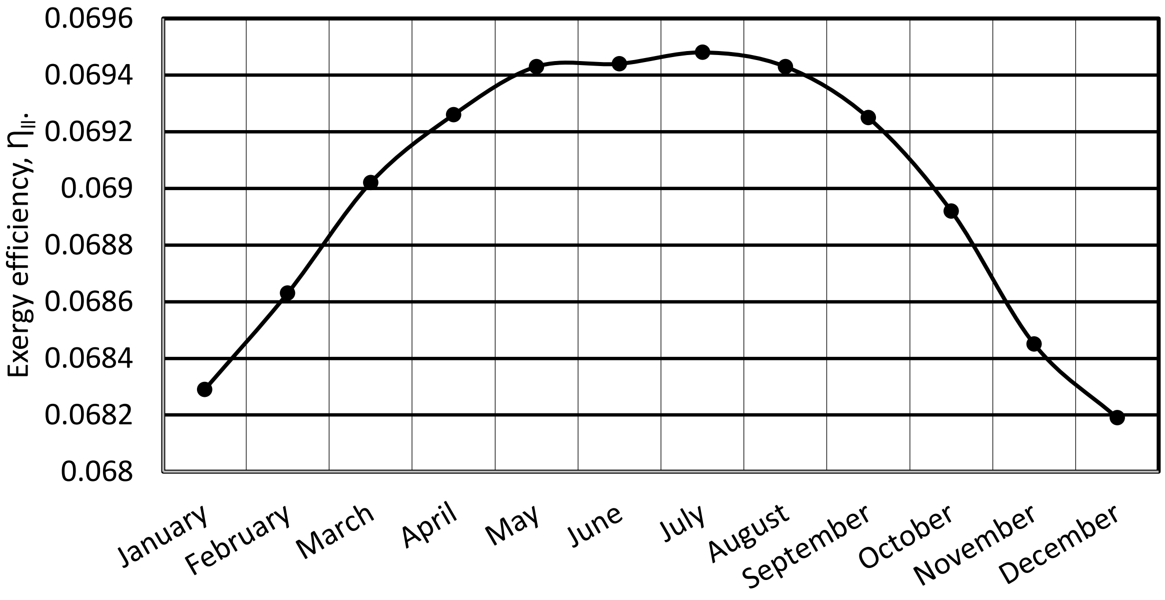

(b) Monthly variation of exergy efficiency.

Figure 6.12 Exergy efficiency of the combined system for Dhahran, Saudi Arabia.

System performance factor was found to be 16.08 % - 16.18 % of the monthly variation curve. The highest average solar irradiation for the month of July was 669.5 W/m^2 and lowest for the month of December with 555.9 W/m^2. The change in average irradiation in between the months are not that much, that is why system performance factor is not changing that much over the year as seen from Figure 6.11. But the due to a significant difference of irradiation over a day, in the curves of daily variation, system performance factor varies significantly. The lowest value was observed to be 13.96% for January-17 at 7:00 and 17:00. In winter, highest performance was 16.11% in January 17 at 13:00. The overall highest performance of 16.57% was observed in June 21 at 12:00. The Exergy efficiency of the combined system showed similar characteristics. Monthly variation of output was not so high when compared to daily variation due to the solar irradiation. Monthly variation of exergy efficiency was 6.82% - 6.95% and for daily variation it was found to be 5.69% -7.25 %. It should be noted that the analysis did not take into account the output conditions at very low irradiation values below 80 W/m^2.

A daytime at 12:00 is selected to make a comparative analysis of the efficiencies of individual cycles and the combined cycle in terms of energy and exergy analysis selecting the fluid R134a. Figure 6.13 is showing the efficiencies of the individual cycles and Figure 6.14 for the overall efficiency of the combined cycle.

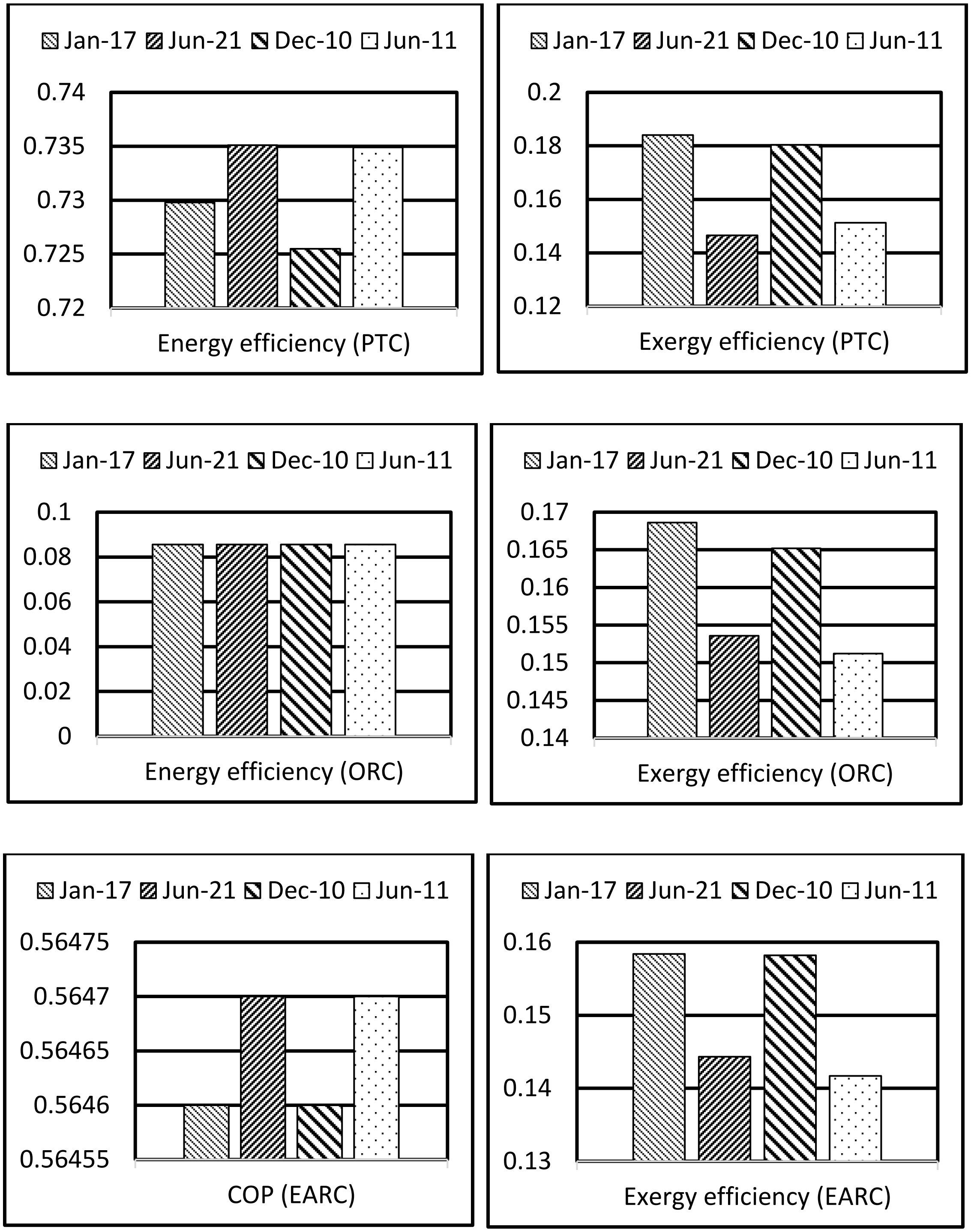

Figure 6.13 First and second law efficiency of individual cycles at 12:00 in the combined system operation.

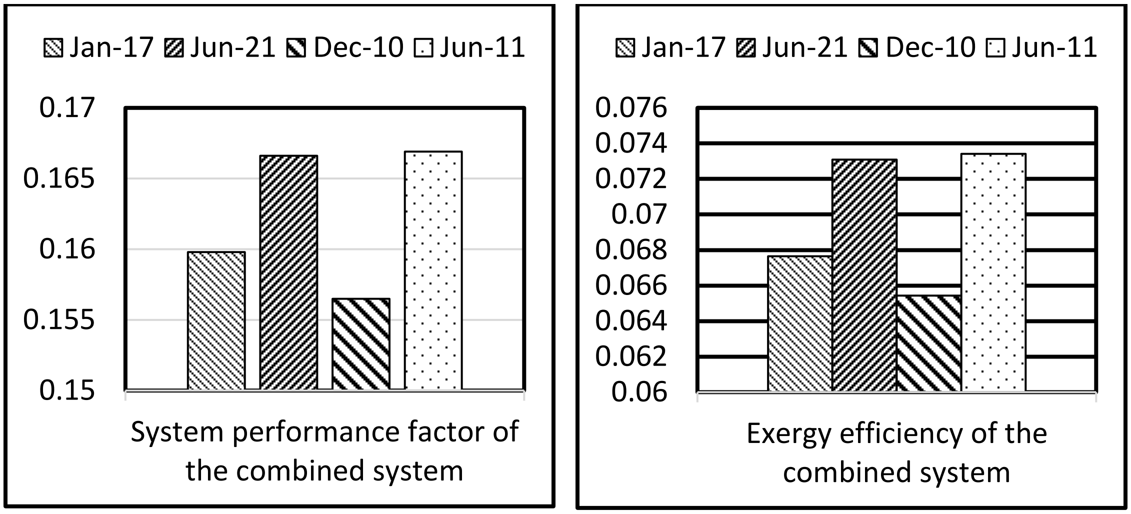

Figure 6.14 System performance factor and exergy efficiency of the combined system at 12:00.

The contribution of the individual cycles for the total exergy destructions with respect to incoming solar irradiations are shown in Figure 6.15 for the designed combined system. PTC is found to be the one mostly responsible for exergy destruction, followed by ORC and EARC. Contribution of exergy destruction of PTC was significantly higher than both ORC and EARC combined. It was gradually reduced from over 80% to 60% with higher solar irradiation. Both ORC and EARC contribution on exergy destruction in the combined cycle were getting higher for higher irradiation. Exergy destruction in HRVG of ORC was found to be the main reason for this sharp increase in the overall exergy destruction of the power cycle.

-

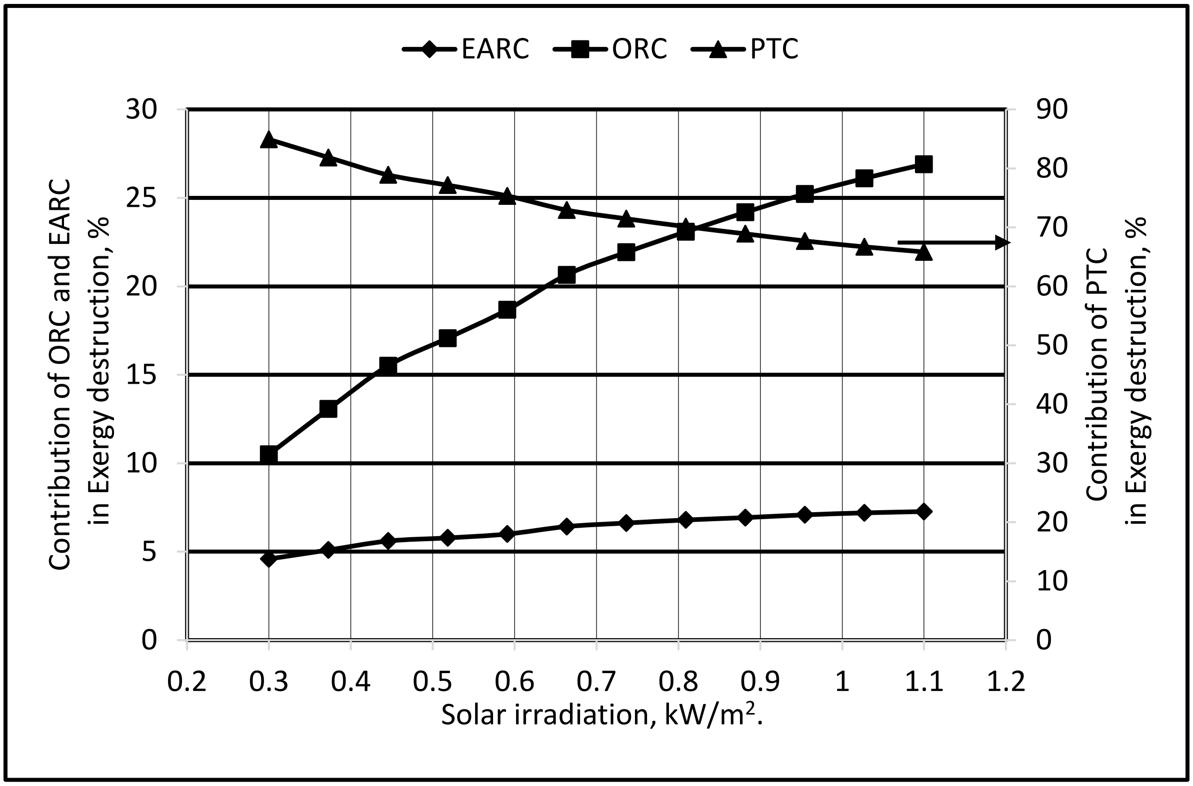

Figure 6.15 Exergy destruction of individual cycles in the combined system.

6.4.2 Performance of the Combined System Using Various ORC Fluids

In this section, performance of the combined system using different ORC fluids is analyzed. Since every ORC fluid has its distinct operating temperature and pressure at which the fluid works on optimum level, the performance of the combined system is calculated at optimum temperatures and pressures of the individual fluids. For example, as observed previously, Toluene has an optimum temperature of 550 K and a pressure of 2500 kPa at which it works at maximum efficiency. So, the performance of the combined cycle is calculated at this optimum temperature and pressure when Toluene was used as the ORC fluid. Respective optimum temperatures and pressures are used to calculate the outputs of the combined system as shown below in Figure 6.16 -Figure 6.20.

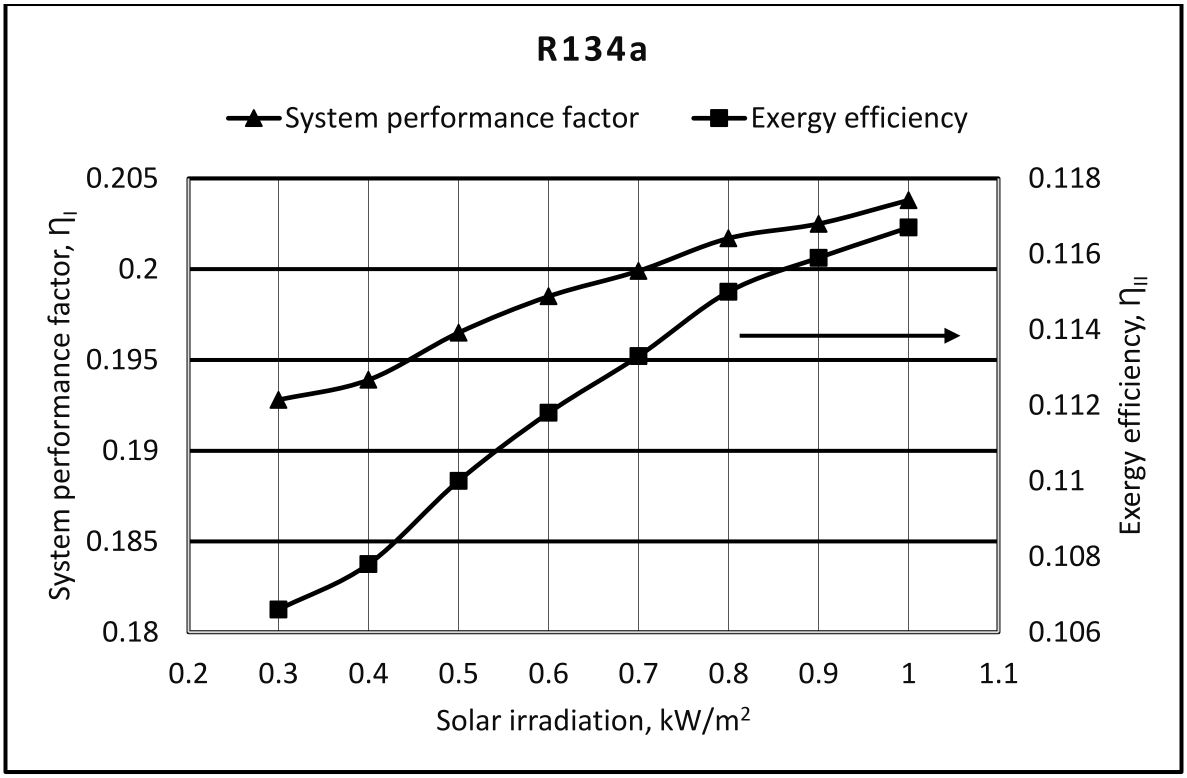

Figure 6.16 Performance of the combined system using R134a as ORC fluid at turbine inlet temperature of 440 K and pressure of 10000 kPa.

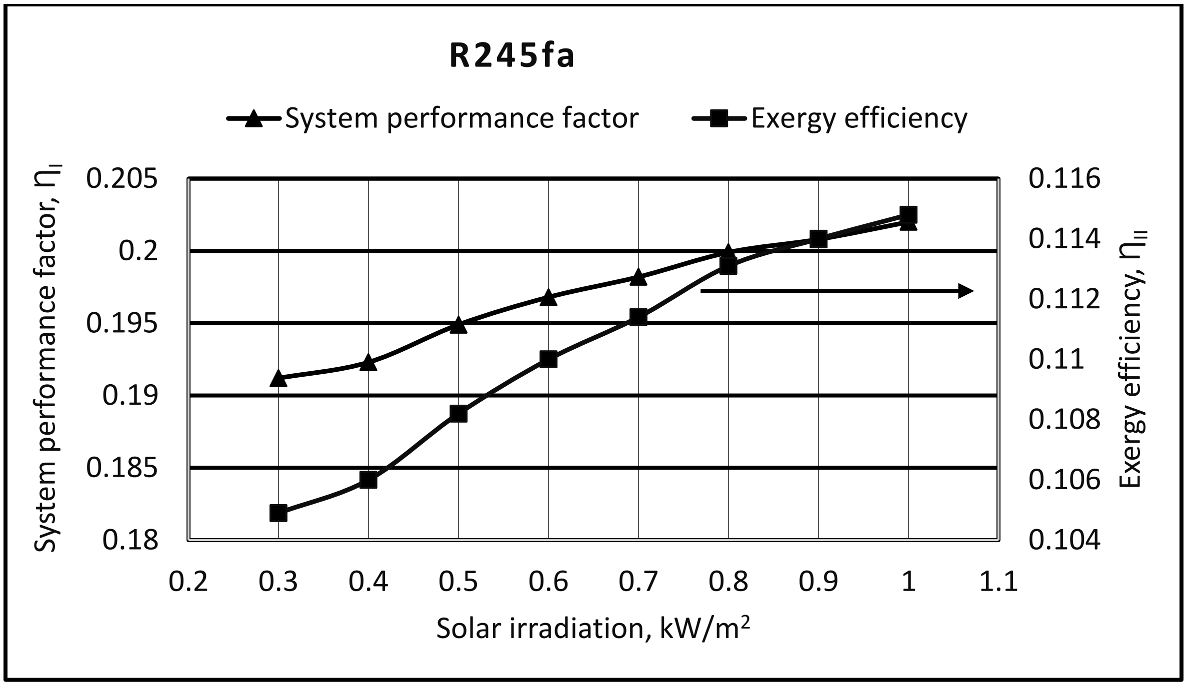

Figure 6.17 Performance of the combined system using R245fa as ORC fluid at turbine inlet temperature of 440 K and pressure of 4500 kPa.

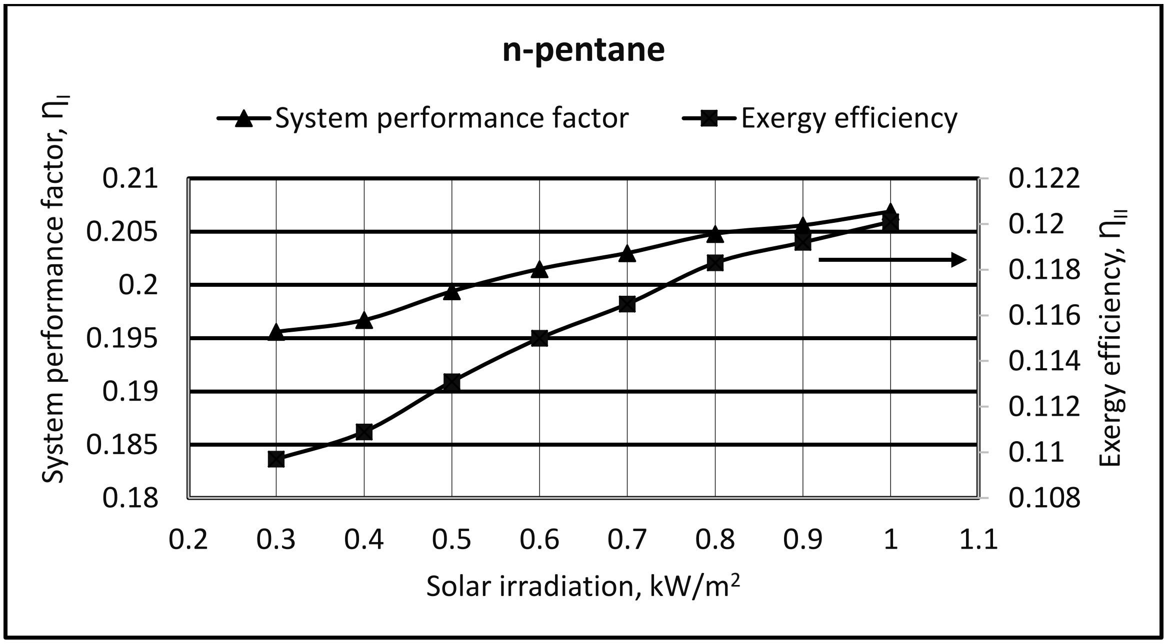

Figure 6.18 Performance of the combined system using n-pentane as ORC fluid at turbine inlet temperature of 460 K and pressure of 3000 kPa.

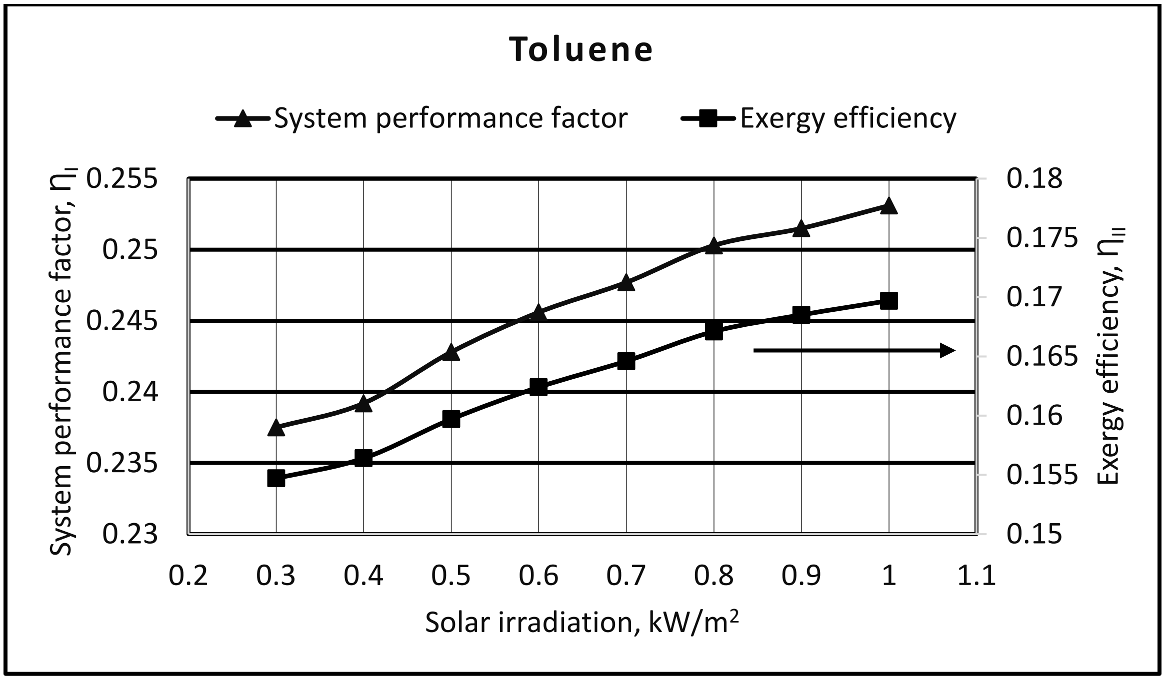

Figure 6.19 Performance of the combined system using Toluene as ORC fluid at turbine inlet temperature of 550 K and pressure of 2500 kPa.

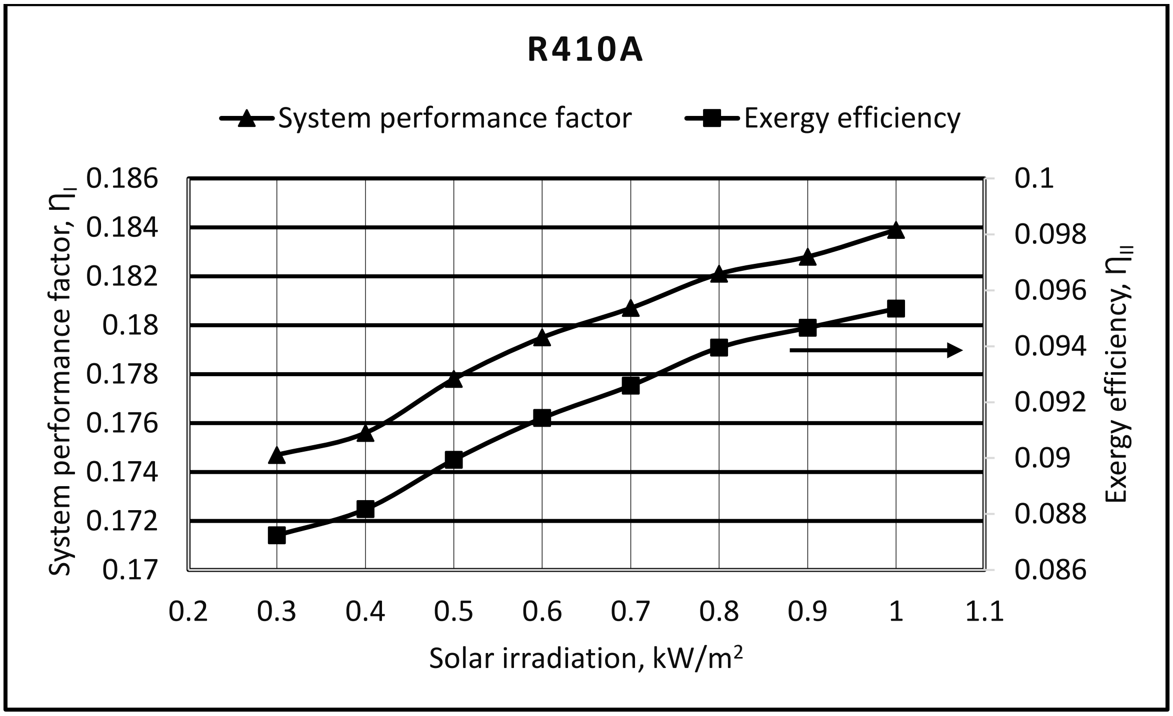

Figure 6.20 Performance of the combined system using R410A as ORC fluid at turbine inlet temperature of 420 K and pressure of 12000 kPa.

From the analysis above, it is observed that Toluene showed the best performance in terms of system performance factor and exergy efficiency. The system performance factor of Toluene is found to be 25.31 % at highest solar irradiation of 1 kW/m^2 whereas for other ORC fluids, system performance factors were found to be 17-20%. The Exergy efficiency of the combined system using Toluene has reached up to 17%, while the rest of the ORC fluids exhibited 8-12% exergy efficiency.

To have a better understanding of the comparison of the performances of different ORC fluids in combined power and cooling system, system performance factors of different fluids are plotted in the following Figure 6.21 at various solar irradiation. It should be noted that the pressure and temperature of each fluids are different as the optimum conditions are used while deriving the efficiencies.

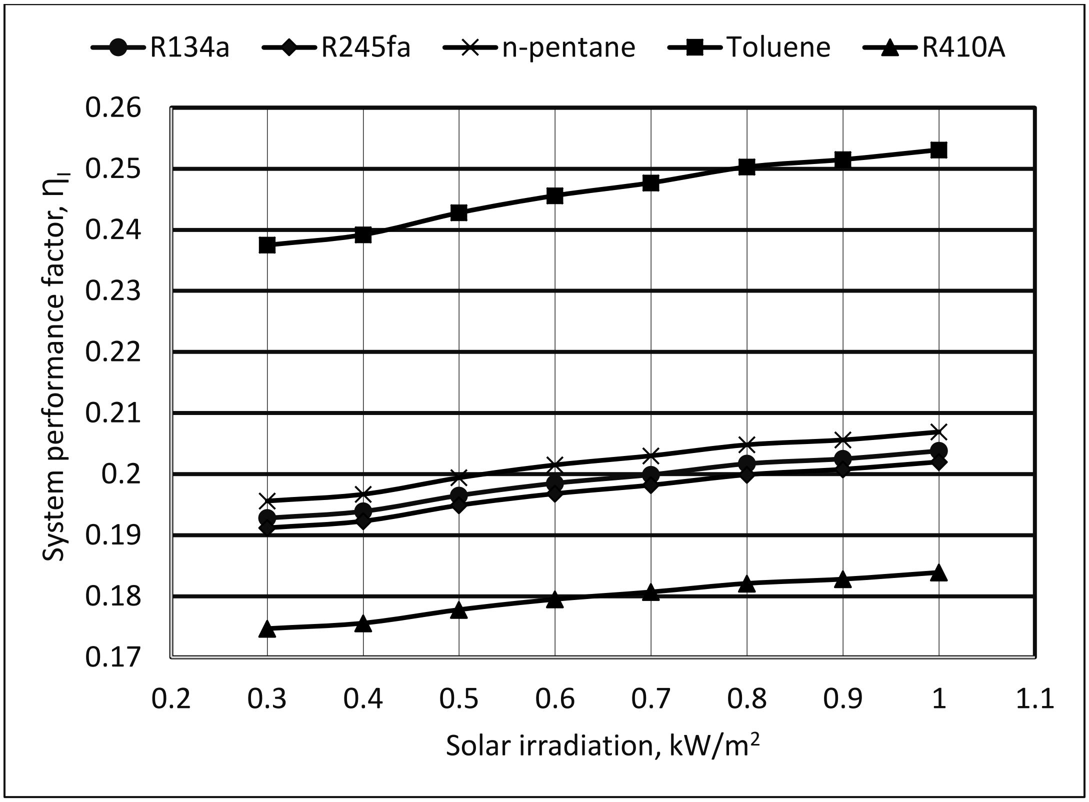

Figure 6.21 Comparison of System performance factors in the combined system using different ORC fluids at their individual optimum operating conditions.

Similarly, exergy efficiency of the combined system using different ORC fluids is also plotted at various solar irradiations in Figure 6.22.

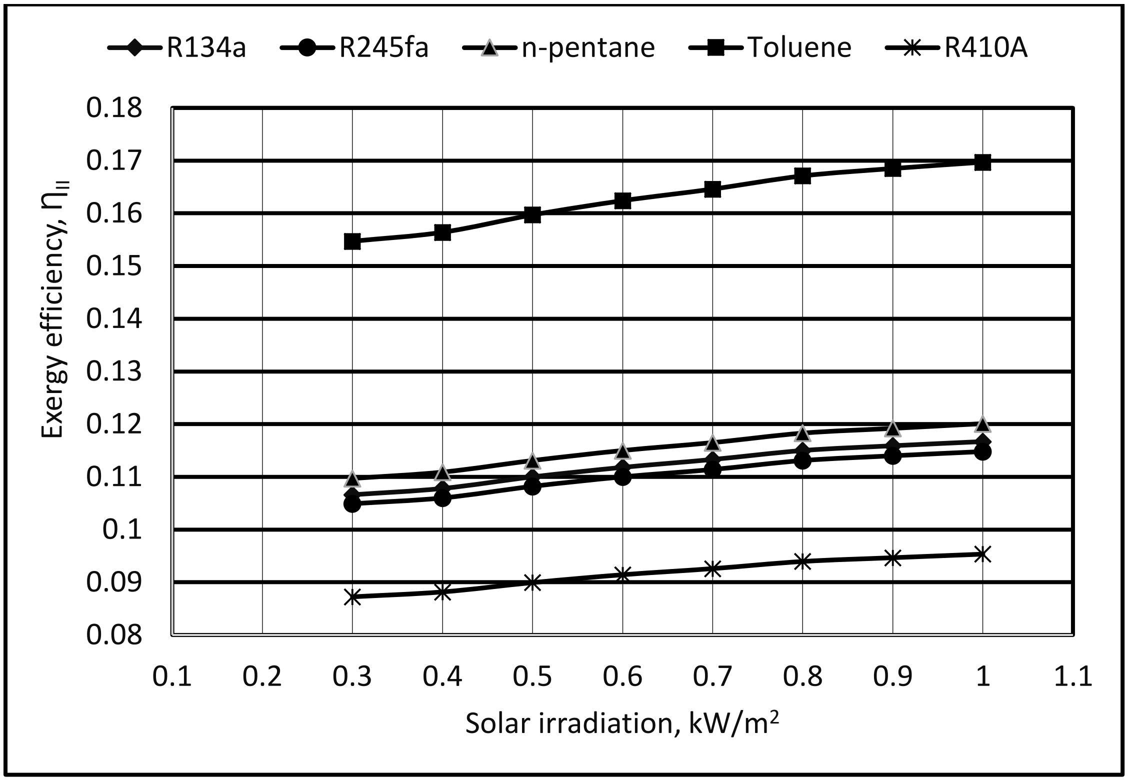

Figure 6.22 Comparison of exergy efficiency in the combined system using different ORC fluids at their individual optimum operating conditions.

From Figure 6.21 and Figure 6.22, it can be visualized that Toluene showed superior performance in both cases. R134a, R245fa and n-pentane showed almost similar performances whereas, R410A was proven to be the least efficient fluid among the ORC fluids used in the combined power and cooling system.

6.5 Concluding Remarks

System performance factors and exergy efficiencies were derived for different fluids along with the monthly and hourly analysis of performance for the combined cycle. R134a was selected to analyze the hourly and monthly analysis of the combined system. System performance factor of the combined system varied from 13.96% - 16.57% as observed from the hourly analysis while for exergy efficiency, it was found in the range of 5.69% - 7.25%.

Toluene showed superior performance exhibiting system performance factor of 25.31% and with an exergy efficiency of 17%. R134a, R245fa and n-pentane showed almost similar performances whereas, R410A was proven to be the least efficient among the ORC fluids used in the combined power and cooling system.

PTC accounted for 60-80% of the total exergy destruction depending on the solar irradiation followed by ORC and EARC. ORC power output is observed to be higher in Summer and lower in winter with decreasing solar intensity. A similar trend is observed in EARC refrigeration output. The low solar intensity caused the PTC inlet temperature of HTF to fall over the time since no thermal energy storage or external heat sources are integrated in this steady state model. So generated heat by PTC was found to be less over time in a day as found from the hourly variation of the power and cooling outputs in Figure 6.9 and Figure 6.10. For stable operation with no fluctuations in output, heat storage [193], [206] or auxiliary heat source accessories like biomass boilers [157] needs to be added to the system to provide uninterrupted supplies.

CHAPTER 7

CONCLUSIONS AND RECOMMENDATIONS

7.1 Conclusions

As the civilization is thriving more towards technological superiority, a growing concern is developed for the implications of carbon-based fossil fuel. Everyday new renewable energy technologies are adding to the grids with a greater speed. In relation to the demand and the environmental concern, a study on solar assisted power and cooling cycle is performed to examine the performance of the existing cycles with solar energy as the input heat source.

Following findings are reported from the study of the parabolic trough collector (PTC),

- PTC energy efficiency (η_{en}) was found to be in the range of 69% - 73.5% within 333 K – 513 K temperature range. Higher inlet temperature reduced the thermal efficiency of the PTC. An increase in fluid flow rate decreased the thermal performance of the system.
- PTC exergy efficiency increased from 12% to 32% and an increasing trend was observed when temperature raised from 333 K to 513 K. It was decreasing with increased fluid flow rate.
- Exergy destruction in PTC was occurring mostly in the process of solar energy received in the absorber from the sun. It is found to be multiple times higher than the exergy destruction caused by the heat transfer process in between the receiver and the fluid inside of it.

Following findings are reported from the study of Organic Rankine Cycle (ORC),

- It was found that every ORC fluid has an optimum pressure and temperature level for a certain solar irradiation level at which it works better than other fluids in ORC. R134a was found to be a suitable fluid at lower turbine inlet temperatures since it exhibited a thermal efficiency of 8.55% at turbine inlet temperature of 362.8 K and with a pressure of 2750 kPa whereas thermal efficiencies of other fluids were less than 5% at that temperature and pressure. R134a also showed superior performance showing the highest exergy efficiency of 21.84% in ORC at that optimum operating condition.
- Toluene was found to be the most suitable fluid at higher turbine inlet temperature. At turbine inlet temperature of 550 K and a pressure of 2500 kPa, Toluene exhibited thermal efficiency of 23.5 %, while the exergy efficiency was found to be 62.89 %.
- HRVG was found to be the highest contributing component in terms of exergy destruction followed by the condenser.

Following findings are reported from the study of Ejector-Absorption Refrigeration Cycle (EARC),

- Introduction of the ejector resulted better performance of the EARC in comparison to conventional ARC. COP was higher for EARC than ARC in all of the temperature ranges.

- Ejector significantly reduced the power consumption in the pump. ARC pump power consumption is found to be multiple times higher than EARC.
- EARC generator temperature and solution heat exchanger (SHX) influence the COP and exergetical performance of the EARC.

The findings for the combined power and cooling cycle can be summarized as follows:

- In hourly and monthly performance of the combined cycle using R134a as ORC fluid, system performance factor varied from 13.96% - 16.57%, while for exergy efficiency, it was found in the range of 5.69% - 7.25%. Highest power and cooling output were observed during the summer due to higher solar irradiation which gradually reduced with the lower irradiation of the sun. Highest outputs of the power and cooling cycles were observed in between 11.00 AM to 1.00 PM.
- When different ORC fluids were used in the combined power and cooling system, Toluene showed the best performance in terms of system performance factor and exergy efficiency. The system performance factor of Toluene is found to be 25.31 % at highest solar irradiation of 1 kW/m^2 whereas for other ORC fluids, system performance factors were found to be 17-20%. The Exergy efficiency of the combined system using Toluene has reached up to 17%, while the rest of the ORC fluids exhibited 8-12% exergy efficiency.
- PTC accounted for 60-80% of the exergy destruction depending on the available irradiation followed by ORC and EARC in the combined system.

7.2 Recommendations and Future Work

- The introduction of thermal storage to the PTC system can enable the system to have a stable inlet temperature for the PTC. It will also store the energy to utilize under low solar radiation.
- A time dependent dynamic simulation can be made for the PTC with TES which can analyze the change of outlet temperature of PTC with varying solar irradiation over a certain time period. It will make the comparison feasible in between the systems incorporating TES and without it.
- In lower solar irradiation period to avoid power cut, PTC can be coupled with some auxiliary heat source like solar biomass or similar renewable heat source for uninterrupted power and cooling output.
- Instead of PTC, LFR can be used and their performance can be put in comparison.
- NH_3-NaSCN working pair can be used in ARC and a comparative analysis can be made with its performance relative to NH_3-$LiNO_3$ and other conventional working pairs.
- A compressor in the Refrigeration cycle can be introduced and its performance can be analyzed.
- The existing model can be implemented in a real experimental set up and its performance can be examined.

BIBLIOGRAPHY

[1] Kalogirou, S. A., 2016, *Advances in Solar Heating and Cooling*, Woodhead Publishing Series in Energy: Number 102, Cambridge, MA 02139, USA, pp.63-80.

[2] Lashin, A., Al Arifi, N., Chandrasekharam, D., Al Bassam, A., Rehman, S., and Pipan, M., *Geothermal Energy Resources of Saudi Arabia: Country Update*. Proceedings World Geothermal Congress 2015 Melbourne, Australia, 19-25 April 2015.

[3] Damoom, M. M., Hashim, S., Aljohani, M. S., and Saleh, M. A., 2018, “Adding Sustainable Sources to the Saudi Arabian Electricity Sector,” Electr. J., **31**(4), pp. 20–28.

[4] Demirbas, A., Hashem, A. A., and Bakhsh, A. A., 2017, “The Cost Analysis of Electric Power Generation in Saudi Arabia,” Energy Sources, Part B Econ. Planning, Policy, **12**(6), pp. 591–596.

[5] Rambo, K. A., Warsinger, D. M., Shanbhogue, S. J., V, J. H. L., and Ghoniem, A. F., 2017, “Water-Energy Nexus in Saudi Arabia,” Energy Procedia, **105**, pp. 3837–3843.

[6] Said, S. A. M., Spindler, K., El-Shaarawi, M. A., Siddiqui, M. U., Schmid, F., Bierling, B., and Khan, M. M. A., 2016, “Design, Construction and Operation of a Solar Powered Ammonia-Water Absorption Refrigeration System in Saudi Arabia,” Int. J. Refrig., **62**, pp. 222–231.

[7] Almasoud, A. H., and Gandayh, H. M., 2015, “Future of Solar Energy in Saudi

Arabia," J. King Saud Univ. - Eng. Sci., **27**(2), pp. 153–157.

[8] Nemati, A., Nami, H., Ranjbar, F., and Yari, M., 2017, "A Comparative Thermodynamic Analysis of ORC and Kalina Cycles for Waste Heat Recovery: A Case Study for CGAM Cogeneration System," Case Stud. Therm. Eng., **9**(November 2016), pp. 1–13.

[9] Mondejar, M. E., Andreasen, J. G., Pierobon, L., Larsen, U., Thern, M., and Haglind, F., 2018, "A Review of the Use of Organic Rankine Cycle Power Systems for Maritime Applications," Renew. Sustain. Energy Rev., **91**, pp. 126–151.

[10] Girgin, I., and Ezgi, C., 2017, "Design and Thermodynamic and Thermoeconomic Analysis of an Organic Rankine Cycle for Naval Surface Ship Applications," Energy Convers. Manag., **148**, pp. 623–634.

[11] Mahmoudi, A., Fazli, M., and Morad, M. R., 2018, "A Recent Review of Waste Heat Recovery by Organic Rankine Cycle," Appl. Therm. Eng., **143**(July), pp. 660–675.

[12] Patel, B., Desai, N. B., and Kachhwaha, S. S., 2017, "Optimization of Waste Heat Based Organic Rankine Cycle Powered Cascaded Vapor Compression-Absorption Refrigeration System," Energy Convers. Manag., **154**(March), pp. 576–590.

[13] Tashtoush, B. M., Al-Nimr, M. A., and Khasawneh, M. A., 2019, "A Comprehensive Review of Ejector Design, Performance, and Applications," Appl. Energy, **240**, pp. 138–172.

[14] Constantino, G., Freitas, M., Fidelis, N., Pereira, M., Constantino, G., Freitas, M., Fidelis, N., and Pereira, M. G., 2018, “Adoption of Photovoltaic Systems Along a Sure Path: A Life-Cycle Assessment (LCA) Study Applied to the Analysis of GHG Emission Impacts,” Energies, **11**(10), p. 2806.

[15] Desai, N. B., and Bandyopadhyay, S., 2016, “Thermo-Economic Comparisons between Solar Steam Rankine and Organic Rankine Cycles,” Appl. Therm. Eng., **105**, pp. 862–875.

[16] Tartière, T., 2017, “A World Overview of the Organic Rankine Cycle Market,” Energy Procedia, **129**, pp. 2–9.

[17] “Analysis of the Organic Rankine Cycle Market” [Online]. Available: https://orc-world-map.org/analysis. [Accessed: 29-Mar-2019].

[18] Landelle, A., Tauveron, N., Haberschill, P., Revellin, R., and Colasson, S., 2017, “Organic Rankine Cycle Design and Performance Comparison Based on Experimental Database,” Appl. Energy, **204**, pp. 1172–1187.

[19] Markvart, T., and Castañer, L., 2003, *Practical Handbook of Photovoltaics : Fundamentals and Applications*, Elsevier Advanced Technology, Academic Press, 2012,pp. 1-3, ISBN 9780123859341, https://doi.org/10.1016/B978-0-12-385934-1.00044-1.

[20] Sivaram, V., 2018, *Taming the Sun : Innovations to Harness Solar Energy and Power the Planet*, MIT Press. Available: https://mitpress.mit.edu/books/taming-sun. [Accessed: 29-Mar-2019].

[21] Chen, A., Yossef, M., and Zhang, C., 2018, “Strain Effect on the Performance of Amorphous Silicon and Perovskite Solar Cells,” Sol. Energy, **163**, pp. 243–250.

[22] Ondraczek, J., 2014, “Are We There yet? Improving Solar PV Economics and Power Planning in Developing Countries: The Case of Kenya,” Renew. Sustain. Energy Rev., **30**, pp. 604–615.

[23] Velilla, E., Ramirez, D., Uribe, J.-I., Montoya, J. F., and Jaramillo, F., 2019, “Outdoor Performance of Perovskite Solar Technology: Silicon Comparison and Competitive Advantages at Different Irradiances,” Sol. Energy Mater. Sol. Cells, **191**, pp. 15–20.

[24] Wang, K., Jin, Z., Liang, L., Bian, H., Bai, D., Wang, H., Zhang, J., Wang, Q., and Shengzhong, L., 2018, “All-Inorganic Cesium Lead Iodide Perovskite Solar Cells with Stabilized Efficiency beyond 15%,” Nat. Commun., **9**(1), p. 4544.

[25] Blanco, M., and Santigosa, L. R., *Advances in Concentrating Solar Thermal Research and Technology*, Woodhead Publishing, 2017,Pages 3-25, ISBN 9780081005163.

[26] Hasanuzzaman, M., Malek, A. B. M. A., Islam, M. M., Pandey, A. K., and Rahim, N. A., 2016, “Global Advancement of Cooling Technologies for PV Systems: A Review,” Sol. Energy, **137**, pp. 25–45.

[27] Barlev, D., Vidu, R., and Stroeve, P., 2011, “Innovation in Concentrated Solar Power,” Sol. Energy Mater. Sol. Cells, **95**(10), pp. 2703–2725.

[28] Janda, K., 2018, “Slovak Electricity Market and the Price Merit Order Effect of

Photovoltaics," Energy Policy, **122**(July), pp. 551–562.

[29] Aguilar-Jiménez, J. A., Velázquez, N., Acuña, A., Cota, R., González, E., González, L., López, R., and Islas, S., 2018, "Techno-Economic Analysis of a Hybrid PV-CSP System with Thermal Energy Storage Applied to Isolated Microgrids," Sol. Energy, **174**(May), pp. 55–65.

[30] Qu, W., Hong, H., Li, Q., and Xuan, Y., 2018, "Co-Producing Electricity and Solar Syngas by Transmitting Photovoltaics and Solar Thermochemical Process," Appl. Energy, **217**(February), pp. 303–313.

[31] Icaza, D., and Sami, S., 2018, "Modeling, Simulation and Stability Analysis Using MATLAB of a Hybrid System Solar Panel and Wind Turbine in The Locality of Puntahacienda-Quingeo In Ecuador," Int. J. Manag. Sustain., **7**(1), pp. 1–24.

[32] Renno, C., 2018, "Experimental and Theoretical Analysis of a Linear Focus CPV/T System for Cogeneration Purposes," Energies, **11**(11), p. 2960.

[33] Xiao, M., Tang, L., Zhang, X., Lun, I. Y. F., and Yuan, Y., 2018, "A Review on Recent Development of Cooling Technologies for Concentrated Photovoltaics (CPV) Systems," Energies, **11**(12).

[34] Ben Youssef, W., Maatallah, T., Menezo, C., and Ben Nasrallah, S., 2018, "Modeling and Optimization of a Solar System Based on Concentrating Photovoltaic/Thermal Collector," Sol. Energy, **170**(April), pp. 301–313.

[35] Riverola, A., Moreno, A., and Chemisana, D., 2018, "Performance of a Dielectric PVT Concentrator for Building-Façade Integration," Opt. Express, **26**(18), p.

A892.

[36] Rahbar, K., Riasi, A., Khatam Bolouri Sangjoeei, H., and Razmjoo, N., 2019, "Heat Recovery of Nano-Fluid Based Concentrating Photovoltaic Thermal (CPV/T) Collector with Organic Rankine Cycle," Energy Convers. Manag., **179**(July 2018), pp. 373–396.

[37] Uche, J., Acevedo, L., Círez, F., Usón, S., Martínez-Gracia, A., and Bayod-Rújula, Á. A., 2019, "Analysis of a Domestic Trigeneration Scheme with Hybrid Renewable Energy Sources and Desalting Techniques," J. Clean. Prod., **212**, pp. 1409–1422.

[38] Pina, E. A., Lozano, M. A., and Serra, L. M., "Opportunities for the Integration of Solar Thermal Heat , Photovoltaics and Biomass in a Brazilian Hospital." , DOI 10.18086/eurosun2018.05.03, Date Accessed: 2019-04-01URLS, www.researchgate.net/publication/327797840.

[39] Sadeghi, S., and Askari, I. B., 2019, "Prefeasibility Techno-Economic Assessment of a Hybrid Power Plant with Photovoltaic, Fuel Cell and Compressed Air Energy Storage (CAES)," Energy, **168**, pp. 409–424.

[40] Chen, X., Zhang, T., Xue, X., Chen, L., Li, Q., and Mei, S., 2018, "A Solar–Thermal-Assisted Adiabatic Compressed Air Energy Storage System and Its Efficiency Analysis," Appl. Sci., **8**(8), p. 1390.

[41] Islam, M. T., Huda, N., Abdullah, A. B., and Saidur, R., 2018, "A Comprehensive Review of State-of-the-Art Concentrating Solar Power (CSP) Technologies: Current Status and Research Trends," Renew. Sustain. Energy Rev., **91**(April), pp.

987–1018.

[42] Kasaeian, A., Tabasi, S., Ghaderian, J., and Yousefi, H., 2018, “A Review on Parabolic Trough/Fresnel Based Photovoltaic Thermal Systems,” Renew. Sustain. Energy Rev., **91**(March 2017), pp. 193–204.

[43] Manikandan, G. K., Iniyan, S., and Goic, R., 2019, “Enhancing the Optical and Thermal Efficiency of a Parabolic Trough Collector – A Review,” Appl. Energy, **235**(November 2018), pp. 1524–1540.

[44] Pantaleo, A. M., Camporeale, S. M., Sorrentino, A., Miliozzi, A., Shah, N., and Markides, C. N., 2018, “Hybrid Solar-Biomass Combined Brayton/Organic Rankine-Cycle Plants Integrated with Thermal Storage: Techno-Economic Feasibility in Selected Mediterranean Areas,” Renew. Energy, DOI :10.1016/J.RENENE.2018.08.022, ISSN : 0960-1481.

[45] Mata-torres, C., Zurita, A., Cardemil, J. M., and Escobar, R. A., 2018, “Cost Allocation Analysis of a CSP + MED Plant Considering Time-Varying Conditions,”, Conference: SolarPaces 2018.

[46] Mata-torres, C., Zurita, A., Cardemil, J. M., and Escobar, R. A., 2019, “Exergy Cost Analysis of a CSP-Rankine Cycle Coupled with a MED Plant Considering Time- Varying Conditions and Part-Load Operation,”, Energy Conversion and Management 192:114-132, DOI: 10.1016/j.enconman.2019.04.023.

[47] Loni, R., Pavlovic, S., Bellos, E., Tzivanidis, C., and Asli-Ardeh, E. A., 2018, “Thermal and Exergy Performance of a Nanofluid-Based Solar Dish Collector with Spiral Cavity Receiver,” Appl. Therm. Eng., **135**(November 2017), pp. 206–

217.

[48] Patil, V. R., Biradar, V. I., Shreyas, R., Garg, P., Orosz, M. S., and Thirumalai, N. C., 2017, "Techno-Economic Comparison of Solar Organic Rankine Cycle (ORC) and Photovoltaic (PV) Systems with Energy Storage," Renew. Energy, **113**, pp. 1250–1260.

[49] Bellos, E., and Tzivanidis, C., 2018, "Assessment of Linear Solar Concentrating Technologies for Greek Climate," Energy Convers. Manag., **171**(June), pp. 1502–1513.

[50] Morin, G., Dersch, J., Platzer, W., Eck, M., and Häberle, A., 2012, "Comparison of Linear Fresnel and Parabolic Trough Collector Power Plants," Sol. Energy, **86**(1), pp. 1–12.

[51] Colonna, P., Casati, E., Trapp, C., Mathijssen, T., Larjola, J., Turunen-Saaresti, T., and Uusitalo, A., 2015, "Organic Rankine Cycle Power Systems: From the Concept to Current Technology, Applications, and an Outlook to the Future," J. Eng. Gas Turbines Power, **137**(10), p. 100801.

[52] "Concentrating Solar Power Projects | Concentrating Solar Power Projects" [Online]. Available: https://solarpaces.nrel.gov/sites/default/files/project-export.csv. [Accessed: 15-Dec-2018].

[53] Ballestrín, J., Burgess, G., and Cumpston, J., 2012, *Concentrating Solar Power Technology,* © Woodhead Publishing Limited, 2012, Philadelphia.

[54] "ORC Units for Solar Collectors | TURBODEN" [Online]. Available:

https://www.turboden.com/applications/1056/concentrated-solar-power. [Accessed: 18-Feb-2018].

[55] Bellos, E., Tzivanidis, C., and Tsimpoukis, D., 2018, “Optimum Number of Internal Fins in Parabolic Trough Collectors,” Appl. Therm. Eng., **137**, pp. 669–677.

[56] Solapure, P. V. S., Ithape, S. S., Gugale, S. M., Deshmukh, P. D., and Bankar, S. R., 2018, “Parabolic Trough Solar Concentrator,” **8**(1275), pp. 1275–1284.

[57] Ghazouani, K., Skouri, S., Bouadila, S., and Guizani, A. A., 2018, “Thermal Study of Solar Parabolic Trough Concentrator,” 2018 9th Int. Renew. Energy Congr. IREC 2018, (Irec), pp. 1–4.

[58] Cascio, E. Lo, Ma, Z., and Schenone, C., 2018, “Performance Assessment of a Novel Natural Gas Pressure Reduction Station Equipped with Parabolic Trough Solar Collectors,” Renew. Energy, **128**, pp. 177–187.

[59] Mehrpooya, M., tosang, E., and Dadak, A., 2018, “Investigation of a Combined Cycle Power Plant Coupled with a Parabolic Trough Solar Field and High Temperature Energy Storage System,” Energy Convers. Manag., **171**(June), pp. 1662–1674.

[60] Quoilin, S., Broek, M. Van Den, Declaye, S., Dewallef, P., and Lemort, V., 2013, “Techno-Economic Survey of Organic Rankine Cycle (ORC) Systems,” Renew. Sustain. Energy Rev., **22**, pp. 168–186.

[61] Bellos, E., Tzivanidis, C., and Papadopoulos, A., 2018, “Daily, Monthly and

Yearly Performance of a Linear Fresnel Reflector," Sol. Energy, **173**, pp. 517–529.

[62] Sarkar, J., 2015, "Review and Future Trends of Supercritical CO2 Rankine Cycle for Low-Grade Heat Conversion," Renew. Sustain. Energy Rev., **48**, pp. 434–451.

[63] Moloney, F., Almatrafi, E., and Goswami, D. Y., 2017, "Working Fluid Parametric Analysis for Regenerative Supercritical Organic Rankine Cycles for Medium Geothermal Reservoir Temperatures," Energy Procedia, **129**, pp. 599–606.

[64] Kim, Y. M., Sohn, J. L., and Yoon, E. S., 2017, "Supercritical CO2 Rankine Cycles for Waste Heat Recovery from Gas Turbine," Energy, **118**, pp. 893–905.

[65] Hosseinpour, J., Chitsaz, A., Eisavi, B., and Yari, M., 2018, "Investigation on Performance of an Integrated SOFC-Goswami System Using Wood Gasification," Energy, **148,** pp. 614-628.

[66] Shankar, R., and Srinivas, T., 2018, "Performance Investigation of Kalina Cooling Cogeneration Cycles," Int. J. Refrig., **86**, pp. 163–185.

[67] Zhang, X., He, M., and Zhang, Y., 2012, "A Review of Research on the Kalina Cycle," Renew. Sustain. Energy Rev., **16**(7), pp. 5309–5318.

[68] Rao, W. J., Zhao, L. J., Liu, C., and Zhang, M. G., 2013, "A Combined Cycle Utilizing LNG and Low-Temperature Solar Energy," Appl. Therm. Eng., **60**(1–2), pp. 51–60.

[69] "Labothap - ORCNext" [Online]. Available: http://www.labothap.ulg.ac.be/cmsms/index.php?page=orcnext-2. [Accessed: 26-Jan-2019].

[70] Quoilin, S., 2008, “An Introduction to Thermodynamics Applied to Organic Rankine Cycle,” STG Int., (November). Available: https://orbi.uliege.be/handle/2268/138797. [Accessed: 26-Jan-2019].

[71] Aboelwafa, O., Fateen, S. E. K., Soliman, A., and Ismail, I. M., 2018, “A Review on Solar Rankine Cycles: Working Fluids, Applications, and Cycle Modifications,” Renew. Sustain. Energy Rev., **82**(July 2017), pp. 868–885.

[72] Liang, Y., and Yu, Z., 2019, “Working Fluid Selection for a Combined System Based on Coupling of Organic Rankine Cycle and Air Source Heat Pump Cycle,” Energy Procedia, **158**(2018), pp. 1485–1490.

[73] Rayegan, R., and Tao, Y. X., 2011, “A Procedure to Select Working Fluids for Solar Organic Rankine Cycles (ORCs),” Renew. Energy, **36**(2), pp. 659–670.

[74] Vivian, J., Manente, G., and Lazzaretto, A., 2015, “A General Framework to Select Working Fluid and Configuration of ORCs for Low-to-Medium Temperature Heat Sources,” Appl. Energy, **156**, pp. 727–746.

[75] Saloux, E., Sorin, M., Nesreddine, H., and Teyssedou, A., 2018, “Reconstruction Procedure of the Thermodynamic Cycle of Organic Rankine Cycles (ORC) and Selection of the Most Appropriate Working Fluid,” Appl. Therm. Eng., **129**, pp. 628–635.

[76] Desai, N. B., and Bandyopadhyay, S., 2016, “Thermo-Economic Analysis and Selection of Working Fluid for Solar Organic Rankine Cycle,” Appl. Therm. Eng., **95**, pp. 471–481.

[77] Tzivanidis, C., Bellos, E., and Antonopoulos, K. A., 2016, “Energetic and Financial Investigation of a Stand-Alone Solar-Thermal Organic Rankine Cycle Power Plant,” Energy Convers. Manag., **126**, pp. 421–433.

[78] Dai, X., Shi, L., An, Q., and Qian, W., 2016, “Screening of Hydrocarbons as Supercritical ORCs Working Fluids by Thermal Stability,” Energy Convers. Manag., **126**, pp. 632–637.

[79] Invernizzi, C. M., Iora, P., Manzolini, G., and Lasala, S., 2017, “Thermal Stability of N-Pentane, Cyclo-Pentane and Toluene as Working Fluids in Organic Rankine Engines,” Appl. Therm. Eng., **121**, pp. 172–179.

[80] T Tartièrea, 2017, “ A World Overview of the Organic Rankine Cycle Market The Overview the Organic Rankine Assessing the Feasibility of the Heat,”, Energy Procedia, 129, pp. 2-9..

[81] Yao Manu Seshie, Yézouma Coulibaly, and Kokouvi Edem N’Tsoukpoe, 2017, “Optimal Operating Conditions of an Organic Rankine Cycle under Steady Heat Input,” J. Energy Power Eng., **11**(12), pp. 759–770.

[82] Petrollese, M., Oyekale, J., Tola, V., and Cocco, D., 2018, “Optimal ORC Configuration for the Combined Production of Heat and Power Utilizing Solar Energy and Biomass,” ECOS.

[83] Danieli, P., Rech, S., and Lazzaretto, A., 2018, “Supercritical CO2 and air Brayton-Joule versus ORC systems for heat recovery from glass furnaces: Performance and economic evaluation.”, Energy **168**, pp. 295-309.

[84] Hou, S., Cao, S., Yu, L., Zhou, Y., Wu, Y., and Zhang, F. Y., 2018, “Performance Optimization of Combined Supercritical CO2recompression Cycle and Regenerative Organic Rankine Cycle Using Zeotropic Mixture Fluid,” Energy Convers. Manag., **166**(April), pp. 187–200.

[85] Zhang, H., Guan, X., Ding, Y., and Liu, C., 2018, “Emergy Analysis of Organic Rankine Cycle (ORC) for Waste Heat Power Generation,” J. Clean. Prod., **183**, pp. 1207–1215.

[86] Freeman, J., Guarracino, I., Kalogirou, S. A., and Markides, C. N., 2017, “A Small-Scale Solar Organic Rankine Cycle Combined Heat and Power System with Integrated Thermal-Energy Storage,” Appl. Therm. Eng., **127**, pp. 1543–1554.

[87] Navarro-Esbrí, J., Molés, F., Peris, B., Mota-Babiloni, A., Pascual Martí, J., Collado, R., and González, M., 2017, “Combined Cold, Heat and Power System, Based on an Organic Rankine Cycle, Using Biomass as Renewable Heat Source for Energy Saving and Emissions Reduction in a Supermarket,” Energy Procedia, **129**, pp. 652–659.

[88] Zhang, J., Zhao, L., Wen, J., and Deng, S., 2016, “An Overview of 200 KW Solar Power Plant Based on Organic Rankine Cycle,” Energy Procedia, **88**, pp. 356–362.

[89] Canada, S., Cohen, G., Cable, R., Brosseau, D., and Price, H., 2005, “Parabolic Trough Organic Rankine Cycle Solar Power Plant,” 2004 DOE Sol. Energy Technol., **1**(January), pp. 1–2.

[90] Raush, J. R., Chambers, T. L., Russo, B., and Iii, K. a R., 2013, “Demonstration of Pilot Scale Large Aperture Parabolic Trough Organic Rankine Cycle Solar

Thermal Power Plant in Louisiana," J. Power Energy Eng., **2013**(December), pp. 29–39.

[91] Heberle, F., Hofer, M., and Brüggemann, D., 2017, "A Retrofit for Geothermal Organic Rankine Cycles Based on Concentrated Solar Thermal Systems," Energy Procedia, **129**, pp. 692–699.

[92] Morrone, P., Algieri, A., and Castiglione, T., 2019, "Hybridisation of Biomass and Concentrated Solar Power Systems in Transcritical Organic Rankine Cycles: A Micro Combined Heat and Power Application," Energy Convers. Manag., **180**(November 2018), pp. 757–768.

[93] Khan, Y., and Mishra, R. S., 2018, "International Journal of Research in Engineering and Innovation Thermodynamic (Energy-Exergy) Analysis of Combined Cycle Power Plant for Improving Thermal Energetic and Exergetic Efficiencies by Integration of Organic Rankine Cycle (ORC)," **1**(1), pp. 86–92.

[94] Quoilin, S., Orosz, M., Hemond, H., and Lemort, V., 2011, "Performance and Design Optimization of a Low-Cost Solar Organic Rankine Cycle for Remote Power Generation," Sol. Energy, **85**(5), pp. 955–966.

[95] He, Y.-L., Mei, D.-H., Tao, W.-Q., Yang, W.-W., and Liu, H.-L., 2012, "Simulation of the Parabolic Trough Solar Energy Generation System with Organic Rankine Cycle," Appl. Energy, **97**, pp. 630–641.

[96] Calise, F., Capuozzo, C., Carotenuto, A., and Vanoli, L., 2014, "Thermoeconomic Analysis and Off-Design Performance of an Organic Rankine Cycle Powered by Medium-Temperature Heat Sources," Sol. Energy, **103**, pp. 595–609.

[97] Ferrara, F., Gimelli, A., and Luongo, A., 2014, “Small-Scale Concentrated Solar Power (CSP) Plant: ORCs Comparison for Different Organic Fluids,” Energy Procedia, **45**, pp. 217–226.

[98] Xu, G., Song, G., Zhu, X., Gao, W., Li, H., and Quan, Y., 2015, “Performance Evaluation of a Direct Vapor Generation Supercritical ORC System Driven by Linear Fresnel Re Fl Ector Solar Concentrator,” Appl. Therm. Eng., **80**, pp. 196–204.

[99] Cocco, D., and Cau, G., 2015, “Energy and Economic Analysis of Concentrating Solar Power Plants Based on Parabolic Trough and Linear Fresnel Collectors,” Proc. Inst. Mech. Eng. Part A J. Power Energy, **229**(6), pp. 677–688.

[100] Su, W., Hwang, Y., Deng, S., Zhao, L., and Zhao, D., 2018, “Thermodynamic Performance Comparison of Organic Rankine Cycle between Zeotropic Mixtures and Pure Fl Uids under Open Heat Source,” Energy Convers. Manag., **165**(March), pp. 720–737.

[101] Wang, X. D., and Zhao, L., 2009, “Analysis of Zeotropic Mixtures Used in Low-Temperature Solar Rankine Cycles for Power Generation,” Sol. Energy, **83**(5), pp. 605–613.

[102] M.E. Mondejar, J.G. Andreasen, M. Regidor, S. Riva, G. Kontogeorgis, G. Persico, et al., "Prospects of the use of nanofluids as working fluids for organic Rankine cycle power systems", Energy Procedia, 129 (2017), pp. 160-167, ISSN 1876–6102.

[103] Li, L., Ge, Y. T., Luo, X., and Tassou, S. A., 2018, “Design and Dynamic

Investigation of Low-Grade Power Generation Systems with CO 2 Transcritical Power Cycles and R245fa Organic Rankine Cycles,” **8**(March), pp. 211–222.

[104] Andreasen, J.G.; Kærn, M.R.; Pierobon, L.; Larsen, U.; Haglind, F., 2016, "Multi-objective optimization of organic Rankine cycle power plants using pure and mixed working fluids. Energies ", 9, pp. 322.

[105] Dong, B., Xu, G., Luo, X., Zhuang, L., and Quan, Y., 2017, “Potential of Low Temperature Organic Rankine Cycle with Zeotropic Mixtures as Working Fluid,” Energy Procedia, **105**, pp. 1489–1494.

[106] Hou, S., Cao, S., Yu, L., Zhou, Y., Wu, Y., and Zhang, F., 2018, “Performance Optimization of Combined Supercritical CO 2 Recompression Cycle and Regenerative Organic Rankine Cycle Using Zeotropic Mixture Fl Uid,” Energy Convers. Manag., **166**(April), pp. 187–200.

[107] Singh, R., and Singh, O., 2018, “Comparative Study of Combined Solid Oxide Fuel Cell-Gas Turbine-Organic Rankine Cycle for Di Ff Erent Working Fl Uid in Bottoming Cycle,” Energy Convers. Manag., **171**(June), pp. 659–670.

[108] Saadatfar, B., Fakhrai, R., and Fransson, T., 2014, “Conceptual Modeling of Nano Fluid ORC for Solar Thermal Polygeneration,” Energy Procedia, **57**, pp. 2696–2705.

[109] Saadatfar, B., Fakhrai, R., and Fransson, T., 2014, “Exergo-Environmental Analysis of Nano Fluid ORC Low-Grade Waste Heat Recovery for Hybrid Trigeneration System,” Energy Procedia, **61**, pp. 1879–1882.

[110] Dincer I Ratlamwala T., *Integrated Absorption Refrigeration Systems*. Comparative Energy and Exergy Analyses 2016,© Springer International Publishing 2016. pp: 47-69.

[111] Dincer, I., and Rosen, M. A., 2015, *Exergy Analysis of Heating, Refrigerating and Air Conditioning: Methods and Applications*. . 2015 pp: 99-129.

[112] Dincer, I., and Ratlamwala, T., 2016, *Integrated Absorption Refrigeration Systems*, © Springer International Publishing 2016, Switzerland, pp. 2-5.

[113] Farshi, L. G., Infante Ferreira, C. A., Mahmoudi, S. M. S., and Rosen, M. A., 2014, "First and Second Law Analysis of Ammonia/Salt Absorption Refrigeration Systems," Int. J. Refrig., **40**, pp. 111–121.

[114] Aliane, A., Abboudi, S., Seladji, C., and Guendouz, B., 2016, "An Illustrated Review on Solar Absorption Cooling Experimental Studies," Renew. Sustain. Energy Rev., **65**, pp. 443–458.

[115] Anand, Y., Tyagi, S. K., and Anand, S., 2018, "Variable Capacity Absorption Cooling System Performance for Building Application," J. Therm. Eng., **4**(5), pp. 2303–2317.

[116] Shirazi, A., Taylor, R. A., Morrison, G. L., and White, S. D., 2018, "Solar-Powered Absorption Chillers: A Comprehensive and Critical Review," Energy Convers. Manag., **171**(May), pp. 59–81.

[117] Xu, Z. Y., and Wang, R. Z., 2016, "Absorption Refrigeration Cycles: Categorized Based on the Cycle Construction," Int. J. Refrig., **62**, pp. 114–136.

[118] Jelinek, M., Levy, A., and Borde, I., 2012, "Performance of a Triple-Pressure Level Absorption/Compression Cycle," Appl. Therm. Eng., **42**, pp. 2–5.

[119] Sözen, A., Özalp, M., and Arcaklioğlu, E., 2004, "Prospects for Utilisation of Solar Driven Ejector-Absorption Cooling System in Turkey," Appl. Therm. Eng., **24**(7), pp. 1019–1035.

[120] Vereda, C., Ventas, R., Lecuona, A., and Venegas, M., 2012, "Study of an Ejector-Absorption Refrigeration Cycle with an Adaptable Ejector Nozzle for Different Working Conditions," Appl. Energy, **97**, pp. 305–312.

[121] Ventas, R., Vereda, C., Lecuona, A., and Venegas, M., 2012, "Experimental Study of a Thermochemical Compressor for an Absorption/Compression Hybrid Cycle," Appl. Energy, **97**, pp. 297–304.

[122] Besagni, G., Mereu, R., and Inzoli, F., 2016, "Ejector Refrigeration: A Comprehensive Review," Renew. Sustain. Energy Rev., **53**, pp. 373–407.

[123] "Ejectors | Natural Resources Canada" [Online]. Available: http://www.nrcan.gc.ca/node/3895. [Accessed: 18-Feb-2018].

[124] Sözen, A., and Yücesu, H. S., 2007, "Performance Improvement of Absorption Heat Transformer," Renew. Energy, **32**(2), pp. 267–284.

[125] Chen, L.-T., 1988, "A New Ejector-Absorber Cycle to Improve the COP of an Absorption Refrigeration System," Appl. Energy, **30**(1), pp. 37–51.

[126] Little, A. B., Garimella, S., 2011, "A Review of Ejector Technology for Refrigeration Applications," Int. J. Air-Conditioning Refrig., **19**(01), pp. 1–15.

[127] Levy, a, Jelinek, M., and Borde, I., 2002, “Numerical Study on the Design Parameters of a Jet Ejector for Absorption Systems,” **72**, pp. 467–478.

[128] Levy, A., Jelinek, M., Borde, I., and Ziegler, F., 2004, “Performance of an Advanced Absorption Cycle with R125 and Different Absorbents,” Energy, **29**(12–15), pp. 2501–2515.

[129] Jelinek, M., Levy, A., and Borde, I., 2008, “The Performance of a Triple Pressure Level Absorption Cycle (TPLAC) with Working Fluids Based on the Absorbent DMEU and the Refrigerants R22, R32, R124, R125, R134a and R152a,” Appl. Therm. Eng., **28**(11–12), pp. 1551–1555.

[130] Jelinek, M., Levy, A., and Borde, I., 2008, “The Performance of a Triple Pressure Level Absorption Cycle (TPLAC) with Working Fluids Based on the Absorbent DMEU and the Refrigerants R22, R32, R124, R125, R134a and R152a,” Appl. Therm. Eng., **28**(11–12), pp. 1551–1555.

[131] Vereda, C., Ventas, R., Lecuona, A., and López, R., 2014, “Single-Effect Absorption Refrigeration Cycle Boosted with an Ejector-Adiabatic Absorber Using a Single Solution Pump,” Int. J. Refrig., **38**(1), pp. 22–29.

[132] Sun, D.-W., Eames, I. W., and Aphornratana, S., 1996, “Evaluation of a Novel Combined Ejector-Absorption Refrigeration Cycle — I: Computer Simulation,” Int. J. Refrig., **19**(3), pp. 172–180.

[133] Chen, J., Havtun, H., and Palm, B., 2014, “Investigation of Ejectors in Refrigeration System: Optimum Performance Evaluation and Ejector Area Ratios Perspectives,” Appl. Therm. Eng., **64**(1–2), pp. 182–191.

[134] Nguyen, V. ., Riffat, S. ., and Doherty, P. ., 2001, “Development of a Solar-Powered Passive Ejector Cooling System,” Appl. Therm. Eng., **21**(2), pp. 157–168.

[135] Dennis, M., and Garzoli, K., 2011, “Use of Variable Geometry Ejector with Cold Store to Achieve High Solar Fraction for Solar Cooling,” Int. J. Refrig., **34**(7), pp. 1626–1632.

[136] Besagni, G., Milano, P., Milano, P., Inzoli, F., Milano, P., Besagni, G., Mereu, R., and Inzoli, F., 2016, “Ejector Refrigeration : A Comprehensive Review Ejector Refrigeration : A Comprehensive Review,” **53**(January), pp. 373–407.

[137] Abed, A. M., Alghoul, M. A., Sopian, K., Majdi, H. S., Al-Shamani, A. N., and Muftah, A. F., 2017, “Enhancement Aspects of Single Stage Absorption Cooling Cycle: A Detailed Review,” Renew. Sustain. Energy Rev., **77**(January), pp. 1010–1045.

[138] Hong, D., Chen, G., Tang, L., and He, Y., 2011, “A Novel Ejector-Absorption Combined Refrigeration Cycle,” Int. J. Refrig., **34**(7), pp. 1596–1603.

[139] Abdulateef, J. M., Murad, N. M., Alghoul, M. A., Zaharim, A., and Sopian, K., 2011, “Experimental Study On Combined Solar- Assisted Ejector Absorption Refrigeration System,” Recent Res. Geogr. Geol., pp. 162–166.

[140] Garousi Farshi, L., Mahmoudi, S. M. S., and Rosen, M. A., 2013, “Exergoeconomic Comparison of Double Effect and Combined Ejector-Double Effect Absorption Refrigeration Systems,” Appl. Energy, **103**, pp. 700–711.

[141] Garousi Farshi, L., Mosaffa, A. H., Infante Ferreira, C. A., and Rosen, M. A., 2014, “Thermodynamic Analysis and Comparison of Combined Ejector–absorption and Single Effect Absorption Refrigeration Systems,” Appl. Energy, **133**, pp. 335–346.

[142] Abed, A. M., Sopian, K., Alghoul, M. A., Majadi, H. S., and Al-Shamani, A. N., 2017, “Experimental Evaluation of Single Stage Ejector-Absorption Cooling Cycle under Different Design Configurations,” Sol. Energy, **155**, pp. 130–141.

[143] Leiva-Illanes, R., Escobar, R., Cardemil, J. M., Alarcón-Padilla, D.-C., Uche, J., and Martínez, A., 2019, “Exergy Cost Assessment of CSP Driven Multi-Generation Schemes: Integrating Seawater Desalination, Refrigeration, and Process Heat Plants,” Energy Convers. Manag., **179**(September 2018), pp. 249–269.

[144] Qiu, S., Gao, Y., Rinker, G., and Yanaga, K., 2019, “Development of an Advanced Free-Piston Stirling Engine for Micro Combined Heating and Power Application,” Appl. Energy, **235**(June 2018), pp. 987–1000.

[145] Arabkoohsar, A., 2018, “An Integrated Subcooled-CAES and Absorption Chiller System for Cogeneration of Cold and Power,” 2018 Int. Conf. Smart Energy Syst. Technol., pp. 1–5.

[146] Arabkoohsar, A., and Andresen, G. B., 2019, “Design and Optimization of a Novel System for Trigeneration,” Energy, **168**, pp. 247–260.

[147] Mosaffa, A. H., Ghaffarpour, Z., and Garousi Farshi, L., 2019, “Thermoeconomic Assessment of a Novel Integrated CHP System Incorporating Solar Energy Based

Biogas-Steam Reformer with Methanol and Hydrogen Production," Sol. Energy, **178**(December 2018), pp. 1–16.

[148] Calise, F., Libertini, L., and Vicidomini, M., 2018, "Dynamic Simulation and Thermoeconomic Analysis of a Novel Solar Cooling System for a Triple-Pressure Combined Cycle Power Plant," Energy Convers. Manag., **170**, pp. 82–96.

[149] Khan, M. S., Abid, M., and Ratlamwala, T. A. H., 2018, "Energy, Exergy and Economic Feasibility Analyses of a 60 MW Conventional Steam Power Plant Integrated with Parabolic Trough Solar Collectors Using Nanofluids," Iran. J. Sci. Technol. Trans. Mech. Eng., **3456789**.

[150] Rostamzadeh, H., Gargari, S. G., Namin, A. S., and Ghaebi, H., 2019, "A Novel Multigeneration System Driven by a Hybrid Biogas-Geothermal Heat Source, Part II: Multi-Criteria Optimization," Energy Convers. Manag., **180**(November 2018), pp. 859–888.

[151] GAO, G., FENG, J., Dabwan, Y. N., Li, J., and Pei, G., 2019, "Performance Analysis of Integrated Linear Fresnel Reflector with a Conventional Cooling, Heat, and Power Tri-Generation Plant," Renew. Energy, 2019 vol: 138 pp: 639-650.

[152] Mokheimer, E. M. A., and Dabwan, Y. N., 2018, "Performance Analysis of Integrated Solar Tower with a Conventional Heat and Power Co-Generation Plant," J. Energy Resour. Technol., **141**(February), pp. 1–13.

[153] Dabwan, Y. N., Gang, P., Li, J., Gao, G., and Feng, J., 2018, "Development and Assessment of Integrating Parabolic Trough Collectors with Gas Turbine

Trigeneration System for Producing Electricity, Chilled Water, and Freshwater," Energy, **162**, pp. 364–379.

[154] Bellos, E., Vellios, L., Theodosiou, I. C., and Tzivanidis, C., 2018, "Investigation of a Solar-Biomass Polygeneration System," Energy Convers. Manag., **173**(June), pp. 283–295.

[155] Yilmaz, F., Ozturk, M., and Selbas, R., 2018, "Energy and Exergy Performance Assessment of a Novel Solar-Based Integrated System with Hydrogen Production," Int. J. Hydrogen Energy, ISSN 0360-3199.

[156] Abed, K. A., Amin, A. M. A., El-samahy, A. A., and Shaaban, A. M. A., 2018, "Modeling and Simulation of Multi Purposes Concentrated Solar Power System," Journal, E., **5**(6), pp. 375–385.

[157] Patel, B., Desai, N. B., and Kachhwaha, S. S., 2017, "Thermo-Economic Analysis of Solar-Biomass Organic Rankine Cycle Powered Cascaded Vapor Compression-Absorption System," Sol. Energy, **157**(September), pp. 920–933.

[158] Patel, B., Desai, N. B., Kachhwaha, S. S., Jain, V., and Hadia, N., 2017, "Thermo-Economic Analysis of a Novel Organic Rankine Cycle Integrated Cascaded Vapor Compression–absorption System," J. Clean. Prod., **154**(September), pp. 920–933.

[159] Jain, V., Sachdeva, G., and Kachhwaha, S. S., 2015, "Thermodynamic Modelling and Parametric Study of a Low Temperature Vapour Compression-Absorption System Based on Modified Gouy-Stodola Equation," Energy, **79**(C), pp. 407–418.

[160] Jain, V., Kachhwaha, S. S., and Sachdeva, G., 2013, "Thermodynamic

Performance Analysis of a Vapor Compression – Absorption Cascaded Refrigeration System," Energy Convers. Manag., **75**, pp. 685–700.

[161] Desai, N. B., and Bandyopadhyay, S., 2009, "Process Integration of Organic Rankine Cycle," Energy, **34**(10), pp. 1674–1686.

[162] Nikolaidis, C., and Probert, D., 1998, "Exergy-Method Analysis of a Two-Stage Vapour- Compression Refrigeration-Plants Performance," Applied Energy. 1998 vol: **60 (4)** pp: 241-256.

[163] Tchanche, B. F., Lambrinos, G., Frangoudakis, A., and Papadakis, G., 2010, "Exergy Analysis of Micro-Organic Rankine Power Cycles for a Small Scale Solar Driven Reverse Osmosis Desalination System," Appl. Energy, **87**(4), pp. 1295–1306.

[164] Nikulshin, V., Wu, C., and Nikulshina, V., 2002, "Exergy Efficiency Calculation of Energy Intensive Systems by Graphs," Int. J. Appl. Thermodyn., **5**(2), pp. 67–74.

[165] Nikulshin, V., and Wu, C., 2001, "Thermodynamic Analysis of Energy Intensive Systems Based on Exergy–topological Models," Exergy, An Int. J., **1**(3), pp. 173–179.

[166] Nikulshin, V., Bailey, M., and Nikulshina, V., 2006, "Thermodynamic Analysis of Air Refrigerator on Exergy Graph", Nikulshin, 102. Thermal Science: Vol., V.10, pp. 99–110.

[167] Jradi, M., and Riffat, S., 2014, "Experimental Investigation of a Biomass-Fuelled

Micro-Scale Tri-Generation System with an Organic Rankine Cycle and Liquid Desiccant Cooling Unit," Energy, **71**, pp. 80–93.

[168] Desai, N. B., Kedare, S. B., and Bandyopadhyay, S., 2014, " Optimization of Design Radiation for Concentrating Solar Thermal Power Plants without Storage," Sol. Energy, **107**, pp. 98–112.

[169] Baghernejad, A., Yaghoubi, M., and Jafarpur, K., 2016, "Exergoeconomic Optimization and Environmental Analysis of a Novel Solar-Trigeneration System for Heating, Cooling and Power Production Purpose," Sol. Energy, **134**, pp. 165–179.

[170] Duffie, J., and Beckman, W., 2013, *Solar Engineering of Thermal Processes, 4th Ed.*, John Wiley & Sons, Inc., Hoboken, New Jersey pp.323-370.

[171] Adrian Bejan, George Tsatsaronis, Michael Moran, 1995, "Thermal Design and Optimization-John Wiley & Sons. pp: 542."

[172] Buonomano, A., Calise, F., Palombo, A., and Vicidomini, M., 2015, "Energy and Economic Analysis of Geothermal – Solar Trigeneration Systems : A Case Study for a Hotel Building in Ischia," Appl. Energy, **138**, pp. 224–241.

[173] Boyaghchi, F. A., Mahmoodnezhad, M., and Sabeti, V., 2016, "Exergoeconomic Analysis and Optimization of a Solar Driven Dual-Evaporator Vapor Compression-Absorption Cascade Refrigeration System Using Water/CuO Nanofluid," J. Clean. Prod., **139**, pp. 970–985.

[174] Al-Sulaiman, F. A., Dincer, I., and Hamdullahpur, F., 2011, "Exergy Modeling of

a New Solar Driven Trigeneration System," Sol. Energy, **85**(9), pp. 2228–2243.

[175] Al-Sulaiman, F. A., Hamdullahpur, F., and Dincer, I., 2012, "Performance Assessment of a Novel System Using Parabolic Trough Solar Collectors for Combined Cooling, Heating, and Power Production," Renew. Energy, **48**, pp. 161–172.

[176] Al-Sulaiman, F. A., Dincer, I., and Hamdullahpur, F., 2012, "Energy and Exergy Analyses of a Biomass Trigeneration System Using an Organic Rankine Cycle," 24th Int. Conf. Effic. Cost, Optim. Simul. Environ. Impact Energy, ECOS 2011, **45**(1), pp. 975–985.

[177] Suleman, F., Dincer, I., and Agelin-Chaab, M., 2014, "Development of an Integrated Renewable Energy System for Multigeneration," Energy, **78**, pp. 196–204.

[178] Bellos, E., Tzivanidis, C., Bellos, E., and Tzivanidis, C., 2018, "Analytical Expression of Parabolic Trough Solar Collector Performance," Designs, **2**(1), p. 9.

[179] Kalogirou, S. A., 2016, Advances in Solar Heating and Cooling, Woodhead Publishing Series in Energy: Number 102, Cambridge, MA 02139, USA, pp.63-80.

[180] Bellos, E., and Tzivanidis, C., 2017, "A Detailed Exergetic Analysis of Parabolic Trough Collectors," Energy Convers. Manag., **149**, pp. 275–292.

[181] Bellos, E., Tzivanidis, C., and Antonopoulos, K. A., 2017, "A Detailed Working Fluid Investigation for Solar Parabolic Trough Collectors," Appl. Therm. Eng., **114**, pp. 374–386.

[182] Bellos, E., Tzivanidis, C., " Assessment of the thermal enhancement methods in parabolic trough collectors", 2018, Int J Energy Environ Eng., **9**, pp. 59–70. https://doi.org/10.1007/s40095-017-0255-3.

[183] Al-Sulaiman, F. A., 2014, “Exergy Analysis of Parabolic Trough Solar Collectors Integrated with Combined Steam and Organic Rankine Cycles,” Energy Convers. Manag., **77**, pp. 441–449.

[184] “Lienhard A Heat Transfer Textbook. [Online]. Available: http://web.mit.edu/lienhard/www/ahtt.html” [Accessed: 01-Mar-2019.]

[185] Ferraro, V., Imineo, F., and Marinelli, V., 2013, “An Improved Model to Evaluate Thermodynamic Solar Plants with Cylindrical Parabolic Collectors and Air Turbine Engines in Open Joule e Brayton Cycle,” EGY, **53**, pp. 323–331.

[186] Behar, O., Khellaf, A., and Mohammedi, K., 2015, “A Novel Parabolic Trough Solar Collector Model – Validation with Experimental Data and Comparison to Engineering Equation Solver (EES),” Energy Convers. Manag., **106**, pp. 268–281.

[187] Petela, R., 2003, “Exergy of Undiluted Thermal Radiation,” **74**(June), pp. 469–488.

[188] Sun, W., Yue, X., and Wang, Y., 2017, “Exergy Efficiency Analysis of ORC (Organic Rankine Cycle) and ORC-Based Combined Cycles Driven by Low-Temperature Waste Heat,” Energy Convers. Manag., **135**, pp. 63–73.

[189] Herold, Keith E.,Reinhard Radermacher, S. A. K., 2016, *Absorption Chiller and*

Heat Pumps. 2nd Edition, CRC Press, ISBN 9781498714341.

[190] Garousi Farshi, L., Mosaffa, A. H., Infante Ferreira, C. A., and Rosen, M. A., 2014, "Thermodynamic Analysis and Comparison of Combined Ejector-Absorption and Single Effect Absorption Refrigeration Systems," Appl. Energy, **133**, pp. 335–346.

[191] Shi, C., Chen, H., Chen, W., Zhang, S., Chong, D., and Yan, J., 2015, "1D Model to Predict Ejector Performance at Critical and Sub-Critical Operation in the Refrigeration System," Energy Procedia, **75**, pp. 1477–1483.

[192] Daniel Salavera, Simona Libotean, Kashinath R. Patil, Xavier Esteve, Alberto Coronas, 2006, "Densities and Heat Capacities of the Ammonia + Water + NaOH and Ammonia + Water + KOH Solutions.", Journal of Chemical & Engineering, 2006, 51 (3), 1020-1025 , DOI: 10.1021/je050512z.

[193] Bellos, E., and Tzivanidis, C., 2017, "Parametric Analysis and Optimization of a Solar Driven Trigeneration System Based on ORC and Absorption Heat Pump," J. Clean. Prod., **161**(May), pp. 493–509.

[194] "EES: Engineering Equation Solver | F-Chart Software : Engineering Software" [Online]. Available: http://fchart.com/ees/. [Accessed: 18-Nov-2018].

[195] Dudley, V. E., Evans, L. R., and Matthews, C. W., 1995, *Test Results, Industrial Solar Technology Parabolic Trough Solar Collector*, Albuquerque, NM, and Livermore, CA (United States).

[196] Moss, T. A., and Brosseau, D. A., 2005, *Final Test Results for the Schott HCE on*

a LS-2 Collector., Albuquerque, NM, and Livermore, CA (United States).

[197] Forristall, R., and R., 2003, *Heat Transfer Analysis and Modeling of a Parabolic Trough Solar Receiver Implemented in Engineering Equation Solver*, Golden, CO (United States).

[198] "Therminol VP1 | Synthetic Heat Transfer Fluids" [Online]. Available: https://www.therminol.com/products/Therminol-VP1. [Accessed: 18-Nov-2018].

[199] Al-Abbadi, N. M., 2005, "Wind Energy Resource Assessment for Five Locations in Saudi Arabia," Renew. Energy, **30**(10), pp. 1489–1499.

[200] Yousef Naji Dabwan, 2013, Thermodynamic Performance Assessment Of A Novel Waste Heat Based Triple Effect Refrigeration Cycle", Master's Thesis, King Fahd University Of Petroleum & Dhahran , Saudi Arabia."

[201] "Maps and Graphs" [Online]. Available: https://rratlas.energy.gov.sa/RRMMDataPortal/en/MapTool. [Accessed: 26-Mar-2019].

[202] Libotean, S., Salavera, D., Valles, M., Esteve, X., and Coronas, A., 2007, "Vapor-Liquid Equilibrium of Ammonia + Lithium Nitrate + Water and Ammonia + Lithium Nitrate Solutions from (293.15 to 353.15) K," J. Chem. Eng. Data, **52**(3), pp. 1050–1055.

[203] Libotean, S., Martı, A., Salavera, D., Valles, M., Esteve, X., and Coronas, A., 2008, "Densities , Viscosities , and Heat Capacities of Ammonia + Lithium Nitrate and Ammonia + Lithium Nitrate + Water Solutions between (293 . 15 and 353 .

15) K," J. Chem. Eng., pp. 2383–2388.

[204] Libotean, S., Martín, A., Salavera, D., Valles, M., Esteve, X., and Coronas, A., 2008, "Densities, Viscosities, and Heat Capacities of Ammonia + Lithium Nitrate and Ammonia + Lithium Nitrate + Water Solutions between (293.15 and 353.15) K," J. Chem. Eng. Data, **53**(10), pp. 2383–2388.

[205] Odeh, S. D., Morrison, G. L., and Behnia, M., 1998, "Modelling of Parabolic Trough Direct Steam Generation Solar Collectors," Sol. Energy, **62**(6), pp. 395–406.

[206] Bellos, E., and Tzivanidis, C., 2018, "Parametric Analysis and Optimization of a Cooling System with Ejector-Absorption Chiller Powered by Solar Parabolic Trough Collectors," Energy Convers. Manag., **168**(July), pp. 329–342.

[207] Cacciola, G., Restuccia, G., and Aristov, Y., 1995, "Vapor Pressure of (Potassium Hydroxide + Ammonia + Water) Solutions," J. Chem. Eng. Data, **40**(1), pp. 267–270.

[208] Bellos, E., Tzivanidis, C., and Antonopoulos, K. A., 2016, "Exergetic, Energetic and Financial Evaluation of a Solar Driven Absorption Cooling System with Various Collector Types," Appl. Therm. Eng., **102**(April 2016), pp. 749–759.

APPENDICES

Appendix - A Calculation of NH_3-$LiNO_3$ Solution Properties

Refrigerant (NH_3) thermophysical properties are taken directly from EES. But absorbent (NH_3-$LiNO_3$) thermophysical properties are not readily available. Liquid-vapor pressures of NH_3-$LiNO_3$ are calculated from the correlations provided by [202] and density from [203]. An excellent correlation is provided by Farshi et al. [113] for calculating the enthalpy and entropy of Ammonia-Lithium Nitrate solutions.

A.1 Pressure calculation of NH_3-$LiNO_3$

Libotean et al. [202] measured the pressure of Ammonium Lithium-Nitrate by a static method within 20°-80°C temperature range while ammonia mass fraction (x) range was from 0.2 to 0.6. The experimental values of pressure (P), temperature (T) and ammonia mass fractions (x) was correlated using a polynomial equation similar to that proposed by Cacciola et al. [207].

$$\ln\left(\frac{p}{\mathrm{kPa}}\right) = \sum_{i=0}^{3} A_i \times x^i + \frac{\sum_{i=0}^{i=3} B_i \times x^i}{\mathrm{T/K}} \tag{A.1}$$

The values of the adjustable parameter A_i and B_i are shown in the following table.

Appendix Table A - 1 Coefficient for pressure equation of NH_3-$LiNO_3$ system.

Coefficient	Value	Coefficient	Value
A_0	4.99×10^0	B_0	-1.79×10^3
A_1	8.85×10^1	B_1	-2.23×10^4
A_2	-1.98×10^2	B_2	6.13×10^4
A_3	1.35×10^2	B_3	-4.52×10^4

A.2 Density Calculation of NH_3-$LiNO_3$

Libotean et al. [204] measured the density of Ammonium Lithium-Nitrate within 20°-80°C temperature range while ammonia mass fraction range was from 0.2 to 0.6. The density equation data were fitted using equations similar to that of Salavera et al. [192].

$$\rho\left(\frac{\mathrm{g}}{\mathrm{cm}^3}\right) = A + B/T(\mathrm{K}) \tag{A.2}$$

A and B are composition dependent parameters for binary mixture of NH3-$LiNO_3$ formulated as follows:

$$A = \sum_{i=0}^{1} x^i \times a_i \tag{A.3}$$

$$B = \sum_{i=0}^{1} x^i \times b_i \tag{A.4}$$

Coefficients for A and B are tabulated below.

Appendix Table A - 2 Coefficients for density calculation of NH_3-$LiNO_3$

Coefficient	Value
a_0	1.521×10^{0}
a_1	-4.528×10^{-1}
b_0	-1.961×10^{-5}
b_1	-1.726×10^{-3}

A.3 Enthalpy Calculation for NH_3-$LiNO_3$

Farshi [113] formulated correlations to simplify the calculations for the specific enthalpy data of NH_3-$LiNO_3$ upon values of Ammonia concentration and solution temperature provided as inputs.

For, ammonia concentration, $x \leq 0.54$ specific enthalpy for NH_3-$LiNO_3$ is formulated as follows:

$$h = (a \times x - b) + c \times (d - x)^2 + (e + f \times x) \times (T - 273.15) + (g + h \times x) \times (T^2 - 273.15^2) \qquad \text{(A.5)}$$

For, ammonia concentration, $x \geq 0.54$ specific enthalpy for NH_3-$LiNO_3$ is formulated as follows:

$$h = (a \times x - b) + c \times (d - x)^{1.5} + (e + f \times x) \times (T - 273.15) + (g + h \times x) \times (T^2 - 273.15^2) \qquad \text{(A.6)}$$

Coefficients for the calculation of specific enthalpy values are given in the following table.

Appendix Table A - 3 Coefficients for calculating enthalpy of NH_3-$LiNO_3$

Coefficients	Value
a	200
b	215
c	1570
d	0.54
e	5.59×10^{-1}
f	3.241
g	1.039×10^{-3}
h	0.924×10^{-3}

A.4 Entropy calculation for NH_3-$LiNO_3$

For calculating the entropy of NH_3-$LiNO_3$ following formulation is also provided by Farshi [113] using ammonia concentration (x) and solution temperature (T) as inputs.

$$s = \left(a + b \times x + c \times x^2 + d \times x^3 + e \times (T - 273.15)\right)/(1 + f \times x + g \times x^2 + h \times x^3 + i \times (T - 273.15) + j \times (T - 273.15)^2) \tag{A.7}$$

Coefficients for the calculation of specific entropy values are given in the following table.

Appendix Table A - 4 Coefficients for calculating entropy of NH_3-$LiNO_3$.

Coefficients	Values
a	8.70310×10^{-1}
b	-3.98268
c	6.42203
d	-3.21434
e	4.19479×10^{-3}
f	-2.90321
g	4.13376
h	-2.19727
i	8.8621162×10^{-4}
j	-1.62347×10^{-6}

It should be noted that all the Temperature (T) values in the equations above are in Kelvin (K).

Appendix - B Data Tables of Validations and ORC Fluid Characterizations.

B.1 PTC Validation

PTC validation [180] results comparing the outlet temperature, energy and exergy efficiency data are shown in the following table.

Appendix Table B - 1 PTC validation results with SNL tests.

G_b (W/m^2)	**T_{in} (°C)**	**u_{air} (m/s)**	**T_{am} (°C)**	**V_{fluid} (L/min)**	**PTC outlet temperature, T_{out} (°C)**			**PTC energy efficiency, η_{en} (%)**			**PTC exergy efficiency, η_{ex} (%)**		
					Model	**Reference** [180]	**Deviation (%)**	**Model**	**Reference** [180]	**Deviation (%)**	**Model**	**Reference** [180]	**Deviation. (%)**
933.7	102.2	2.6	21.2	47.7	124.2	124	0.161	72.43	72.51	-0.110	18.49	18.74	-1.334
968.2	151	3.7	22.4	47.8	173.7	173.3	0.230	71.56	70.9	0.931	24.67	24.98	-1.241
982.3	197.5	2.5	24.3	49.1	219.9	219.5	0.182	70.54	70.17	0.527	28.96	29.28	-1.093
909.5	250.7	3.3	26.3	54.7	269.3	269.4	-0.037	70.25	68.81	2.093	32.4	32.66	-0.796
937.9	297.8	1.0	26.2	55.5	316.7	316.4	0.095	67.05	67.03	0.030	34.88	34.88	0.000
880.6	299	2.9	28.8	55.6	316.6	317.2	-0.190	66.58	68.92	-3.395	34.37	34.38	-0.029
903.2	355.9	4.2	27.5	56.3	374.1	374	0.027	63.34	63.82	-0.752	36	35.3	1.983
920.9	379.5	2.6	31.1	56.8	398.2	398	0.050	61.95	62.34	-0.626	36.01	34.9	3.181

B.2 ORC Validation

ORC validation results along with relevant data comparing the enthalpy and exergy data [183] are shown in the following table.

Appendix Table B - 2 ORC Validation comparing enthalpy and exergy.

Components.	**Stream**	**Mass flow rate (kg/s)**	**Temperature (K)**	**Pressure (kPa)**	**Enthalpy (kJ/kg)**			**Exergy (kJ/kg)**		
					Ref. [183]	**Model**	**Deviation (%)**	**Reference** [183]	**Model**	**Deviation (%)**
Vaporizer Outlet/Turbine Inlet	4	591.8	362.8	2678.9	296.1	296.2	-0.034	71.4	71.41	-0.014
Turbine Exhaust	5	591.8	315.5	887.5	277	277.4	-0.014	49	48.63	0.755
Pump Inlet / HX Outlet	6	591.8	308.2	887.5	100.9	101.4	-0.496	43.2	43.23	-0.069
Pump Outlet	7	591.8	309.6	2678.9	102.8	102.9	-0.097	44.8	44.81	-0.022
Condenser Inlet	18	2343	298.15	101.325	104.8	104.9	-0.095	0	0	0
Condenser Outlet	19	2343	308.15	101.325	149.3	146.7	1.741	0.8	0.6856	14.3

B.3 Validation of NH_3-$LiNO_3$ Properties

Data for the validation of pressure [202] and density [204] of NH_3-$LiNO_3$ are given in the Following tables.

Appendix Table B - 3 Pressure model validation for NH_3-$LiNO_3$.

Temperature (T) (K)	**NH_3 Mass Fraction, x (%)**	**$Pr_{exp.}$ (kPa)** [202]	**Pr_{model} (kPa)**	**Deviation (%)**
293.15	34.92	43.01	43.03	0.047
313.09	39.78	188.5	182.2	-3.342
353.15	43.41	1007.2	991.5	- 1.559
353.08	48.97	1522.5	1484	-2.529
333.13	53.78	1223.7	1164	-4.879

Appendix Table B - 4 Density model validation for NH_3-$LiNO_3$.

Temperature (T) (°C)	**Ammonia Mass Fraction, x**	**ρ_{exp} (kg/m^3)** [204]	**ρ_{model} (kg/m^3)**	**Deviation (%)**
20	0.5	1030	1036	0.583
30	0.5	1022.1	1027	0.479
40	0.4499	1062.6	1068	0.508
50	0.5	1006.1	1009	0.288
60	0.5	998	1001	0.301
70	0.4499	1040	1036	-0.385
80	0.4499	1032	1036	0.388

B.4 Absorption Model Validation

The developed absorption model is validated from [113] and tabulated below.

Appendix Table B - 5 Validation of basic ARC without ejector.

EES Compatibility	**Locations.**	**Temperature (°C)**	**NH_3 Conc. X_{NH3}**	**Pr_{ref} (kPa.)** [113]	**Pr_{model} (kPa.)**	**Enthalpy (kJ/kg)**			**Entropy (kJ/kg-K)**		
						h_{ref} [113]	**h_{model}**	**Deviation (%)**	**s_{ref}** [113]	**s_{model}**	**Deviation (%)**
EES NH_3-H_2O Function.	Generator refrigerant exit	90	1.00	1350.82	1351	1646.23	1646	-0.014	5.68	5.681	0.0176
	Condenser refrigerant exit	35	1.00	429.56	429.6	366.08	366.1	0.0055	1.57	1.566	-0.255
	Evaporator refrigerant exit	0	1.00	429.56	429.6	1462.23	1462	-0.016	5.62	5.624	0.0712
EES user written NH_3-$LiNO_3$ function	Absorber solution exit	35	0.51	429.56	446.2	-4.54	-3.433	-24.38	0.71	0.6924	-2.4789
	Generator solution inlet	66.76	0.51	1350.82	1351	96.22	97.91	1.76	1.02	1.023	0.2941
	Generator solution exit	90	0.44	1350.82	1351	149.62	150.2	0.388	1.12	1.156	3.21
	Absorber solution inlet	51.81	0.44	429.56	431	36.18	36.66	1.33	0.79	0.8078	2.253

B.5 Ejector- Absorption Model Validation

The developed absorption model for EARC is validated from [141] and tabulated below.

Appendix Table B - 6 Validation of ARC with ejector.

Streams	Temperature (°C)	Pressure (Reference) (kPa)	Pressure (Model) (kPa)	Mass flow rate (kg/s)	NH_3 Conc.	Specific Enthalpy (kJ/kg)			Specific Entropy (kJ/kg-K)		
						Reference [141]	**Model**	**% Deviation.**	**Reference** [141]	**Model.**	**% Deviation**
1	35	1350.82	1351	0.27	1.0	366.08	366.1	0.005	1.57	1.566	-0.255
2	0	429.56	429.6	0.27	1.0	366.08	366.1	0.005	1.61	1.608	-0.124
3	0	429.56	429.6	0.27	1.0	1462.23	1462	-0.016	5.62	5.624	0.071
4	35	441.65	446.2	1.89	0.51	-3.75	-3.433	-8.453	0.72	0.6924	-3.833
5	35.3	1350.82	1351	2.17	0.51	-2.81	-2.49	-11.388	0.72	0.6957	-3.375
6	66.41	1350.82	1351	2.17	0.51	96.3	96.78	0.498	1.02	1.02	0.000
14	90	1350.82	1351	0.27	1.0	1446.23	1646	13.813	5.68	5.681	0.018
15	90	1350.82	1375	1.89	0.44	149.62	150.2	0.388	1.12	1.156	3.214
16	51.81	1350.82	1351	1.89	0.44	36.18	36.36	0.498	0.79	0.8078	2.253
17	46.17	441.65	453.5	2.17	0.44	216.3	216.1	-0.092	1.41	1.418	0.567
18	100	101.32	101.3	0.24	-	2675.73	2676	0.010	7.35	7.355	0.068

Streams	**Temperature (°C)**	**Pressure (Reference) (kPa)**	**Pressure (Model) (kPa)**	**Mass flow rate (kg/s)**	**NH_3 Conc.**	**Specific Enthalpy (kJ/kg)**			**Specific Entropy (kJ/kg-K)**		
						Reference [141]	**Model**	**% Deviation.**	**Reference** [141]	**Model.**	**% Deviation**
19	100	101.32	101.3	0.24	-	419.06	419	-0.014	1.31	1.307	-0.229
20	27	4.76	4.76	16.75	-	113.12	113.2	0.071	0.4	0.3952	-1.200
21	32	4.76	4.76	16.75	-	134.04	134.1	0.045	0.46	0.4642	0.913
22	8	1.07	1.07	14.29	-	33.61	33.21	-1.190	0.12	0.1198	-0.167
23	3	1.07	1.07	14.29	-	12.61	12.6	-0.079	0.05	0.4589	-8.220
24	27	4.76	4.76	22.79	-	113.12	113.2	0.071	0.4	0.3952	-1.200
25	32	4.76	4.76	22.79	-	134.04	134.1	0.045	0.46	0.4642	0.913

B.6 ORC Fluid Performance Characteristics in ORC

Six ORC fluids that were discussed in section 4.7.2 . Their characterization data on with respect to temperature and pressure are mentioned in the following tables. Essential input parameters can be found in section 4.7.1 .

Appendix Table B - 7 Performance characteristics of R245fa in ORC.

Turbine inlet temperature, K.	Turbine inlet pressure, kPa.	Energy efficiency	Exergy efficiency
340	1000	0.02242	0.06001
350	1000	0.03622	0.09693
360	1000	0.04942	0.1323
370	1250	0.06156	0.1648
380	1500	0.07363	0.1971
390	2000	0.08511	0.2278
400	2250	0.09724	0.2603
420	3250	0.1221	0.3268
440	4500	0.1541	0.4124

Appendix Table B - 8 Performance characteristics of R134a in ORC.

Turbine inlet temperature, K.	Turbine inlet pressure, kPa.	Energy efficiency	Exergy efficiency
340	2000	0.0222	0.05942
350	2000	0.07396	0.198
360	2750	0.0775	0.2074
370	3250	0.08802	0.2356
380	3750	0.1014	0.2714
390	4250	0.1179	0.3155
400	5000	0.1262	0.3377
420	7000	0.14	0.3746
440	10000	0.1568	0.4198

Appendix Table B - 9 Performance characteristics of n-pentane in ORC.

Turbine inlet temperature, K.	Turbine inlet pressure, kPa.	Energy efficiency	Exergy efficiency
340	500	0.0234	0.06262
350	500	0.03672	0.09829
360	500	0.0496	0.1328
370	1000	0.06052	0.162
380	1000	0.07293	0.1952
390	1000	0.08496	0.2274
400	1250	0.09618	0.2574
420	1750	0.1182	0.3163
440	2250	0.1398	0.3743
460	3000	0.1618	0.4331
480	14000	0.1655	0.4429

Appendix Table B - 10 Performance characteristics of Toluene in ORC.

Turbine inlet temperature, K.	Turbine inlet pressure, kPa.	Energy efficiency	Exergy efficiency
340	100	0.02549	0.06882
350	100	0.03824	0.1023
360	100	0.05072	0.1358
370	100	0.06288	0.1683
380	100	0.07472	0.2
390	150	0.08611	0.2305
400	200	0.09721	0.2602
420	300	0.1186	0.3174
450	500	0.1486	0.3977
500	1200	0.1939	0.5189
550	2500	0.235	0.6289

Appendix Table B - 11 Performance characteristics of R410A in ORC.

Turbine inlet temperature, K.	Turbine inlet pressure, kPa.	Energy efficiency	Exergy efficiency
340	3750	0.03901	0.1044
350	4250	0.05447	0.1458
360	5000	0.06575	0.176
370	6000	0.07354	0.1968
380	6500	0.09109	0.2438
390	8000	0.09342	0.25
400	9000	0.1063	0.2845
420	12000	0.1254	0.3356

Appendix Table B - 12 Performance characteristics of R744 (CO2) in ORC.

Turbine inlet temperature, K.	Turbine inlet pressure, kPa.	Energy efficiency	Exergy efficiency
300	3750	0.07166	0.1918
350	6500	0.1363	0.3649
400	11000	0.385	0.5064
450	17500	0.4533	0.6302
500	25000	0.2815	0.7536

Appendix Table B - 13 Summary of energy and exergy efficiencies of ORC fluids at various turbine inlet temperatures.

Turbine inlet temperature, K	Energy efficiency					Exergy efficiency				
	R134a	R245fa	n-pentane	Toluene	R410A	R134a	R245fa	n-pentane	Toluene	R410A
340	0.02220	0.02242	0.02340	0.02549	0.03901	0.05942	0.06001	0.06262	0.06882	0.10440
350	0.07396	0.03622	0.03672	0.03824	0.05447	0.19800	0.09693	0.09829	0.10230	0.14580
360	0.07750	0.04942	0.04960	0.05072	0.06575	0.20740	0.13230	0.13280	0.13580	0.1760
370	0.08802	0.06156	0.06052	0.06288	0.07354	0.23560	0.16480	0.16200	0.16830	0.19680
380	0.10140	0.07363	0.07293	0.07472	0.09109	0.27140	0.19710	0.19520	0.20000	0.24380
390	0.11790	0.08511	0.08496	0.08611	0.09342	0.31550	0.22780	0.22740	0.23050	0.25000
400	0.12620	0.09724	0.09618	0.09721	0.10630	0.33770	0.26030	0.25740	0.26020	0.28450
420	0.14000	0.12210	0.11820	0.11860	0.12540	0.37460	0.32680	0.31630	0.31740	0.33560
440	0.15680	0.15410	0.13980	-	-	0.41980	0.41240	0.37430	-	-
450	-	-	-	0.14860	-	-	-	-	0.39770	-
460	-	-	0.1618	-	-	-	-	0.4331	-	-
480	-	-	0.1655	-	-	-	-	0.4429	-	-
500	-	-	-	0.19390	-	-	-	-	0.51890	-
550	-	-	-	0.23500	-	-	-	-	0.62890	-

B.7 Performance of PTC Integrated ORC for different ORC Fluids

Performance of the combined PTC and ORC is investigated for different ORC fluids. First and second law efficiency of the combined PTC and ORC system are calculated and tabulated below. Essential input parameters can be found in section 4.7.1.

Appendix Table B - 14 Performance of PTC integrated ORC for R134a at turbine inlet temperature of 440 K and pressure of 10000 kPa.

Solar irradiation, G_b (kW/m^2)	Net work output, W_{net} (kW).	First law efficiency	Second law efficiency
0.3	211.8	0.1207	0.1296
0.4	286.2	0.1223	0.1314
0.5	364.3	0.1246	0.1338
0.6	442	0.1259	0.1353
0.7	522.1	0.1275	0.1369
0.8	605	0.1293	0.1388
0.9	692.8	0.1316	0.1413
1	777.2	0.1329	0.1427

Appendix Table B - 15 Performance of PTC integrated ORC for R245fa at turbine inlet temperature of 440 K and pressure of 4500 kPa.

Solar irradiation, G_b (kW/m^2)	Net work output, W_{net} (kW).	First law efficiency	Second law efficiency
0.3	208.1	0.1185	0.1273
0.4	281.1	0.1201	0.129
0.5	357.9	0.1224	0.1314
0.6	434.2	0.1237	0.1329
0.7	512.8	0.1252	0.1345
0.8	594.3	0.127	0.1364
0.9	680.5	0.1293	0.1388
1	763.5	0.1305	0.1402

Appendix Table B - 16 Performance of PTC integrated ORC for n-pentane at turbine inlet temperature of 460 K and pressure of 3000 kPa.

Solar irradiation, G_b (kW/m^2)	Net work output, W_{net} (kW).	First law efficiency	Second law efficiency
0.3	218.5	0.1245	0.1337
0.4	295.3	0.1262	0.1355
0.5	375.9	0.1285	0.138
0.6	456	0.1299	0.1395
0.7	538.6	0.1315	0.1413
0.8	624.1	0.1334	0.1432
0.9	714.7	0.1357	0.1458
1	801.8	0.1371	0.1472

Appendix Table B - 17 Performance of PTC integrated ORC for Toluene at turbine inlet temperature of 550 K and pressure of 2500 kPa.

Solar irradiation, G_b (kW/m^2)	**Net work output, W_{net} (kW).**	**First law efficiency**	**Second law efficiency**
0.3	317.3	0.1808	0.1942
0.4	428.7	0.1832	0.1968
0.5	545.8	0.1866	0.2004
0.6	662.2	0.1887	0.2026
0.7	782.1	0.191	0.2051
0.8	906.3	0.1937	0.208
0.9	1038	0.1971	0.2117
1	1164	0.1990	0.2138

Appendix Table B - 18 Performance of PTC integrated ORC for R410A at turbine inlet temperature of 420 K and pressure of 12000 kPa.

Solar irradiation, G_b (kW/m^2)	**Net work output, W_{net} (kW).**	**First law efficiency**	**Second law efficiency**
0.3	169.3	0.09647	0.1036
0.4	228.8	0.09776	0.105
0.5	291.2	0.09956	0.1069
0.6	353.3	0.1007	0.1081
0.7	417.3	0.1019	0.1095
0.8	483.6	0.1033	0.111
0.9	553.7	0.1052	0.113
1	621.3	0.1062	0.1141

B.8 Performance of the Combined System with Various ORC Fluids

System performance factor and exergy efficiency of the solar assisted combined power and cooling system are calculated for different ORC fluid at their highest performance conditions. Essential input parameters can be found in section 6.3.1.

Appendix Table B - 19 Performance of the combined system for R134a at turbine inlet temperature of 440 K and pressure of 10000 kPa.

Solar irradiation, G_b (kW/m^2)	Net work output, W_{net} (kW).	Cooling output, Q_{ev} (kW)	System performance factor, η_I	Exergy efficiency, η_{II}
0.3	157.7	180.6	0.1928	0.1066
0.4	212.8	240.8	0.1939	0.1078
0.5	271.8	302.9	0.1965	0.11
0.6	332.2	364.6	0.1985	0.1118
0.7	393	425.7	0.1999	0.1133
0.8	456.5	487.4	0.2017	0.115
0.9	517.9	548.4	0.2025	0.1159
1	579.7	612.3	0.2038	0.1167

Appendix Table B - 20 Performance of the combined system for R245fa at turbine inlet temperature of 440 K and pressure of 4500 kPa.

Solar irradiation, G_b (kW/m^2)	Net work output, W_{net} (kW).	Cooling output, Q_{ev} (kW)	System performance factor, η_I	Exergy efficiency, η_{II}
0.3	154.9	180.6	0.1912	0.1049
0.4	209.1	240.8	0.1923	0.106
0.5	267	302.9	0.1949	0.1082
0.6	326.3	364.6	0.1968	0.11
0.7	386.1	425.7	0.1982	0.1114
0.8	448.4	487.4	0.1999	0.1131
0.9	508.7	548.4	0.2008	0.114
1	569.5	612.3	0.202	0.1148

Appendix Table B - 21 Performance of the combined system for n-pentane at turbine inlet temperature of 460 K and pressure of 3000 kPa.

Solar irradiation, G_b (kW/m^2)	Net work output, W_{net} (kW).	Cooling output, Q_{ev} (kW)	System performance factor, η_I	Exergy efficiency, η_{II}
0.3	162.7	180.6	0.1956	0.1097
0.4	219.6	240.8	0.1967	0.1109
0.5	280.4	302.9	0.1994	0.1131
0.6	342.7	364.6	0.2015	0.115
0.7	405.4	425.7	0.203	0.1165
0.8	470.9	487.4	0.2048	0.1183
0.9	534.3	548.4	0.2056	0.1192
1	598.1	612.3	0.2069	0.1201

Appendix Table B - 22 Performance of the combined system for Toluene at turbine inlet temperature of 550 K and pressure of 2500 kPa.

Solar irradiation, G_b (kW/m^2)	Net work output, W_{net} (kW).	Cooling output, Q_{ev} (kW)	System performance factor, η_I	Exergy efficiency, η_{II}
0.3	236.3	180.6	0.2375	0.1547
0.4	318.8	240.8	0.2392	0.1564
0.5	407.2	302.9	0.2428	0.1597
0.6	497.6	364.6	0.2456	0.1624
0.7	588.8	425.7	0.2477	0.1646
0.8	683.8	487.4	0.2503	0.1671
0.9	775.8	548.4	0.2515	0.1685
1	868.4	612.3	0.2531	0.1697

Appendix Table B - 23 Performance of the combined system for R410A at turbine inlet temperature of 420 K and pressure of 12000 kPa.

Solar irradiation, G_b (kW/m^2)	Net work output, W_{net} (kW).	Cooling output, Q_{ev} (kW)	System performance factor, η_I	Exergy efficiency, η_{II}
0.3	126.1	180.6	0.1747	0.08724
0.4	170.1	240.8	0.1756	0.08817
0.5	217.3	302.9	0.1778	0.08994
0.6	265.5	364.6	0.1795	0.09143
0.7	314.1	425.7	0.1807	0.09259
0.8	364.9	487.4	0.1821	0.09395
0.9	414	548.4	0.1828	0.09466
1	463.4	612.3	0.1839	0.09534

Appendix - C Integration of Thermal Energy Storage

Thermal energy storage is a very essential accessory to add with CSP systems to store energy and utilize this stored energy when there is no solar energy or solar irradiation is very low. It also makes the system stable by removing fluctuation in inputs.

The storage tank is modelled with mixing zone theory where three mixing zones constitutes the TES. For every zone an energy balance is made with an energy balance equation. Following mathematical formulations are given to design the TES [208].

For every zone,

$$Storage = Input - Output - Losses \tag{C.1}$$

Assumptions,

$$T_{st,1} = T_{01} \tag{C.2}$$

$$T_{st,3} = T_{col,in} \tag{C.3}$$

$$m_{htf} = m_{storage} \tag{C.4}$$

Heat transfer coefficient,

$$U_{tank} = 0.5 \times 10^{-3} \tag{C.5}$$

Tank volume,

$$V_{tank} = {}^{Area_{total}}/_{30} = \frac{\pi}{4} \times (D_{tank})^2 \times h_{tank} \tag{C.6}$$

Tank height,

$$h_{tank} = D_{tank} \tag{C.7}$$

Tank length,

$$L_{tank} = \frac{D_{tank}}{2} \tag{C.8}$$

Tank mass,

$$M_{tank} = {}^{\rho_{fluid} \times V_{tank}}/_{3} \tag{C.9}$$

Area of first level,

$$A_{st,1} = {}^{\pi}/_{4} \times D_{tank}{}^{2} + {}^{\pi}/_{3} \times D_{tank} \times L_{tank} \tag{C.10}$$

Area of second level,

$$A_{st,3} = {}^{\pi}/_{3} \times D_{tank} \times L_{tank} \tag{C.11}$$

Area of third level

$$A_{st,3} = {}^{\pi}/_{4} \times {D_{tank}}^{2} + {}^{\pi}/_{3} \times D_{tank} \times L_{tank} \tag{C.12}$$

For steady state conditions,

$$\begin{aligned} m_{htf} \times c_p \times \left(T_{col,out} - T_{st,1}\right) & \\ + \ m_{storage} \times c_p \times \left(T_{st,2} - T_{st,1}\right) & \\ - U_{tank} \times A_{st,1}. \times \left(T_{st,1} - T_{am}\right) = 0 & \end{aligned} \tag{C.13}$$

$$\begin{aligned} m_{htf} \times c_p \times \left(T_{st,1} - T_{st,2}\right) & \\ + \ m_{storage} \times c_p \times \left(T_{st,3} - T_{st,2}\right) & \\ - U_{tank} \times A_{st,2}. \times \left(T_{st,2} - T_{am}\right) = 0 & \end{aligned} \tag{C.14}$$

$$\begin{aligned} m_{htf} \times c_p \times \left(T_{st,2} - T_{st,3}\right) & \\ + \ m_{storage} \times c_p \times \left(T_{03} - T_{st,3}\right) & \\ - U_{tank} \times A_{st,3}. \times \left(T_{st,3} - T_{am}\right) = 0 & \end{aligned} \tag{C.15}$$

If TES is added to the existing system of PTC integrated ORC, the system will be as follows:

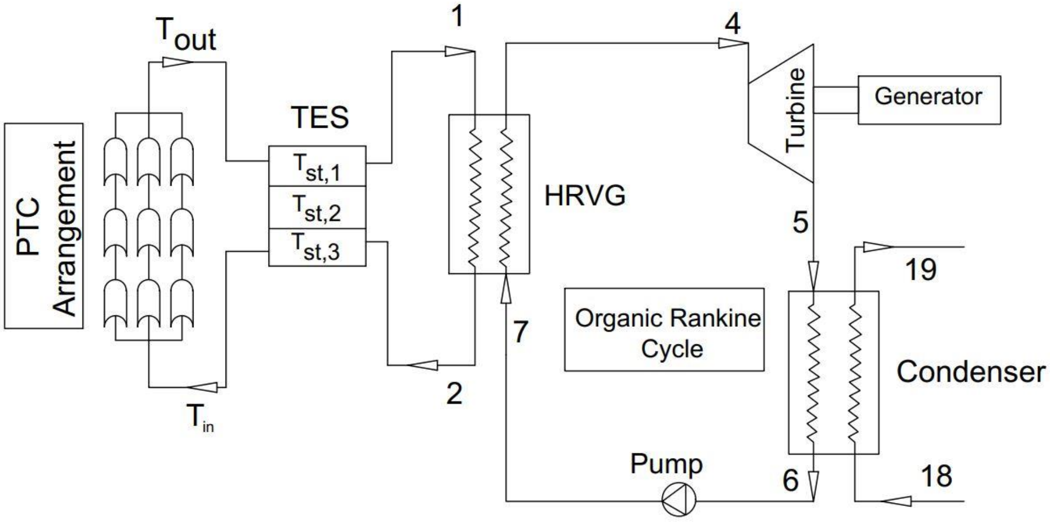

Appendix Figure C - 1 Schematic of solar assisted PTC integrated ORC with TES.

The first and second law efficiency of the system are shown in Appendix Figure C - 2. It is observed that higher solar irradiation resulted better efficiency of the overall system. After utilizing the heat in HRVG, the thermal storage stores rest of the energy the storage and stabilize the inlet temperature of HTF into PTC. This removes fluctuations in the power output and ensure a stable system.

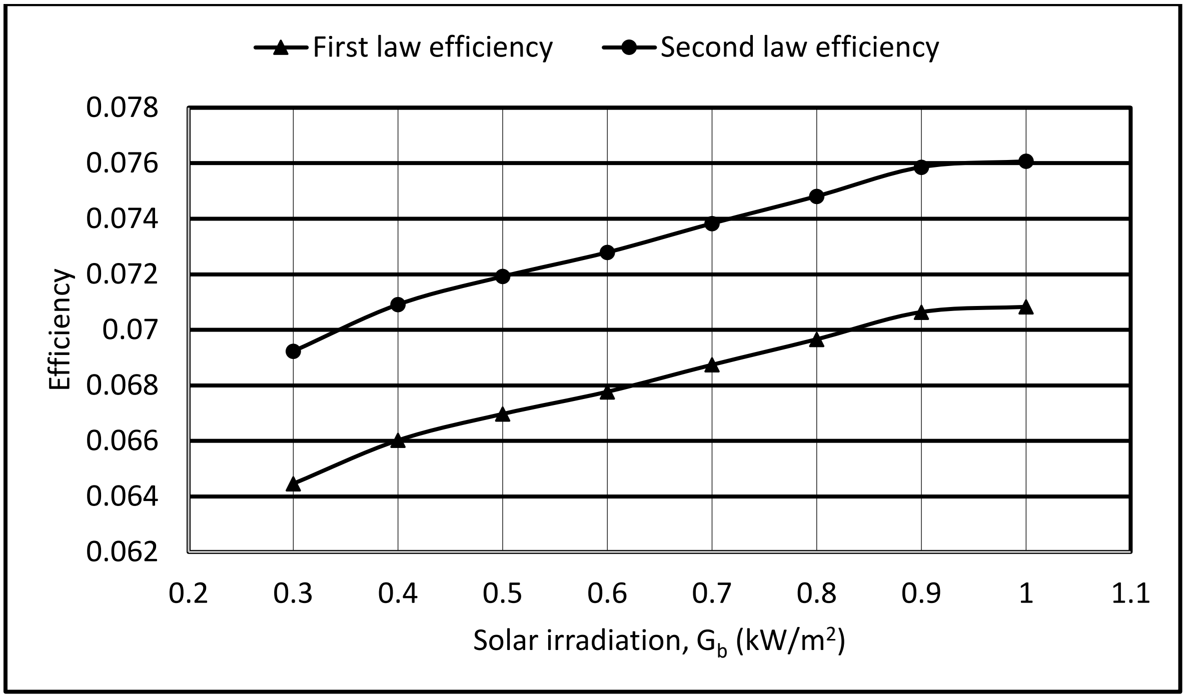

Appendix Figure C - 2 System performance factor and exergy efficiency of the PTC integrated ORC with TES.

In the following figures, a relative comparison is shown for the PTC integrated ORC systems with and without TES in terms of first and second law efficiency.

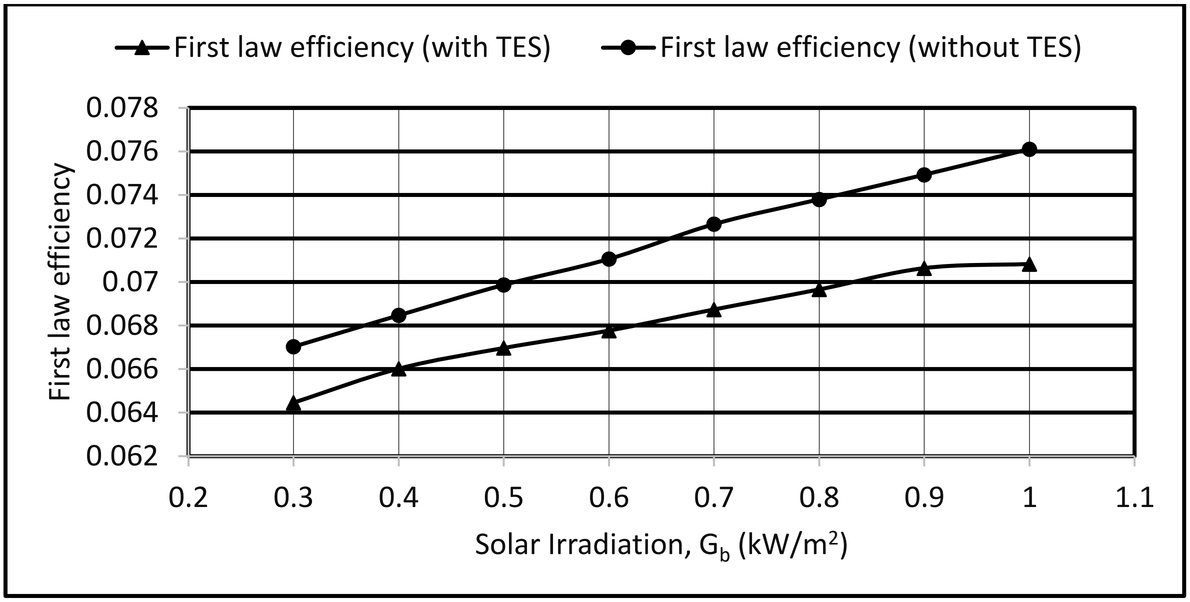

Appendix Figure C - 3 Comparison of first law efficiency of PTC integrated ORC systems with and without TES.

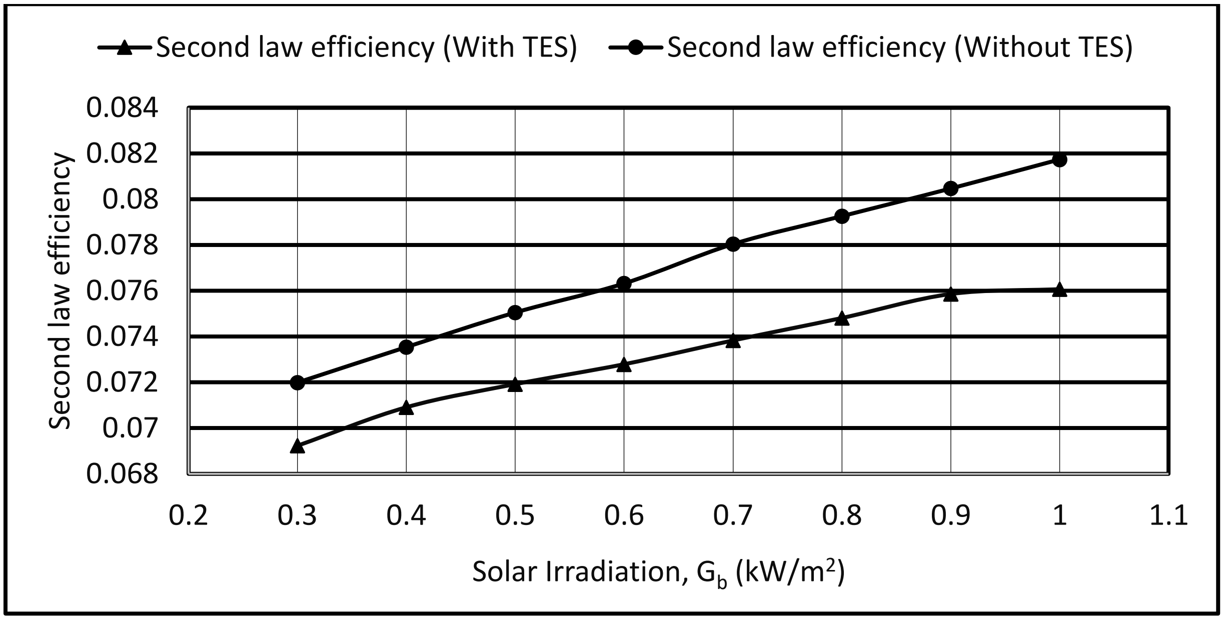

Appendix Figure C - 4 Comparison of second law efficiency of PTC integrated ORC systems with and without TES.

If TES is added to the existing combined system for simultaneous generation of power and cooling the system will be as shown in the following figure.

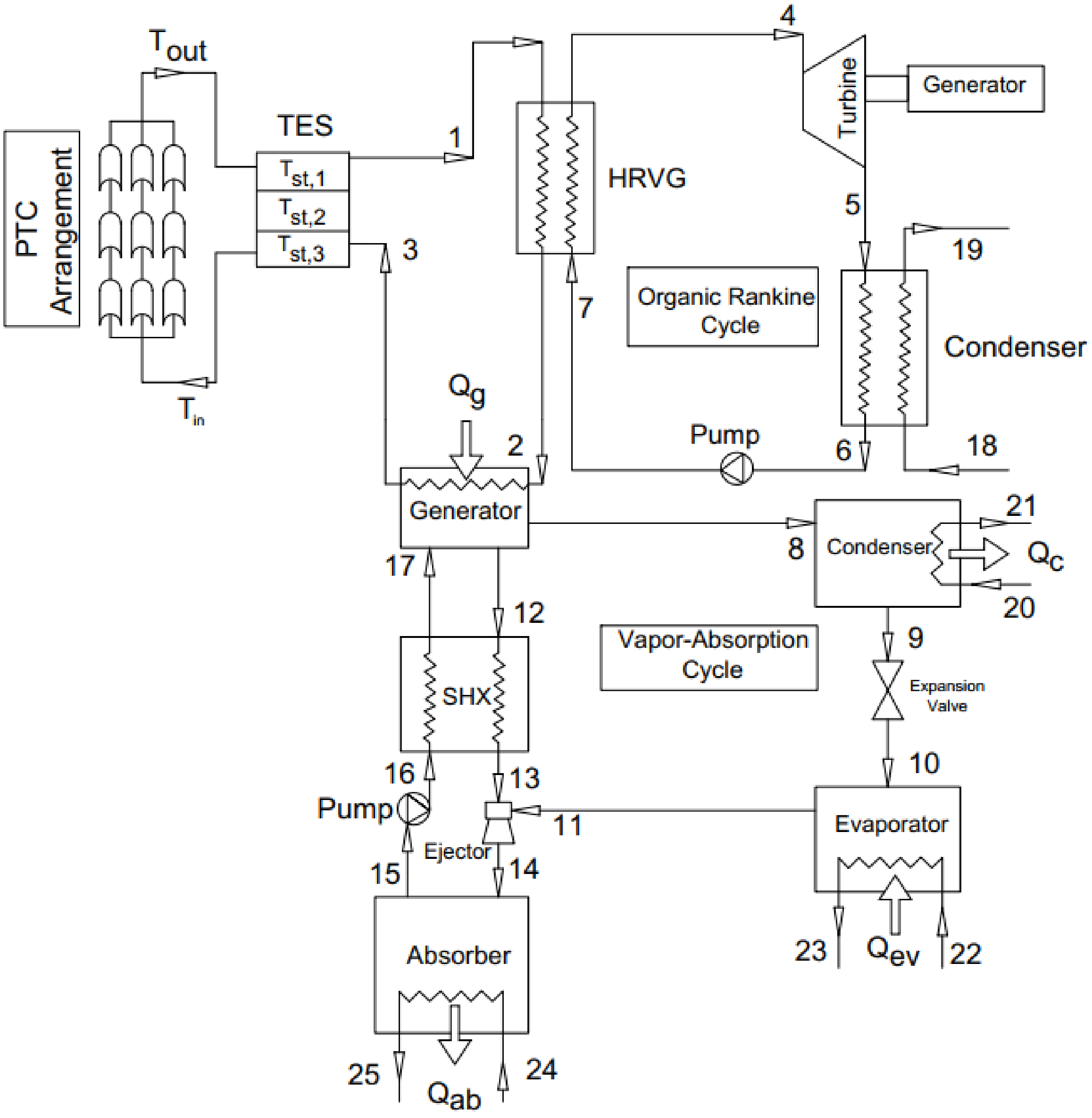

Appendix Figure C - 5 Schematic of solar assisted combined power and cooling cycle with TES.

System performance factor and exergy efficiency of the combined system are shown below.

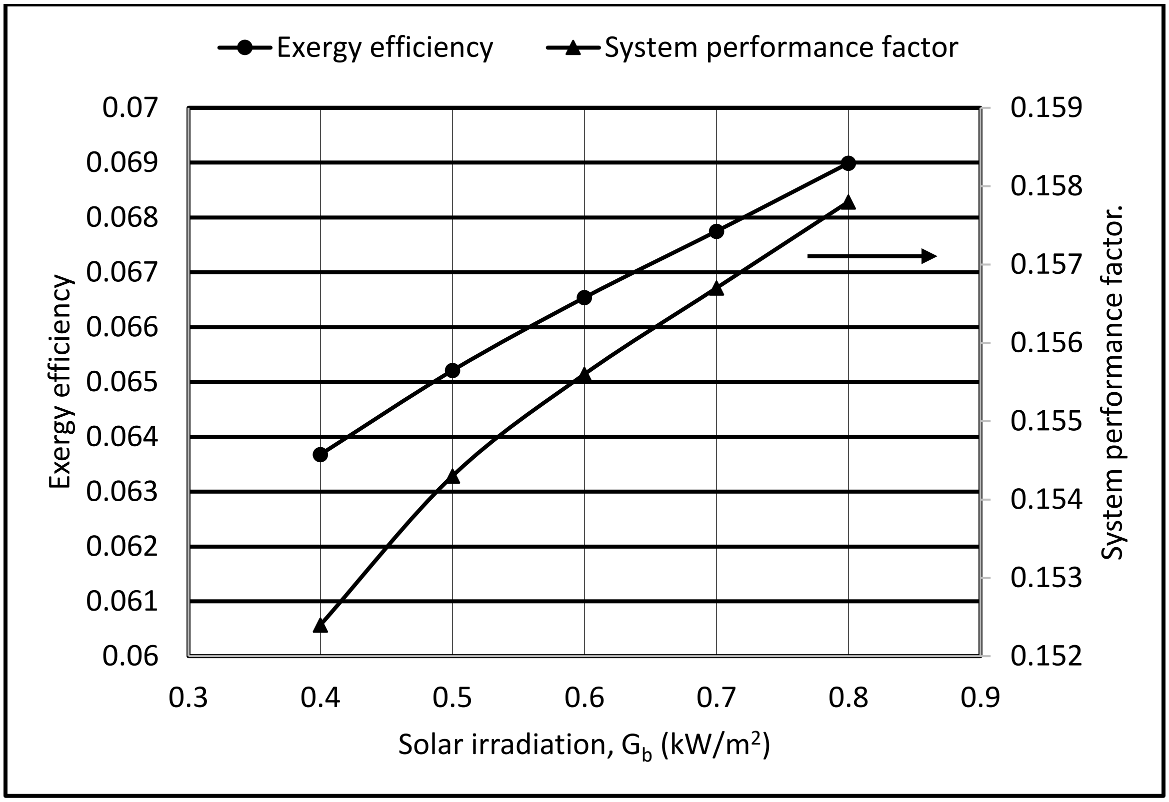

Appendix Figure C - 6 System performance factor and exergy efficiency of the combined system with TES.

In the following figures, a relative comparison is shown for the combined systems with and without TES in terms of system performance factor and exergy efficiency.

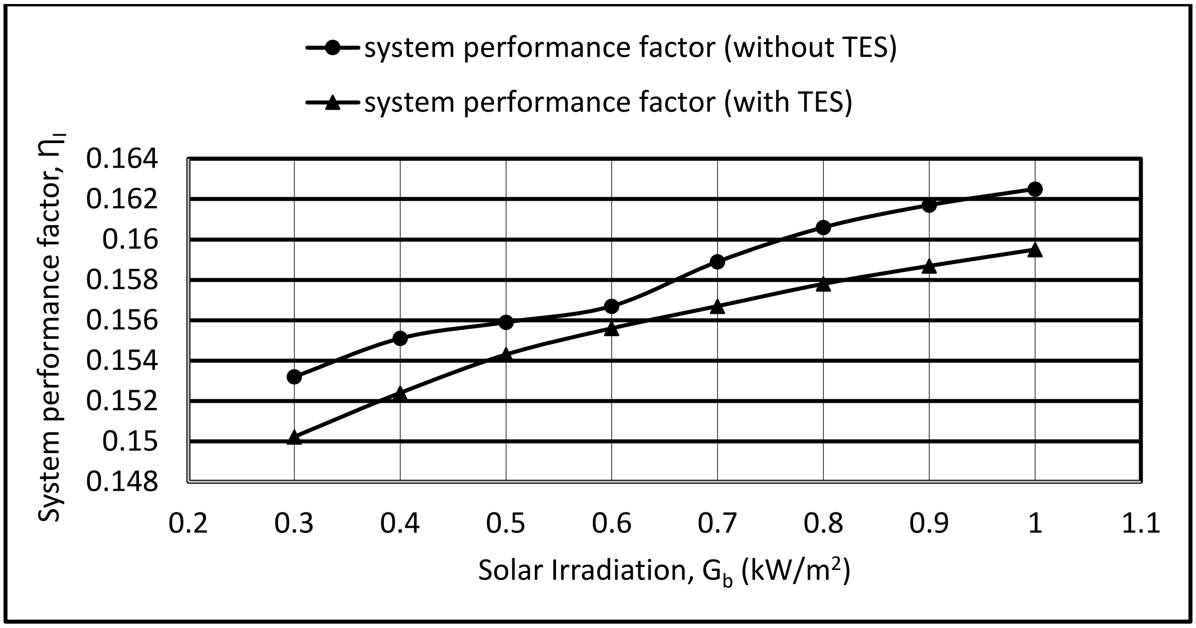

Appendix Figure C - 7 Comparison of System performance factor for the combined systems with and without TES.

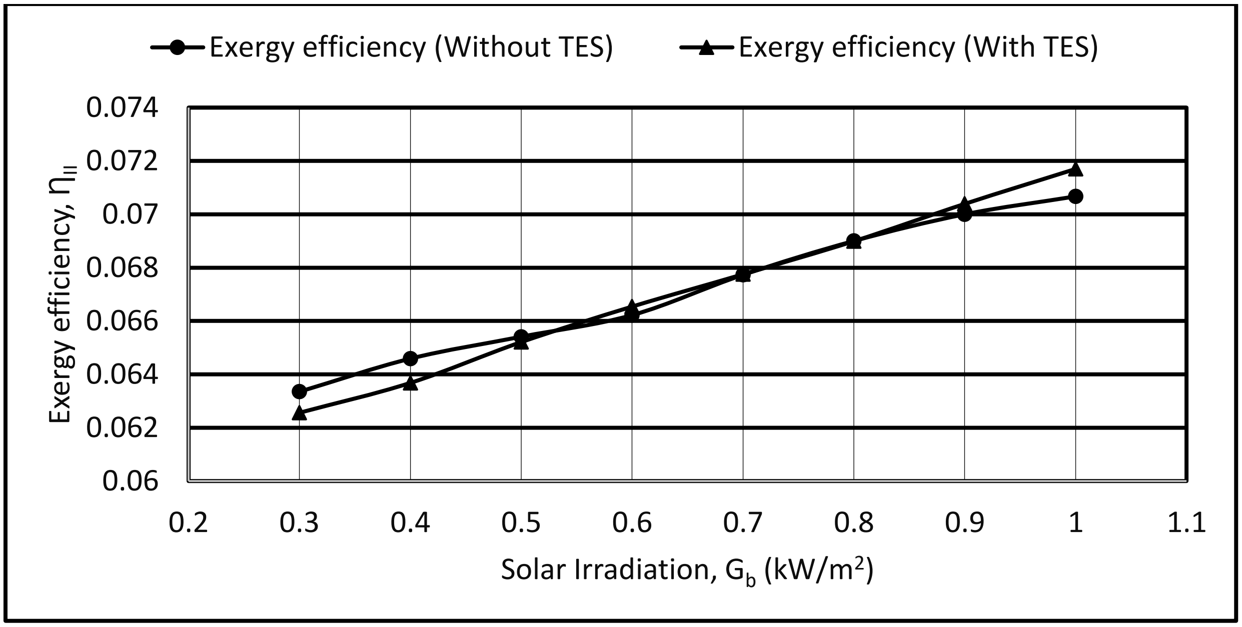

Appendix Figure C - 8 Comparison of exergy efficiency for the combined systems with and without TES.

It should be noted that, to precisely compare the effect of system with and without TES, a time dependent dynamic simulation is necessary. Because, in steady state analysis all the energy generated by the PTC is utilized by its components like HRVG, EARC generator. Otherwise, the inlet temperature of the PTC (Tin) and the outlet temperature of the generator (T03) would not be same. On the other hand, a system that incorporates TES, the energy consumed by the components are not necessarily equal to the energy generated by the heat source, PTC in this case. With the progress of solar irradiation, TES stores a portion of the energy generated and release the rest of the energy for the consumption of the heat driven components like HRVG , EARC generators. So, it is not feasible to compare the two system in a steady state analysis. An unsteady state analysis which can record the progress of necessary input and output parameters over time, is needed to secure that objective.

Appendix - D PERMISSIONS OF CONTENTS

Permission for using LFR plant schematic [61] from Figure 2.4 is shown below.

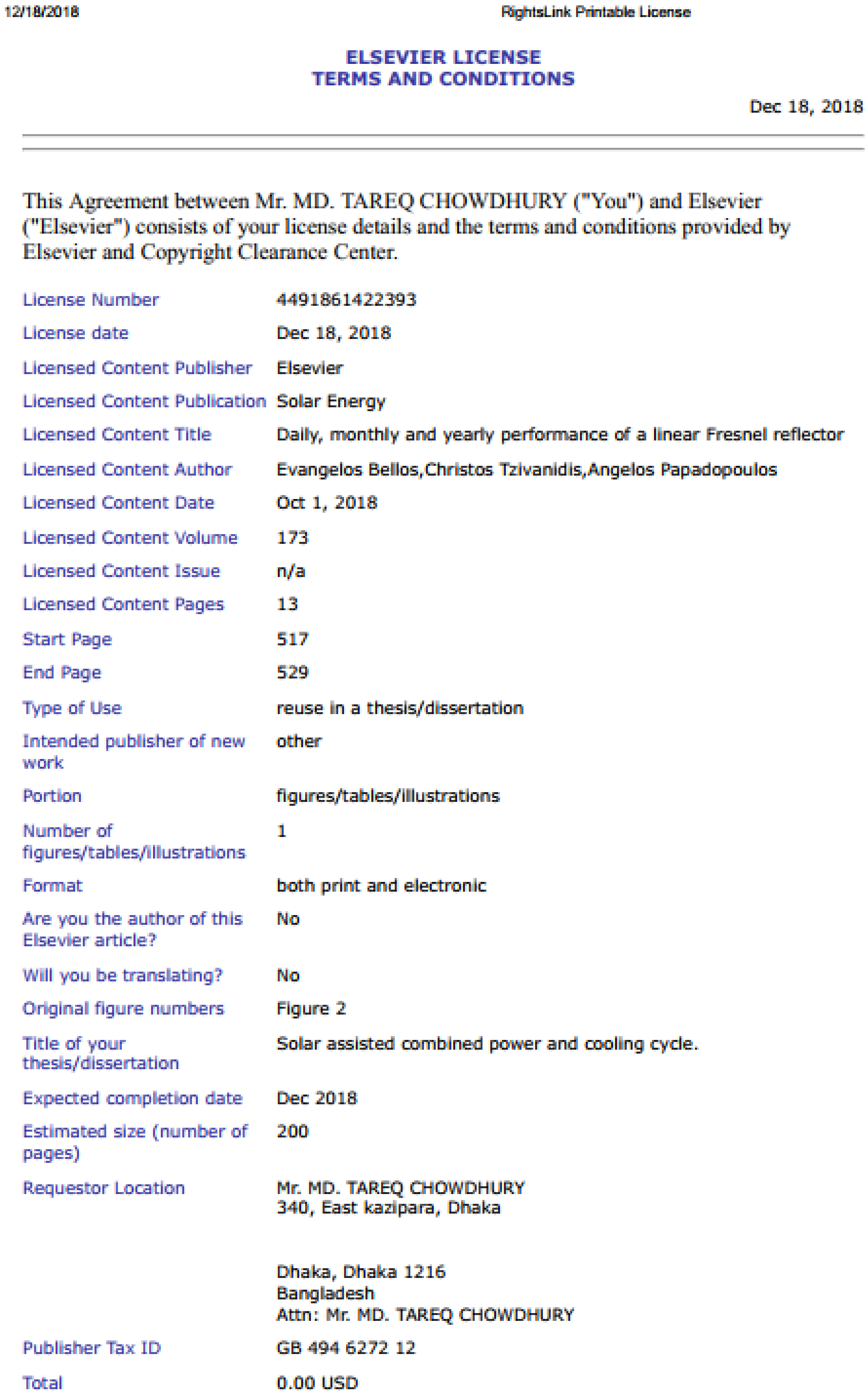

12/18/2018 RightsLink Printable License

ELSEVIER LICENSE
TERMS AND CONDITIONS

Dec 18, 2018

This Agreement between Mr. MD. TAREQ CHOWDHURY ("You") and Elsevier ("Elsevier") consists of your license details and the terms and conditions provided by Elsevier and Copyright Clearance Center.

License Number	4491861422393
License date	Dec 18, 2018
Licensed Content Publisher	Elsevier
Licensed Content Publication	Solar Energy
Licensed Content Title	Daily, monthly and yearly performance of a linear Fresnel reflector
Licensed Content Author	Evangelos Bellos,Christos Tzivanidis,Angelos Papadopoulos
Licensed Content Date	Oct 1, 2018
Licensed Content Volume	173
Licensed Content Issue	n/a
Licensed Content Pages	13
Start Page	517
End Page	529
Type of Use	reuse in a thesis/dissertation
Intended publisher of new work	other
Portion	figures/tables/illustrations
Number of figures/tables/illustrations	1
Format	both print and electronic
Are you the author of this Elsevier article?	No
Will you be translating?	No
Original figure numbers	Figure 2
Title of your thesis/dissertation	Solar assisted combined power and cooling cycle.
Expected completion date	Dec 2018
Estimated size (number of pages)	200
Requestor Location	Mr. MD. TAREQ CHOWDHURY 340, East kazipara, Dhaka Dhaka, Dhaka 1216 Bangladesh Attn: Mr. MD. TAREQ CHOWDHURY
Publisher Tax ID	GB 494 6272 12
Total	0.00 USD

Permission for using Figure 2.6 regarding the importance of pinch point temperature [10] is shown below.

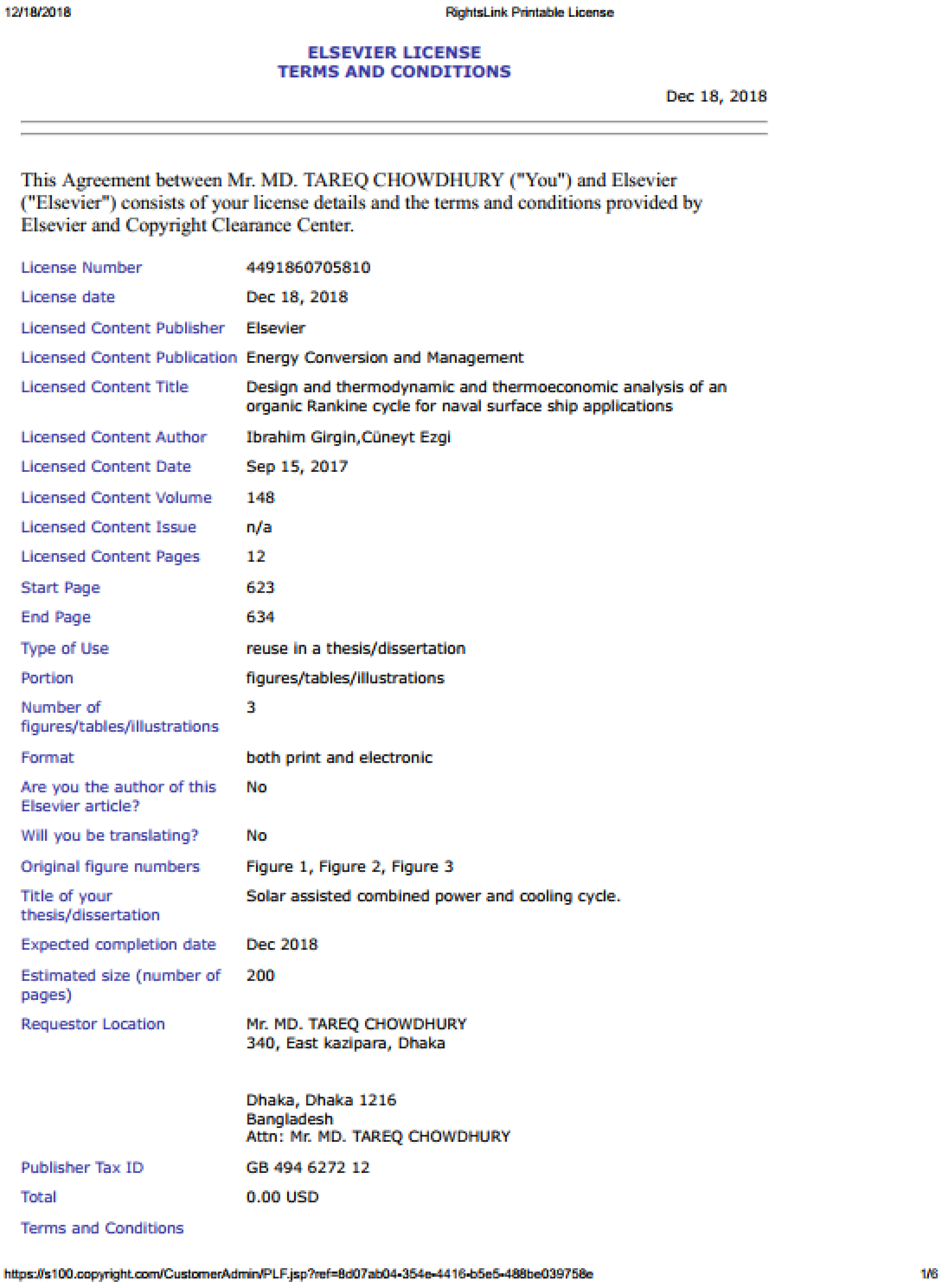

12/18/2018 RightsLink Printable License

ELSEVIER LICENSE
TERMS AND CONDITIONS

Dec 18, 2018

This Agreement between Mr. MD. TAREQ CHOWDHURY ("You") and Elsevier ("Elsevier") consists of your license details and the terms and conditions provided by Elsevier and Copyright Clearance Center.

License Number	4491860705810
License date	Dec 18, 2018
Licensed Content Publisher	Elsevier
Licensed Content Publication	Energy Conversion and Management
Licensed Content Title	Design and thermodynamic and thermoeconomic analysis of an organic Rankine cycle for naval surface ship applications
Licensed Content Author	Ibrahim Girgin,Cüneyt Ezgi
Licensed Content Date	Sep 15, 2017
Licensed Content Volume	148
Licensed Content Issue	n/a
Licensed Content Pages	12
Start Page	623
End Page	634
Type of Use	reuse in a thesis/dissertation
Portion	figures/tables/illustrations
Number of figures/tables/illustrations	3
Format	both print and electronic
Are you the author of this Elsevier article?	No
Will you be translating?	No
Original figure numbers	Figure 1, Figure 2, Figure 3
Title of your thesis/dissertation	Solar assisted combined power and cooling cycle.
Expected completion date	Dec 2018
Estimated size (number of pages)	200
Requestor Location	Mr. MD. TAREQ CHOWDHURY 340, East kazipara, Dhaka Dhaka, Dhaka 1216 Bangladesh Attn: Mr. MD. TAREQ CHOWDHURY
Publisher Tax ID	GB 494 6272 12
Total	0.00 USD
Terms and Conditions	

https://s100.copyright.com/CustomerAdmin/PLF.jsp?ref=8d07ab04-354e-4416-b5e5-488be039758e 1/6

The permission to reuse the partially modified Table 2.7 taken from Xu et al. [117] is attached as follows.

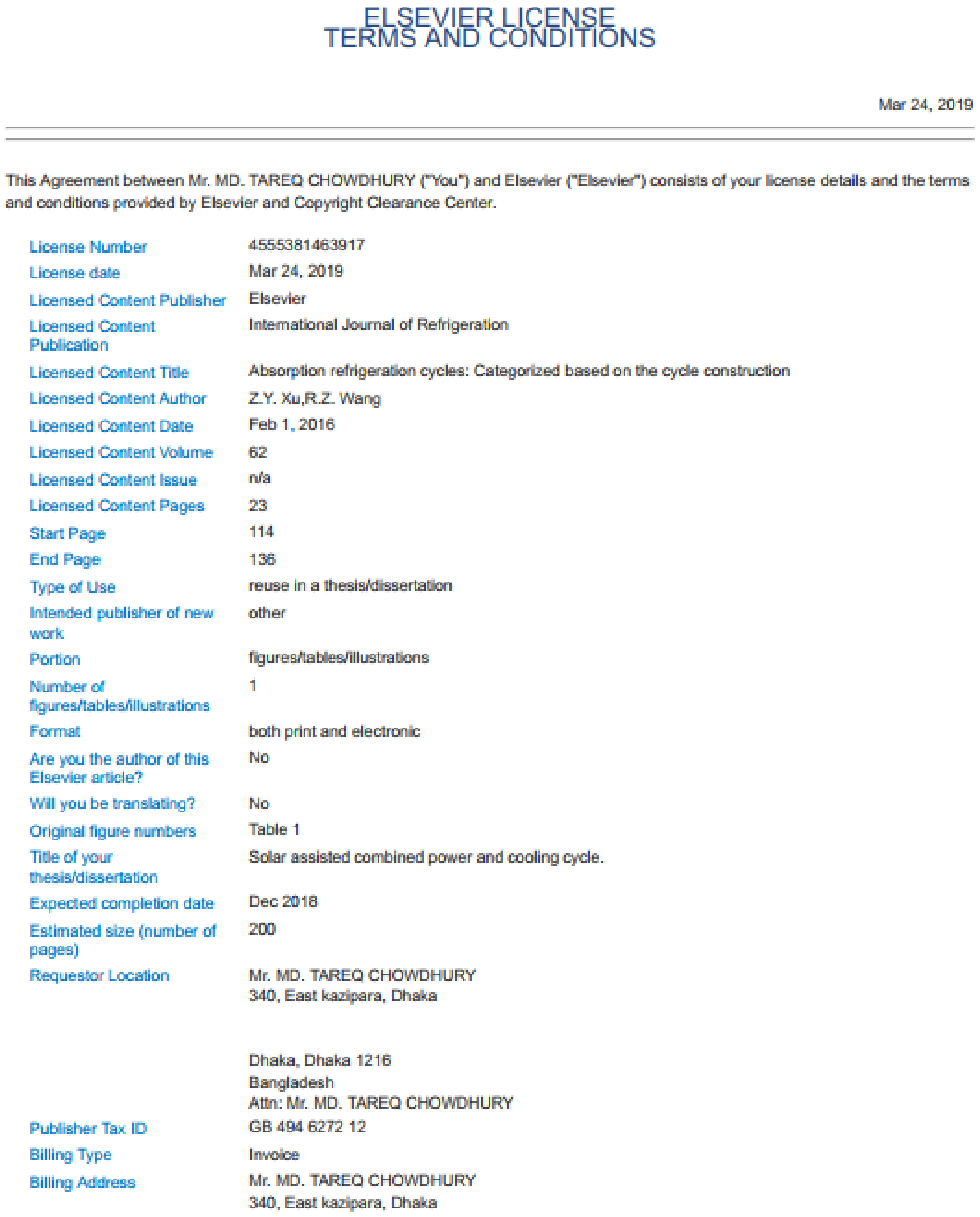

ELSEVIER LICENSE TERMS AND CONDITIONS

Mar 24, 2019

This Agreement between Mr. MD. TAREQ CHOWDHURY ("You") and Elsevier ("Elsevier") consists of your license details and the terms and conditions provided by Elsevier and Copyright Clearance Center.

License Number	4555381463917
License date	Mar 24, 2019
Licensed Content Publisher	Elsevier
Licensed Content Publication	International Journal of Refrigeration
Licensed Content Title	Absorption refrigeration cycles: Categorized based on the cycle construction
Licensed Content Author	Z.Y. Xu,R.Z. Wang
Licensed Content Date	Feb 1, 2016
Licensed Content Volume	62
Licensed Content Issue	n/a
Licensed Content Pages	23
Start Page	114
End Page	136
Type of Use	reuse in a thesis/dissertation
Intended publisher of new work	other
Portion	figures/tables/illustrations
Number of figures/tables/illustrations	1
Format	both print and electronic
Are you the author of this Elsevier article?	No
Will you be translating?	No
Original figure numbers	Table 1
Title of your thesis/dissertation	Solar assisted combined power and cooling cycle.
Expected completion date	Dec 2018
Estimated size (number of pages)	200
Requestor Location	Mr. MD. TAREQ CHOWDHURY 340, East kazipara, Dhaka Dhaka, Dhaka 1216 Bangladesh Attn: Mr. MD. TAREQ CHOWDHURY
Publisher Tax ID	GB 494 6272 12
Billing Type	Invoice
Billing Address	Mr. MD. TAREQ CHOWDHURY 340, East kazipara, Dhaka

VITAE

Name	Md. Tareq Chowdhury.
Nationality	Bangladeshi.
Date of Birth	October 01, 1991.
Email	tareq.me.kuet@gmail.com.
Address	Plot: 010, Road No. 404B, Sector:17, RAJUK Purbachal New Town. P.O. : Rupganj, P.C. : 1460, District: Narayanganj, Bangladesh.
Academic Background	B.Sc. in Mechanical Engineering, Department of Mechanical Engineering, Khulna University of Engineering & Technology, Khulna, Bangladesh. B.Sc. Graduation Date: September 2013.